PROBABILISTIC SEISMIC DEMAND ANALYSIS, SMRF CONNECTION FRACTURES, AND NEAR-SOURCE EFFECTS

A DISSERTATION
SUBMITTED TO THE DEPARTMENT OF CIVIL AND ENVIRONMENTAL ENGINEERING
AND THE COMMITTEE ON GRADUATE STUDIES
OF STANFORD UNIVERSITY
IN PARTIAL FULFILLMENT OF THE REQUIREMENTS
FOR THE DEGREE OF
DOCTOR OF PHILOSOPHY

Nicolas Luco
June 2002

© Copyright by Nicolas Luco 2002
All Rights Reserved

I certify that I have read this dissertation and that, in my opinion, it is fully adequate in scope and quality as a dissertation for the degree of Doctor of Philosophy.

Prof. C. Allin Cornell (Principal Advisor)

I certify that I have read this dissertation and that, in my opinion, it is fully adequate in scope and quality as a dissertation for the degree of Doctor of Philosophy.

Prof. Helmut Krawinkler

I certify that I have read this dissertation and that, in my opinion, it is fully adequate in scope and quality as a dissertation for the degree of Doctor of Philosophy.

Prof. Eduardo Miranda

Approved for the University Committee on Graduate Studies:

Abstract

Probabilistic Seismic Demand Analysis (PSDA) is an approach for computing the mean annual frequency (or annual probability) of exceeding a specified seismic demand for a given structure at a designated site. In short, PSDA combines a ground motion (e.g., spectral acceleration) hazard curve for the designated site, with demand (e.g., drift) results from nonlinear dynamic analysis of the given structure under a suite of earthquake ground motion records. PSDA is already at the core of two recent performance-based seismic guidelines, namely FEMA 350-353 for steel moment-resisting frame buildings, and the draft ISO Offshore Structures Standard. In this dissertation, PSDA is applied, extended, and used as a framework to study two topics in structural engineering that have recently received major attention, particularly since the Northridge earthquake of 1994.

Prompted by damage found after the Northridge event, the first topic of research is the effect of brittle fractures of welded beam-column connections on the seismic performance of steel moment-resisting frame (SMRF) buildings. In an effort to concisely quantify these effects across a range of ground motion intensity levels, PSDA is applied for several SMRF buildings modeled with either brittle or ductile beam-column connections. As a general rule, the additional effects of connection fractures are found to depend on the structural demand level relative to the connection capacities against fracture. An extension of PSDA that quantifies the safety of an earthquake-damaged building that has been only partially inspected for fractured connections is also developed.

Again stimulated by the Northridge earthquake, the second topic of research is how to account for the effects of near-source ground motions on nonlinear structural response in assessing the performance of a building. For several SMRF buildings, it is demonstrated that the nonlinear response to near-source ground motions can be significantly different

than it is for ordinary (i.e., non-near-source) ground motions. Accounting for these differences entails certain modifications to the customary PSDA approach used in assessing structural performance. In particular, new ground motion intensity measures (*IM*'s) and criteria for choosing between alternative *IM*'s are introduced, which when employed in PSDA are demonstrated to ensure its accuracy at a near-fault site.

Acknowledgements

Much of the research regarding SMRF connection fractures that is reported in the first half of this dissertation was conducted pursuant to a contract with the Federal Emergency Management Agency (FEMA) through the SAC Joint Venture.[1] The research regarding near-source effects that is reported in the second half of this dissertation, on the other hand, was largely supported by the U.S.-Japan Cooperative Research in Urban Earthquake Disaster Mitigation Project (NSF 98-36), under grant number CMS-9821096. In addition to these two sources of funding, the author gratefully acknowledges the sponsorship of the National Science Foundation Minority Graduate Fellowships program.

Furthermore, the author appreciatively recognizes the substantial collaboration of Prof. Helmut Krawinkler and now-Dr. Akshay Gupta in researching SMRF connection fractures. Likewise, the author acknowledges the receptive cooperation of Prof. Yasuhiro Mori of Nagoya University and Prof. Masayoshi Nakashima of Kyoto University, as well as of Prof. Gregory Beroza and now-Dr. Martin Mai of Stanford's Department of Geophysics.

The author also would like to thank (i) the signing readers of this dissertation, which included the attentive Prof. Eduardo Miranda, and (ii) the author's dissertation defense committee, which included the involved Dr. Steven Winterstein, Prof. Gregory Deierlein, and Prof. Charles Menun. Last but foremost, the author wholeheartedly thanks his advisor, or more appropriately his mentor, Prof. C. Allin Cornell.

---

[1] SAC is a partnership of the Structural Engineers Association of California (SEAOC), the Applied Technology Council (ATC), and the California Universities for Research in Earthquake Engineering (CUREE). The opinions expressed in this dissertation are those of the author. No warranty is offered with regard to the results, findings, and recommendations, either by FEMA, the SAC Joint Venture, the individual joint venture partners, their directors, members, or employees. These organizations and individuals do not assume any legal liability for the accuracy, completeness, or usefulness of any of the information or processes included in this dissertation.

Contents

Abstract **iv**

Acknowledgements **vi**

1 Introduction **1**

1.1 Overview 1
1.2 Brief Review of Probabilistic Seismic Demand Analysis (PSDA) 2
1.3 Effects of SMRF Connection Fractures 4
1.4 Effects of Near-Source Ground Motions 6
1.5 Organization 10

2 Effects of Connection Fractures on SMRF Seismic Drift Demands **13**

2.1 Introduction 13
2.1.1 Buildings and Earthquake Ground Motion Records 14
2.1.2 Seismic Demand Measures 14
2.1.3 Statistics 15
2.2 Modeling 16
2.2.1 Model Structures 16
2.2.2 Beam-Flange Connection Fracture Model 17
2.2.3 Column Fracture Model 19
2.3 Approach for Sensitivity Studies 20
2.4 Base-Case Fracture Model Parameters 21
2.5 Brittle Base-Case Results 22
2.5.1 Brittle Base-Case Results for Los Angeles 9-Story 22
2.5.2 Brittle Base-Case Results for All Structures 26

2.5.3 Summary of Brittle Base-Case Results 30
2.6 Results of Sensitivity Studies 31
2.6.1 Early Fractures 31
2.6.2 Plastic Rotation Capacity, θ_{f+} 35
2.6.3 Residual Moment Strength, M_{red+} 37
2.6.4 Summary of Results of Sensitivity Studies 37
2.7 Top and Bottom Beam-Flange Connection Fractures 38
2.8 Top- and Bottom-Flange (TBF) Connection Fracture Results 39
2.8.1 TBF Connection Fracture Results for Los Angeles 9-Story 39
2.8.2 TBF Connection Fracture Results for All Structures 43
2.8.3 Anticipating Effect of TBF Connection Fractures 45
2.8.4 Summary of TBF Connection Fracture Results 49
2.9 Column Fractures at Connections 50
2.10 Column Fracture Results 51
2.10.1 Bottom Flange Only (BFO) Column Fracture Case 51
2.10.2 "Pattern" of Column Fracture Triggers in Lower Stories 52
2.10.3 Top and Bottom Flange (TBF) Column Fracture Cases 54
2.10.4 Summary of Column Fracture Results 55
2.11 The Effects of Interior Frames; the M1+ Model 55
2.11.1 Collapses 56
2.11.2 $\theta_{\max}$ Statistics 57
2.11.3 Summary 59
2.12 Conclusions 60

3 Effects of Connection Fractures on SMRF Seismic Drift Demand Hazard 62
3.1 Introduction 62
3.2 Closed-Form Solution of PSDA Integral 63
3.3 Accounting for "Collapses" in PSDA 66
3.4 PSDA for the L.A. 3-Story Building Model 67
3.4.1 Spectral Acceleration Hazard 67
3.4.2 Distribution of Drift Demand given Spectral Acceleration 69
3.4.3 Drift Demand Hazard 72
3.5 PSDA for the L.A. 9- and 20-Story Building Models 74
3.5.1 Spectral Acceleration Hazard 74
3.5.2 Distribution of Drift Demand given Spectral Acceleration Barring Collapse 74

3.5.3 Probability of Collapse given Spectral Acceleration 77
3.5.4 Drift Demand Hazard 80
3.6 Limitations 82
3.7 Conclusions 83

4 Annual Limit-State Frequencies for Partially-Inspected Damaged Buildings 88
4.1 Introduction 88
4.2 Background 89
4.2.1 PSDA 89
4.2.2 Aftershock Ground Motion Hazard 90
4.3 Definitions 90
4.3.1 Limit State 90
4.3.2 Damage State Measure 91
4.4 Procedure 91
4.4.1 Estimating $\lambda_{D|F}(d_{LS} \mid z)$ via PSDA 92
4.4.2 Inferring $f_F(z)$ from Partial Inspection Results 93
4.4.3 Integrating to Arrive at λ_{LS} 95
4.5 Example 96
4.5.1 $\lambda_D(d_{LS})$ Assuming No Damage 97
4.5.2 $\lambda_{D|F}(d_{LS} \mid z)$ for Assumed Damage 99
4.5.3 $f_F(z)$ Inferred from Partial Inspection Results 101
4.5.4 λ_{LS} for Partially-Inspected Damaged Building 103
4.6 Conclusions 105

5 Ground Motion Intensity Measures for Structural Performance Assessment at Near-Fault Sites 106
5.1 Introduction 106
5.2 Criteria for Selecting an Appropriate *IM* to be employed in PSDA 108
5.2.1 "Efficiency" of an *IM* 108
5.2.2 "Sufficiency" of an *IM* 108
5.2.3 Computability of Ground Motion Hazard, λ_{IM} 110
5.3 Shortcomings of $S_a(T_1)$ for PSDA Applications 111
5.3.1 For Near-Source Ground Motions 111
5.3.2 For Tall, Long Period Buildings 112
5.4 Alternative Ground Motion Intensity Measures 112
5.4.1 Elastic-First-Mode Ground Motion Intensity Measure, IM_{1E} 113

5.4.2 Inelastic-First-Mode Ground Motion Intensity Measure, IM_{1I} 113
5.4.3 Elastic-First-and-Second-Mode Ground Motion Intensity Measure, $IM_{1E\&2E}$ 114
5.4.4 Inelastic-First-Mode and Elastic-Second-Mode Ground Motion Intensity Measure, $IM_{1I\&2E}$ 115
5.4.5 "Equivalent"-First-Mode Ground Motion Intensity Measure, IM_{1eq} 115
5.4.6 "Effective"-First-Mode Ground Motion Intensity Measure, IM_{1eff} 116
5.4.7 Vector-Valued Ground Motion Intensity Measures 116
5.4.8 Definition of Participation Factors 117
5.4.9 Definition of Yield Displacement 118
5.5 Approach for Quantifying the Efficiency and Sufficiency of an *IM* 120
5.6 Other PSDA-Based Approaches for Computing λ_{LS} Accurately 123
5.7 Summary 124

6 Evaluation of Alternative Intensity Measures for Near-Source and Ordinary Earthquake Ground Motions 126
6.1 Introduction 126
6.2 Earthquake Ground Motion Records 127
6.3 Building Models 129
6.4 Results with respect to $\theta_{\max}$ 130
6.4.1 $IM_{1E\&2E}$ vs. IM_{1E} for LA20 under Ordinary Ground Motions 130
6.4.2 IM_{1I} vs. IM_{1E} for LA3 under Near-Source Ground Motions 136
6.4.3 $IM_{1I\&2E}$ vs. IM_{1E} for LA9 under Ordinary and Near-Source Ground Motions 140
6.4.4 Summary of Results for IM_{1E}, $IM_{1E\&2E}$, IM_{1I}, and $IM_{1I\&2E}$ 143
6.4.5 IM_{1eq} vs. IM_{1I} for LA3 under Ordinary and Near-Source Ground Motions 145
6.4.6 IM_{1eff} vs. IM_{1I} for LA3 under Ordinary and Near-Source Ground Motions 146
6.4.7 $IM_{1I\&2E}$ with an EPP vs. Negative-Strain-Hardening Backbone Curve for LA20 under Ordinary and Near-Source Ground Motions 147
6.4.8 Summary of Results for IM_{1eq}, IM_{1eff}, and $IM_{1B\&2E}$ 150
6.5 Results with respect to θ_{ave} 150
6.5.1 $IM_{1I\&2E}$ vs. IM_{1E} for LA9 under Ordinary and Near-Source Ground Motions 150
6.5.2 Summary of Results for $IM_{1I\&2E}$ 151

6.6 Results with respect to θ_i 152
6.6.1 $IM_{1I\&2E}$ vs. IM_{1E} for LA9 under Ordinary and Near-Source Ground Motions 152
6.6.2 Summary of Results for $IM_{1I\&2E}$ 156
6.7 Conclusions (bearing in mind the computability of λ_{IM}) 157

7 Demonstration of PSDA at a Near-Fault Site using Simulated Earthquake Ground Motions 161
7.1 Introduction 161
7.2 Characteristic Events on the HRC Fault System 163
7.3 Simulated Earthquake Records at a UCB Site 164
7.3.1 Earthquake Moment Magnitude given Rupture Source Area 165
7.3.2 Spatial Distribution of Slip on Rupture Plane given Seismic Moment 165
7.3.3 Rise Time given Seismic Moment 165
7.3.4 Location of Hypocenter 166
7.4 Ground Motion Hazard at the UCB Site 167
7.5 Drift Demand Hazard for the LA9 Building Model at the UCB Site 172
7.5.1 Simulation-Based Approach 172
7.5.2 PSDA Approach 174
7.6 Conclusions 181

8 Concluding Remarks 185
8.1 Overview 185
8.2 Practical Implications 185
8.2.1 Contributions to FEMA 350-353 Design and Evaluation Guidelines 185
8.2.2 Future Modeling and Testing of SMRF Beam-Column Connections 186
8.2.3 Evaluation of Earthquake-Damaged SMRF Buildings 187
8.2.4 Structural Performance Assessment at Near-Fault Sites 188
8.2.5 Attenuation Relations for New Ground Motion Intensity Measures 188
8.2.6 Simplified Nonlinear Structural Analysis Procedures 189
8.3 Limitations and Future Work 190
8.3.1 Connection Fracture Sensitivity Studies 190
8.3.2 Inspection Guidelines for Earthquake-Damaged SMRF Buildings 190
8.3.3 PSDA at Sites Susceptible to Both Near-Source and Ordinary Ground Motions 191

8.3.4 Additional Evaluations of New Ground Motion Intensity Measures..... 191
8.3.5 Links between SMRF Connection Fractures and Near-Source Effects .. 192

A Earthquake Ground Motion Records for Near-Source Research 194
A.1 Overview..... 194
A.2 Nearby-Field, Intermediate-Field, and Far-Field Earthquake Record Sets..... 197
A.2.1 Forward-Directivity and Backward-Directivity Earthquake Record Subsets..... 198
A.2.2 Supplemental "Pulse-Like" Earthquake Records..... 200

B Building Models for Near-Source Research 233
B.1 Overview..... 233
B.2 Analysis Models..... 234
B.3 Loads 236
B.4 Modal Vibration Properties 237

List of References 253

List of Tables

2-1 Brittle base-case values for the parameters of the connection fracture model. 21

2-2 Counted median and 1-sigma level values of $\theta_{\max}$ under the 10/50 ground motions for all six of the buildings modeled with ductile and with brittle base-case connections. 29

2-3 Median and 1-sigma level $\theta_{\max}$ statistics under the assumption of two different values of p, the probability of "early" (i.e., pre-yield) fracture. 32

2-4 Counted median and 1-sigma level values of $\theta_{\max}$ for the L.A. 9-story modeled with "early" fracturing connections all located in either the lower or upper stories. 33

2-5 Median and 1-sigma level $\theta_{\max}$ statistics under the assumption of a *smaller* plastic rotation capacity against fracture in positive bending (i.e., θ_{f+}) than that assumed in the brittle base case. 36

2-6 Median and 1-sigma level $\theta_{\max}$ statistics under the assumption of a *larger* plastic rotation capacity against fracture in positive bending (i.e., θ_{f+}) than that assumed in the brittle base case. 36

2-7 Median and 1-sigma level $\theta_{\max}$ statistics under the assumption of a smaller residual moment strength in positive bending (i.e., M_{red+}) than that assumed in the brittle base case. 37

2-8 Counted median and 1-sigma level $\theta_{\max}$ statistics for the L.A. 9-story model assuming three different values of the plastic rotation capacity against fracture in negative bending (i.e., θ_{f-}). The counted 1-sigma level $\theta_{\max}$ under the 2/50 ground motions (i.e., seventeenth largest of the twenty values) is a collapse in all of the TBF cases. 40

2-9 Percentage of "extreme" drifts (i.e., θ_{max}>0.10, including collapses) and proportion of collapses among the 2/50 ground motions for the L.A. 9-story model with TBF connection fractures. 42

2-10 Counted 1-sigma level θ_{max} values under the 10/50 ground motions for all six of the buildings modeled with "optimistic" (i.e., $\theta_{f\text{-}}$=0.045) and "pessimistic" (i.e., $\theta_{f\text{-}}$=0.015) TBF connection fractures. "NA" denotes cases that were not considered. 44

2-11 Counted median θ_{max} values under the 2/50 ground motions for all six of the buildings modeled with "optimistic" (i.e., $\theta_{f\text{-}}$=0.045) and "pessimistic" (i.e., $\theta_{f\text{-}}$=0.015) TBF connection fractures. "NA" denotes cases that were not considered. 44

2-12 Percentage of extreme drifts (i.e., θ_{max}>0.10, including collapses) and proportion of collapses among the 2/50 earthquake records for all six of the buildings modeled with "optimistic" (i.e., $\theta_{f\text{-}}$=0.045) and "pessimistic" (i.e., $\theta_{f\text{-}}$=0.015) TBF connection fractures. "NA" denotes cases that were not considered. 45

2-13 Increases in the counted median and 1-sigma level values of θ_{max} for the three Seattle buildings modeled with ductile versus with TBF connection fractures. 48

2-14 Counted median and 1-sigma level values of θ_{max} for the L.A. 9-story model structure in the BFO base case (i.e., with beam-flange fractures) and in the otherwise identical case with column fractures. 52

2-15 Counted median and 1-sigma level values of θ_{max} for the L.A. 9-story model structure in the BFO base case (i.e., with beam-flange fractures) and in the otherwise identical case with column fractures all located in the lower stories. 53

2-16 Counted median and 1-sigma level values of θ_{max} for the L.A. 9-story model structure in the pessimistic TBF case (i.e., with beam-flange fractures) and in the otherwise identical case with column fractures. 54

2-17 Values of θ_{max} for the M1+ models of the L.A. 9-story building subjected to the six earthquake records that cause collapse of the M1 model in the "pessimistic" TBF case (i.e., $\theta_{f\text{-}}$=0.015). Note that the median θ_{max} values are across the six earthquake records, and the percentage increases are with respect to the ductile case. 57

2-18 Counted θ_{max} statistics for the M1+ (and M1) models of three of the SAC buildings. For the L.A. 9-story and Seattle 3-story buildings, the percentage increases in the θ_{max} statistics from the BFO base case to the "optimistic" TBF case (i.e., $\theta_{f\text{-}}$=0.045) are noted. 58

3-1 Median values of S_{a1} and θ_{max} for the L.A. 3-story model and the LA01-LA30 earthquake records. 70

3-2 Estimates of b, a, and σ for the two different $\theta_{max}=a(S_{a1})^b\varepsilon$ fits of the L.A. 3-story model results. 72

3-3 Mean annual frequencies of θ_{max} exceeding 0.03 and 0.08 radians for the L.A. 3-story building models. 72

3-4 Parameters defining the spectral acceleration hazard curves for the L.A. 9-story and L.A. 20-story models. 74

3-5 Median values of S_{a1} and θ_{max}, barring collapse, for the L.A. 9- and 20-story models. 75

3-6 Estimates of b, a, and σ for the two different $\theta_{max}=a(S_{a1})^b\varepsilon$ fits of the L.A. 9-and 20-story model results, barring collapses. 76

3-7 Least-squares regression estimates of b in $\theta_i=a(S_{a1})^b\varepsilon$ for the L.A. 9-story building model. 77

3-8 L.A. earthquake records that cause collapse of the L.A. 9- and/or 20-story models. 78

3-9 Binary regression estimates of the parameters $(s_{a1})_o$ and β. 78

3-10 Mean annual frequencies of θ_{max} exceeding 0.03 and 0.08 radians for the L.A. 3-story building models. 82

3-11 Earthquake record-by-record S_{a1} and θ_{max} results for the ductile and brittle connections cases of the L.A. 3-story building. 85

3-12 Earthquake record-by-record S_{a1} and θ_{max} results for the ductile and brittle connections cases of the L.A. 9-story building. 86

3-13 Earthquake record-by-record S_{a1} and θ_{max} results for the ductile and brittle connections cases of the L.A. 20-story building. 87

4-1 Mean annual frequencies of exceeding the "local" and "global" limit states given the proportion of TFF's among un-inspected connections, F (or the total number of TFF's, M). 101

4-2 Coefficients of the quadratic formulae established for $\lambda_{D|F}(d_{LS}|z)$ with the PSDA estimates of the "local" and "global" annual limit-state frequencies for M=0, 6, and 14 (related to values of F by Equation 4-3 with n=90, n'=10, and m'=1). 104

4-3 Annual limit-state frequencies for the damaged building assuming different partial inspection results with the same observed proportion of TFF's. 104

5-1 $\theta_{\max}$ on IM regression results for the "LA9" building model demonstrating a dependence on M for the relatively insufficient IM_{1E} but not for the relatively sufficient $IM_{1I\&2E}$. 109

6-1 First- and second-mode properties of the three SMRF building models. 129

6-2 Regression analysis results for LA20 subjected to 59 "ordinary" earthquake records, *assuming elastic building response*. In effect, the results compare the bias, efficiency, and sufficiency of the SRSS rule of modal combination with one, two, or three modes. 131

6-3 Regression analysis results for LA3 subjected to 31 near-source earthquake records, *assuming elastic building response*. In effect, the results compare the bias, efficiency, and sufficiency of the SRSS rule of modal combination with one or two modes. 136

6-4 Regression analysis results for LA9 subjected to "ordinary" and near-source earthquake records, *assuming elastic building response*. In effect, the results compare the bias, efficiency, and sufficiency of the SRSS rule of modal combination with one, two, or three modes. 141

6-5 Regression analysis results, for LA9 subjected to "ordinary" and near-source earthquake records, comparing the bias, efficiency, and sufficiency of the ground motion intensity measures $IM_{1I\&2E}$ and IM_{1E}. 142

6-6 Summary of regression analysis results comparing the bias, efficiency, and sufficiency of the four "primary" intensity measures for every combination of the two sets of ground motions and three building models considered. 144

6-7 Regression analysis results, for LA3 subjected to "ordinary" and near-source earthquake records, comparing the bias, efficiency, and sufficiency of the ground motion intensity measures IM_{1eq} and IM_{1I}. 145

6-8 Regression analysis results, for LA3 subjected to "ordinary" and near-source earthquake records, comparing the bias, efficiency, and sufficiency of the ground motion intensity measures IM_{1eff} and IM_{1I}. 147

6-9 Regression analysis results, for LA20 subjected to ordinary and near-source earthquake records, comparing the bias, efficiency, and sufficiency of the ground motion intensity measures $IM_{1B\&2E}$ and $IM_{1I\&2E}$. 149

6-10 Regression analysis results, for LA9 subjected to ordinary and near-source earthquake records, comparing the bias, efficiency, and sufficiency of the intensity measures $IM_{1I\&2E}$ and IM_{1E} with respect to θ_{ave}. 151

7-1 Mean annual recurrence rates and rupture areas for six potential rupture sources, or "characteristic events," on the HRC Fault system, from WG99..... 163

7-2 Mean M_w for each of the HRC rupture sources (of area given in Table 7-1), from WG99. 165

7-3 Median and dispersion of IM_{1E} and of $IM_{1I\&2E}$ from the 30 earthquake records simulated for each HRC rupture source (and scaled up by a factor of two). 170

7-4 Median and dispersion of θ_{max} for the LA9 building model subjected to the 30 earthquake records simulated for each of the HRC rupture sources (and scaled up by a factor of two). 173

7-5 Regression of θ_{max} on IM_{1E} and on $IM_{1I\&2E}$ results for the LA9 building model using the six different sets of 30 earthquake records simulated for the six HRC rupture sources (and scaled up by a factor of two). 179

A-1 Source-to-site distance ranges for earthquake record sets. 195

A-2 Correlation between GM and USGS soil classifications. 196

A-3 "Nearby-field" earthquake record set..... 201

A-4 "Intermediate-field" earthquake record set. 204

A-5 "Far-field" earthquake record set..... 207

A-6 Directivity parameters and modification factors for the nearby-field earthquake records ("forward-directivity" earthquake records in bold). 211

A-7 Directivity parameters and modification factors for the far-field earthquake records ("forward-directivity" earthquake records in bold). 213

A-8 Strike-slip, "forward-directivity" earthquake records of the nearby-field set ranked according to their directivity modification factors..... 215

A-9 Dip-slip, "forward-directivity" earthquake records of the nearby-field set ranked according to their directivity modification factors. 218

A-10 Strike-slip, "forward-directivity" earthquake records of the far-field set ranked according to their directivity modification factors. 221

A-11 Dip-slip, "forward-directivity" earthquake records of the far-field set ranked according to their directivity modification factors. 222

A-12 Supplemental "pulse-like" earthquake records (from Somerville). 224

B-1 Assumed dead and live loads. 236

B-2 Modal periods. 237

B-3 Consolidated sections. 247

B-4 Summary of beam (distributed) gravity loads for LA3. 248

B-5 Summary of column (point) gravity loads for LA3. 248

B-6 Summary of beam (distributed) gravity loads for LA9. 249

B-7 Summary of column (point) gravity loads for LA9. 250

B-8 Summary of beam (distributed) gravity loads for LA20. 251

B-9 Summary of column (point) gravity loads for LA20. 252

List of Figures

1-1 Acceleration and velocity time histories for the (a) Meloland Overpass and (b) Bonds Corner ground motions of the 1979 Imperial Valley earthquake. 7

1-2 Inelastic (normalized by elastic) response spectra for the (a) Meloland Overpass and (b) Bonds Corner ground motions of the 1979 Imperial Valley earthquake. 8

2-1 Moment-rotation hysteretic behavior for the connection fracture model of (a) "early" fracture of the bottom beam-flange only, and (b) top and bottom beam-flange fracture. 18

2-2 Median and 1-sigma level values of (a) θ_{max} and (b) θ_{ave} for the L.A. 9-story modeled with ductile and with brittle (i.e., Bottom Flange Only) base-case connections. Percentage increases from the ductile case to the BFO base case are shown as white bars. 23

2-3 Spatial distribution of the median and 1-sigma level values of θ_i over the height of the L.A. 9-story modeled with ductile and with brittle base-case connections. 25

2-4 Counted median values of (a) θ_{max} and (b) θ_{ave} under the 2/50 ground motions for all six of the buildings modeled with ductile and with brittle (i.e., Bottom Flange Only) base-case connections. Percentage increases from the ductile case to the BFO base case are shown as white bars. 27

2-5 Counted 1-sigma level values of θ_{max} under the 2/50 ground motions for all six of the buildings modeled with ductile and with brittle (i.e., Bottom Flange Only) base-case connections. Percentage increases from the ductile case to the BFO base case are shown as white bars. 28

2-6 Percentage of "extreme" drifts (i.e., θ_{max}>0.10, including collapses) under the 2/50 ground motions for all six of the buildings modeled with ductile and with brittle (i.e., Bottom Flange Only) base-case connections. The minimum θ_{max} in ductile case that becomes an extreme drift in the brittle base case is also noted. 30

2-7 Spatial distribution of the counted median θ_i values over the height of the L.A. 9-story modeled with "early" fracturing connections all located in the *lower* stories and subjected to the 2/50 ground motions. 34

2-8 Spatial distribution of the counted median θ_i values over the height of the L.A. 9-story modeled with "early" fracturing connections all located in the *upper* stories and subjected to the 2/50 ground motions. 35

2-9 Spatial distribution of the counted median θ_i values over the height of the L.A. 9-story modeled with TBF connection fractures and subjected to the 2/50 ground motions. 41

2-10 Increases in the counted median θ_{max} values under the 2/50 ground motions for the three Los Angeles buildings modeled with ductile versus with BFO or TBF connection fractures. 46

2-11 Anticipating the effects of TBF connection fractures on the θ_{max} statistics for all six of the model buildings subjected to the 10/50 and 2/50 earthquake records. Note that the percentage increases are with respect to the ductile case. 49

3-1 Hazard curve for $S_a(T=1.03\text{sec}, \zeta=2\%)$. 68

3-2 S_{a1} versus θ_{max} and least-squares regression results for the LA3 building model with (a) ductile, (b) BFO base case, (c) TBF base case, and (d) TBF extreme case connections. The data points marked with arrows indicate θ_{max} values larger than 0.10 radians. 69

3-3 Comparison of least-squares regression and median-to-median fit approaches to estimating *a* and *b* for the L.A. 3-story modeled with BFO (base case) brittle connections. 71

3-4 Annual hazard curve for maximum story drift angle demand. 73

3-5 Estimated probability of non-collapse versus S_{a1} obtained using binary regression. 79

3-6 Estimated probability of non-collapse versus S_{a1} obtained using binary regression. 80

3-7 Drift demand hazard curves for the L.A. 9-story building modeled with ductile and with brittle connections (for which collapses are observed). 81

3-8 Drift demand hazard curves for the L.A. 20-story building modeled with ductile and with brittle connections (for which collapses are observed). 81

4-1 Ground motion hazard curves for the Stanford site before and after a rupture of the entire Peninsula segment of the San Andreas fault..... 98

4-2 Seismic drift demand hazard curves (computed by PSDA) for the building after the main earthquake, assuming no damage (M=0) or several TFF's (M=6 and M=14)..... 99

4-3 Locations of TFF's and BFF's among the moment-resisting connections in the (9-story, 5-bay) damaged-building models for a given M. Note that the beam-column connections along the right-most column line are not moment-resisting, and that the ground floor is laterally restrained. 100

4-4 Nonlinear dynamic analysis results for those earthquake records that do not cause collapse of the building modeled with three different levels of damage. Along with the ground motion hazard curve depicted in Figure 4-1, these results are used to compute $\lambda_{D|F}(d_{LS}|z)$ via PSDA. 102

4-5 Probability density function for the proportion of TFF's among un-inspected connections given partial inspection results (i.e., m' and n')..... 103

5-1 Illustration of procedure for estimating d_y via NSP..... 119

6-1 Regression of $\theta_{\max}$, for LA20 subjected to "ordinary" earthquake records, on the ground motion intensity measure IM_{1E}, in order to quantify the bias (a) and efficiency (σ) of IM_{1E}..... 133

6-2 Regression of $\varepsilon|IM_{1E}$ (residuals from Figure 6-1) on M, in order to quantify the sufficiency (p–value) of IM_{1E} with respect to M..... 133

6-3 Regression of $\theta_{\max}$, for LA20 subjected to "ordinary" earthquake records, on the ground motion intensity measure $IM_{1E\&2E}$, in order to quantify the bias (a) and efficiency (σ) of $IM_{1E\&2E}$..... 135

6-4 Regression of $\varepsilon|IM_{1E\&2E}$ (residuals from Figure 6-3) on M, in order to quantify the sufficiency (p–value) of $IM_{1E\&2E}$ with respect to M..... 135

6-5 Regression of $\theta_{\max}$, for LA3 subjected to near-source earthquake records, on the ground motion intensity measure IM_{1E}, in order to quantify the bias (a) and efficiency (σ) of IM_{1E}..... 138

6-6 Regression of $\varepsilon|IM_{1E}$ (residuals from Figure 6-5) on R, in order to quantify the sufficiency (p–value) of IM_{1E} with respect to R. 138

6-7 Regression of $\theta_{\max}$, for LA3 subjected to near-source earthquake records, on the ground motion intensity measure IM_{1I}, in order to quantify the bias (a) and efficiency (σ) of IM_{1I}. 139

6-8 Regression of $\varepsilon|IM_{1I}$ (residuals from Figure 6-7) on R, in order to quantify the sufficiency (p–value) of IM_{1I} with respect to R. 139

6-9 First-mode nonlinear static pushover curve for the LA20 building model and the assumed elastic-perfectly-plastic versus bilinear-with-negative-strain-hardening backbone curves. 148

6-10 Regressions of θ_i, for LA9 subjected to "ordinary" earthquake records, on the ground motion intensity measure IM_{1E}, in order to quantify the bias (a) and efficiency (σ) of IM_{1E} for each story (ordered top-left to bottom-right). 153

6-11 Regressions of θ_i, for LA9 subjected to "ordinary" earthquake records, on the ground motion intensity measure $IM_{1I\&2E}$, in order to quantify the bias (a) and efficiency (σ) of $IM_{1I\&2E}$ for each story (ordered top-left to bottom-right)..... 154

6-12 Regressions of θ_i, for LA9 subjected to near-source earthquake records, on the ground motion intensity measure IM_{1E}, in order to quantify the bias (a) and efficiency (σ) of IM_{1E} for each story (ordered top-left to bottom-right). 155

6-13 Regressions of θ_i, for LA9 subjected to near-source earthquake records, on the ground motion intensity measure $IM_{1I\&2E}$, in order to quantify the bias (a) and efficiency (σ) of $IM_{1I\&2E}$ for each story (ordered top-left to bottom-right)..... 156

7-1 Schematic representation of HRC Fault system and UCB site (map view)..... 163

7-2 Probability distributions for the (a) depth and (b) along-strike position of the hypocenter. 166

7-3 Normal probability plots of the log(IM_{1E}) data from the 30 earthquake records simulated for each of the six HRC rupture sources (and scaled up by a factor of two)..... 168

7-4 Normal probability plots of the log($IM_{1I\&2E}$) data from the 30 earthquake records simulated for each of the six HRC rupture sources (and scaled up by a factor of two)..... 169

7-5 Ground motion hazard in terms of IM_{1E} and $IM_{1I\&2E}$ at the UCB site computed using the earthquake records simulated for six "characteristic events" on the HRC Fault system (rather than via PSHA). Recall that the simulated earthquake records have been scaled up by a factor of two. 171

7-6 "Exact" drift demand (i.e., $\theta_{\max}$) hazard for the LA9 building model at the UCB site, compared with the ground motion hazard at the UCB site (from Figure 7-5). Recall that the simulated earthquake records used to compute these hazard curves have been scaled up by a factor of two. 174

7-7 Regressions of $\theta_{\max}$ (from NDA of the LA9 building model) on (a) IM_{1E} and (b) $IM_{1I\&2E}$ for the earthquake records simulated for the SH+NH+RC rupture source (and scaled up by a factor of two). 177

7-8 Regressions of (a) $\varepsilon|IM_{1E}$ and (b) $\varepsilon|IM_{1I\&2E}$ (i.e., residuals from Figure 7-7) on M_w, demonstrating the insufficiency of IM_{1E} and the sufficiency of $IM_{1I\&2E}$ with respect to M_w. 178

7-9 Drift demand hazard for LA9 building model at UCB site computed via PSDA using six different sets of (simulated) earthquake records and employing (a) IM_{1E} or (b) $IM_{1I\&2E}$. Recall that the ground motion hazard (in terms of IM_{1E} or $IM_{1I\&2E}$) has been computed using all of the simulated earthquake records (scaled up by a factor of two). 182

A-1 Contour plot of directivity modification factor for simplified fault geometry and hypocenter location based on (a) the strike-slip Imperial Valley earthquake of 1979, and (b) the dip-slip Northridge earthquake of 1994 210

A-2 Time histories for the "pulse-like" NS23 ground motion (i.e., strike-normal component of IMPVALL\H-EMO from nearby-field set). 225

A-3 Time histories for the "pulse-like" NS21 ground motion (i.e., strike-normal component of IMPVALL\H-E06 from nearby-field set). 225

A-4 Time histories for the "pulse-like" NF09 ground motion (i.e., strike-normal component of ERZIKAN\ERZ from nearby-field set). 226

A-5 Time histories for the "pulse-like" NS31 ground motion (i.e., strike-normal component of NORTHR\NWH from nearby-field set). 226

A-6 Time histories for the "pulse-like" NF13 ground motion (i.e., strike-normal component of NORTHR\RRS from nearby-field set). 227

A-7 Time histories for the "pulse-like" NS33 ground motion (i.e., strike-normal component of NORTHR\SPV from nearby-field set)..... 227

A-8 Time histories for the "pulse-like" NF15 ground motion (i.e., strike-normal component of NORTHR\SYL from nearby-field set). 228

A-9 Time histories for the "pulse-like" NF17 ground motion (i.e., strike-normal component of KOBE\KJM from nearby-field set). 228

A-10 Time histories for the (a) strike-normal (.fn) and (b) strike-parallel (.fp) component of the MORGAN\AND ground motion. 229

A-11 Time histories for the "pulse-like" NF03 ground motion (i.e., strike-normal component of Loma Prieta-Los Gatos from Somerville)..... 230

A-12 Time histories for the "pulse-like" NF05 ground motion (i.e., strike-normal component of Loma Prieta-Lexington Dam from Somerville). 230

A-13 Time histories for the "pulse-like" NF11 ground motion (i.e., strike-normal component of Landers-Lucerne from Somerville). 231

A-14 Time histories for the "pulse-like" NF19 ground motion (i.e., strike-normal component of Kobe-Takatori from Somerville)..... 231

A-15 Time histories for the "pulse-like" NS25 ground motion (i.e., strike-normal component of Kobe-Port Island from Somerville). 232

A-16 Time histories for the "pulse-like" NS29 ground motion (i.e., strike-normal component of Morgan Hill-Coyote Lake Dam from Somerville). 232

B-1 Comparing SPO's for M1, M1#, & M1+ models of LA9. 235

B-2 Moment-rotation model for shear connections. 236

B-3 L.A. 3-story typical floor plan..... 238

B-4 L.A. 3-story perimeter MRF (N-S elevation)..... 239

B-5 L.A. 3-story (consolidated) interior gravity frame (N-S elevation)..... 239

B-6 L.A. 9-story typical floor plan..... 240

B-7 L.A. 9-story perimeter MRF (N-S elevation)..... 241

B-8 L.A. 9-story (consolidated) interior gravity frame (N-S elevation)..... 242

B-9 L.A. 20-story typical floor plan. 243

B-10 L.A. 20-story perimeter MRF (N-S elevation). 244

B-11 L.A. 20-story interior gravity frame (N-S elevation)..... 245

B-12 L.A. 20-story (consolidated) exterior gravity column (N-S elevation). 246

Chapter 1

Introduction

1.1 Overview

In this dissertation, an approach known as Probabilistic Seismic Demand Analysis (PSDA) is applied, extended, and used as a framework to study two topics in structural engineering that have recently received major attention, particularly since the Northridge earthquake of 1994. Prompted by damage found after the Northridge earthquake, the first topic of research is the effects of brittle fractures of welded beam-column connections on the seismic performance of steel moment-resisting frame (SMRF) buildings. In addition to applying PSDA to quantify the effects of such fractures for previously undamaged buildings, an extension of PSDA is developed for quantifying the safety of an earthquake-damaged building that has only been partially inspected for fractured connections. Also stimulated by the Northridge earthquake, the second topic of research is how to account for the effects of near-source earthquake ground motions on nonlinear structural response in assessing the performance of SMRF buildings at near-fault sites. Considering primarily the effects of "ordinary" (i.e., non-near-source) ground motions, PSDA is already at the core of post-Northridge design and evaluation recommendations for SMRF buildings (i.e., FEMA 350-353). Accounting for the effects of near-source ground motions, however, requires some modifications to the customary PSDA approach in order to ensure its accuracy. Before describing in more detail the two topics of research, a review of PSDA is due.

1.2 Brief Review of Probabilistic Seismic Demand Analysis (PSDA)

Probabilistic Seismic Demand Analysis (PSDA) is an approach for computing the mean annual frequency (or annual probability) of exceeding a specified seismic demand for a given structure at a designated site (Cornell 1996). Analogous to a ground motion hazard curve computed by Probabilistic Seismic Hazard Analysis (PSHA) (Cornell 1968), the principal result of PSDA is a structural demand hazard curve. As PSDA itself is not the focus of this dissertation, only a brief review of the approach is supplied here. A history of the development of PSDA can be found in (Shome 1999), and comparisons with similar approaches taken by other researchers, such as Wen (e.g., Collins *et al.* 1995) and Ellingwood (e.g., Song & Ellingwood 1999) can be found in (Bazzurro 1998) and (Shome 1999).

In short, PSDA combines a ground motion (e.g., spectral acceleration) hazard curve for the designated site, typically computed via PSHA, with the demand (e.g., drift) results from nonlinear dynamic analysis (NDA for short) of the given structure under a suite of earthquake ground motion records. The approach is an application of the "total probability theorem" (e.g., Benjamin & Cornell 1970), which is also at the foundation of PSHA. With *DM* denoting a structural demand measure (e.g., drift response)[1] and *IM* a ground motion intensity measure (e.g., spectral acceleration), PSDA is expressed mathematically in Equation 1-1 (e.g., Cornell & Krawinkler 2000).

$$\lambda_{DM}(y) = \int G_{DM|IM}(y \mid x) \;\; |\, \mathrm{d}\lambda_{IM}(x) \,| \tag{1-1}$$

The mean annual frequency (MAF for short) of *DM* exceeding the value y, or the *DM* hazard, is denoted $\lambda_{DM}(y)$; likewise, $\lambda_{IM}(x)$ is the ground motion hazard in terms of *IM* (evaluated at x), and $\mathrm{d}\lambda_{IM}(x)$ denotes its differential with respect to *IM* (also evaluated at x). In simplistic terms, $\mathrm{d}\lambda_{IM}(x)$ is the (annual) probability of observing a particular ground motion intensity. Strictly it is the mean ground motion hazard *density*, $\frac{\mathrm{d}\lambda_{IM}}{\mathrm{d}x}(x)$, times the differential $\mathrm{d}x$. The term $G_{DM|IM}(y|x)$, which is customarily estimated using NDA results for a suite of earthquake records, denotes the probability of *DM* exceeding the value y given (i.e., conditioned on knowing) that *IM* equals x. Note that $G_{DM|IM}(y|x)$

[1] Note that the Pacific Earthquake Engineering Research (PEER) community now uses *DM* as an abbreviation for *damage measure*, and instead denotes the engineering demand parameter of interest as *EDP*.

intrinsically accounts for the variability of structural demand given the level of ground motion intensity, which is due to differences among ground motions.

With structural capacity information, the results of PSDA (i.e., λ_{DM}) can be used to compute the MAF of exceeding a specified limit state (e.g., the collapse limit state), often referred to as an "annual limit-state frequency." Denoted λ_{LS}, the MAF of exceeding the limit state *LS* is given by Equation 1-2.

$$\lambda_{LS} = \int G_{LS|DM}(y) \; |\, \mathrm{d}\lambda_{DM}(y) \,| \tag{1-2}$$

In Equation 1-2, $\mathrm{d}\lambda_{DM}(y)$ denotes the differential of the structural demand hazard with respect to *DM* (evaluated at *y*); in effect, it is the (annual) probability of observing a particular value of *DM*. The term $G_{LS|DM}(y)$ denotes the probability of exceeding the limit state *LS*, given that *DM* equals *y*. Typically, a limit state is characterized by a random-valued capacity with the same units as *DM*, in which case $G_{LS|DM}(y)$ is simply the probability that this capacity is less than *y*. Estimating dynamic structural capacities (e.g., Vamvatsikos 2001) is not within the scope of this research; therefore, the limit states considered in this dissertation are simply defined by deterministic values of structural (e.g., drift) capacity. In this case, $G_{LS|DM}(y)$ is simply an indicator function equal to one if *y* is greater than the deterministic capacity (zero otherwise), and λ_{LS} is equivalent to $\lambda_{DM}(y)$ evaluated at this capacity.

A structural demand hazard curve (i.e., λ_{DM}) or an annual limit-state frequency (i.e., λ_{LS}) computed via Equation 1-1 or 1-2, respectively, can be used in a performance-based design or evaluation. For example, λ_{LS} can be used to make decisions about the adequacy of a structural design (e.g., Cornell *et al.* 2001, Carballo 2000), or the need to retrofit an existing structure. In fact, a closed-form solution of Equation 1-2 for λ_{LS} has been transformed to a Load and Resistance Factor Design (LRFD) type format in two recent performance-based seismic guidelines, namely FEMA 350-353 (2001) for SMRF buildings, and the draft ISO Offshore Structures Standard (Younan *et al.* 2001). The Pacific Earthquake Engineering Research (PEER) center has also recently adopted PSDA as a "foundation on which performance assessment can be based" (Cornell & Krawinkler 2000). Yet another notable application of PSDA is structure-specific expected-loss estimation, which can be accomplished by combining a demand hazard curve with demand-to-damage and damage-to-cost relationships (e.g., Porter 2001). As outlined in the previous subsection, in this dissertation PSDA is used as a vehicle to (i) investigate the effects of connection fractures, and (ii) to account for the effects of near-source

ground motions, both in terms of the seismic performance of SMRF buildings. An introduction to these two structural engineering problems is provided in the following two subsections.

1.3 Effects of SMRF Connection Fractures

After the Northridge earthquake of 1994, a significant number of welded beam-column connections in steel moment-resisting frame (SMRF) buildings were found to have experienced brittle fracture. As reported by subsequent (and some previous) laboratory tests (e.g., FEMA 289), fracture can significantly reduce the strength and stiffness of such connections. Even so, the SMRF buildings subjected to Northridge ground motions met the basic objective of design codes in that they did not collapse. However, the buildings did not behave in the expected ductile manner, and significant economic losses resulted. Furthermore, in many of the SMRF buildings, connections fractured despite relatively mild ground motions, raising questions about their ability to withstand stronger motions. Although new, "post-Northridge" connection designs (e.g., reduced beam sections) aim to avoid (or at least delay) fractures in new designs and retrofits, there exists a large stock of presumably undamaged and still un-inspected or partially-inspected damaged SMRF buildings with "pre-Northridge" connections. Hence, there remains a concern as to how SMRF buildings might perform in future earthquakes of different intensities.

Within a year of the Northridge earthquake, the SAC[2] Steel Project began an extensive study of the seismic performance of SMRF buildings, with funding from the Federal Emergency Management Agency (FEMA). In order to standardize, yet also generalize the study, SAC commissioned structural design firms in three different geographical regions to design a low-rise, a mid-rise, and a high-rise SMRF building according to pre-Northridge practices. Furthermore, for each of the geographical regions several suites of earthquake ground motion records were compiled (Somerville *et al.* 1997a). As part of Phase II of the SAC Steel Project, which culminated in the FEMA 350-353 seismic guidelines for SMRF buildings, the research reported in this dissertation on the effects of connection fractures on SMRF seismic demands and safety was

[2] SAC is an acronym for SEAOC (Structural Engineers Association of California), ATC (Applied Technology Council), and CUREe (California Universities for Research in Earthquake Engineering).

conducted (Subtask 5.4.6).[3] Other researchers who have studied the effects of connection fractures include Shi & Foutch (1997), Song & Ellingwood (1998), Maison (1999), Yun & Foutch (2000), and Lee & Foutch (2002).

In this dissertation (as for the SAC project), the effects of brittle connection behavior on the seismic performance of the SAC (pre-Northridge) SMRF buildings are assessed by carrying out NDA (nonlinear dynamic analysis) using the SAC earthquake records. The presumably undamaged buildings are modeled with (i) brittle connections that are susceptible to fracture under large enough rotational demands, and (ii) perfectly ductile connections. In this way, the effects of brittle connection behavior are quantified relative to the ductile connection response of SMRF buildings that was anticipated prior to the Northridge event. Lacking a practical theoretical model that can accurately predict beam-column connection fracture, an empirical analysis model for brittle connection behavior is employed. Despite testing and analysis, there remains major uncertainty associated with when and why a given connection will fracture and how fracture adversely affects the strength and stiffness of a connection. Also, connection fracture is apparently random in nature (i.e., different for nominally identical connections). Hence, although the parameters of the brittle connection model are calibrated with the limited field and laboratory data, they are also varied systematically in order to study the corresponding sensitivities of the structural response (e.g., inter-story drift demands). By doing so, an improved understanding of the possible effects of connection fractures is developed, which can be applied to "interpolate" the effects of brittle connection behavior even if slightly different assumptions are made for the fracture model. In turn, the results of such sensitivity studies can help to determine the most important aspects of connection fracture to capture in experimental tests (e.g., it was learned that tests should be continued until both beam-flange connections fracture), as well as in local finite-element analysis, fracture-model parameter estimation, and future guidelines and limitations. The results of the sensitivity studies have also guided subsequent SAC analyses aimed at establishing global structural-collapse capacities for the FEMA 350-353 guidelines (Yun & Foutch 2000).

Just as the response of a structure can vary significantly from earthquake record to earthquake record, so can the effects of connection fractures. Thus, in addition to quantifying the effects of connection fractures on structural demands for the SAC earthquake record sets, PSDA is employed as a concise way to summarize the effects

[3] Much of the SMRF connection-fracture research described in this dissertation (Chapters 2-4) was first reported in a technical background document for SAC (Cornell & Luco 1999), which is expected to become available from ATC at some future date.

across a range of ground motion intensity levels. Structural demand hazard curves (computed via PSDA for a range of structural demand levels) are compared for the originally undamaged SAC buildings modeled with brittle versus with ductile connections; in this way, the effects of connection fractures are concisely quantified relative to ductile response. In order to assess the safety of an earthquake-damaged SMRF building that has been only partially inspected for fractured beam-column connections (e.g., due to the expense of inspecting), an extension of PSDA is also developed. The approach estimates an annual limit-state frequency for a damaged building that reflects the uncertainty in the true state of damage; this estimate can be compared to either a prescribed standard or to the results assuming no damage. Clearly, PSDA provides a foundation for assessing the performance of both undamaged and damaged pre-Northridge SMRF buildings.

1.4 Effects of Near-Source Ground Motions

Also during the Northridge earthquake of 1994, numerous ground motions were recorded at stations near the fault rupture. Similar to certain records observed during, for example, the Imperial Valley earthquake of 1979, a number of these earthquake records exhibited the low frequency, large amplitude "pulse" in the velocity time history of the strike-normal component that has become synonymous with near-source ground motions.[4] Such pulses are basically the result of a superposition of shear waves that travel at about the same speed as the fault rupture[5] in the direction of the rupture propagation (i.e., towards the "forward rupture-directivity" region). The radiation pattern of shear waves, which are strongly excited by shear dislocation sources like the Northridge and Imperial Valley shallow crustal earthquakes, causes the strong pulse to be oriented perpendicular to the fault (e.g., Somerville *et al.* 1997b). By significantly increasing the limited number of near-source earthquake records available, the Northridge event renewed interest in the effects of near-source ground motions on structural performance.

Since the 1994 earthquake, several researchers have demonstrated that the nonlinear response of structures to near-source ground motions can be significantly different than it

---

[4] As defined more precisely in Chapter 6 (and Appendix A), the term "near-source" is used in this dissertation to describe ground motions at sites that are not only close to a fault-rupture, but are also located in the forward rupture-directivity region. Many, but not necessarily all, of these ground motions can be further classified as "pulse-like."

[5] Typical fault rupture velocities are 80% to 90% of the shear wave velocity.

is for ordinary (i.e., non-near-source) ground motions (Alavi & Krawinkler 2000, Hall 1998, Hall *et al.* 1995, Heaton *et al.* 1995, Iwan 1996, Attalla *et al.* 1998, Bozorgnia & Mahin 1998). More specifically, there is ample evidence that near-source ground motions can cause substantially larger nonlinear structural demands than do ordinary ground motions of comparable intensity. As an example, consider the 1979 Imperial Valley earthquake ground motions recorded at the Meloland Overpass (labeled EMO) and Bonds Corner (labeled BCR) stations, which are depicted in Figure 1-1. Both stations are located very close to the rupture surface (i.e., 0.5km for EMO and 2.5km for BCR), but only the EMO station is in the forward rupture-directivity region. Note the "pulse-like" nature of the EMO earthquake record (a manifestation of forward rupture directivity) compared to the more ordinary BCR earthquake record (despite its proximity to the fault).

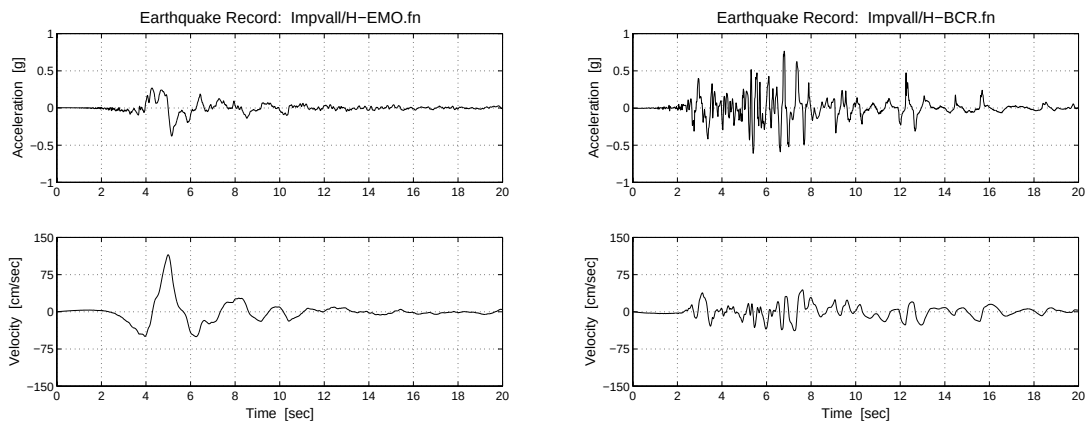

Figure 1-1. Acceleration and velocity time histories for the **(a)** Meloland Overpass and **(b)** Bonds Corner ground motions of the 1979 Imperial Valley earthquake.

Next consider the response of simple elastic and inelastic oscillators to these ground motions. In Figure 1-2, the ratio of the inelastic (i.e., elastic-perfectly-plastic) to elastic spectral displacements at initial periods ranging from 0 to 2.5 seconds is plotted for strength reduction factors of 1, 2, 4, and 8. Clearly the inelastic response (relative to the elastic response) can be significantly larger for a pulse-like ground motion like EMO than it is for an ordinary ground motion like BCR. This can be true even at the moderate periods for which the "equal displacements rule"[6] (Veletsos & Newmark 1960), based

[6] The equal displacements rule asserts that a moderate-period inelastic spectral displacement is approximately equal to its elastic counterpart. The rule is based on inelastic and elastic earthquake time-history analysis results (for single-degree-of-freedom oscillators).

predominantly on ordinary ground motions, is expected to apply. Even before the Northridge earthquake, the same phenomenon had been demonstrated for SDOF (single-degree-of-freedom) oscillators by several researchers (e.g., Veletsos & Newmark 1965, Bertero *et al.* 1978, Anderson & Bertero 1987); more recently, Baez & Miranda (2000) have reported this effect of near-fault ground motions on inelastic (to elastic) displacement ratios. It should be noted that the elastic spectral displacements can also differ for pulse-like versus ordinary ground motions, even from earthquakes of the same magnitude at the same distance from the site. In fact, Somerville *et al.* (1997b) have modified existing attenuation relations to correct for the fact that, in the forward rupture-directivity region, elastic spectral acceleration at periods above 0.6 seconds tend to be larger than those predicted by the existing relations.

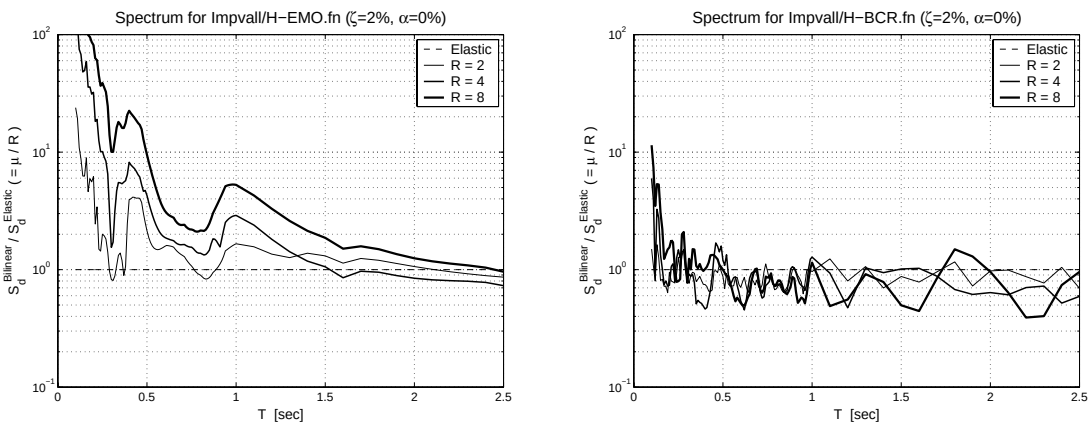

Figure 1-2. Inelastic (normalized by elastic) response spectra for the **(a)** Meloland Overpass and **(b)** Bonds Corner ground motions of the 1979 Imperial Valley earthquake.

Given the potential effects of near-source ground motions, the focus in this dissertation is on how to account for these effects in assessing the performance of a structure at a near-fault site. As mentioned above, PSDA has already been implemented in recent performance assessment schemes, but primarily for ordinary ground motions; here the goal is to also account for the effects of near-source ground motions within the framework of PSDA. Conventionally (e.g., for the SAC Steel Project), the ground motion intensity measure (i.e., *IM*) employed for PSDA is spectral acceleration (at or near the fundamental period of the given structure, typically with a damping ratio of 5%). Compared to peak ground acceleration (PGA), for example, spectral acceleration is more closely related to structural demands (as it is period-specific) and thus it reduces the

number of NDA's under different earthquake records that are necessary for PSDA (Shome *et al.* 1998). However, the observed differences in nonlinear structural demands due to near-source versus ordinary ground motions with the same (elastic) spectral acceleration suggest that alternative ground motion intensity measures (*IM*'s) may be more effective. Furthermore (as explained in Chapter 5), an *IM* other than spectral acceleration may be necessary to ensure the accuracy of the PSDA integral expressed in Equation 1-1; otherwise, the form of the PSDA integral must be adjusted, at the expense of complicating the procedure.

In this dissertation, several alternative structure-specific *IM*'s are investigated, paying close attention to their correlation to nonlinear demands for SMRF buildings subjected to near-source and ordinary ground motions. The suites of near-source and ordinary earthquake records are compiled from the PEER strong motion database. Once again, the SAC SMRF buildings are used and structural demands are computed via NDA. As the investigation is part of the U.S.-Japan Cooperative Research in Urban Earthquake Disaster Mitigation (funded by the National Science Foundation), additional SMRF buildings and ground motions specific to Japan have been considered in collaboration with Professor Y. Mori of Nagoya University and Professor M. Nakashima of Kyoto University (Luco *et al.* 2002a). The collaborators have also made use of "fish-bone" models of SMRF buildings (e.g., Nakashima *et al.* 2002). In the research community, finding alternative ground motion intensity measures has also recently become a goal of the PEER center. At a workshop held in late 2000, PEER researchers laid plans "to build a consensus on ground motion intensity measures critical for evaluating structural and geotechnical performance indices, and to propose ways to develop seismic hazard data for such ground motion intensity measures." The latter of these two goals is also addressed in this dissertation, as introduced next.

In assessing the seismic performance of a structure, recall that PSDA makes use of the ground motion hazard at the site in terms of *IM*. Whereas spectral acceleration hazard curves are readily available (e.g., from the U.S. Geological Survey) or commonly computed, the seismic hazard at a site in terms of the alternative structure-specific *IM*'s remains to be computed. To do so via PSHA, for example, requires an attenuation relation for *IM* that is applicable in the near field. Given the limited number of recorded near-source ground motions available, simulated earthquake records are particularly valuable for this purpose. In a cooperative effort, the near-source earthquake records that can be used to compute the ground motion hazard at a site in terms of the alternative *IM*'s have been simulated by Professor G. Beroza and Ph.D. Candidate M. Mai of Stanford's Department of Geophysics (Mai 2002). Although developing attenuation relations for

alternative *IM*'s is beyond the scope of this dissertation, simulated ground motions are used here to demonstrate an alternate approach to computing the ground motion hazard at a site in terms of any *IM*. The simulation-based approach accounts for many of the variabilities inherent in the details of earthquake rupture. Of course, the simulations can also be used to investigate the nature of near-source ground motions.

1.5 Organization

The first half of this dissertation (i.e., Chapters 2-4) covers the effects of connection fractures on the structural demands and safety for SMRF buildings. The second half (i.e., Chapters 5-7) explores ways to account for the effects of near-source ground motions on nonlinear response in assessing the seismic performance of SMRF buildings. Links between the two topics, as well as practical implications and limitations of the research, are discussed in Chapter 8. Details of the earthquake ground motion records and building models used in the near-source research are reported in Appendix A and B, respectively.

More specifically, in Chapter 2 the effects of connection fractures on the seismic drift demands (computed via NDA) are quantified for the SAC SMRF buildings subjected to the SAC sets of earthquake records at two different probability levels. Drift demand statistics for each of the two ground motion sets are compared for the buildings modeled with brittle versus with ductile connections. The sensitivities of the drift demand statistics to variations in the parameters of the empirical analysis model for brittle connection behavior are also studied. In particular, the case when only bottom beam-flange connections fracture is contrasted with the case of both top and bottom beam-flange fracture. The effects of connection fractures that propagate into the column flange/web rather than the beam flange/web are also considered. Based on the resulting drift demand statistics, a simple way to anticipate the effects of top and bottom beam-flange fractures is demonstrated.

In Chapter 3, the effects of connection fractures on the seismic drift demand *hazard*, computed via PSDA using the drift demand results from Chapter 2, are quantified for several of the SMRF buildings. Taking advantage of certain simplifying assumptions, a closed-form solution of the PSDA integral (i.e., Equation 1-1) is employed for the building models that do not "collapse" under any of the ground motions; an expansion of the PSDA integral is applied to account for "collapses." A comparison of drift demand hazard curves for the buildings modeled with brittle versus with ductile connections leads to conclusions similar to those reached in Chapter 2, but in a much more concise manner.

In Chapter 4, an extension of PSDA is developed for estimating an annual limit-state frequency for an earthquake-damaged SMRF building that has been partially inspected for fractured beam-column connections. The new approach accounts for the uncertainty, due to incomplete inspection, in the total number and locations of fractured connections. Since an aftershock ground motion hazard curve can be used in PSDA, an annual limit-state frequency estimated for the damaged building can serve as a basis for deciding, for example, whether it is safe to permit occupancy soon after a main-shock. Conversely, an estimated annual limit-state frequency can be used to guide inspection decisions, such as whether to inspect more connections and thereby reduce the uncertainty in the state of damage. As an example, the approach is demonstrated for one of the SAC SMRF buildings, again using some of the SAC earthquake records.

In Chapter 5, a few ways of accounting for (within the framework of PSDA) the effects of near-source ground motions on nonlinear response in assessing the performance of a structure are explained. In particular, several alternative (e.g., to the conventional spectral acceleration) ground motion intensity measures (*IM*'s) are introduced that are meant to ensure the accuracy and precision of the PSDA integral (i.e., Equation 1-1) at a near-fault site. Two criteria that facilitate a comparison of such *IM*'s are defined, namely the "efficiency" and "sufficiency" of an *IM*. An approach is outlined for quantifying these criteria via (i) NDA of the given structure under a suite of earthquake records, and (ii) linear regression analysis. The other schemes discussed for ensuring an accurate application of PSDA include an expansion of Equation 1-1 or the incorporation of site seismicity information from disaggregation of the ground motion hazard.

In Chapter 6, the criteria defined in Chapter 5 for comparing alternative ground motion intensity measures that are intended for use in a structural performance assessment at a near-fault site (via PSDA) are evaluated. Specifically, the "efficiency" and "sufficiency" of the alternative *IM*'s introduced in Chapter 5 are quantified (via the approach outlined in Chapter 5) and compared using the results for three of the SAC SMRF building models (detailed in Appendix B) subjected to near-source and ordinary ground motions (detailed in Appendix A). An apparent trade-off between (i) the efficiency and sufficiency of the alternative ground motion intensity measures, and (ii) the computability of the ground motion hazard for each of the alternative intensity measures are also discussed.

In Chapter 7, a structural performance assessment is carried out via PSDA for one of the SAC SMRF buildings hypothetically located a site near the Hayward-Rogers Creek (HRC) Fault system. In additional to spectral acceleration (at or near the fundamental

period of the building), one of the alternative ground motion intensity measures introduced in Chapter 5 and demonstrated to be "efficient" and "sufficient" in Chapter 6 is employed. Rather than applying conventional PSHA, the ground motion hazard at the near-fault site is computed using simulated earthquake records for six possible earthquake rupture sources on the HRC Fault system that are considered by the 1999 U.S. Geological Survey Working Group on California Earthquake Probabilities. The structural demand hazard at the near-fault site is also computed directly with this approach, and compared to the results of PSDA using the two different ground motion intensity measures.

Chapter 2

Effects of Connection Fractures on SMRF Seismic Drift Demands

2.1 Introduction

In a subsequent chapter (i.e., Chapter 3), PSDA is carried out in order to evaluate the effects of brittle beam-column connection fractures on the seismic drift demand hazard for SMRF buildings. As a first step, though, the effects of connection fractures on the drift demands themselves are quantified in this chapter. This is done by comparing the results of NDA (nonlinear dynamic analysis) for buildings modeled with all brittle versus with all ductile connections. As one might expect, the effects of connection fractures can depend on the building model, the earthquake ground motion, and the structural demand measure considered. Accordingly, several building designs and earthquake records were considered during Phase II of the SAC Steel Project (which culminated in FEMA 350-355, 2000). Although the focus of this dissertation is narrowed to drift demands in general, several different measures of drift demand are considered. Rather than comparing these demand measures for the brittle versus ductile connections cases on an earthquake record-to-records basis, several different statistics across earthquake records are considered.

In computing the seismic drift demands via NDA, an empirical analysis model for brittle connection behavior is employed. Wherever possible, the parameters of the model are calibrated with field and laboratory data. However, because the quantity of available test data is limited, the model parameters are also varied systematically to measure the

sensitivity of the resulting drift demands. In particular, the case in which only the bottom beam-flange connections may fracture (i.e., infinite resistance against fracture at the top beam-flange) is contrasted with the case of both top and bottom beam-flange fracture. The effects of connection fractures that propagate into an adjacent column flange, and perhaps web, are also investigated. Using the results of such sensitivity studies, a means of anticipating the effects of connection fractures is derived based on the capacities of the beam-column connections against fracture and the ductile response of the building. Note that portions of this chapter have been published, in similar form, as an article in the *ASCE Journal of Structural Engineering* (Luco & Cornell 2000)

2.1.1 Buildings and Earthquake Ground Motion Records

The SMRF buildings investigated in this chapter (and throughout this dissertation) are a subset of the low-rise (3-story), medium-rise (9-story), and high-rise (20-story) buildings designed by consulting structural engineers as part of the SAC Steel Project (FEMA 355C, 2000). The designs considered here were carried out according to pre-Northridge practices (i.e., UBC 1994) for conditions in Los Angeles and Seattle. In all, six different building designs are investigated (i.e., three different heights and two different geographical regions). Details of the three Los Angeles buildings, which are also considered in Chapters 3-7, are provided in Appendix B. Note that all of the buildings considered are perimeter SMRF's of four to six bays.

For both the Los Angeles and Seattle regions, several sets of corresponding earthquake ground motion records were gathered for the SAC Steel Project as well. Among them, the sets of twenty earthquake records at the 10% in 50 years (denoted 10/50) and the 2% in 50 years (denoted 2/50) probability levels specific to each region are utilized in this chapter (as well as in Chapters 3 and 4). The earthquake records consist of both simulated and recorded ground motions, and were scaled to match (in a weighted-least-squares residual sense) the 1997 USGS mapped spectral values (for each of the two probability levels) at four periods near the fundamental periods of the SAC buildings (Somerville *et al.* 1997a). In all, eighty ground motions are considered (i.e., twenty for each of the two probability levels and two geographical regions).

2.1.2 Seismic Demand Measures

As a compromise between global response measures such as roof drift and local demands such as beam plastic hinge rotations, inter-story drift angle (i.e., story drift

normalized by story height) is the primary seismic response parameter of interest in this dissertation and for the SAC project in general. Peak (over time) story drift angles are commonly expected to correlate well with structural and certain types of nonstructural damage, as well as with structural stability (NEHRP 1997). In this chapter, maximum (among all stories) peak story drift angle (denoted as $\theta_{\max}$) is used as a convenient scalar demand measure that characterizes the collapse-level drift response. Similarly, average (over all stories) peak story drift angle (denoted θ_{ave}) is considered as a scalar demand measure associated with overall building damage. The spatial variation of peak story drift angle demands (denoted as θ_{i} for i^{th} story) is also compared for each building modeled with brittle versus ductile connections.

2.1.3 Statistics

Rather than comparing the drift demands for each of the SMRF buildings modeled with brittle versus ductile connections on an earthquake record-to-record basis, drift demand statistics for the 10/50 and 2/50 sets of ground motions are evaluated. Specifically, the "median" and the "1-sigma level" statistics are calculated for the drift demands ($\theta_{\max}$, θ_{ave}, or θ_{i}) resulting from the 20 earthquake records at each probability level (i.e., 10/50 or 2/50). The median is ordinarily estimated here by the geometric mean, or equivalently the exponential of the average of the natural logs of the data, as expressed in Equation 2-1.

$$\text{"median"} \equiv \exp\left[\frac{1}{n}\sum_{i=1}^{n}\ln(x_i)\right] \tag{2-1}$$

The geometric mean is a logical estimator of the true median, especially if the data are at least approximately lognormally distributed. Correspondingly, the 1-sigma level is estimated here in most cases as the median multiplied by the exponential of the standard deviation of the natural logs of the data, as expressed in Equation 2-2.

$$\text{"1-sigma level"} \equiv \text{"median"} \cdot \exp\left[\sqrt{\frac{1}{n-1}\sum_{i=1}^{n}[\ln(x_i)-\ln(\text{"median"})]^2}\right] \tag{2-2}$$

The square root term in Equation 2-2, referred to loosely as the "dispersion," is approximately equal to the conventional coefficient of variation (i.e., the standard deviation divided by the mean) for values less than about 0.3.

If a building model "collapses" for one or more of the twenty ground motions in each set (i.e., 10/50 and 2/50), the drift demands are effectively infinite, and the median and 1-sigma level statistics defined above are not finite. In this case, the "*counted* median" and "*counted* 1-sigma level" statistics are utilized. The counted median and 1-sigma level are defined here as the tenth and seventeenth largest of the twenty values of drift demand, respectively. Note that if more than three collapses are observed, the counted 1-sigma level is effectively infinite, as is the counted median if more than ten collapses occur. When available, the counted estimates of the median and 1-sigma level are typically within 10% of those computed according to Equations 2-1 and 2-2.

In addition to the median and 1-sigma level statistics, within each set of (twenty) earthquake records the percentage of "collapses" of the building model and the percentage of "extreme" drifts are considered. Note that collapse is assumed whenever the structural analysis results in essentially infinite peak story drifts, or is unable to arrive at a solution. An extreme drift is defined here as $\theta_{\max} > 0.10$ (including collapses). As demonstrated by the results presented below, these latter two statistics (which can be computed regardless of the number of collapses) are useful in quantifying the effects of connection fractures at high levels of drift demand.

Considering the median and 1-sigma level drift demand statistics for the 10/50 and 2/50 earthquake records is consistent with the approach taken by SAC. Along these lines, each statistic (e.g., 2/50 median) is compared for each building modeled with ductile versus with brittle connections. In hindsight, however, it may have been more appropriate, because the brittle and ductile results are "paired," to first take the ratio of the brittle to ductile demands for each earthquake record, and then consider the statistics (e.g., median and 1-sigma level) of these ratios.

2.2 Modeling

2.2.1 Model Structures

Each of the symmetric SMRF buildings considered in this chapter is modeled for NDA (nonlinear dynamic analysis) as a two-dimensional centerline frame using DRAIN-2DX (Prakash *et al.* 1993). For most of the analyses, only one of the four perimeter moment-resisting frames of each building is included in the model. In this case, *P-Δ* effects due to half the weight of the building are accounted for via a *P-Δ* column. This type of model, referred to as an "M1" model, was the standard model investigated during the SAC project, mainly because it was consistent with the current state of practice. A

second model of each building that includes the contribution of parallel interior gravity frames to the lateral resistance has also been analyzed in some cases. This model, referred to as an "M1+" model, accounts for the limited strength and stiffness of shear-tab beam-column connections in the interior gravity frames (and elsewhere), as detailed in Appendix B. For each M1+ model, half of the parallel interior gravity frames and their shear connections are consolidated into an "equivalent" one-bay frame (Gupta & Krawinkler 1999) that is linked to the perimeter moment-frame under the assumption of a rigid diaphragm. The *P-Δ* effects due to the weight of the building on the perimeter and interior frames are still included. Particularly for higher intensity ground motions, the story drift demands from NDA of an M1 model are generally conservative, as compared with the results obtained using the more realistic M1+ model. Nevertheless, the general conclusions drawn from the results for either model are similar, as demonstrated in Section 2.11.

Whether M1 or M1+, a centerline model of each building is analyzed rather than explicitly modeling the panel zones because the interaction between large panel zone deformations and beam-column connection fractures has not been extensively studied. Unless this interaction is properly accounted for, weak panel zones could unrealistically inhibit connection fractures by limiting demands in the connected beams. Because panel zones are not explicitly modeled here, to be consistent, peak total (beam plus panel zone) plastic rotations observed prior to fracture in laboratory tests are used to calibrate the plastic rotation fracture capacity discussed below. Note that Gupta & Krawinkler (1999) demonstrate that explicitly modeling panel zones rather than using a centerline model does not generally have a significant effect on story drift demands for the SAC buildings modeled with ductile connections. The approach for modeling beam-end and column-end plastic hinging and/or fracture is described next.

2.2.2 Beam-Flange Connection Fracture Model

As commonly done in modeling structures with ductile connections, plastic hinging (i.e., point plasticity) at the beam-ends is captured via nonlinear rotational springs connected to the ends of elastic beam elements. To emulate beam-flange connection fracture, rather than a rigid-plastic rotational spring that is used to model ductile behavior, a rotational spring fracture element that mimics the moment-rotation relationship observed in full-scale laboratory tests of pre-Northridge type connections is implemented in DRAIN-2DX, as developed by Foutch & Shi (1996). For a model

structure with brittle connections, every connection is assumed to have the potential to fracture during dynamic analysis if the local demands are sufficiently high.

Field as well as experimental observations indicate that beam-flange connection fracture can occur before significant yielding in the beam (FEMA 289, 1997); typically, however, connection fracture is assumed to occur when the plastic rotation in the beam reaches a particular amplitude, which can be thought of as a plastic rotation capacity. Accordingly, the fracture elements employed here can fracture either "early," that is, at a specified fraction of the beam plastic moment (as in Figure 2-1a), or at a specified plastic rotation amplitude (as in Figure 2-1b). Due to the influence of a slab, a backup bar, or an access hole, a beam-column connection may fracture at different plastic rotation amplitudes in positive and negative bending. Hence, different plastic rotation capacities can be specified in positive and negative bending (as demonstrated in Figure 2-1b), corresponding to bottom and top beam-flange fracture, respectively. Prior to fracture, the moment-rotation hysteretic behavior of the element is rigid-plastic with strain hardening, as for a ductile connection. Note that because the fracture element is used to capture inelastic behavior only, its elastic stiffness is effectively rigid so that the total rotation of the fracture element is equivalent to the plastic rotation of the connection.

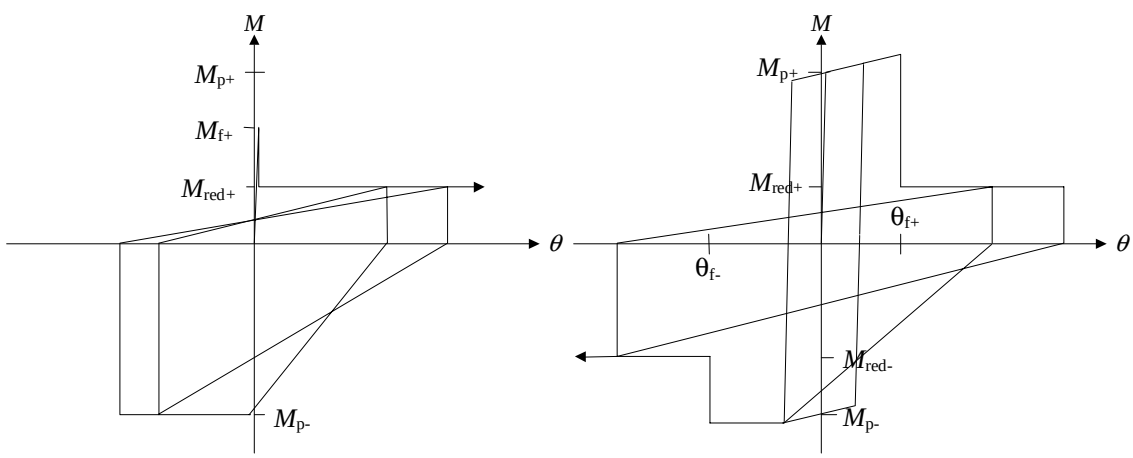

Figure 2-1. Moment-rotation hysteretic behavior for the connection fracture model of **(a)** "early" fracture of the bottom beam-flange only, and **(b)** top and bottom beam-flange fracture.

As observed in laboratory tests of fractured beam-column connections removed from buildings damaged during the Northridge earthquake (Anderson *et al.* 1998), after fracture the moment strength of the connection element drops to a small portion of the plastic moment capacity. When one of the beam-flange connections has fractured (e.g.,

Figure 2-1a), this reduced moment strength takes effect only for bending that causes "tension" in the fractured beam-flange, or opening of the crack; for bending that causes compression in the fractured beam-flange, or closing of the crack, the full moment strength is assumed to be maintained. For fracture of both beam-flange connections (e.g., Figure 2-1b), the drop in moment strength applies for both positive and negative bending. As also illustrated in Figure 2-1, after fracture the moment-rotation stiffness becomes "peak-oriented" (amounting to a reduction in stiffness), and the pre-fracture strain hardening is lost.

2.2.3 Column Fracture Model

In addition to fractures of the top and/or bottom beam-flange connections (e.g., Figure 2-1), weld fractures that propagate into the adjacent column flange (and perhaps web) above or below a joint panel zone have also been observed. As for beam-flange fractures, such "column fractures" are incorporated into the analysis model using rotational springs that are placed at the ends of the column elements above and below every moment-resisting connection. These "column springs," however, behave differently than those used to emulate beam-flange fracture. As detailed below, the fracture element described in the previous subsection and the existing DRAIN-2DX bilinear rotational spring element are both modified in order to incorporate the desired column fracture behavior.

Consistent with the idea that connection fracture initiates at a beam-flange weld, but can propagate either through the beam flange/web or across the column flange/web, it is assumed that column fracture is "triggered" by an adjacent beam-flange connection. If a beam spring designated as a column fracture trigger reaches the plastic rotation (or, for "early" fracturing connections, the fraction of M_p) at which it would normally fracture its top or bottom beam-flange, it instead triggers column fracture in the column spring above or below the joint, respectively (i.e., bottom beam flange triggers column fracture below the joint, top flange above). Meanwhile, the beam spring which acts as a column fracture trigger remains ductile, reflecting the scenario in which the crack has propagated into the column flange/web instead of the beam flange/web.

Once column fracture is triggered, the affected column spring becomes rigid-perfectly plastic with reduced moment strength. This moment strength (in both positive and negative bending), denoted $M_{red,col}$, is some small fraction (i.e., 10% or 20%) of the plastic moment of the column, $M_{p,col}$. If column fracture is not triggered, the rotational springs at the ends of each column act rigidly, with effectively infinite strength. Any

plastic hinging at the column ends, therefore, is captured by the inelastic element used to model the columns. In other words, unless column fracture is triggered, the column springs have no effect on the strength or stiffness of the columns. Note that the column elements have been modeled with *P-M* interaction.

Field observations suggest that approximately 20% of welded moment-resisting connection fractures propagate into the column flange/web (Bonowitz, informal communication). In what fraction of these cases, if any, the crack also propagated through the beam flange/web is unclear. Since we cannot predict when fracture will propagate into a connected column (instead of the connected beam) the locations of column fracture triggers are randomly simulated assuming that the probability that a connection fracture will propagate into the column flange/web rather than the adjacent beam flange/web is 25%. This amounts to randomly designating approximately 25% of the beam flange connections (bottom or top) as column fracture triggers. Note that the same procedure is used to designate bottom beam-flange connections that may fracture early (i.e., pre-yield); however, the two random selections are carried out independently.

2.3 Approach for Sensitivity Studies

To make a realistic comparison of the seismic drift demands for model structures with brittle versus ductile connections, values for the parameters defining the empirical fracture model described above must be estimated from experimental and field results. However, due to the apparently random nature of connection fracture and the uncertainties that arise from limited field and test data, it is also important to study the sensitivities of seismic drift response to variations in each of the fracture parameters. By doing so, an improved understanding of the possible effects of connection fractures is developed, which can be applied to "interpolate" the effects of brittle connection behavior when slightly different assumptions are made for the fracture model. In addition, with the knowledge of which parameters of the fracture model are most significant in terms of altering drift response, efforts can be made to obtain more relevant test data, or to randomize influential fracture parameters.

To study the sensitivity of the seismic drift response of model structures with brittle connections to variations in the fracture parameter values, a "star" design method is employed. "Base-case" values of the fracture parameters are designated, which represent best estimates for the average values of the fracture parameters. One parameter at a time, extreme but plausible values of the fracture parameters are adopted. Intermediate values

of the parameter are considered only if significant changes in the seismic drift response (with respect to the base case) are observed. As detailed below, the variations from the base case include, but are not limited to, (i) brittle connections at the top, in addition to the bottom, beam flanges, and (ii) brittle connections that may fracture an adjacent column flange, and perhaps web. Apart from an investigation of the effects of using the "M1+" model (defined in Section 2.2.1), note that the "M1" model of each building is employed in all cases.

2.4 Base-Case Fracture Model Parameters

Based on field and laboratory observations, which suggested relatively few fractures of the top beam-flange connection, an early project decision was made to consider as a base case only the potential of bottom beam-flange connection fracture (i.e., implying an effectively infinite plastic rotation capacity against fracture in negative bending). Later, attention was focused on the possibility of both top and bottom beam-flange connection fracture. The base-case values for the parameters defining the connection fracture model are summarized in Table 2-1.

Table 2-1. Brittle base-case values for the parameters of the connection fracture model.

p	M_{f+} / M_{p+}	θ_{f+}	θ_{f-}	M_{red+} / M_{p+}
25%	75%	0.015 radians	∞	30%

To account for the possibility of pre-yield fracture of the bottom beam-flange connection (described in Section 2.2.2), it is assumed in the base case that the probability p of any particular connection fracturing early, if the local moment demand is sufficiently high, is 25%. Thus, approximately 25% of the connections in a model structure are expected to experience early fracture of the bottom beam-flange. The connections that fracture early are assumed to fracture at 75% of the beam plastic moment in positive bending M_{p+}. The precise locations of these early fracturing connections are assigned randomly, assuming mutual independence of the locations of such connections. Through simulation, a different (and random) spatial distribution, or pattern, of early fracturing connections is designated for each earthquake record used in the dynamic analyses (rather than running multiple simulations for each record). Note that the record-to-record

variability of drift response is observed to dominate over the variability (for each record) resulting from different patterns of early fracturing connections.

For the other approximately 75% of the connections that do not fracture early in the base case, fracture of the bottom beam-flange is assumed to occur when the plastic rotation in positive bending reaches $\theta_{f+} = 0.015$. Once fracture occurs, early or not, for the base case the positive moment capacity is reduced to 30% of M_{p+}, whereas the connection retains its full moment capacity in negative bending (Anderson *et al.* 1998). Note that the average plastic rotation capacity of all the bottom beam-flange connections, including those that fracture early, is only 0.011. This average value of plastic rotation capacity compares well to the average total (i.e., beam plus panel zone) plastic rotation observed at first fracture during the SAC Phase I laboratory tests (FEMA 289, 1997). The twelve tests of pre-Northridge-type connections with 30- and 36-inch-deep beams (without slabs) revealed total plastic rotation capacities ranging from 0.0 to 0.021, with an average of 0.010.

2.5 Brittle Base-Case Results

Before studying the sensitivity of seismic drift response to different values of the various fracture parameters, it is important to first understand how connection fractures affect the drift responses of the model structures in the base case, as compared to the ductile connections case. Although results for all six of the model structures investigated are used to develop general conclusions, detailed results are provided here only for the L.A. 9-story model structure; a brief summary of the results for the other model structures is also included. For more detailed results (e.g., earthquake record-by-record $\theta_{\max}$ results and additional θ_{i} statistics), refer to (Cornell & Luco 1999).

2.5.1 Brittle Base-Case Results for Los Angeles 9-Story

2.5.1.1 $\theta_{\max}$ and θ_{ave} Statistics

The median and 1-sigma level values of $\theta_{\max}$ and θ_{ave} are depicted graphically in Figure 2-2 for the L.A. 9-story model structure with all ductile connections and with all brittle base-case connections, subjected to the 10/50 and 2/50 ground motions. Also shown in the figure are the percentage increases in the $\theta_{\max}$ and θ_{ave} statistics from the ductile case to the brittle base case, which indicate that (base-case) connection fractures

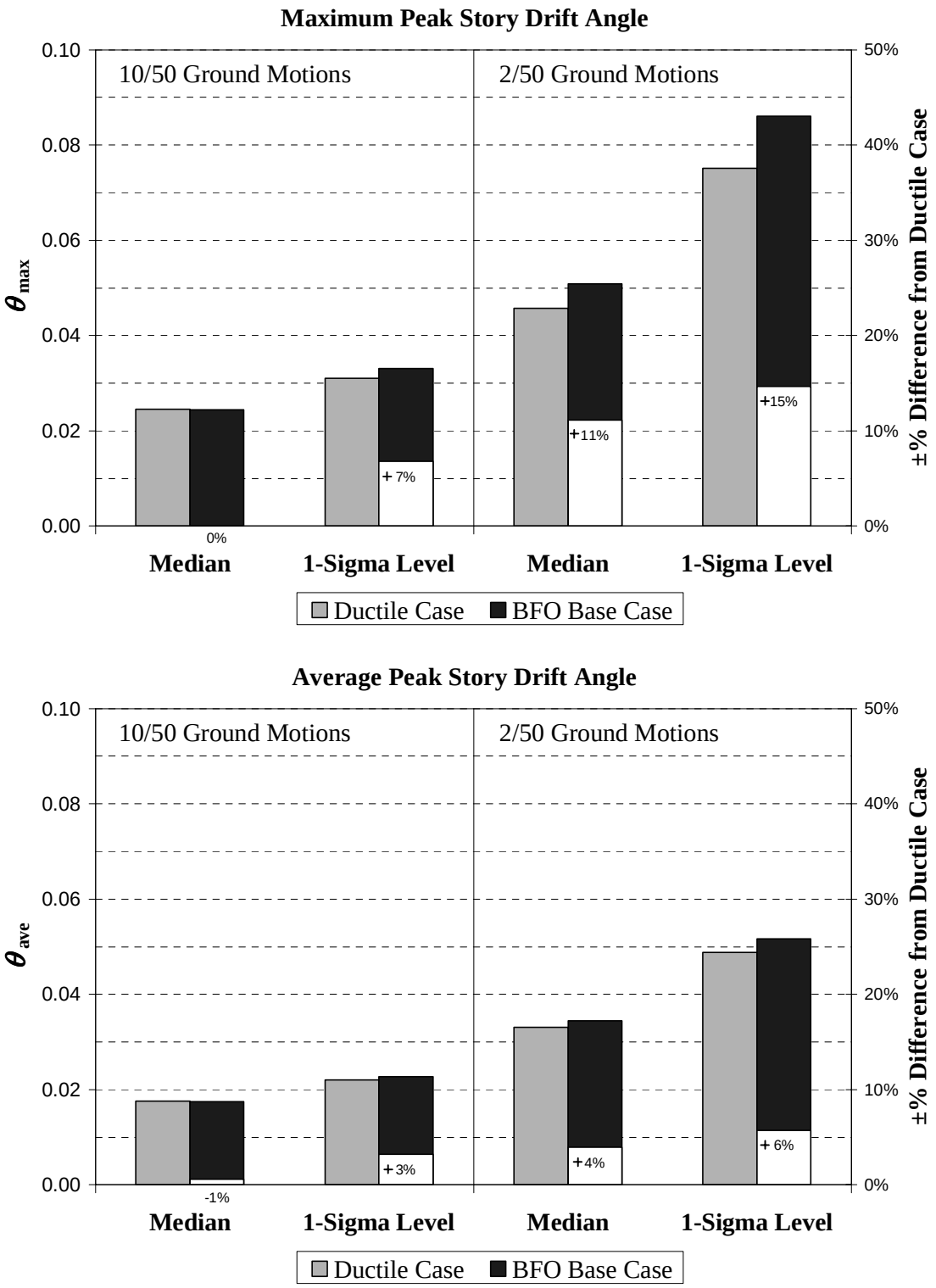

Figure 2-2. Median and 1-sigma level values of **(a)** θ_{max} and **(b)** θ_{ave} for the L.A. 9-story modeled with ductile and with brittle (i.e., Bottom Flange Only) base-case connections. Percentage increases from the ductile case to the BFO base case are shown as white bars.

have less than a 15% effect on the θ_{max} or θ_{ave} statistics for the L.A. 9-story model structure. It is important to note, however, that the percentage increases in the story drift statistics are larger at higher response levels (i.e., when the story drift demands in the ductile case are larger). For example, the percentage increases in the θ_{max} or θ_{ave} statistics are larger for the 2/50 ground motions than for the 10/50 ground motions; the increases are also larger for the 1-sigma level response than for the median response. Also note that the larger percentage increase for the θ_{max} statistics than the θ_{ave} statistics, the values of which are smaller by definition. These results are intuitive, as one would expect more connections to fracture when the story drifts are larger, and hence expect their effects relative to the ductile case to be more pronounced.

2.5.1.2 Spatial Variations of θ_i Statistics

Figure 2-3 shows for the 10/50 and 2/50 ground motions the spatial variations of the median and 1-sigma level θ_i over the height of the L.A. 9-story model structure with ductile connections and with brittle base-case connections. For the most part, the introduction of base-case connection fractures increases the θ_i statistics in the lower stories while decreasing them in the upper stories, with respect to the θ_i statistics in the ductile case. As noted for the θ_{max} and θ_{ave} statistics, the effect is more pronounced under the 2/50 ground motions, but still less than 20%. Even in the ductile connections case, it is evident that increased structural nonlinearity at higher ground motion levels (e.g., 2/50 versus 10/50) tends to concentrate relatively large median and 1-sigma level θ_i in the lower stories. This concentration of large drifts in the lower stories may be due, in part, to *P-Δ* effects and/or to the near-source nature of the SAC 2/50 earthquake records for Los Angeles. In turn, the increase in the lower story drifts, and inelasticity there, may serve to "isolate" the upper stories and lead to the observed reduction of upper-story drifts. However, note that a slight increase from the ductile case to the brittle base case in the 1-sigma level θ_i for the 2/50 ground motions is observed in the upper stories.

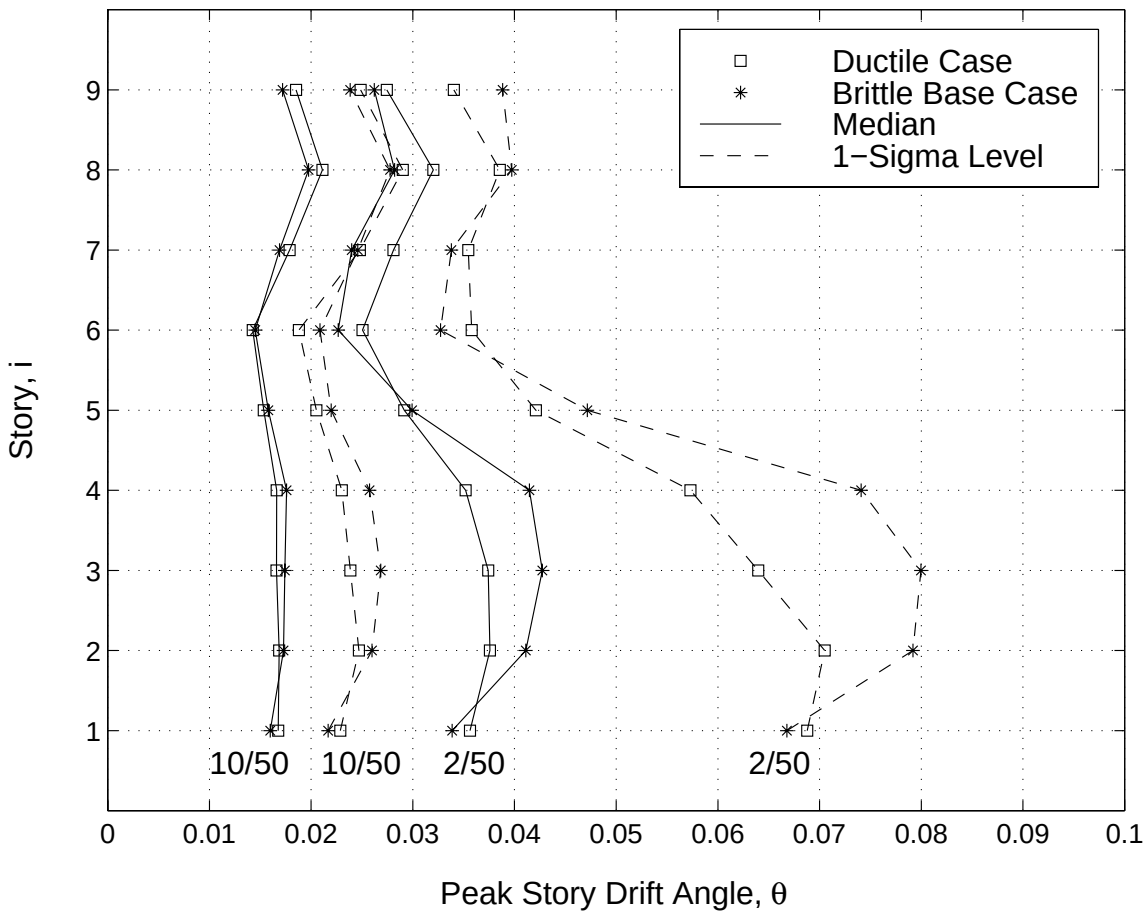

Figure 2-3. Spatial distribution of the median and 1-sigma level values of θ_i over the height of the L.A. 9-story modeled with ductile and with brittle base-case connections.

2.5.1.3 Summary

For the L.A. 9-story model structure with the base-case assumptions discussed above, connection fractures have less than a 20% effect on the story drift demand statistics relative to the ductile connections case. The largest effects occur at higher levels of drift demand, such as for the 1-sigma level θ_{max} under the 2/50 ground motions. Furthermore, the increases in peak story drift angles due to (base-case) connection fractures are somewhat localized, as evidence by the θ_i statistics and the relative large increases in the θ_{max} versus θ_{ave} statistics. It should be noted that the L.A. 9-story model structure with base-case brittle connections does not collapse under any of the ground motions considered; a few extreme drifts ($\theta_{max} > 0.10$) are observed, however, as summarized with the results for the other model structures below.

2.5.2 Brittle Base-Case Results for All Structures

2.5.2.1 θ_{max} and θ_{ave} Statistics

Compared with the L.A. 9-story model structure, similar conclusions regarding the effects of base-case connection fractures (relative to the ductile connections case) on the median and 1-sigma level θ_{max} and θ_{ave} can be drawn for the other SAC model structures. Note that the SAC model structures for Boston are not investigated because even in the ductile connections case the seismic drift demands are small (e.g., Gupta & Krawinkler 2000). As encountered for the L.A. 9-story model structure, if the story drift demands are small, then the effects of brittle connection behavior are minimal because few connections actually fracture. For example, an average of only $18/90 = 20\%$ of the connections fracture in the L.A. 9-story brittle-base-case model structure subjected to the 10/50 ground motions, and their effects on the θ_{max} and θ_{ave} statistics relative to the ductile case are less than 10%. Similar results are found for the other SAC model structures and the corresponding 10/50 ground motions, but first the results for the 2/50 ground motions are presented.

For the corresponding 2/50 ground motions, the "counted" median θ_{max} and θ_{ave} for the Los Angeles and Seattle model structures with ductile connections and with brittle base-case connections are presented graphically in Figure 2-4; also included are the percentage increases in the counted medians from the ductile case to the brittle base case. Recall that the *counted* median (i.e., the 10th largest of the 20 values) and *counted* 1-sigma level (i.e., the 17th largest of 20 values) are employed here as estimators because some of the model structures "collapse" under at least one of the ground motions. For all six of the model structures, the increase in the (counted) median θ_{max} from the ductile case to the brittle base case is no more than 50%; the largest increase in the median θ_{ave} is less than 25%. Nonetheless, across the six model structures it is evident that the effect of base-case connection fractures is largest at the higher story-drift-demand levels (e.g., as measured by θ_{max} from the ductile connections case). For low drift demand levels, the median θ_{max} can actually decrease (e.g., as for the Seattle 20-story model structure).

The counted 1-sigma level θ_{max} values for the 2/50 ground motions, along with the percentage increases from the ductile case to the brittle base case, are shown in Figure 2-5 for all of the model structures. Note that the increases in the (counted) 1-sigma level θ_{max} are somewhat larger than those for the (counted) median θ_{max}, but still

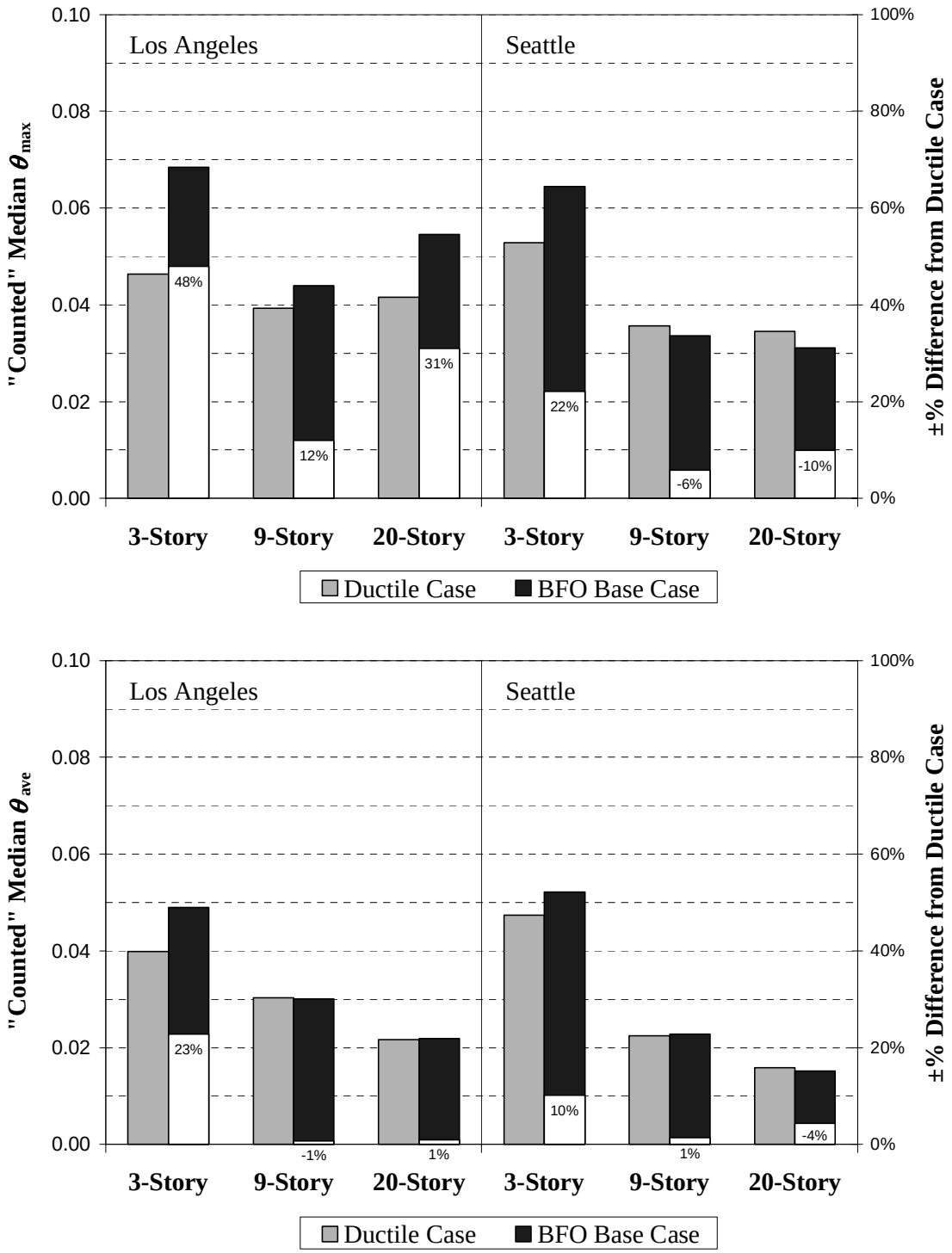

Figure 2-4. Counted median values of **(a)** θ_{max} and **(b)** θ_{ave} under the 2/50 ground motions for all six of the buildings modeled with ductile and with brittle (i.e., Bottom Flange Only) base-case connections. Percentage increases from the ductile case to the BFO base case are shown as white bars.

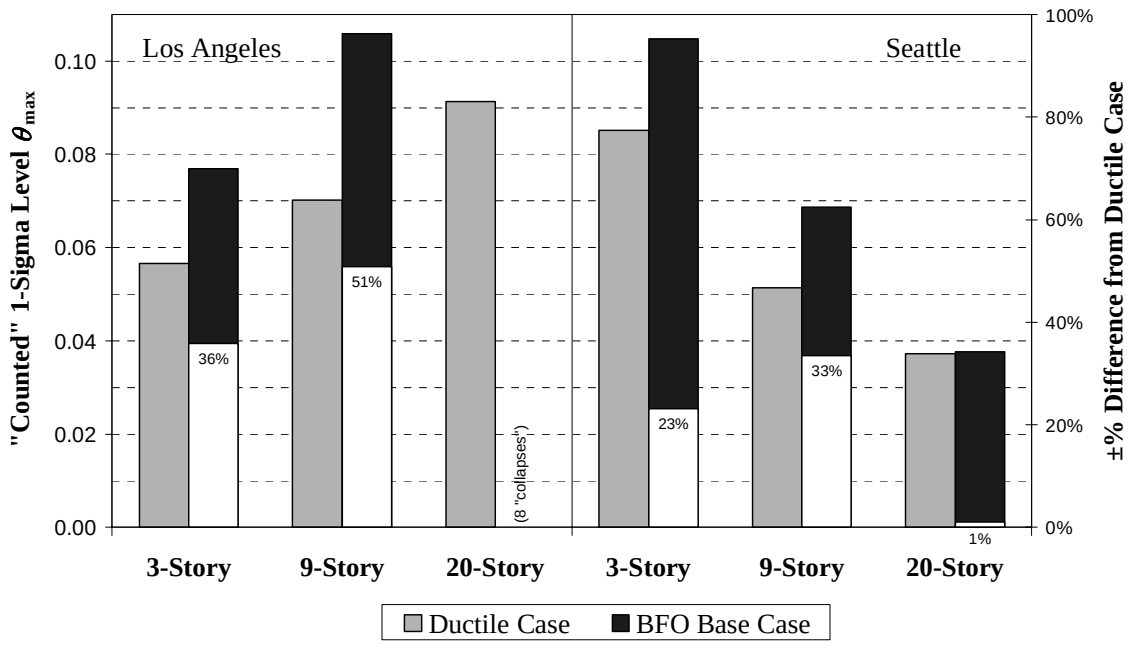

Figure 2-5. Counted 1-sigma level values of θ_{max} under the 2/50 ground motions for all six of the buildings modeled with ductile and with brittle (i.e., Bottom Flange Only) base-case connections. Percentage increases from the ductile case to the BFO base case are shown as white bars.

less than 55% for all but the L.A. 20-story model structure. The number of collapses (more than three) encountered for the L.A. 20-story model structure with brittle base-case connections prohibits calculation of the counted 1-sigma level.

For the corresponding 10/50 ground motions, the counted median and 1-sigma level θ_{max} values for the SAC model structures modeled with ductile or with brittle-base-case connections are listed in Table 2-2. As summarized in the table, the differences in the (counted) median and 1-sigma level θ_{max} between the ductile case and the brittle basecase are even smaller than those for the 2/50 ground motions – in fact, the percentage increases are less than 20%.

2.5.2.2 Extremes and Collapses

It has already been demonstrated that the effects of base-case connection fractures are most pronounced when the story drift demands are relatively large, as is the case for the 2/50 (compared with the 10/50) ground motions and the 1-sigma level (compared with the median) response statistics. The modest increases from the ductile case to the brittle

Table 2-2. Counted median and 1-sigma level values of θ_{max} under the 10/50 ground motions for all six of the buildings modeled with ductile and with brittle base-case connections.

Model Structure	Ductile Case		Brittle Base Case		% Increase	
	Median [rad]	1-σ Level [rad]	Median [rad]	1-σ Level [rad]	Median	1-σ Level
Los Angeles 3-story	0.0244	0.0294	0.0235	0.0351	-4%	19%
" 9-story	0.0229	0.0300	0.0217	0.0326	-5%	9%
" 20-story	0.0190	0.0274	0.0171	0.0276	-10%	1%
Seattle 3-story	0.0216	0.0280	0.0209	0.0302	-3%	8%
" 9-story	0.0210	0.0242	0.0182	0.0250	-13%	3%
" 20-story	0.0149	0.0207	0.0154	0.0191	3%	-8%

base case observed for the median θ_{max} (or θ_{ave}) do not typically reflect well the effects of connection fractures under those particular ground motions that cause the largest story drifts. The 1-sigma level statistic is more appropriate for this purpose, but as witnessed for the L.A. 20-story model structure, the occurrence of more than three collapses prevents calculation of even the counted 1-sigma level statistic. To better quantify the effects of connection fractures under those ground motions (from the 2/50 set, for example) that induce relatively severe story drift demands even in the ductile connections case, the percentage of extreme drifts is calculated. Recall that an extreme drift is defined here as $\theta_{max} > 0.10$ (including collapses). At this story-drift level, both accuracy of the structural model (e.g., degrading versus ductile columns) and the ability to carry gravity loads (e.g., shear connection failures) are in jeopardy (Liu & Astaneh 2000).

The percentage of extreme drifts and the proportion of collapses observed for each of the structural models with ductile connections and with brittle base-case connections is presented graphically in Figure 2-6 for the 2/50 ground motions; under the 10/50 ground motions, no extreme drifts or collapses are observed for the ductile case nor the brittle base case. Also included in the figure is the minimum (among earthquake records) θ_{max} in the ductile case that becomes an extreme θ_{max} in the brittle base case (under the same ground motion). The results indicate that when θ_{max} is larger than 0.05 (radians) for a model structure with ductile connections, the introduction of brittle base-case connections may result in an extreme θ_{max} under the same ground motion. The percentage of extreme drifts at least doubles from the ductile case to the brittle base case for all of the model

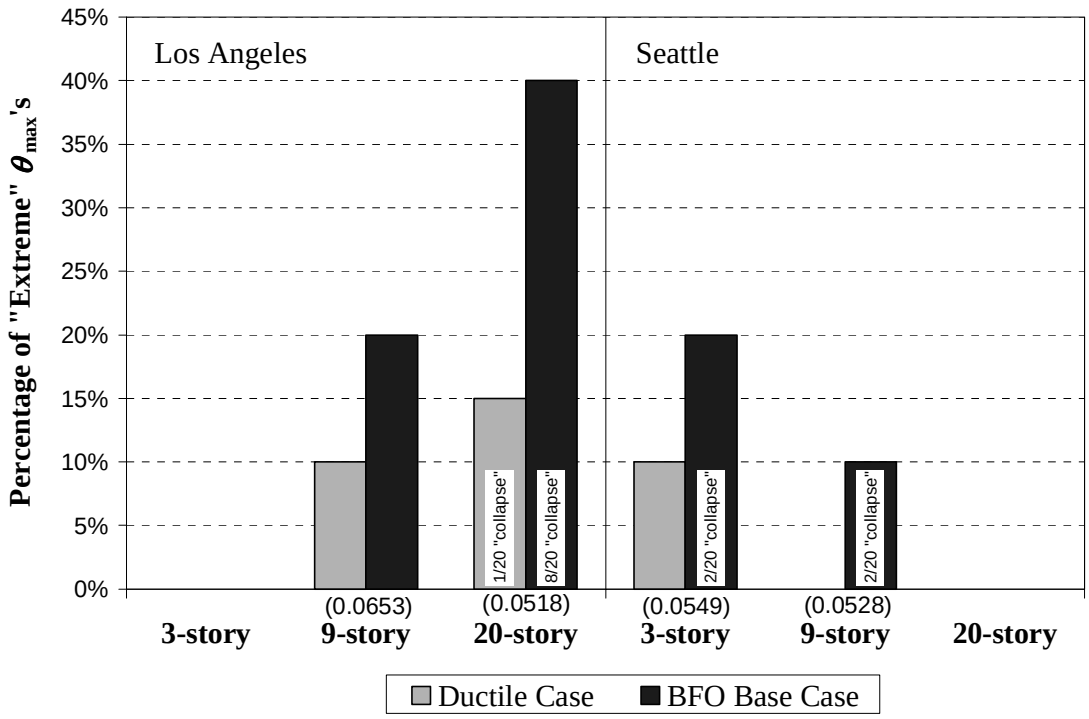

Figure 2-6. Percentage of "extreme" drifts (i.e., θ_{max}>0.10, including collapses) under the 2/50 ground motions for all six of the buildings modeled with ductile and with brittle (i.e., Bottom Flange Only) base-case connections. The minimum θ_{max} in ductile case that becomes an extreme drift in the brittle base case is also noted.

structures that experience extreme drifts. Clearly, even though base-case connection fractures have only a modest effect on the median θ_{max}, for the 2/50 ground motions the increase in the percentage of extreme drifts relative to the ductile case is substantial.

2.5.3 Summary of Brittle Base-Case Results

Overall, with brittle base-case assumptions, the effects of connection fractures on story drift demands (relative to the ductile case) are perhaps less than one might have anticipated. Recall, however, that only bottom beam-flange fractures occur in the base case, and a connection is presumed to retain its full strength when the fractured bottom flange is in compression. Thus, at any one instant, at most one-half of the beam connections in a story will reflect the 70% strength loss associated with base-case fracture. Apparently, the case of only bottom beam-flange fracture is a relatively benign

one, except under some severe ground motions. The potential of top beam-flange fracture in addition to bottom-flange fracture is considered in Sections 2.6 and 2.7.

2.6 Results of Sensitivity Studies

Although the base-case parameter values specified above represent a best estimate, the actual values that define the model of bottom beam-flange connection fracture are uncertain (due to limited empirical data) and likely random (i.e., vary among like connections). Thus, it is important to evaluate the sensitivity of seismic drift response to variations in the parameters of the fracture model. For the most part, the sensitivity studies here are carried out using the L.A. 9-story model structure, occasionally confirming with results for the L.A. 3-story model structure. The sensitivity of story drift demands to each parameter of the fracture model is judged primarily by comparing the median and 1-sigma level $\theta_{\max}$ (under the 10/50 and 2/50 ground motions) for the base case to those for the "perturbed" case (i.e., with the parameter of interest altered).

2.6.1 Early Fractures

For the brittle base case, the probability of a given connection experiencing early (i.e., pre-yield) fracture of the bottom beam-flange was assumed to be $p = 25\%$. As a sensitivity exercise, a perturbed base-case fracture model with $p = 75\%$ is considered, which implies that approximately 75% of the bottom beam-flanges are expected to fracture early (still at 75% of the yield moment, M_{p+}). As summarized in Table 2-3, the increase in p is found to have almost no effect on the story drift demand statistics. The resulting differences in the median and 1-sigma level $\theta_{\max}$ for both the 10/50 and 2/50 ground motions are at most 2% for the L.A. 9-story model structure, and less than 15% for the L.A. 3-story model structure. For the L.A. 9-story model structure, the total number of bottom beam-flange fractures on average doubles when p is increased from 25 to 75%, yet the story drift demands change very little, perhaps due to the limited loss in strength associated with bottom-flange-only fracture (as discussed earlier). Note that the average plastic rotation capacity for the perturbed base case with $p = 75\%$ is 0.004 radians. Given the insensitivity to p, the sensitivity of story drift demands to the percentage of M_{p+} at which early fracture occurs is not investigated.

Table 2-3. Median and 1-sigma level θ_{max} statistics under the assumption of two different values of *p*, the probability of "early" (i.e., pre-yield) fracture.

Model Structure	Earthquake Records	*p* =25% (Base Case)		*p* =75%		% Increase	
		Median [rad]	1-σ Level [rad]	Median [rad]	1-σ Level [rad]	Median [rad]	1-σ Level [rad]
L.A. 3-story	10/50	0.0255	0.0377	0.0280	0.0429	10%	14%
"	2/50	0.0533	0.0897	0.0577	0.0837	8%	-7%
L.A. 9-story	10/50	0.0244	0.0331	0.0250	0.0338	2%	2%
"	2/50	0.0509	0.0861	0.0505	0.0874	-1%	2%

Recall that for the base case the locations of early fracturing connections are randomly assigned for each ground motion. It is possible, however, that early fracturing connections could be clustered spatially (due to, for example, poor welding by a particular welder on a particular day). To examine the sensitivity of story drift demands to clustering of connections that fracture early, two deterministic "worst-case" patterns of early fracturing connections are considered for the L.A. 9-story model structure. From Figure 2-3 it was apparent that the largest story drift demands occur in the upper stories (eight and ninth) for the most of the 10/50 ground motions, and in the lower stories (second and third) for most of the 2/50 ground motions. Hence, for the two sensitivity cases considered here, the approximately 25% of a total of 90 connections that fracture early are all positioned in first one and then the other of these two regions.

The counted median and 1-sigma level θ_{max} for the 10/50 and 2/50 ground motions are listed in Table 2-4 for the cases when the early fracturing connections are all located in the lower stories or all in the upper stories of the L.A. 9- story model structure. The θ_{max} statistics for these two patterns of early fractures are compared with the brittle base-case results, with the percentage increases also included in the table. When all of the early fracturing connections are assigned to the lower stories, the increases in the median and 1-sigma θ_{max} (relative to the base case) are less than 30% for both the 10/50 and 2/50 ground motions. For the 10/50 earthquake records, the concentration of early fractures in the lower stories typically shifts the location of θ_{max} to the lower stories (from the upper stories), but the magnitude of the θ_{max} statistics remain nearly unchanged. Even for the 2/50 ground motions, the θ_{max} statistics are not affected much by the early fractures in the lower stories, likely because the drifts in the lower stories are generally large enough to induce fractures even if the connections do not fracture early. This hypothesis is

Table 2-4. Counted median and 1-sigma level values of θ_{max} for the L.A. 9-story modeled with "early" fracturing connections all located in either the lower or upper stories.

Case	10/50 Earthquake Records		2/50 Earthquake Records	
	Median	1-Sigma Level	Median	1-Sigma Level
(a) Counted θ_{max} Statistics [rad]				
Brittle base case	0.0217	0.0326	0.0440	0.1059
"Early" fractures in lower stories	0.0248	0.0332	0.0420	0.1339
"Early" fractures in upper stories	0.0363	0.0493	0.0655	0.1059
(b) % Increase in Counted θ_{max} Statistics w.r.t. Brittle Base Case				
Brittle base case	--	--	--	--
"Early" fractures in lower stories	14%	2%	-5%	26%
"Early" fractures in upper stories	67%	51%	49%	0%

supported by the counted median θ_i results depicted in Figure 2-7, where the largest median values of θ_i, located in the lower stories, do not increase much with the introduction of early fracturing connections there; at the 1-sigma level, the increase in the lower-story drift demands is somewhat larger. Note that for two of the 2/50 ground motions, concentrating the early fracturing connections in the lower stories results in collapse of the L.A. 9-story model structure, although for the same two earthquake records θ_{max} is already extreme (i.e., greater than 0.10) in the base case.

If the early fracturing connections are concentrated in the upper stories, on the other hand, the increase (relative to the base case) in the median and 1-sigma level θ_{max} is 50% to 70% for both the 10/50 and 2/50 ground motions (with the exception of the 2/50 1-sigma level θ_{max}, to be discussed). It seems that connections in the upper stories that did not fracture in the base case because the story drift demands were relatively small may now be fracturing early, resulting in a shift of the typical location of θ_{max} to the upper stories. This is evidenced by Figure 2-8, which compares the counted median θ_i values under the 2/50 ground motions for the base case and the case with early fractures in the

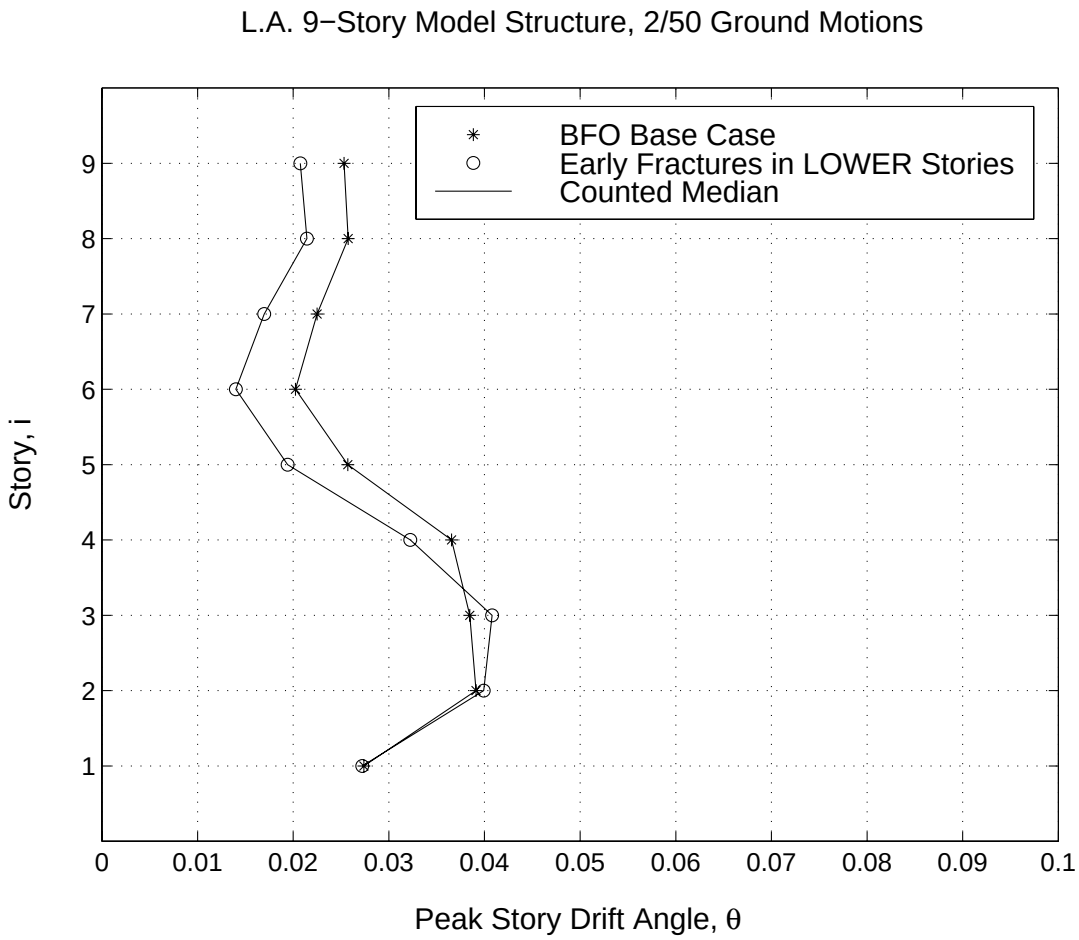

Figure 2-7. Spatial distribution of the counted median θ_i values over the height of the L.A. 9-story modeled with "early" fracturing connections all located in the *lower* stories and subjected to the 2/50 ground motions.

upper stories. For the 1-sigma level drift response under the 2/50 ground motions, however, the drifts in the upper stories increase substantially with early fractures, but the drifts in the lower stories, which do not increase with respect to the base case, still govern; hence, the 1-sigma level $\theta_{\max}$ does not increase.

In summary, although increasing the probability that a bottom beam-flange connection fractures early (i.e., *p*) from 25% to 75% has less than a 15% effect on the $\theta_{\max}$ statistics for the L.A. 9-story and 3-story model structures, in severe scenarios the locations of early-fracturing connections can have a more substantial effect (up to a 70% increase in the $\theta_{\max}$ statistics). However, if the story drift demands are large enough to cause many connections to fracture even without early fractures (i.e., at $\theta_{f+} = 0.015$), the

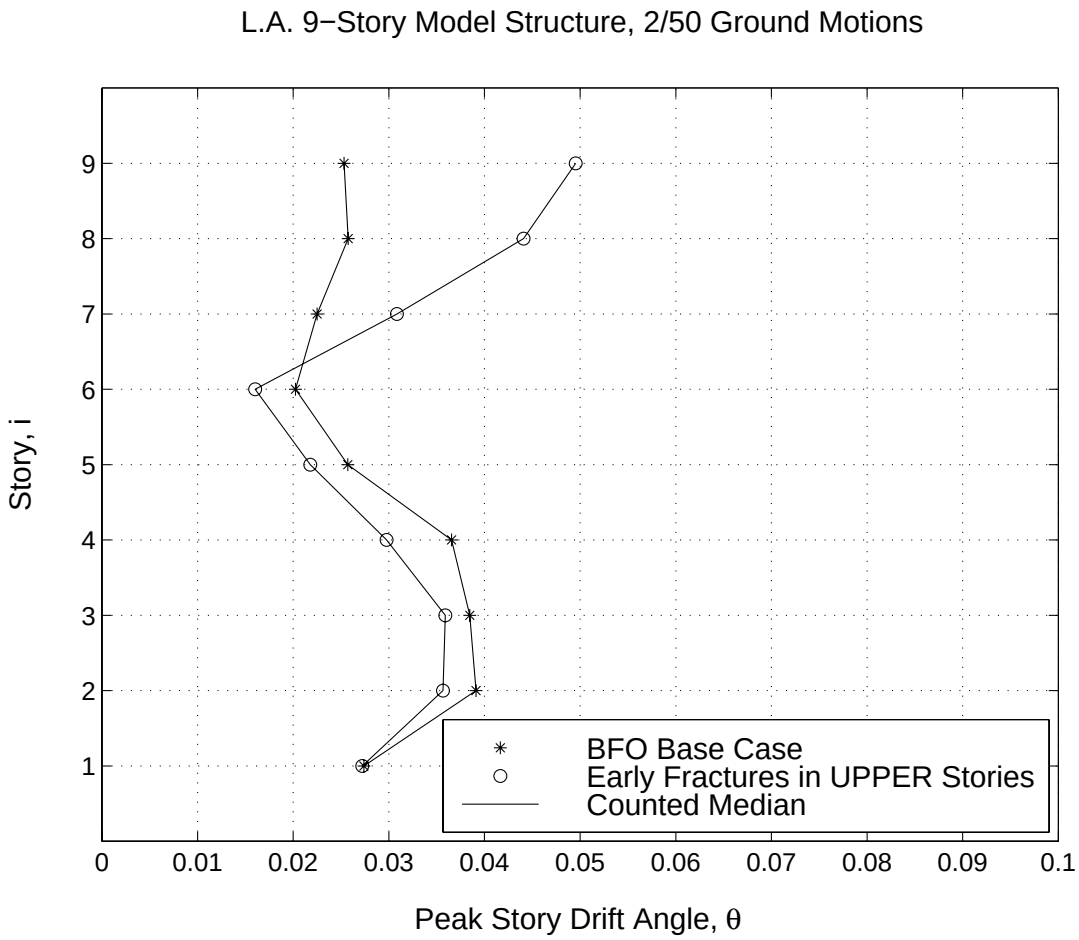

Figure 2-8. Spatial distribution of the counted median θ_i values over the height of the L.A. 9-story modeled with "early" fracturing connections all located in the *upper* stories and subjected to the 2/50 ground motions.

effect of early fractures on story drifts is generally small. In such cases, more sophisticated techniques for simulating the locations of early-fracturing connections (e.g., introducing spatial correlation) are likely not warranted.

2.6.2 Plastic Rotation Capacity, θ_{f+}

Another uncertain and likely random parameter of the fracture model is the plastic rotation capacity in positive bending, which is assumed to be $\theta_{f+} = 0.015$ for the brittle base case. Two broad, but plausible variations on this value of θ_{f+} for pre-Northridge connections are considered, namely, 0.005 and 0.030 (radians). The resulting median and

Table 2-5. Median and 1-sigma level θ_{max} statistics under the assumption of a *smaller* plastic rotation capacity against fracture in positive bending (i.e., θ_{f+}) than that assumed in the brittle base case.

Model Structure	Earthquake Records	θ_{f+}=0.015 (Base Case)		θ_{f+}=0.005		% Increase	
		Median [rad]	1-σ Level [rad]	Median [rad]	1-σ Level [rad]	Median [rad]	1-σ Level [rad]
L.A. 3-story	10/50	0.0255	0.0377	0.0276	0.0426	8%	13%
"	2/50	0.0533	0.0897	0.0582	0.0855	9%	-5%
L.A. 9-story	10/50	0.0244	0.0331	0.0263	0.0368	8%	11%
"	2/50	0.0509	0.0861	0.0529	0.0895	4%	4%

1-sigma level θ_{max} statistics for the L.A. 9-story and 3-story (for the $\theta_{f+} = 0.005$ case) model structures subjected to the 10/50 and 2/50 ground motions are compared in Table 2-5 and Table 2-6.

With $\theta_{f+} = 0.005$, more bottom beam-flange fractures are expected than in the base case, but the resulting median and 1-sigma level θ_{max} demands increase by less than 15% for the L.A. 9-story model structure, as well as for L.A. 3-story model structure. Note that for this "perturbed" base case with $\theta_{f+} = 0.005$, the average plastic rotation capacity, accounting for the connections that fracture early, is 0.004 rad, which is the same as that for the perturbed base case with $p = 75\%$; in both cases the increases in the median and 1-sigma level θ_{max} with respect to the base case are relatively small.

Table 2-6. Median and 1-sigma level θ_{max} statistics under the assumption of a *larger* plastic rotation capacity against fracture in positive bending (i.e., θ_{f+}) than that assumed in the brittle base case.

Model Structure	Earthquake Records	θ_{f+}=0.015 (Base Case)		θ_{f+}=0.030		% Increase	
		Median [rad]	1-σ Level [rad]	Median [rad]	1-σ Level [rad]	Median [rad]	1-σ Level [rad]
L.A. 9-story	10/50	0.0244	0.0331	0.0236	0.0300	-3%	-9%
"	2/50	0.0509	0.0861	0.0469	0.0787	-8%	-9%

With $\theta_{f+} = 0.030$, fewer bottom beam-flange fractures are expected than in the base case. It is conceivable, however, that by delaying connection fractures until the story drift demands are larger, the sudden drop in strength at fracture could have an increased effect. Nevertheless, results for the L.A. 9-story model structure indicate that the median

and 1-sigma level $\theta_{\max}$ for the 10/50 and 2/50 ground motions decrease (but by less than 10%) relative to the base case when θ_{f+} is increased to 0.030 rad.

As a general rule, if the story drift demands are either not large enough to induce many connection fractures even when $\theta_{f+} = 0.005$, or so large that most bottom beam-flanges fracture even when $\theta_{f+} = 0.030$, the differences in θ_{f+} will have little effect. Even if the total number of connections that fracture is altered significantly by changing θ_{f+}, the limited effect of bottom beam-flange fracture only may curb the effect on story drift demands (as discussed earlier).

2.6.3 Residual Moment Strength, M_{red+}

For the brittle base case, the residual moment strength (in positive bending) after fracture, M_{red+}, is assumed to be 30% of M_{p+}. Here, a reduced M_{red+} / M_{p+} of 10% is considered for the L.A. 9-story model structure. As summarized in Table 2-7, the counted median and 1-sigma level $\theta_{\max}$ for the 10/50 and 2/50 ground motions are increased from the base case by less than 20%. A single collapse occurs when $M_{red+} / M_{p+} = 10\%$, but it is under a ground motion that causes an extreme drift in the base case.

Table 2-7. Median and 1-sigma level $\theta_{\max}$ statistics under the assumption of a smaller residual moment strength in positive bending (i.e., M_{red+}) than that assumed in the brittle base case.

Model Structure	Earthquake Records	M_{red+}/M_{p+}=30% (Base Case)		M_{red+}/M_{p+}=10%		% Increase	
		Median [rad]	1-σ Level [rad]	Median [rad]	1-σ Level [rad]	Median [rad]	1-σ Level [rad]
L.A. 9-story	10/50	0.0217	0.0326	0.0222	0.0377	2%	16%
"	2/50	0.0440	0.1059	0.0461	0.1192	5%	13%

For both the L.A. 3-story and 9-story model structures, an M_{red+} / M_{p+} of 20% is also considered; as one might expect, the increases in the $\theta_{\max}$ statistics relative to the base case are even smaller (less than 10%).

2.6.4 Summary of Results of Sensitivity Studies

The story drift demands (specifically $\theta_{\max}$ statistics) for the L.A. 9-story (and, in some cases, L.A. 3-story) model structure with brittle connections exhibit little sensitivity

to variations from the base case of the fracture model parameters. This lack of sensitivity is not unexpected considering that the introduction of brittle base-case connections has less than a 55% effect on the $\theta_{\max}$ statistics relative to the ductile connections case, for any of the model structures considered. Song & Ellingwood (1998), who also studied the effects of bottom beam-flange fractures alone, found similar insensitivity.

Even though the values of the fracture model parameters are uncertain and likely random, the insensitivity of story drift demands to variations in these parameters suggests that it is unlikely worth the effort to randomize (for dynamic analysis) the base-case fracture parameter values; this is particularly true in light of the relatively large earthquake record-to-record variability of drift response. This conclusion is also confirmed by Song & Ellingwood (1998), as well as by Maison & Bonowitz (unpublished data, 1999). As reported below, the plastic rotation capacity associated with top beam-flange connection fracture, on the other hand, is found to be an influential addition to the base case that might well warrant randomization.

2.7 Top and Bottom Beam-Flange Connection Fractures

When only the potential for bottom beam-flange connection fractures is modeled, the limited drop in strength experienced by each story may explain why, in the base case, connection fractures have a less-than-anticipated effect on seismic story drift demands. Clearly the possibility of both top and bottom beam-flange connection fractures is important to consider. Unfortunately, field and laboratory evidence for top-flange connection fractures (with a slab) is sparse. In the field, inspection of beam top flanges is often hindered by the presence of the slab. Meanwhile, most laboratory tests of full-scale beam-column connections do not include a slab, thereby missing its potential effects on fracture of the top beam-flange. Furthermore, most experiments are stopped after fracture of the first, usually bottom, beam-flange connection. Faced with the lack of empirical data that can be used to estimate well the plastic rotation capacity against fracture of the top beam flange (i.e., θ_{f-}), three plausible values are considered.

It is generally believed that the plastic rotation capacity against connection fracture is, on average, greater for the top beam-flange than for the bottom flange (or, in other words, larger in negative bending than in positive bending). In particular, the presence of a slab is thought to delay fracture of the top beam-flange. Thus, as a "pessimistic" case, the same plastic rotation capacity is assigned in both negative and positive bending (i.e., $\theta_{f-} = \theta_{f+} = 0.015$); however, the potential for early (i.e., pre-yield) fracture in negative

bending is not included. Results obtained late in this study for two laboratory tests of full-scale beam-column connections that were continued beyond first (i.e., bottom) beam-flange fracture (Lee *et al.* 2000) prompted the consideration of $\theta_{f-} = 0.030$ as a second sensitivity case. Lastly, an "optimistic" top-flange plastic rotation capacity of $\theta_{f-} = 0.045$ is also considered. Note that for all three of the values of θ_{f-} considered, the residual moment strength of the connection in negative bending after fracture of the top flange is assumed to be 30% of M_{p-} (i.e., the same ratio used in the base case for bottom-flange fracture). The remainder of the fracture-model parameters retain the same values as used in the base case (refer to Table 2-1).

2.8 Top- and Bottom-Flange (TBF) Connection Fracture Results

The effects of top and bottom flange, TBF for short, connection fractures on seismic story drift demands are primarily compared with the effects of the base case, namely bottom-flange only (BFO) connection fractures; the addition of top-flange fractures can be thought of as a variation to the BFO base case. However, as it becomes evident that the effects of TBF connection fractures on story drift demands can be much more pronounced than for the BFO base case, the TBF cases are also compared directly with the ductile connections case. Following the form of the presentation of the BFO base case above, first the seismic drift responses for the L.A. 9-story model structure with TBF brittle connections are examined in some detail. In particular, the $\theta_{\max}$ and θ_{i} (but not θ_{ave}) statistics are reported, as well as the percentages of extreme $\theta_{\max}$ values and collapses. Results for the other SAC model structures are then summarized as more general conclusions are drawn.

2.8.1 TBF Connection Fracture Results for Los Angeles 9-Story

2.8.1.1 $\theta_{\max}$ Statistics

The counted median and 1-sigma level $\theta_{\max}$ under the 10/50 ground motions and the counted median $\theta_{\max}$ under the 2/50 ground motions are listed in Table 2-8 for the L.A. 9-story model structure with TBF brittle connections. The BFO base-case results are included for comparison, and the percentage increases in the medians from the BFO base case to the three TBF cases are reported. The counted 1-sigma level $\theta_{\max}$ under the 2/50 ground motions cannot be calculated for any of the TBF cases because more than three collapses are observed.

Table 2-8. Counted median and 1-sigma level θ_{max} statistics for the L.A. 9-story model assuming three different values of the plastic rotation capacity against fracture in negative bending (i.e., θ_{f-}). The counted 1-sigma level θ_{max} under the 2/50 ground motions (i.e., seventeenth largest of the twenty values) is a collapse in all of the TBF cases.

Connections Case	10/50 Median	10/50 1-σ Level	2/50 Median
(a) Counted θ_{max} Statistics [rad]			
BFO base case	0.0217	0.0326	0.0440
TBF case w/ θ_{f-} = 0.045	0.0217	0.0326	0.0440
TBF case w/ θ_{f-} = 0.030	0.0217	0.0326	0.0447
TBF case w/ θ_{f-} = 0.015	0.0217	0.0429	0.0573
(b) % Increase in Counted θ_{max} Statistics w.r.t. BFO Base Case			
BFO base case	--	--	--
TBF case w/ θ_{f-} = 0.045	0%	0%	0%
TBF case w/ θ_{f-} = 0.030	0%	0%	2%
TBF case w/ θ_{f-} = 0.015	0%	32%	30%

For the 10/50 ground motions, note that the introduction of TBF brittle connections does not change the (counted) median θ_{max} relative to the base case because, on average, $4/90 = 5\%$ or less of the top beam-flanges fracture at such low story drift demands. Even the 1-sigma level θ_{max} under the 10/50 ground motions does not change unless $\theta_{f-} = 0.015$. Similarly, for the 2/50 ground motions the increases in the median θ_{max} relative to the BFO base case are minimal unless TBF connection fractures are assumed to occur at a plastic rotation capacity of only 0.015 (radians). As discussed later, however, the 1-sigma level θ_{max} under the 2/50 ground motions (i.e., the 17th largest of the 20 values of θ_{max}) is a collapse even in the optimistic TBF case (i.e., $\theta_{f-} = 0.045$).

2.8.1.2 Spatial Variations of θ_i Statistics

The spatial variations of the counted median θ_i over the height of the L.A. 9-story model structure with TBF brittle connections are shown for the 2/50 ground motions in Figure 2-9. The results for the TBF cases with $\theta_{f-} = 0.045$ (i.e., the optimistic case) and $\theta_{f-} = 0.015$ (i.e., the pessimistic case) are compared with the BFO base-case results; the

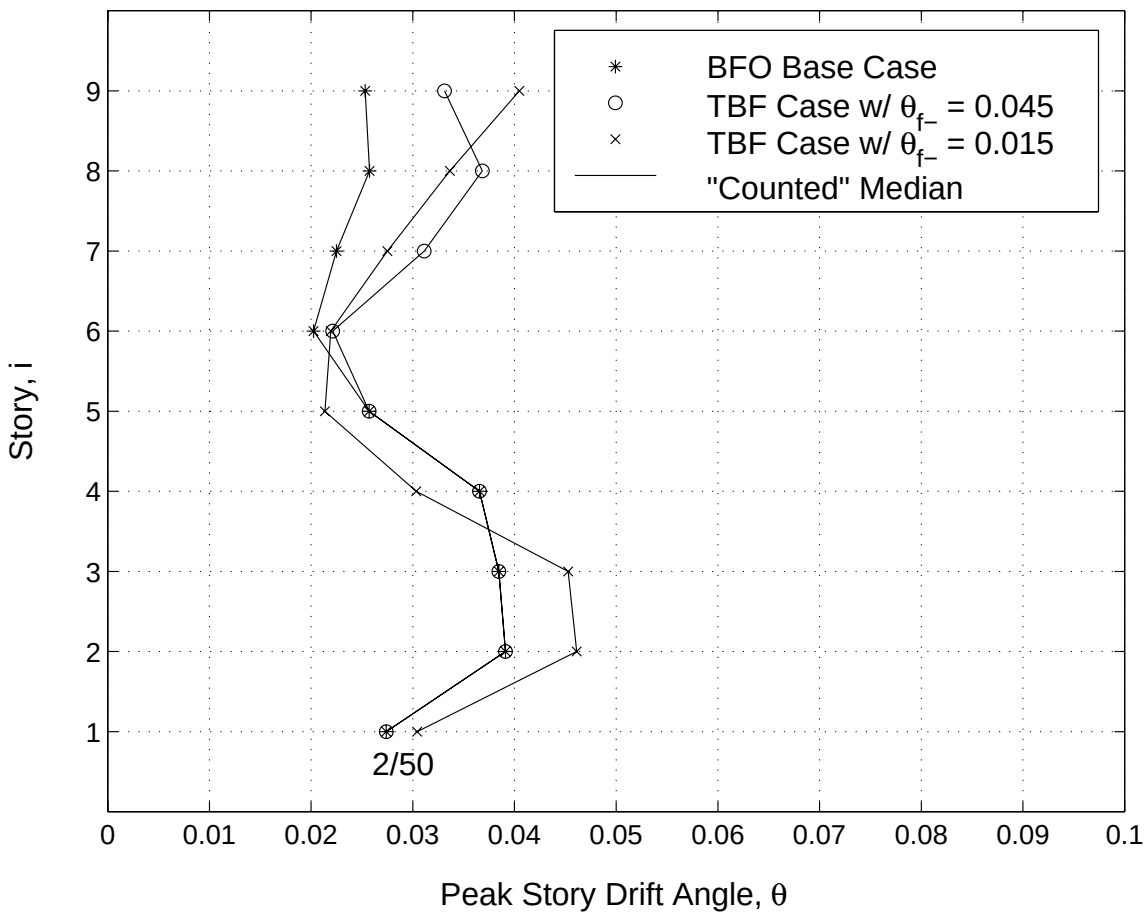

Figure 2-9. Spatial distribution of the counted median θ_i values over the height of the L.A. 9-story modeled with TBF connection fractures and subjected to the 2/50 ground motions.

(counted) median θ_i for the intermediate TBF case (i.e., $\theta_{f-} = 0.030$) are nearly identical to those for the optimistic case. Recall that relative to the ductile case, the BFO base case (for the 2/50 ground motions) exhibits an increase in the median θ_i in the lower stories of the L.A. 9-story model structure, but a decrease in the upper stories. In contrast, the optimistic TBF case experiences an increase (by less than 25%) in the median θ_i relative to the BFO base case only in the upper stories, and the pessimistic TBF case results in increases (by at most 45%) in both the upper and lower stories.

As mentioned above, the number of collapses prohibits calculation of the 1-sigma level θ_i for the 2/50 earthquake records. For the 10/50 ground motions, the changes in the median and 1-sigma level θ_i with the introduction of top-flange connection fractures are minimal, and hence are not shown.

2.8.1.3 Extremes and Collapses

The percentages of extreme story drift demands (i.e., $\theta_{\max} > 0.10$) and proportions of collapses observed under the 2/50 ground motions for the L.A. 9-story model structure with TBF connection fractures are summarized in Table 2-9. No extreme drifts are observed under the 10/50 ground motions.

Table 2-9. Percentage of "extreme" drifts (i.e., $\theta_{\max}$>0.10, including collapses) and proportion of collapses among the 2/50 ground motions for the L.A. 9-story model with TBF connection fractures.

Connections Case	Percentage of Extremes	Proportion of Collapses
BFO base case	20%	0/20
TBF case w/ θ_{f-} = 0.045	25%	5/20
TBF case w/ θ_{f-} = 0.030	25%	5/20
TBF case w/ θ_{f-} = 0.015	40%	6/20

Recall (as noted in the table) that the percentage of extreme $\theta_{\max}$ values in the BFO base case for the L.A. 9-story model structure was 20% (with no collapses). Thus, the percentage of extreme story drifts does not increase by more than five percentage points from the BFO base case to the TBF cases, except when $\theta_{f-} = 0.015$. The extreme drifts in the TBF cases, however, are primarily collapses, whereas no collapses occurred for the BFO base case. Also recall that with respect to the ductile connections case, the percentage of extreme drifts for the L.A. 9-story model structure with BFO (base-case) brittle connections doubled for the 2/50 ground motions; similarly, the percentage of extreme drifts redoubles from the BFO base case to the TBF case with $\theta_{f-} = 0.015$. The number of collapses, however, is approximately the same for all three TBF cases.

2.8.1.4 Summary

As one might expect, the introduction of TBF brittle connections has a larger effect on the story drift demand statistics for the L.A. 9-story model structure when the plastic rotation capacity for the top flange is smaller (e.g., $\theta_{f-} = 0.015$), and when the story drift response level is higher (e.g., 2/50 ground motions). In fact, only the pessimistic TBF case results in more than a 25% increase in the story drift demand statistics relative to the BFO base case. Later, it will be demonstrated that by considering the story drift demands

in the ductile connections case, one can anticipate whether a TBF case with a given θ_{f-} will significantly increase the story drift demands. First, however, the effects of TBF connection fractures for the other SAC model structures are reported.

2.8.2 TBF Connection Fracture Results for All Structures

The effects on story drift demands of top beam-flange connection fractures in addition to bottom beam-flange fractures are similar for the L.A. 9-story model structure and the other SAC model structures. Based on the findings for the L.A. 9-story model structure, the analyses for the other model structures are limited to the TBF cases with $\theta_{f-} = 0.015$ and $\theta_{f-} = 0.045$; for the three Seattle model structures, only one of these two TBF cases is carried out. As will be shown, these additional results for the other model structures are adequate to permit quite general conclusions.

2.8.2.1 $\theta_{\max}$ Statistics, Extremes, and Collapses

For all of the model structures (including the L.A. 9-story), the counted median $\theta_{\max}$ values under the 10/50 ground motions are the same in the "optimistic" TBF case (i.e., $\theta_{f-} = 0.045$), and/or "pessimistic" (i.e., $\theta_{f-} = 0.015$) TBF case, as they are in the BFO base case (refer back to Table 2-2). Similarly, the counted 1-sigma level $\theta_{\max}$ values under the 10/50 ground motions do not change from the BFO base case to the optimistic TBF case. In the pessimistic TBF cases, however, the counted 1-sigma level $\theta_{\max}$ values (for the 10/50 ground motions) increase by as much as 35% with respect to the BFO base case, as summarized in Table 2-10.

When subjected to the 2/50 ground motions, only the pessimistic TBF cases result in an increase of the (counted) median $\theta_{\max}$ by more than 15% relative to the BFO base case, as summarized in Table 2-11. The (counted) 1-sigma level $\theta_{\max}$ (under the 2/50 ground motions), however, cannot be obtained in the optimistic nor pessimistic TBF cases for three of the model structures (i.e., L.A. 9- and 20-story, and Seattle 3-story) due to the number of collapses (i.e., more than three out of twenty).

The percentage of extreme drifts (i.e., $\theta_{\max} > 0.10$) and the proportion of collapses among the 2/50 earthquake records are listed in Table 2-12 for the BFO and TBF cases of all the model structures. Under the 10/50 ground motions, just two collapses occur, in the pessimistic TBF case of the L.A. 20-story model structure. It should be kept in mind, however, that the earthquake records that cause collapse of the M1 models considered

Table 2-10. Counted 1-sigma level θ_{max} values under the 10/50 ground motions for all six of the buildings modeled with "optimistic" (i.e., θ_{f-}=0.045) and "pessimistic" (i.e., θ_{f-}=0.015) TBF connection fractures. "NA" denotes cases that were not considered.

Model Structure	BFO Base Case	"Optimistic" TBF Case		"Pessimistic" TBF Case	
	1-σ Level [rad]	1-σ Level [rad]	% Increase	1-σ Level [rad]	% Increase
Los Angeles 3-story	0.0351	0.0351	0%	0.0475	35%
" 9-story	0.0326	0.0326	0%	0.0429	32%
" 20-story	0.0276	0.0276	0%	0.0313	13%
Seattle 3-story	0.0302	0.0302	0%	NA	NA
" 9-story	0.0250	0.0250	0%	NA	NA
" 20-story	0.0191	NA	NA	0.0191	0%

Table 2-11. Counted median θ_{max} values under the 2/50 ground motions for all six of the buildings modeled with "optimistic" (i.e., θ_{f-}=0.045) and "pessimistic" (i.e., θ_{f-}=0.015) TBF connection fractures. "NA" denotes cases that were not considered.

Model Structure	BFO Base Case	"Optimistic" TBF Case		"Pessimistic" TBF Case	
	Median [rad]	Median [rad]	% Increase	Median [rad]	% Increase
Los Angeles 3-story	0.0685	0.0775	13%	0.0808	18%
" 9-story	0.0440	0.0440	0%	0.0573	30%
" 20-story	0.0545	0.0545	0%	"collapse"	--
Seattle 3-story	0.0645	0.0676	5%	NA	NA
" 9-story	0.0336	0.0336	0%	NA	NA
" 20-story	0.0311	NA	NA	0.0355	14%

Table 2-12. Percentage of extreme drifts (i.e., θ_{max}>0.10, including collapses) and proportion of collapses among the 2/50 earthquake records for all six of the buildings modeled with "optimistic" (i.e., θ_{f-}=0.045) and "pessimistic" (i.e., θ_{f-}=0.015) TBF connection fractures. "NA" denotes cases that were not considered.

Model Structure		BFO Base Case		"Optimistic" TBF Case		"Pessimistic" TBF Case	
		Extremes [%]	Collapses	Extremes [%]	Collapses	Extremes [%]	Collapses
Los Angeles	3-story	0%	0	0%	0	20%	0
"	9-story	20%	0	25%	5/20	40%	6/20
"	20-story	40%	8/20	50%	10/20	60%	12/20
Seattle	3-story	20%	2/20	30%	5/20	NA	NA
"	9-story	10%	2/20	15%	3/20	NA	NA
"	20-story	0%	0	NA	NA	5%	0

here do not necessarily result in collapse of the corresponding M1+ models (as discussed in Section 2.11). As observed for the L.A. 9-story model structure, the percentages of extreme drifts (among the 2/50 ground motions) does not increase by more than ten percentage points over those for the BFO base case unless $\theta_{f-} = 0.015$; in this pessimistic case, the percentages of extreme drifts increase by as much as twenty percentage points relative to the BFO base case. Note that almost all of the extreme drifts are in fact collapses.

2.8.3 Anticipating Effect of TBF Connection Fractures

For the model structures other than the L.A. 9-story, the effects of TBF connection fractures on the story drift demands are not computed for all three of the θ_{f-} values considered. However, as discussed in more detail below, the value of θ_{f-} relative to the story drift demand level (e.g., in the ductile connections case) is generally sufficient to indicate whether TBF connection fractures will significantly affect the drift response. As an example, the counted median θ_{max} under the 2/50 ground motions are displayed graphically in Figure 2-10 for the three Los Angeles model structures and the TBF brittle connections cases with $\theta_{f-} = 0.015$ and $\theta_{f-} = 0.045$. The BFO base-case results are included in the figure, but unlike in the previous subsections, the percentage increases in the (counted) median θ_{max} are reported with respect to the ductile case results, which are also shown. Presented in this way, the effects of TBF (or BFO) connection fractures on

the story drift demands are quantified relative to the pre-Northridge anticipated ductile behavior of these SMRF model structures. More importantly, the ductile-case story drift demands can be used to anticipate the value of the plastic rotation capacity θ_{f-} for which top beam-flange connection fractures are expected to significantly increase the story drift demands.

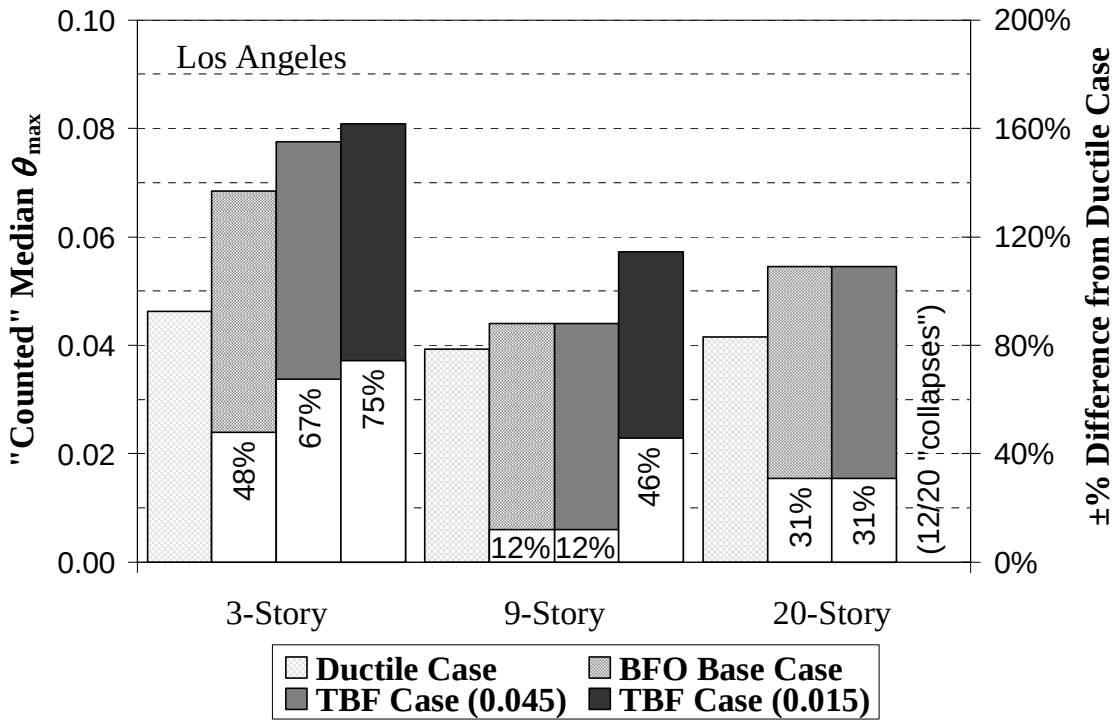

Figure 2-10. Increases in the counted median $\theta_{\max}$ values under the 2/50 ground motions for the three Los Angeles buildings modeled with ductile versus with BFO or TBF connection fractures.

Given that peak story drift angles tend to be good indicators of connection rotation demands (Gupta & Krawinkler 1999), *it is proposed that multiple top-flange connection fractures (in addition to bottom-flange fractures) can be expected when the story drift angle demands (e.g., median* $\theta_{\max}$ *for the ductile case) exceed approximately* $\theta_{f-} + 0.01$, *recognizing that elastic story drift angles are typically about 0.01 (radians).* For example, because the (counted) median $\theta_{\max}$ under the 2/50 ground motions for the L.A. 9-story model structure is approximately 0.04 in the ductile case (refer to Figure 2-10), few top-flange connection fractures are expected unless θ_{f-} is less than 0.03. Indeed, the TBF case with $\theta_{f-} = 0.045$ does not affect the median $\theta_{\max}$ relative to the BFO base case,

and it increases the median $\theta_{\max}$ by only 12% with respect to the ductile case; on the other hand, in the TBF case with $\theta_{f-} = 0.015$ the increase in the median $\theta_{\max}$ relative to the ductile case is 46% (an approximately 30% increase with respect to the BFO base case). The same applies to the *P-Δ* sensitive L.A. 20-story model structure, which also has a median $\theta_{\max}$ of approximately 0.04 in the ductile case; for the TBF case with $\theta_{f-} = 0.015$, the counted median $\theta_{\max}$ (i.e., the tenth largest $\theta_{\max}$ from the twenty 2/50 earthquake records) is a collapse, whereas the (counted) median $\theta_{\max}$ for the TBF case with $\theta_{f-} = 0.045$ is only 31% larger than it is in the ductile case (and is the same as in the BFO base case).

For the L.A. 3-story model structure, the (counted) median $\theta_{\max}$ for the 2/50 ground motions (also illustrated in Figure 2-10) increases by 75% from that in the ductile case when $\theta_{f-} = 0.015$, since it is less than the ductile case median $\theta_{\max}$ of 0.046 minus 0.01. Note, however, that even in the TBF case with $\theta_{f-} = 0.045$ the median $\theta_{\max}$ increase by 67% with respect to the ductile case, despite the fact that $\theta_{f-} > 0.046 - 0.01$. Note, too, that the median $\theta_{\max}$ for the BFO base case already represents an unusually large 48% increase from the ductile case. Apparently, the L.A. 3-story model structure is relatively resistant to the effects of TBF connection fractures. So while the proposal made here for anticipating when TBF connection fractures will significantly effect story drift demands appears to predict the onset of important effects, it does not necessarily predict the magnitude of these effects (e.g., percentage increases in $\theta_{\max}$).

Most of the TBF cases considered for the Seattle model structures also uphold the postulated proposal, as summarized in Table 2-13. For both the Seattle 3- and 9-story model structures, only the TBF case with $\theta_{f-} = 0.045$ is investigated. For either model structure, if the (counted) median or 1-sigma level $\theta_{\max}$ statistic is less than 0.051 (i.e., nearly $0.045 + 0.01$) in the ductile case, the change in the $\theta_{\max}$ statistics due to top-flange connection fractures is less than 15% relative to the ductile case. The median $\theta_{\max}$ for the 3-story (i.e., 0.0528) and the 1-sigma level $\theta_{\max}$ for the 9-story (i.e., 0.0514), both under the 2/50 ground motions, increase by about 30-35% from the ductile case to the TBF case with $\theta_{f-} = 0.045$; with respect to the BFO base case, however, the increase to the TBF case is less than a 5%. In contrast, the relatively large counted 1-sigma level $\theta_{\max}$ in the ductile case for the Seattle 3-story model under the 2/50 earthquake records (i.e., $0.085 > 0.055$) effectively becomes a collapse in the TBF case (because more than 3 of the 20 earthquake records cause collapse). For the Seattle 20-story model structure, which display comparatively which display comparatively low story drift demands in all cases, only the TBF case with $\theta_{f-} = 0.015$ is investigated. The only significant increase (i.e., greater than 10%) in the (counted) $\theta_{\max}$ statistics is that for the 1-sigma level $\theta_{\max}$

under the 2/50 ground motions (i.e., an 81% increase), which is equal to 0.0373 in the ductile case. Although the median $\theta_{\max}$ under the 2/50 ground motions is also greater than $0.015+0.010$ in the ductile case, it increases by only a few percent in the TBF case. This is probably because the large peak story drift angles for the Seattle 20-story are all concentrated in a few upper stories.

Table 2-13. Increases in the counted median and 1-sigma level values of $\theta_{\max}$ for the three Seattle buildings modeled with ductile versus with TBF connection fractures.

Model Structure	Counted Median $\theta_{\max}$			Counted 1-Sigma Level $\theta_{\max}$		
	Ductile Case [rad]	TBF Case [a] [rad]	% Increase	Ductile Case [rad]	TBF Case [a] [rad]	% Increase
(a) 10/50 ground motions						
Seatlle 3-story	0.0216	0.0209	-3%	0.0280	0.0302	8%
Seatlle 9-story	0.0210	0.0182	-13%	0.0242	0.0250	3%
Seatlle 20-story	0.0149	0.0154	3%	0.0207	0.0191	-8%
(b) 2/50 ground motions						
Seatlle 3-story	0.0528	0.0676	28%	0.0851	"collapse"	--
Seatlle 9-story	0.0357	0.0336	-6%	0.0514	0.0700	36%
Seatlle 20-story	0.0345	0.0356	3%	0.0373	0.0675	81%

[a] θ_{f-}=0.045 rad for Seattle 3- and 9-story, and θ_{f-}=0.015 rad for Seattle 20-story

For all the combinations of model structures with TBF brittle connections, suites of earthquake records, and $\theta_{\max}$ statistics considered, the correlation between the ductile case $\theta_{\max}$ statistics and the percentage increases in those statistics due to TBF connection fractures are depicted graphically in Figure 2-11. Note that the ductile case $\theta_{\max}$ statistics are normalized by the top beam-flange plastic rotation capacity against fracture (i.e., θ_{f-}) plus the estimated elastic rotation of 0.01 (radians), and that the percentage increases due to TBF connection fractures are with respect to the ductile case. As demonstrated aboveon a case-by-case basis, from Figure 2-11 it is evident that the percentage increase in the $\theta_{\max}$ statistics from the ductile to the TBF cases is most significant (i.e., about 40% or larger) when the ductile-case $\theta_{\max}$ statistic is larger than $\theta_{f-}+0.01$ (with a few exceptions). Furthermore, it appears that, in a rough sense, the larger the ductile case $\theta_{\max}$ relative to θ_{f-}, the larger the percentage increase in the TBF case.

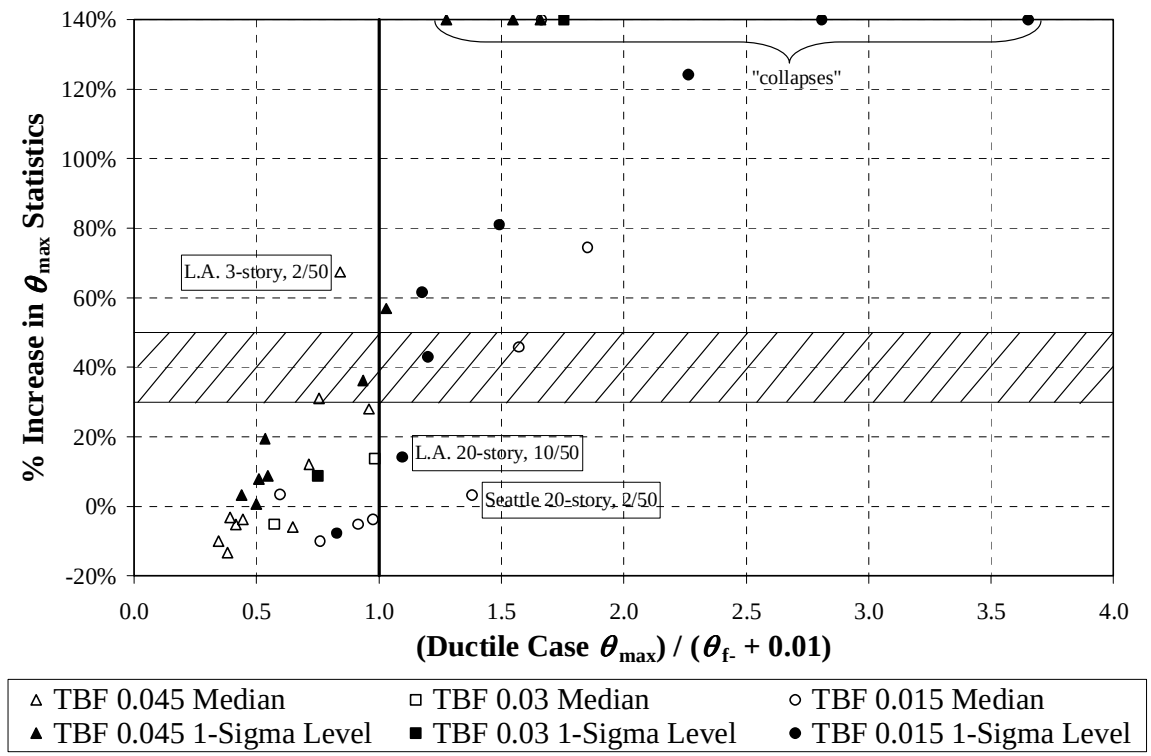

Figure 2-11. Anticipating the effects of TBF connection fractures on the $\theta_{\max}$ statistics for all six of the model buildings subjected to the 10/50 and 2/50 earthquake records. Note that the percentage increases are with respect to the ductile case.

2.8.4 Summary of TBF Connection Fracture Results

It is observed that top beam-flange connection fractures, in addition to bottom-flange fractures, can increase the median $\theta_{\max}$ by 30% or more with respect to the BFO base case, and by 75% or more with respect to the ductile connections case, if the plastic rotation capacity associated with top-flange fracture (i.e., θ_{f-}) is sufficiently low and the ground motion levels are sufficiently high. The value of θ_{f-} for which the median $\theta_{\max}$ is expected to increase by more than 15% with respect to the BFO base case, or by more than about 40% with respect to the ductile case (with a few exceptions), depends on the story-drift demand level, which can be measured by the results for the more conventional ductile connections model of the SMRF structure. Furthermore, for the TBF cases with relatively small values of θ_{f-} (e.g., 0.015 radians), the percentage of extreme story drifts (i.e., $\theta_{\max} > 0.10$) can double relative to the BFO base-case results, and quadruple relative

to the ductile case results, such that extreme story drifts are observed for as many as 60% of the (2/50) earthquake records. For a larger value of θ_{f-} (e.g., 0.045 radians), however, the percentages of extreme story drifts, as well as the $\theta_{\max}$ statistics, remain about the same in the TBF case as they are for the BFO base case.

Under relatively high intensity ground motions (e.g., the 2/50 set), it is apparent that story drift demands for SMRF structures with TBF brittle connections can be very sensitive to the value of θ_{f-}. Given this potential sensitivity to the top beam-flange plastic rotation capacity, new information (e.g., laboratory tests of MRF connections with slabs) that can be used to better estimate θ_{f-} would be valuable. When better estimates of θ_{f-} become available, the results summarized here should remain useful for estimating the effects of TBF connection fractures on seismic drift response. While treated here as the top beam-flange capacity, the same conclusions will likely hold if θ_{f-} is interpreted more generally as the capacity of the second-to-fracture flange (top or bottom). Even so, in light of the potentially significant effects of TBF connection fractures, a full parametric sensitivity study centered on a TBF "base case," rather than on the BFO base case, seems warranted.

2.9 Column Fractures at Connections

As investigated above, fractures of welded moment-resisting connections most commonly propagate into the flange (and possibly the web) of the connected beam, or else remove small "divots" from the connected column flange. However, the propagation of fractures into the connected column flange (and possibly web) has also been observed. The reduction in column moment capacity associated with such "column fractures" may be larger than that for beam fracture, given the absence of a shear tab; furthermore, the potential for forming a story mechanism with column fractures exists. Thus, the possibility of column fractures needs to be considered despite the lack of test data that can be used to estimate when column fracture will occur and how a column will behave after fracture. The analysis model used here to emulate column fracture is detailed above in Section 2.2.3. Note that the model is probably conservative is some respects and non-conservative in others.

2.10 Column Fracture Results

The effects of column fractures are studied here using the L.A. 9-story, by comparing story drift demand results for the model structure with column fractures to the otherwise identical cases with only beam flange fractures. It is important to note that because beam flanges that have been designated as "triggers" of column fracture are themselves no longer allowed to fracture (refer to Section 2.2.3 for a detailed explanation), the total number of fractures (i.e., beam flange *and* column) is expected to remain nearly constant. Based on discussions with David Bonowitz, who has been a major contributor to the SAC Connection Database (e.g., FEMA 289, 1997), it is assumed that there is a 25% probability that a beam flange will act as a column fracture trigger.

2.10.1 Bottom Flange Only (BFO) Column Fracture Case

A variant of the bottom flange only (BFO) base case, in this case only brittle bottom beam flanges act as "triggers," and hence column fractures only occur below beam-column joints (or, in other words, at the top of columns in a story). The residual column moment strength after fracture, $M_{red,col}$, is assumed here to be 10% of $M_{p,col}$ (the column plastic moment strength). A ratio of $M_{red,col} / M_{p,col} = 20\%$, which is thought to be a more reasonable assumption, has also been considered, but the results for this case are not presented here in detail.

As summarized in Table 2-14, there is almost no effect for the 10/50 ground motions on the (counted) median or 1-sigma level $\theta_{\max}$ when column fractures are introduced into the BFO base case. In fact, the earthquake record-by-record effect on $\theta_{\max}$ is less than 15% for all twenty of the 10/50 ground motions (Cornell & Luco 1999). For the 2/50 ground motions, again the effect of column fractures on the median $\theta_{\max}$ (relative to the base case) is less than 10%, but the 1-sigma level $\theta_{\max}$ increases by 34%, indicating some effect on the extremes. Whereas no collapses are observed in the beam-flange-fracture base case, two collapses occur in the column fracture case (when subjected to the 2/50 ground motions). The percentage of extreme drifts (i.e., $\theta_{\max} > 0.10$), however, only increases from 20% for the base case to 25% for the column fracture case.

Table 2-14. Counted median and 1-sigma level values of $\theta_{\max}$ for the L.A. 9-story model structure in the BFO base case (i.e., with beam-flange fractures) and in the otherwise identical case with column fractures.

Earthquake Records	Beam BFO Case		Column BFO Case		% Increase	
	Median [rad]	1-σ Level [rad]	Median [rad]	1-σ Level [rad]	Median	1-σ Level
10/50	0.0217	0.0326	0.0221	0.0316	2%	-3%
2/50	0.0440	0.1059	0.0478	0.1419	9%	34%

In summary, the introduction of column fractures into the BFO base case has virtually no effect of the median $\theta_{\max}$ response and only a mild effect on the 1-sigma level $\theta_{\max}$ for the 2/50 records, even though $M_{red,col} / M_{p,col} = 10\%$. For a few extreme ground motions, however, introducing column fractures leads to "collapse" (of the M1 model). As one might expect, if instead it is assumed that $M_{red,col} / M_{p,col} = 20\%$, the effects of the column fractures with respect to the base case are even smaller.

2.10.2 "Pattern" of Column Fracture Triggers in Lower Stories

Although the residual moment strength associated with column fracture (i.e., $M_{red,col} / M_{p,col} = 20\%$ or 10% in both positive and negative bending) is less than that for beam-flange fracture (i.e., $M_{red} / M_p = 30\%$ when the fractured flange is in tension), the results discussed above suggest that the introduction of column fractures has little effect on the $\theta_{\max}$ response if the column fracture "triggers" are randomly located. Clearly though, with column fractures the potential exists for forming a story mechanism. With only beam-flange fractures, in contrast, even the fracture of every beam on a floor (or floors above and below a story) can at most result in an effectively larger story height.

To consider a "worst-case" scenario in which several (or all) of the column ends in a single story fracture, a deterministic "pattern" of column fracture triggers in the lower stories of the L.A. 9-story model structure is considered as a variant of the BFO base case. The total number of bottom beam-flange triggers (i.e., approximately 25% of the ninety bottom beam flanges) is kept the same as in the randomly located triggers case (in Section 2.10.1), but here all the triggers are placed in the first through fourth stories. Keep in mind that beam flanges that are designated as triggers remain ductile, and that for interior connections, only one of the two bottom beam flanges adjacent to the column

below the joint will actually trigger column fracture. As a result, here only one of the bottom beam flanges adjacent to a column is designated as a trigger so that beam-flange fractures may still occur in the lower stories. The assumed residual moment strength ratio for the columns here is $M_{red,col} / M_{p,col} = 20\%$.

As summarized in Table 2-15, under the 10/50 ground motions the effects of the lower-story pattern of column-fracture triggers on the (counted) median and 1-sigma level $\theta_{\max}$ statistics are small (i.e., less than 10%) relative to the beam-flange-fracture BFO base case. This is likely because few column fractures actually occur. For the 2/50 ground motions, however, the median $\theta_{\max}$ increases by 32% for the model with column fractures in the lower stories. Also, five collapses (which is too many to count the 1-sigma level $\theta_{\max}$) and three extreme drifts (i.e., $\theta_{\max} > 0.10$) are observed in the column fracture case under the 2/50 ground motions. Recall (e.g., from Table 2-12) that for the BFO base case, only four extreme $\theta_{\max}$ responses resulted from the 2/50 ground motions, and no collapses. No extremes or collapses are observed under the 10/50 ground motions.

Table 2-15. Counted median and 1-sigma level values of $\theta_{\max}$ for the L.A. 9-story model structure in the BFO base case (i.e., with beam-flange fractures) and in the otherwise identical case with column fractures all located in the lower stories.

Earthquake Records	Beam BFO Case		Column Pattern Case		% Increase	
	Median [rad]	1-σ Level [rad]	Median [rad]	1-σ Level [rad]	Median	1-σ Level
10/50	0.0217	0.0326	0.0231	0.0356	6%	9%
2/50	0.0440	0.1059	0.0579	"collapse"	32%	--

In summary, if many column fractures are concentrated in a few stories, the effects relative to the beam-flange-fracture base case can be substantial under some extreme ground motions. It is interesting to note that, for the 2/50 ground motions, the effects of the pattern of column-fracture triggers appear to be larger than the effects of the patterns of bottom-beam-flange "early" (i.e., pre-yield) fractures discussed in Section 2.6.1. For example, with the pattern of early fracturing beam flanges in the lower stories, the median $\theta_{\max}$ (under the 2/50 records) was almost unchanged from the BFO base case; likewise, only two collapses and two extreme drifts were recorded. For the 10/50 earthquake records, however, the effects of a pattern of "early" fracturing beam flanges in

the lower stories are somewhat larger than that of column fractures in the lower stories, since the "early" beam flanges will fracture at lower drifts. The effects of randomly located column fractures above *and* below each beam-column joint are considered next. A lower-story (or other) pattern of column fractures above and below each joint is not considered, although it is anticipated that such a case would have the greatest potential for the formation of a story mechanism.

2.10.3 Top and Bottom Flange (TBF) Column Fracture Cases

As variants of the cases in which top and bottom *beam* flanges fracture (i.e., the TBF cases), here several cases in which column fractures above and/or below a joint may be triggered are considered. Although the three TBF cases in which top beam-flange fracture (or triggering of column fracture) is assumed to occur at maximum plastic rotations of $\theta_{f-} = 0.045$, 0.030, or 0.015 (radians) are considered, detailed results are presented here only for the "pessimistic" $\theta_{f-} = 0.015$ case. For all of these TBF column fracture cases, it is assumed that $M_{red,col} / M_{p,col} = 20\%$.

As for the BFO case discussed in the previous subsection, the introduction of column fractures into the pessimistic TBF case has little effect on the (counted) median $\theta_{\max}$ response (under either the 10/50 or 2/50 ground motions), as summarized in Table 2-16. Under the 10/50 ground motions, note also that the 1-sigma level $\theta_{\max}$ *decreases* by 16% when column fractures are introduced, which reflects the fact that the largest change in the $\theta_{\max}$ response among the 10/50 records is a 35% decrease (Cornell & Luco 1999). Under the 2/50 ground motions, the number of collapses with or without column fractures prohibits calculation of the (counted) 1-sigma level $\theta_{\max}$. Whereas the model structure collapses under six of the 2/50 ground motions in the TBF case without column fractures,

Table 2-16. Counted median and 1-sigma level values of $\theta_{\max}$ for the L.A. 9-story model structure in the pessimistic TBF case (i.e., with beam-flange fractures) and in the otherwise identical case with column fractures.

Earthquake Records	Beam TBF Case		Column TBF Case		% Increase	
	Median [rad]	1-σ Level [rad]	Median [rad]	1-σ Level [rad]	Median	1-σ Level
10/50	0.0217	0.0429	0.0221	0.0361	2%	-16%
2/50	0.0573	"collapse"	0.0579	"collapse"	1%	--

it collapses under just five of those ground motions in the case with column fractures. Similarly, the percentage of extreme drifts (among the 2/50 earthquake records) is 40% without column fractures, but 30% with them.

In summary, the introduction of column fractures above and below moment-resisting joints, in addition to and triggered by top and bottom beam-flange fractures, has little added effect on the $\theta_{\max}$ response statistics (including the proportion of collapses) for the L.A. 9-story model structure subjected to either the 10/50 or 2/50 ground motions. This is true when the top-flange plastic rotation capacity against fracture is assumed to be $\theta_{f-} = 0.015$, and even more so when $\theta_{f-} = 0.030$ or $\theta_{f-} = 0.045$. The exceptions are few, and most of these exceptions actually show a decrease in the $\theta_{\max}$ response for the model structure with column fractures. It is important to keep in mind, however, that the total number of fractures remains unchanged with the introduction of column fractures because the beam-flange "triggers" themselves do not fracture.

2.10.4 Summary of Column Fracture Results

Except for a few of the 2/50 ground motions, if column fracture "triggers" are randomly located within a model structure, the effect of column fractures on the $\theta_{\max}$ response is not much different than that of the otherwise identical beam-flange-fracture case. However, if a deterministic worst-case "pattern" of column-fracture triggers in the lower stories is considered, the effect is larger on the median $\theta_{\max}$ (i.e., a 30% increase) and the column fractures result in twice as many collapses or extremes (i.e., $\theta_{\max} > 0.10$) compared to a model structure with only beam-flange fractures. Further field study of the potential for clustering of column fractures, a more rigorous (e.g., fiber) model of column fracture, and additional laboratory test results are all needed for a more comprehensive investigation of the effects of column fractures.

2.11 The Effects of Interior Frames; the M1+ Model

As summarized above in Table 2-12, all of the model structures considered suffered "collapses" and extreme drifts (i.e., $\theta_{\max} > 0.10$) under some of the 2/50 ground motions when top and bottom beam-flange (TBF) connection fractures with $\theta_{f-} = 0.015$ were incorporated into the simple centerline (i.e., "M1") models. In fact, half of the model structures experienced extreme drifts even in the ductile case, and half of the model structures experienced collapses in the bottom-flange-only (BFO) connection-fracture base case. As investigated by Gupta & Krawinkler (1999) during Phase II of the SAC

Steel Project, the effects of improved analytical modeling can be significant for such extreme cases, to the extent that collapses of the M1 model may be "saved" by the improvements. Primarily to check whether connection fractures will still lead to collapses or extreme drifts when an improved analytical model is used, here the "M1+" models of several of the SAC buildings with connection fractures are analyzed.

As introduced briefly in Section 2.2.1, the M1+ model of a structure accounts for the strength and stiffness of interior gravity frames and shear connections. For an M1 model, the mass of interior gravity frames is accounted for, as it contributes to the inertial loads and *P-Δ* effects, but the stiffness and strength of these frames are assumed to be negligible. However, because interior columns are continuous members and may be fixed at their base (e.g., L.A. 3-story, Seattle 3-story), or pinned at their base but restrained at the ground level (e.g., L.A. 9-story), the interior frames contribute some stiffness and strength. In addition, if the limited strength and stiffness of shear connections is accounted for rather than assuming that they act as pure pins, the interior gravity frames will contribute additional stiffness and strength. As done by Gupta & Krawinkler (1999), interior gravity frames are included in the M1+ model (referred to as the "M1A" model by Gupta & Krawinkler) via a single "equivalent bay." The shear connections (in both the interior gravity frame and exterior moment-resisting frames) are modeled with rotational springs that become perfectly plastic at a rotation of 2% and a moment equal to 20% of the beam plastic moment (i.e., $M_{p,beam}$) in positive bending, and at a rotation of 1% and moment of 10% of $M_{p,beam}$ in negative bending – refer to Appendix B for an illustration. The larger moment strength assigned in positive bending reflects the contribution of the slab in compression.

2.11.1 Collapses

As an example of the potential of the M1+ model to "save" collapses that occur for the M1 model, consider the L.A. 9-story structure and the six 2/50 ground motions that cause collapse of its M1 model in the "pessimistic" TBF case (i.e., $\theta_{f-} = 0.015$). As alluded to above in Table 2-12, five of these six 2/50 earthquake records also cause collapse of the L.A. 9-story M1 model in the "optimistic" TBF case (i.e., $\theta_{f-} = 0.045$), but no collapses occur in the BFO base case or the ductile case. Four of the six earthquake records, though, cause extreme drifts in the BFO base case, as do two of them in ductile case. For the M1+ model of the L.A. 9-story structure, the maximum story drift angles (i.e., $\theta_{\max}$) for the six ground motions of interest are listed in Table 2-17.

Table 2-17. Values of θ_{max} for the M1+ models of the L.A. 9-story building subjected to the six earthquake records that cause collapse of the M1 model in the "pessimistic" TBF case (i.e., θ_{f-}=0.015). Note that the median θ_{max} values are across the six earthquake records, and the percentage increases are with respect to the ductile case.

Earthquake Record	Ductile Case	BFO Base Case		"Optimistic" TBF Case		"Pessimistic" TBF Case	
	θ_{max} [rad]	θ_{max} [rad]	% Increase	θ_{max} [rad]	% Increase	θ_{max} [rad]	% Increase
LA24	0.0757	0.0848	12%	0.0862	14%	0.1037	37%
LA30	0.0435	0.0607	40%	0.0643	48%	0.0976	124%
LA35	0.0711	0.0853	20%	0.0955	34%	0.1090	53%
LA36	0.0735	0.0835	14%	0.0920	25%	0.0969	32%
LA37	0.0569	0.0617	8%	0.0679	19%	0.1291	127%
LA38	0.0771	0.0861	12%	0.1067	38%	0.1263	64%
Median	0.0650	0.0761	17%	0.0841	29%	0.1097	69%

Note, first of all, that the improved M1+ model does not collapse under any of the six ground motions. This is true even in the pessimistic TBF case, although the resulting drifts are all nearly "extreme" (i.e., $\theta_{max} > 0.10$). In the ductile case and BFO base case, the M1+ model reduces the median θ_{max} for the six records by 25% (to 0.0650 radians) and 23% (to 0.0761 radians), respectively, with no extreme drifts in either case. Secondly, note that the effects of the three different connection fracture scenarios (with respect to the ductile case) on the M1+ model θ_{max} values and median appear to be about the same as the effects seen for the M1 model. That is, on average, BFO fractures alone have a relatively small effect on θ_{max}, whereas TBF fractures can have a significant effect on θ_{max}, particularly if $\theta_{f-} = 0.015$. Whether this observation also holds for the θ_{max} statistics across all the 10/50 and the 2/50 earthquake records is investigated in the next subsection.

2.11.2 θ_{max} statistics

In addition to the analyses of the L.A. 9-story M1+ model structure presented above, the M1+ models of the following structures and connection fracture cases are also analyzed under all of the 10/50 and 2/50 ground motions: (i) the L.A. 3-story structure with BFO base case connection fractures, (ii) the L.A. 9-story with BFO base case and optimistic TBF case (i.e., $\theta_{f-} = 0.045$) connection fractures, and (iii) the Seattle 3-story with BFO base case and optimistic TBF case connection fractures. By subjecting the

M1+ model structures to both the 10/50 and 2/50 earthquake records, the effects of improved modeling on story drift demands can be assessed for ground motions of various intensities, not just those which cause extreme drifts or collapse of the M1 model. In addition, for the L.A. 9-story and Seattle 3-story structures, the difference between the BFO base case and the optimistic TBF case using the M1+ model can be compared to the difference between the two cases using the M1 model. The counted median and 1-sigma level θ_{max} statistics for the M1+ and M1 models of the buildings and connection fracture cases listed above are summarized in Table 2-18.

Table 2-18. Counted θ_{max} statistics for the M1+ (and M1) models of three of the SAC buildings. For the L.A. 9-story and Seattle 3-story buildings, the percentage increases in the θ_{max} statistics from the BFO base case to the "optimistic" TBF case (i.e., $\theta_{f\text{-}}$=0.045) are noted.

Model Structure	Connection Case	Counted Median θ_{max}			Counted 1-Sigma Level θ_{max}		
		M1 [rad]	M1+ [rad]	% Incr.	M1 [rad]	M1+ [rad]	% Incr.
(a) 10/50 earthquake records							
L.A. 3-story	BFO	0.0235	0.0229	-3%	0.0351	0.0372	6%
L.A. 9-story	BFO	0.0217	0.0213	-2%	0.0326	0.0305	-6%
"	TBF	0.0217	0.0213	-2%	0.0326	0.0305	-6%
(% Increase)		(0%)	(0%)		(0%)	(0%)	
Seattle 3-story	BFO	0.0209	0.0211	1%	0.0302	0.0319	6%
"	TBF	0.0209	0.0211	1%	0.0302	0.0319	6%
(% Increase)		(0%)	(0%)		(0%)	(0%)	
(b) 2/50 earthquake records							
L.A. 3-story	BFO	0.0685	0.0553	-19%	0.0769	0.0609	-21%
L.A. 9-story	BFO	0.0440	0.0505	15%	0.1059	0.0837	-21%
"	TBF	0.0440	0.0505	15%	"collapse"	0.0862	--
(% Increase)		(0%)	(0%)		(--)	(3%)	
Seattle 3-story	BFO	0.0645	0.0513	-20%	0.1048	0.0775	-26%
"	TBF	0.0676	0.0513	-24%	"collapse"	0.0881	--
(% Increase)		(5%)	(0%)		(--)	(14%)	

It is apparent from Table 2-18 that the differences in the (counted) θ_{max} statistics for the M1+ versus M1 models are small (i.e., less than 10%) for the 10/50 earthquake records. For the 2/50 records, on the other hand, the changes in the median θ_{max} from the M1 models to the M1+ models are about 15-25%. For the L.A. 9-story structure, the M1+ model results in a smaller median θ_{max}, but for the Los Angeles and Seattle 3-story structures, the median θ_{max} values for the M1+ model are actually larger than those for the M1 model. The 1-sigma level θ_{max} values (under the 2/50 ground motions) for the

M1+ models are about 20-25% smaller than the corresponding M1 model statistics (when the number of M1 model collapses is few enough to find the counted 1-sigma level $\theta_{\max}$). Note that none of the M1+ models suffer any collapses.

For the L.A. 9-story and Seattle 3-story structures, the optimistic TBF case (i.e., $\theta_{f-} = 0.045$) and BFO base case results (both listed in Table 2-18) can be compared for the M1+ models just as they were compared for the M1 models in Section 2.8.2. As discovered for the M1 models, under the 10/50 ground motions the $\theta_{\max}$ statistics for the optimistic TBF case are identical to those for the BFO base case when the M1+ models are used. Recall that this is because few top beam-flanges actually fracture under the 10/50 ground motions in the optimistic TBF case. Under the 2/50 ground motions, the median $\theta_{\max}$ values in the optimistic TBF cases and BFO base cases are also identical when the M1+ model is used, and are nearly identical for the M1 models. Finally, note that whereas the number of collapses of the M1 models in the optimistic TBF cases prohibited calculation of the (counted) 1-sigma level $\theta_{\max}$ values under the 2/50 ground motions, these statistics can be calculated for the non-collapsing M1+ models. For the M1+ models, the (counted) 1-sigma level $\theta_{\max}$ in optimistic TBF case increases by less than 15% with respect to the BFO base case.

2.11.3 Summary

On the whole, the more realistic M1+ models (as compared to M1 models) have a major beneficial effect on the extreme drift cases, but only a mild effect on the "body" of drifts that establish the median. Likewise, the effect on the 1-sigma level drifts is substantial only if the 1-sigma level drift is extreme (e.g., in the TBF cases under the 2/50 ground motions). Evidently, the inclusion of interior frames and (perhaps to a lesser extent) shear connections in the model is critical to the accurate prediction of these important extreme drifts. Moreover, an M1+ model is likely necessary to accurately estimate the likelihood of SMRF collapse, with or without fracturing connections. At a minimum, extreme drifts predicted by M1 models should be "adjusted" in some way to reflect the interior frames. Without this leavening, the M1 model predictions of extreme drifts may be taken out of context. Nevertheless, the results presented here for M1+ versus M1 models suggest that the effects of connection fractures may be similar for the two models. In Chapters 5 through 7 below, M1+ models, each with a "full" rather than a single-bay equivalent interior frame, are considered exclusively.

2.12 Conclusions

In summarizing the effects of beam-column connection fractures on story drift demands for the SAC model structures, it is convenient to consider three subsets of ground motions: "mild," "moderate," and "rogue." These subsets consist of different earthquake records for different structures and the boundaries between the subsets are not crisp. Before carrying out (at least) ductile nonlinear dynamic analyses, it is not yet feasible to identify the subsets of a given pool of earthquake records. Nevertheless, the effects of connection fractures for ground motions within each of the three subsets have common characteristics, which makes the subsets useful descriptively.

For "mild" ground motions (e.g., all of the 10/50 ground motions in this study), the anticipated effects of BFO or TBF connection fractures on story drift responses are minimal, primarily because the demands are not large enough to induce more than a few fractures (under the adopted connection fracture model assumptions). For example, because the ductile-case median $\theta_{\max}$ for the 10/50 ground motions is less than 0.025 radians for all of the model structures, even the "pessimistic" TBF case (i.e., $\theta_{f-} = 0.015$), when considered, has less than a 20% effect on the median story drift demands with respect to the ductile case. In fact, for several of the model structures, the median $\theta_{\max}$ under mild ground motions actually decreases slightly when the structure is modeled with brittle rather than with ductile connections. An effect of less than 20% should be put in perspective of the 60 to 100% or more earthquake record-to-record variability of drift demands in ductile SMRF model structures subjected to multiple ground motions from earthquakes of like magnitude and distance (Shome & Cornell 1999).

Under "moderate" ground motions (e.g., most of the 2/50 ground motions), BFO base-case connection fractures (or even the sensitivity variants of the base case) have a relatively small (i.e., less than 50% with respect to the ductile case) effect on median $\theta_{\max}$ demands. The effect is also small for the TBF cases, unless the plastic rotation capacity associated with top-flange fracture, θ_{f-}, is smaller than the story drift demands in the ductile case by at least 0.01 radians, which is approximately the elastic drift angle. In this situation, a significant number of top-flange connection fractures can be expected and the story drift demands may therefore increase significantly.

When subjected to "rogue" earthquake records, namely those records that cause relatively large story drifts in the ductile case (e.g., a small subset of the 2/50 records), even the model structures with BFO brittle connections may experience extreme story

drifts (i.e., $\theta_{\max} > 0.10$), including collapses. Clearly, under such records the TBF cases will also experience extreme drifts, but the percentage of extreme drifts increases little until the most pessimistic TBF case considered (i.e., $\theta_{f-} = 0.015$). In this way, the effects of connection fractures under rogue ground motions are not significantly different for the BFO and TBF cases. Given that little difference is observed between the BFO and TBF cases for the mild ground motions as well, it may be concluded that it is only for the moderate ground motions that the BFO case and the TBF cases (with different plastic rotation capacities) may have significantly different effects on story drift response.

It should be kept in mind, however, that extreme drifts such as those encountered under the rogue ground motions (for example) are typically reduced when the contributions of interior gravity frames and shear connections are added to the exterior MRF model structures, as demonstrated in Section 2.11. In the BFO and TBF cases considered, collapses are not observed if interior gravity frames and shear connections are accounted for in the model. With fewer extreme drifts, the effects of connection fractures under the rogue earthquake records described above may become more sensitive to θ_{f-}, as is the case for the moderate ground motions.

Clearly, the effects of connection fractures on story drift demands depend on the ground motion level. In the next chapter, PSDA is employed as a concise way to summarize the effects of connection fractures over a range of ground motion intensities. The same drift demands computed in this chapter are used there to compute "drift demand hazard curves" for a subset of the SAC buildings modeled with ductile and with brittle connections. More importantly, the understanding developed in this chapter of the sensitivity of drift demands to the assumptions made for the empirical model of connection fracture are used in Chapter 3 to decide on the building models and fracture properties to consider.

Chapter 3

Effects of Connection Fractures on SMRF Seismic Drift Demand Hazard

3.1 Introduction

A more concise way of summarizing the effects of connection fractures described in Chapter 2 is to compare the seismic drift demand hazard, computed via PSDA, for each of the SMRF buildings modeled with brittle versus with ductile connections. Recall (from Chapter 1) that PSDA couples the ground motion hazard at a site (i.e., PSHA results) with the conditional distribution of drift demand given the ground motion intensity. Hence, rather than measuring the effects of brittle connection behavior on the median and 1-sigma level drift demand statistics for the SAC suites of earthquake records, PSDA involves estimating the median and dispersion of drift demand *given* the ground motion intensity. Recall that in Chapter 2 the effects of connection fractures are observed to depend on the drift demand level, which in turn is related to the ground motion intensity here in Chapter 3. By conditioning on ground motion intensity, the resulting drift demand statistics can be used to measure the effects of connection fractures in a manner that is less dependent on the earthquake records chosen by SAC, and the way in which they were scaled. Ultimately, PSDA computes the MAF (mean annual frequency) of exceeding a specified drift demand, which is a single value that can be compared for a building model with brittle versus with ductile connections. The effect of connection fractures over a range of drift demand levels is measured by comparing the drift demand hazard curves.

In this chapter, drift demand hazard curves for the SAC Los Angeles 3-, 9-, and 20-story buildings modeled with ductile versus with brittle connections are computed (via PSDA) and compared. In increasing order of severity beyond the ductile connections case, the brittle connections cases considered are (i) the BFO (bottom flange only) fracture "base case," (ii) the TBF (top and bottom flange) fracture "base case" (i.e., $\theta_{f\text{-}}$=0.045rad), and (iii) the TBF fracture "extreme case" (i.e., $\theta_{f\text{-}}$=0.015rad). The "M1" model of each of the three L.A. buildings (i.e., exterior MRF alone) is considered here, and the ground motions used are the SAC LA01-LA40 earthquake records (i.e., the nominally 10/50 and 2/50 earthquake records).

In order to make computation of the drift demand hazard curves via PSDA more convenient, a closed-form solution (under a few reasonable assumptions) of the PSDA integral (i.e., Equation 1-1 in Chapter 1) is employed. The PSDA integral is also expanded in order to deal with the "collapses" under some of the SAC earthquake records of the L.A. 9-story (with brittle connections) and L.A. 20-story building models (first observed in Chapter 2). Although PSDA can be implemented for any local or global structural demand measure, here it is applied for $\theta_{\max}$ (i.e., maximum peak inter-story drift angle) only. Also note that the ground motion intensity measure used here is the elastic spectral acceleration at the fundamental period and damping of the model structure, denoted S_{a1}. As demonstrated by Shome *et al.* (1998), S_{a1} is usually an effective structure-specific ground motion intensity measure for the nonlinear response of buildings with a period of around one second (like the L.A. 3-story) but not necessarily for taller, longer period buildings (like the L.A. 9- and 20-story). Other ground motion intensity measures are investigated in Chapters 6.

3.2 Closed-Form Solution of PSDA Integral

The PSDA integral for drift demand hazard expressed in Chapter 1 is rewritten here in Equation 3-1 specifically for the demand measure $\theta_{\max}$ and the ground motion intensity measure S_{a1}.

$$\lambda_{\theta_{\max}}(y) = \int G_{\theta_{\max}|S_{a1}}(y \mid x) \; |\mathrm{d}\lambda_{S_{a1}}(x)| \tag{3-1}$$

Recall that the drift demand hazard $\lambda_{\theta_{\max}}(y)$ is strictly the MAF of $\theta_{\max}$ exceeding the value y. Likewise, the ground motion hazard $\lambda_{S_{a1}}(x)$ is the MAF of S_{a1} exceeding the

value x. The term $G_{\theta_{\max}|S_a}(y \mid x)$ denotes the probability of $\theta_{\max}$ exceeding the value y given that S_{a1} equals x.

Under the simplifying assumptions detailed below, the PSDA integral for $\lambda_{\theta_{\max}}$ expressed in Equation 3-1 can be solved analytically (Cornell 1996). The resulting closed-form solution for the drift demand hazard is expressed in Equation 3-2a.

$$\lambda_{\theta_{\max}}(y) = \lambda_{S_{a1}}(S_{a1}(y)) \cdot CF_{\sigma} \tag{3-2a}$$

Here, $S_{a1}(y)$ is the spectral acceleration corresponding to y according to Equation 3-2b. The correction factor CF_{σ} primarily accounts for the variability in $\theta_{\max}$ given S_{a1}, and is expressed in Equation 3-2c. The parameters a, b, k, and σ are detailed below.

$$S_{a1}(y) = (y/a)^{1/b} \tag{3-2b}$$

$$CF_{\sigma} = \exp\left[\frac{1}{2}(k\sigma/b)^2\right] \tag{3-2c}$$

Note that Equation 3-2 indicates that $\lambda_{\theta_{\max}}(y)$ can simply be calculated as the MAF of exceeding the value of S_{a1} that corresponds to y, multiplied by a correction factor that accounts (primarily) for the variability in $\theta_{\max}$ given S_{a1}.

The closed-form solution for $\lambda_{\theta_{\max}}$ expressed in Equation 3-2 assumes the following:

(a) a log-log linear form of the spectral acceleration hazard curve, as expressed in Equation 3-3, where k is the log-log slope and k_0 can be thought of as the MAF of exceeding a unit S_{a1}.

$$\lambda_{S_{a1}}(x) = k_0 x^{-k} \tag{3-3}$$

At least locally, this form of $\lambda_{S_{a1}}$ is typically a reasonable assumption. Thus, k in Equation 3-2c for CF_{σ} may be taken as the log-log slope of the spectral acceleration hazard curve near $S_{a1}(y)$. In Equation 3-2a, $\lambda_{S_{a1}}(S_{a1}(y))$ may be calculated via Equation 3-3, or it may be read directly from the S_{a1} hazard curve.

(b) a lognormal conditional probability distribution of $\theta_{\max}$ given S_{a1}. This assumption has been verified by Shome & Cornell (1999), and to some extent is confirmed in

Chapter 6. Under this assumption, $G_{\theta_{\max}|S_{a1}}$ in Equation 3-1 for $\lambda_{\theta_{\max}}$ is given by Equation 3-4, where Φ is the standard normal (i.e., Gaussian) cumulative distribution function (CDF), and η and σ denote the median and dispersion[1] of $\theta_{\max}$ given S_{a1} (more precisely, $\eta_{\theta_{\max}|S_{a1}}$ and $\sigma_{\theta_{\max}|S_{a1}}$).

$$G_{\theta_{\max}|S_{a1}}(y \mid x) = 1 - \Phi\left[\frac{\ln y - \ln \eta(x)}{\sigma}\right] \tag{3-4}$$

As one might expect, the median $\theta_{\max}$ given S_{a1} (i.e., $\eta(x)$) is a function of the value of S_{a1}. The dispersion of $\theta_{\max}$ given S_{a1} (i.e., σ), on the other hand, is assumed (and for the most part is observed) to be independent of S_{a1} (i.e., constant σ), at least locally near $S_{a1}(y)$.

(c) a log-log linear functional form for $\eta(x)$ (the median $\theta_{\max}$ given S_{a1}), as expressed in Equation 3-5, where a and b are parameters to be estimated.

$$\eta(x) = a \cdot x^b \quad \Leftrightarrow \quad \ln \eta(x) = \ln a + b \cdot \ln x \tag{3-5}$$

As demonstrated by Shome & Cornell (1999) and in the results below, this functional form is reasonable over a considerable range of $\theta_{\max}$ (or S_{a1}) values. The exponent (or log-log slope) b is intended to capture "softening" of a nonlinear structure, or in other words, a more than proportional increase in $\theta_{\max}$ with S_{a1} (i.e., $b>1$). Of course, a value of b equal to one indicates that $\theta_{\max}$ is (on average) proportional to S_{a1}, which is true in the elastic range (at least for a first-mode dominated structure). In the inelastic range, the familiar "equal displacements rule" (Veletsos & Newmark 1960), which suggests that the displacement of an inelastic oscillator (of moderate-period) is approximately equal to that of an elastic oscillator with the same initial period, also translates to $b=1$. Finally, note that Equation 3-2b for $S_{a1}(y)$ is the inverse of Equation 3-5; thus, $S_{a1}(y)$ is the value of S_{a1} such that the median $\theta_{\max}$ given $S_{a1}(y)$ is equal to y, which is not (necessarily) the median value of S_{a1} given that $\theta_{\max}$ equals y.

---

[1] Recall (from Chapter 2) that the term "median" is used here to refer to the geometric mean, which is calculated as the exponential of the average of the natural logarithms of the data. Correspondingly, the "dispersion" refers to the standard deviation of the natural logarithms of the data. The median and dispersion are the natural parameter estimates for the lognormal distribution (e.g., Benjamin & Cornell 1970).

Customarily (e.g., Shome & Cornell 1999), the parameters a and b are estimated via a log-log linear least-squares regression of $\theta_{\max}$ on S_{a1} (for a suite of ground motions). The regression model is expressed in Equation 3-6, where ε is the random error with, by definition, median 1 and dispersion σ. In accord with assumption (b) above, ε is assumed (and for the most part is observed) to be lognormally distributed.

$$\theta_{\max} = a \cdot S_{a1}{}^{b} \cdot \varepsilon \quad \Leftrightarrow \quad \ln \theta_{\max} = \ln a + b \cdot \ln S_{a1} + \ln \varepsilon \tag{3-6}$$

An alternative approach to least-squares regression for estimating a and b is presented in Section 3.4.2 for use with the SAC earthquake records. By either approach, σ is estimated as the mean squared deviation of the residuals about the fit parameterized by a and b (i.e., the observed values of ε), as expressed in Equation 3-7. Here, n is the number of (S_{a1}, $\theta_{\max}$) data points.

$$\sigma = \sqrt{\frac{1}{n-2} \sum [\ln(\theta_{\max}) - \ln(a \cdot S_{a1}{}^{b})]^2} \tag{3-7}$$

3.3 Accounting for "Collapses" in PSDA

As explained above, the term $G_{\theta_{\max}|S_{a1}}$ in the PSDA integral (i.e., Equation 3-1) is customarily estimated for a given structure via a (log-log linear) regression of $\theta_{\max}$ on S_{a1} for a suite of earthquake records. However, the $\theta_{\max}$ and S_{a1} data for ground motions that cause "collapse" of the analysis model of the structure (i.e., NDA does not converge to a solution) cannot be included in such a regression. Because collapse implies an "infinite" demand, $G_{\theta_{\max}|S_{a1}}(y \mid x)$ can be expanded as the probability of collapse (given S_{a1}=x) plus the probability of the joint event of non-collapse and $\theta_{\max}$ exceeding y (also given S_{a1}=x). Substituting into Equation 3-1 and rearranging the terms yields Equation 3-8, where C is an indicator variable for collapse.

$$\begin{aligned} \lambda_{\theta_{\max}}(y) = & \int G_{\theta_{\max}|S_{a1},C=0}(y \mid x) \; |\, \mathrm{d}\lambda_{S_{a1}}(x) \,| \\ & + \int [1 - G_{\theta_{\max}|S_{a1},C=0}(y \mid x)]\, P_{C=1|S_{a1}}(x) \; |\, \mathrm{d}\lambda_{S_{a1}}(x) \,| \end{aligned} \tag{3-8}$$

Note that Equation 3-8 is written as an addition (i.e., the second term) to the integral in Equation 3-1 applied for the non-collapse data only (i.e., the first term). In applying

Equation 3-8, $G_{\theta_{\max}|S_{a1},C=0}$ is estimated via a (log-log linear) regression of the non-collapse data, whereas the probability of collapse given the ground motion intensity measure, $P_{C=1|S_{a1}}$, is estimated via a binary regression of C on S_{a1} (Shome & Cornell 2000).

The functional form assumed for $P_{C=1|S_{a1}}$ is expressed in Equation 3-9, where $(s_{a1})_o$ and β are the binary regression parameters to be estimated.

$$P_{C=1|S_{a1}} = \begin{cases} 0 & \text{for } 0 \le x \le (s_{a1})_o \\ 1-[x/(s_{a1})_o]^{-\beta} & \text{for } x > (s_{a1})_o \end{cases} \tag{3-9}$$

Note that $(s_{a1})_o$ is the value of S_{a1} below which the probability of collapse is assumed to be zero, and β measures how quickly the probability of collapse increases with increasing S_{a1}. Although the functional form of Equation 3-9 allows for an analytical solution of the second integral in Equation 3-8 (Shome & Cornell 1999), numerical integration is used in the examples below. The closed-form solution (detailed in Section 3.2) of the first integral in Equation 3-8 is used throughout for the non-collapsing data, however, even though numerical integration is also an option.

3.4 PSDA for the L.A. 3-Story Building Model

In some detail, drift demand hazard curves (i.e., $\lambda_{\theta_{\max}}$) for the L.A. 3-story building modeled with ductile and with brittle connections are computed here (using Equation 3-2) and compared. Recall (from Chapter 2) that the fundamental period and damping ratio for the L.A. 3-story model are T_1=1.03sec and ζ_1=2%. Also recall that, for reasons discussed in Chapter 2, the LA31-LA40 simulated earthquake records are not used in analyzing the L.A. 3-story model (but are for the L.A. 9- and 20-story models). The earthquake record-by-record S_{a1} and $\theta_{\max}$ results for the L.A. 3-story model are listed at the end of this chapter in Table 3-11.

3.4.1 Spectral Acceleration Hazard

A spectral acceleration hazard curve (i.e., $\lambda_{S_{a1}}$) for the L.A. 3-story model is obtained here by simply fitting a line (in log-log space) to the two points defined by

(i) the 10% in 50 years and 2% in 50 years exceedance probabilities,[2] and (ii) the median values of S_{a1} for the 10/50 and 2/50 earthquake records. As illustrated in Figure 3-1, in this case the log-log slope of the spectral acceleration hazard curve, k, is simply 3.03. Note that since the two median values of S_{a1} are for a damping ratio of 2%, the simple hazard curve used here is for a damping ratio of 2% rather than for the 5% value typically reported by USGS. Also, because the SAC earthquake records are from firm soil sites (or else were modified to reflect firm soil conditions), the simple hazard curve created here reflects a firm soil site rather than the soft rock site used as a basis by USGS (Somerville, 1997a). The same S_{a1} hazard curve is used in computing $\lambda_{\theta_{\max}}$ for the ductile and brittle connections cases, so perhaps the particulars of the S_{a1} hazard are not critical to the ductile versus brittle comparison.

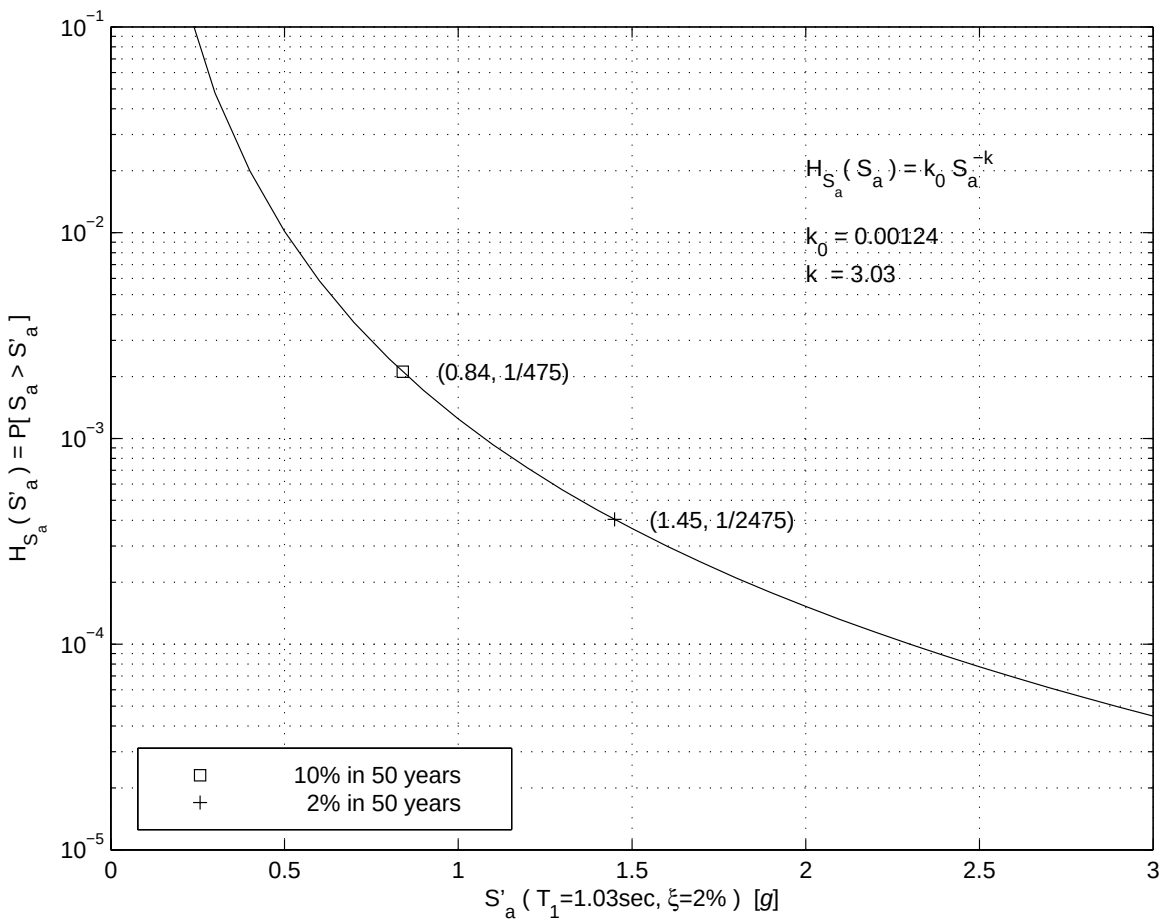

Figure 3-1. Hazard curve for $S_a(T$=1.03sec,ζ=2%).

[2] Assuming a Poisson process, the 10/50 and 2/50 exceedance probabilities correspond to MAF's of exceedance (i.e., λ's) of 1/475 and 1/2475, respectively.

3.4.2 Distribution of Drift Demand given Spectral Acceleration

The $\theta_{\max}$ versus S_{a1} results for the LA01-LA30 earthquake records are plotted in Figure 3-2 for the L.A. 3-story modeled with ductile and with brittle connections.[3] Note that for the TBF "extreme case" (i.e., $\theta_{f\text{-}}$=0.015rad) two of the points are plotted with arrows because their $\theta_{\max}$ values are greater than 0.10 radians (specifically, $\theta_{\max}$ equals 0.15 and 0.17 for the LA23 and LA27 earthquake records). The least-squares regression fits and estimates of a, b, and σ (defined in Section 3.2) are also shown in Figure 3-2.

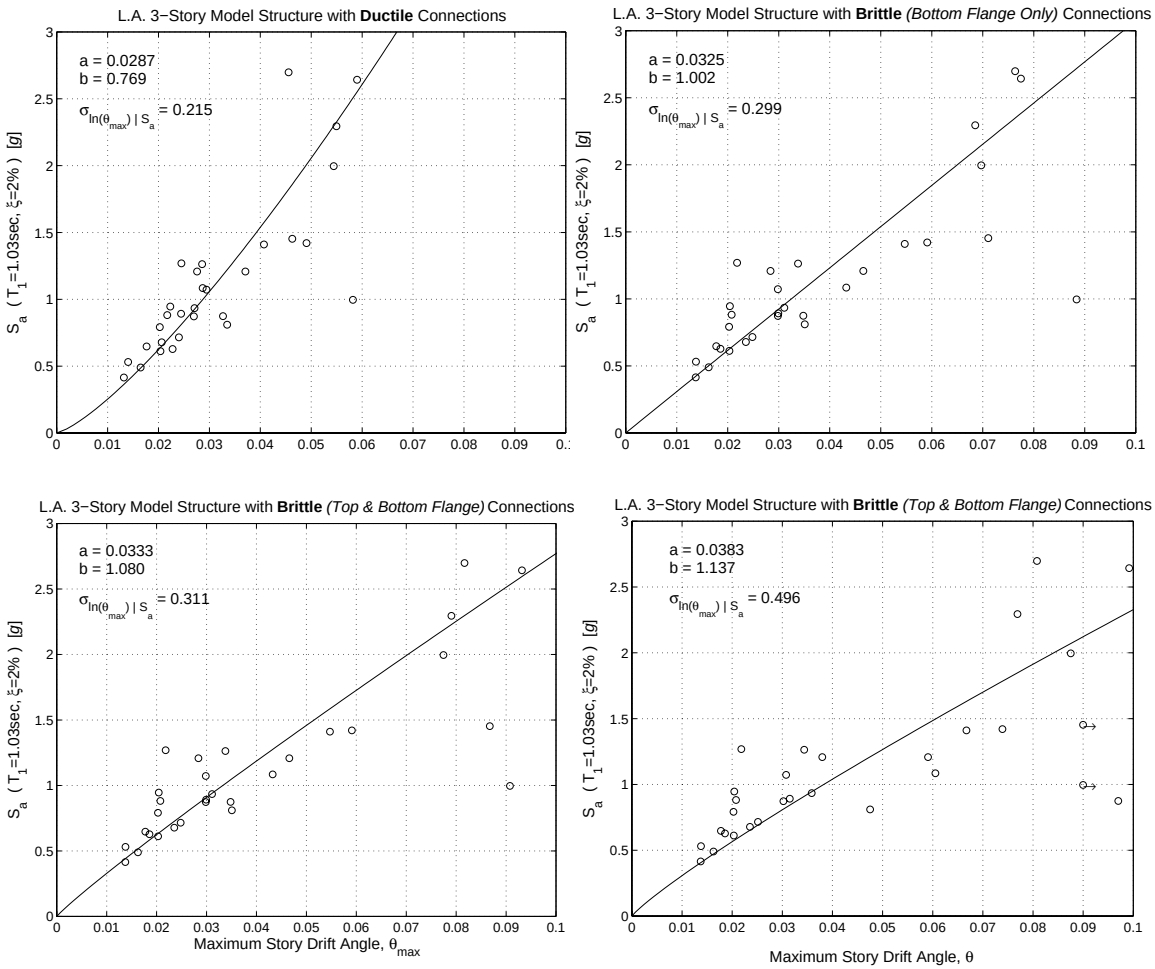

Figure 3-2. S_{a1} versus $\theta_{\max}$ and least-squares regression results for the LA3 building model with **(a)** ductile, **(b)** BFO base case, **(c)** TBF base case, and **(d)** TBF extreme case connections. The data points marked with arrows indicate $\theta_{\max}$ values larger than 0.10 radians.

[3] Note that Figure 3-2 is in arithmetic scale, despite the fact that a log-log linear form is used to relate $\theta_{\max}$ to S_{a1}.

Note that the values of a, which can each be interpreted as the value of $\theta_{\max}$ corresponding to a unit S_{a1} (here in units of g's), increase with increasing severity of the connection fracture case. The values of b, which each measure the sensitivity of $\theta_{\max}$ to changes in S_{a1}, also increase with increasing severity of the connections case, as do the values of σ.[4] The value of b, in particular, can be used to quantify the effects of connection fractures over a range of ground motion intensity levels. In the case of ductile connections (i.e., Figure 3-2a), it is interesting to note that the regression estimate of b is significantly smaller than one (by more than two times the standard error of estimation of b). Rather than the "softening" behavior that the parameter b is intended to measure, $b<1$ indicates "hardening" (i.e., less than a proportional increase in $\theta_{\max}$ with S_{a1}).[5]

Rather than estimating the parameters a and b (that relate the median $\theta_{\max}$ to S_{a1}) via least squares regression, Cornell & Luco (1999) suggest an alternative approach that is less sensitive to the way in which the SAC earthquake records were scaled (Somerville 1997a). The parameters a and b can instead be estimated by fitting a line (in log-log space) to the two points defined by the median $\theta_{\max}$ and median S_{a1} for the 10/50 and 2/50 earthquake records, which are summarized in Table 3-1. (Recall that the median values of S_{a1} were used above in establishing an S_{a1} hazard curve, and that the median values of $\theta_{\max}$ were first reported in Chapter 2.) Still, σ can be estimated from the mean squared deviation of the residuals about the fit defined by a and b (i.e., Equation 3-7).

Table 3-1. Median values of S_{a1} and $\theta_{\max}$ for the L.A. 3-story model and the LA01-LA30 earthquake records.

Connections Case	(Median S_{a1} , Median $\theta_{\max}$)	
	10/50	2/50
	([g] , [rad])	([g] , [rad])
Ductile Case	(0.837 , 0.0238)	(1.45 , 0.0424)
BFO Base Case	(0.837 , 0.0255)	(1.45 , 0.0533)
TBF Base Case	(0.837 , 0.0255)	(1.45 , 0.0573)
TBF Extreme Case	(0.837 , 0.0277)	(1.45 , 0.0743)

[4] Closer inspection reveals that the majority of the increase in σ from the ductile to the brittle connection cases is due to fundamental differences in the dynamics of the ductile and brittle building models, rather than differences in the random locations of "early" fracturing connections, which only accounts for about 5% of the total dispersion. Note also that the dispersions of $\theta_{\max}$ given S_{a1} (i.e., σ) are substantially smaller than the dispersions of $\theta_{\max}$ (implied by the ratio of the 1-sigma level to the median reported in Chapter 2) for the 10/50 or 2/50 earthquake records.

[5] In many cases, "hardening" behavior can be explained by a switch in the direction or a shift in the story in which $\theta_{\max}$ occurs (Vamvatsikos 2001).

A comparison of the two approaches for fitting *a* and *b* is illustrated in Figure 3-3 for the BFO connection fracture base case; both the median-to-median fit and least squares regression estimates of *a*, *b*, and σ are listed in Table 3-2 for all of the ductile and brittle connections cases. Note that the median-to-median estimates of *b* are consistently larger than those from least-squares regression, and they are all greater than unity. The two different estimates of *a* happen to be nearly equal, and by definition the estimates of σ are somewhat larger for the median-to-median fits than for the least-squares regression analysis. By either approach, the values of *b*, *a*, and σ increase (or at least do not decrease) with the increasing severity of the connection fracture cases. Accordingly, an increase in the drift demand hazard is expected (at $\theta_{\max}$ values greater than ~0.03 radians).

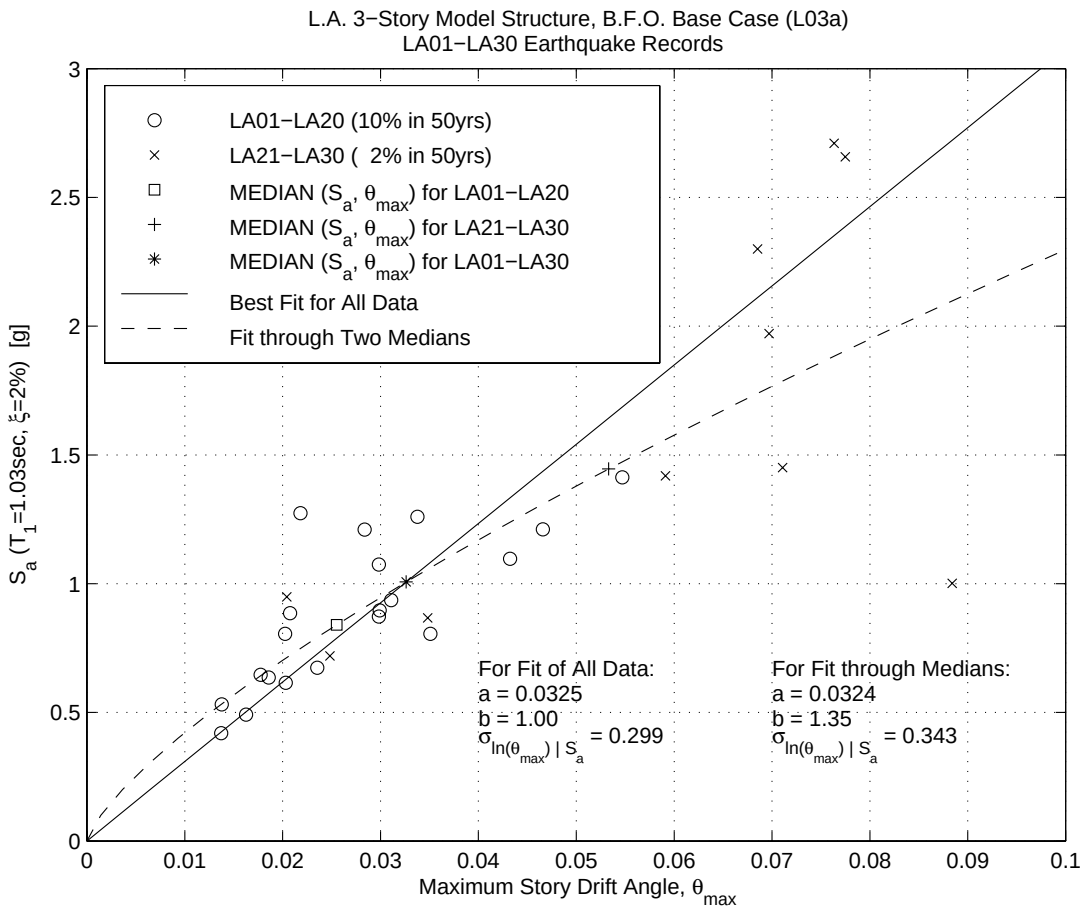

Figure 3-3. Comparison of least-squares regression and median-to-median fit approaches to estimating *a* and *b* for the L.A. 3-story modeled with BFO (base case) brittle connections.

Table 3-2. Estimates of b, a, and σ for the two different $\theta_{\max}=a(S_{a1})^b\varepsilon$ fits of the L.A. 3-story model results.

Connections Case	Median-to-Median Line			Least-Squares Regression		
	b	a	σ	b	a	σ
Ductile Case	1.06	0.029	0.26	0.77	0.029	0.22
BFO Base Case	1.35	0.032	0.34	1.00	0.033	0.30
TBF Base Case	1.48	0.033	0.37	1.08	0.033	0.31
TBF Extreme Case	1.81	0.038	0.59	1.14	0.038	0.50

As explained further in Chapter 5, with S_{a1} as the ground motions intensity measure, it is suspected that the way in which the SAC earthquake records were scaled (Somerville 1997a) may render the least-squares regression fits innacurate. In contrast, the median S_{a1} and median $\theta_{\max}$ for the 10/50 or 2/50 earthquake records, and thereby the median-to-median fit estimates of b, a, and σ, are expected to be less sensitive to paticulars of the SAC scaling scheme. Hence, in calculating the drift demand hazard the median-to-median fit estimates are utilized.

3.4.3 Drift Demand Hazard

With the spectral acceleration hazard (parameterized by k and k_0), and the distribution of drift demand given spectral acceleration (parameterized by b, a, and σ), the drift demand hazard $\lambda_{\theta_{\max}}$ is calculated according to Equation 3-2. The resulting drift demand hazard curves for values of $\theta_{\max}$ ranging from 0.02 to 0.10 (radians) are plotted in Figure 3-4 for the L.A. 3-story model with ductile and with brittle connections.

As expected, brittle connection behavior causes an increase (over the ductile case) in the MAF of exceeding a specified $\theta_{\max}$ demand (i.e., $\lambda_{\theta_{\max}}$), or alternatively an increase

Table 3-3. Mean annual frequencies of $\theta_{\max}$ exceeding 0.03 and 0.08 radians for the L.A. 3-story building models.

Connections Case	$\lambda_{\theta\max}(y)$	
	y = 0.03 rad	y = 0.08 rad
Ductile Case	$1.4\text{x}10^{-3}$	$0.86\text{x}10^{-4}$
BFO Base Case	$2.0\text{x}10^{-3}$	$2.2\text{x}10^{-4}$
TBF Base Case	$2.0\text{x}10^{-3}$	$2.7\text{x}10^{-4}$
TBF Extreme Case	$3.0\text{x}10^{-3}$	$5.9\text{x}10^{-4}$

in the $\theta_{\max}$ demand for a given hazard level). This increase, which is larger for more severe connection fracture cases, is a consequence of both a larger median and a larger dispersion of $\theta_{\max}$ given S_{a1}. As demonstrated in Chapter 2 for other drift demand statistics, the difference in $\lambda_{\theta_{\max}}$ between the ductile and brittle connections cases is greater at larger levels of drift demand. For example, as listed in Table 3-2, $\lambda_{\theta_{\max}}$ (0.03) for the TBF extreme case is only 2.1 times that for the ductile case, whereas $\lambda_{\theta_{\max}}$ (0.08) is 6.9 times larger for the TBF extreme case than it is for the ductile case. Note that in Chapter 4, deterministic $\theta_{\max}$ capacities of 0.03 and 0.08 radians are chosen (for the L.A. 9-story) to represent a local (e.g., a connection losing gravity load carrying ability) and a global (e.g., building collapse) limit state, as recommended in the recent SAC guidelines (FEMA 351).

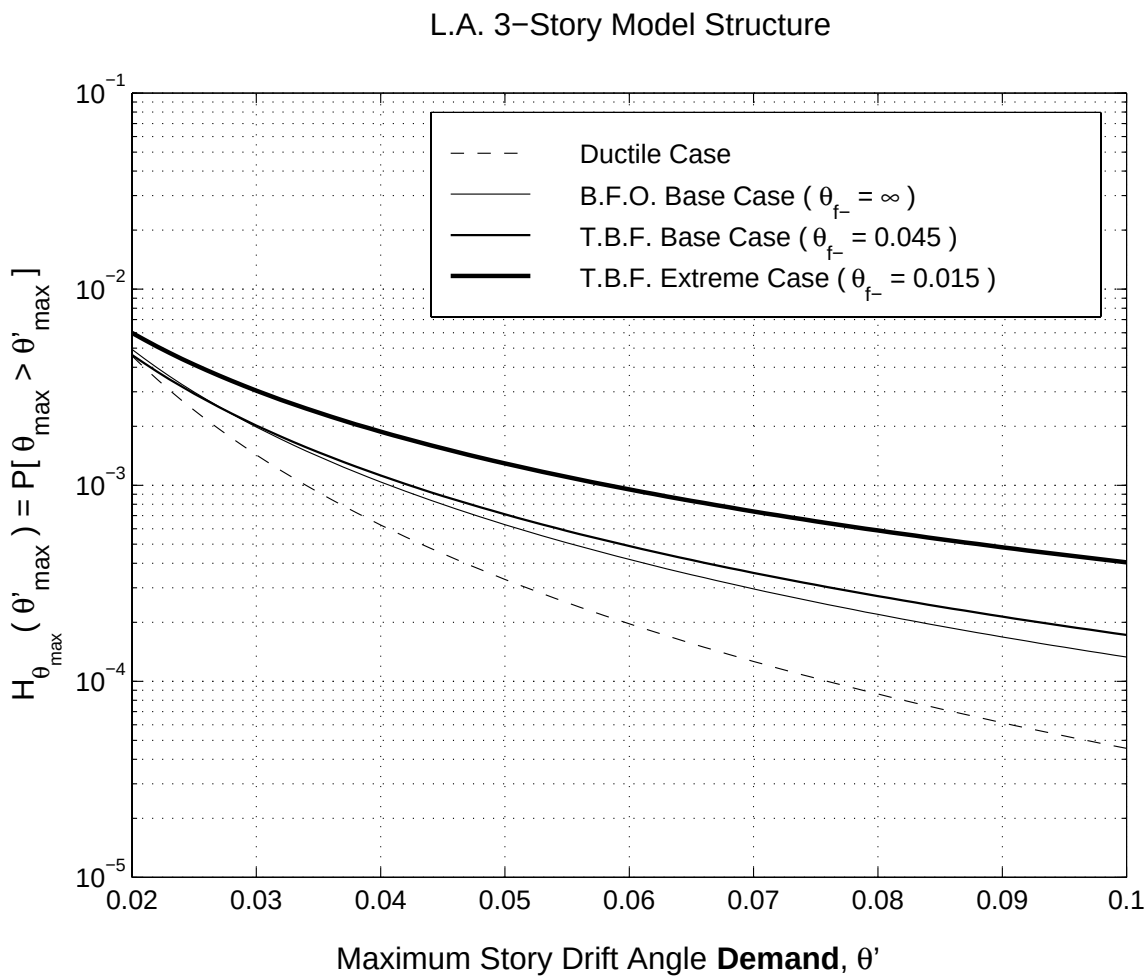

Figure 3-4. Annual hazard curve for maximum story drift angle demand.

3.5 PSDA for the L.A. 9- and 20-Story Building Models

Accounting for "collapses" (which were not observed for the L.A. 3-story model), drift demand hazard curves (i.e., $\lambda_{\theta_{\max}}$) for the L.A. 9- and 20-story buildings modeled with ductile and with brittle connections are computed here (using Equation 3-8) and compared. Recall that the fundamental periods of the L.A. 9- and 20-story models are T_1=2.34sec and T_1=3.98sec, respectively, and the fundamental-mode damping ratio for both models is ζ_1=2% (as for the L.A. 3-story model). The LA01-LA40 earthquake record-by-record S_{a1} and $\theta_{\max}$ results are listed in Table 3-12 and Table 3-13.

3.5.1 Spectral Acceleration Hazard

As done for the L.A. 3-story model (in Section 3.4.1), an approximate S_{a1} hazard curve of the form $\lambda_{S_{a1}}(x) = k_0\, x^{-k}$ for the L.A. 9-story model and for the L.A. 20-story model is constructed from the two median values of S_{a1} for the 10/50 (λ=1/475) and the 2/50 (λ=1/2475) earthquake records. The median values of S_{a1} are listed in Table 3-4, along with the resulting values of k (the log-log slope of the S_{a1} hazard curve) and k_0.

Table 3-4. Parameters defining the spectral acceleration hazard curves for the L.A. 9-story and L.A. 20-story models.

Ground Motion Intensity Measure	Median S_{a1}		Hazard Curve Param.'s	
	10/50 [g]	2/50 [g]	k	k_0
$S_a(T_1$=2.34s, ζ_1=2%)	0.341	0.677	2.41	$1.58\text{x}10^{-4}$
$S_a(T_1$=3.98s, ζ_1=2%)	0.148	0.276	2.65	$1.33\text{x}10^{-5}$

3.5.2 Distribution of Drift Demand given Spectral Acceleration Barring Collapse

The "collapses" of the L.A. 9-story (with brittle connections) or L.A. 20-story models under some of the LA earthquake records necessitate an expansion (detailed above in Section 3.3) of the customary PSDA approach that was applied for the L.A. 3-story model.[6] Nonetheless, the $\theta_{\max}$ versus S_{a1} results for the earthquake records that do not

[6] Although "counted" medians can be employed (provided that the number of collapses is small enough) to estimate a and b via a median-to-median fit, the customary estimate of σ (i.e., Equation 3-7) still cannot incorporate collapse data. Obviously, a least-squares regression of $\theta_{\max}$ on S_{a1} cannot incorporate collapse data either.

cause collapse are processed in the same way that the L.A. 3-story model results were processed (in Section 3.4.2). The collapse data, on the other had, is dealt with in the next subsection.

Although the $\theta_{\max}$ versus S_{a1} results (listed in Table 3-12 and Table 3-13) are not plotted here, the (median S_{a1}, median $\theta_{\max}$) pairs for the 10/50 and 2/50 earthquake records that do not cause collapse are listed in Table 3-5 for the L.A. 9- and 20-story buildings modeled with ductile and brittle connections. As for the L.A. 3-story models, the pairs in Table 3-5 are used to establish the median-to-median line estimates of the parameters *b* and *a*, in this case barring collapse of the L.A. 9- or 20-story models.

Table 3-5. Median values of S_{a1} and $\theta_{\max}$, barring collapse, for the L.A. 9- and 20-story models.

Connections Case	(Median S_{a1} , Median $\theta_{\max}$) [a]	
	10/50 ([g] , [rad])	2/50 ([g] , [rad])
(a) LA9		
Ductile Case	(0.341 , 0.0245)	(0.677 , 0.0458)
BFO Base Case	(0.341 , 0.0244)	(0.677 , 0.0509)
TBF Base Case	(0.341 , 0.0244)	*(0.578 , 0.0402)*
TBF Extreme Case	(0.341 , 0.0267)	*(0.563 , 0.0496)*
(b) LA20		
Ductile Case	(0.148 , 0.0197)	*(0.268 , 0.0400)*
BFO Base Case	(0.148 , 0.0199)	*(0.214 , 0.0329)*
TBF Base Case	(0.148 , 0.0199)	*(0.194 , 0.0278)*
TBF Extreme Case	*(0.140 , 0.0185)*	*(0.186 , 0.0259)*

[a] pairs in *italics* exclude earthquake records that cause "collapse"

Note the for the L.A. 20-story model subjected to the 2/50 ground motions, for example, the median $\theta_{\max}$ actually decreases with increasing severity of the connections case. This is primarily due to the increasing number of collapses under earthquake records that previously resulted in only relatively large (compared to the median) values of $\theta_{\max}$. Similarly, the median S_{a1} tends to decrease with increasing number of collapses (due to increasing severity of the connections case) because most of the earthquake records that cause collapse have a relatively large S_{a1}. Recall from Chapter 2 that the "counted" median values of $\theta_{\max}$, which reflect the number of collapses, do in fact increase with increasing severity of the connections case.

Based on the statistics in the Table 3-5, the median-to-median fit estimates of *b*, *a*, and σ for the L.A. 9- and 20-story models are listed in Table 3-6. Also listed in the table are the least-squares regression estimates of the three parameters. As for the L.A. 3-story model, the median-median fit estimates of *b* are (i) larger than the least-squares regression estimates, and (ii) approximately (within one standard error of estimation of *b*) larger than one. The median-to-median fit estimates of *a* also happen to be larger than the least-squares estimates. Unlike for the L.A. 3-story model, the values of *b*, *a*, and σ do not necessarily increase with increasing severity of the connections case. Again this is because collapses are excluded from the fits; as one might expect, most of the earthquake records that are excluded (because they cause collapse) are from the 2/50 set.

Table 3-6. Estimates of *b*, *a*, and σ for the two different $\theta_{max}=a(S_{a1})^b\varepsilon$ fits of the L.A. 9- and 20-story model results, barring collapses.

Connections Case	Median-to-Median Line			Least-Squares Regression		
	b	*a*	σ	*b*	*a*	σ
(a) L.A. 9-story						
Ductile Case	0.91	0.065	0.34	0.67	0.055	0.31
BFO Base Case	1.07	0.077	0.36	0.81	0.064	0.33
TBF Base Case [a]	0.95	0.068	0.31	0.62	0.051	0.26
TBF Extreme Case [a]	1.23	0.101	0.41	0.86	0.073	0.36
(b) L.A. 20-story						
Ductile Case [a]	1.18	0.190	0.38	0.93	0.125	0.35
BFO Base Case [a]	1.35	0.262	0.45	0.81	0.100	0.37
TBF Base Case [a]	1.20	0.199	0.42	0.65	0.072	0.34
TBF Extreme Case [a]	1.20	0.194	0.41	0.57	0.060	0.30

[a] results exclude earthquake records that cause "collapse"

It is interesting to note that for the L.A. 9-story modeled with ductile or with BFO (base case) brittle connections, which does not collapse under any of the LA earthquake records, the least-squares regression estimate of *b* is significantly (more than two standard errors of *b*) less than one. For both of these cases, the least-squares regression estimates of *b* for each of the nine peak inter-story drift angles (i.e., θ_i instead of θ_{max}) are listed in Table 3-7. For the ductile case, and similarly for the BFO base case, the values of *b* range monotonically from 0.25 for the top story to 0.97 (virtually one) for the second story, with the first floor value being slightly less (i.e., 0.90). Evidently, θ_i for an upper

story grows much less rapidly with S_{a1} than θ_i for a lower story, presumably due to the "base isolation" effects of yielding and/or fracture at the lower floors. As observed in Chapter 2, θ_{max} (i.e., the maximum θ_i) tends to occur in an upper story under lower intensity ground motions, but ultimately shifts to a lower story at higher ground motion intensity levels. The least-squares regression estimates of b in Table 3-6 (i.e., 0.67 for the ductile case and 0.81 for the BFO base case) represent the net of the story-by-story results in Table 3-7.

Table 3-7. Least-squares regression estimates of b in $\theta_i = a(S_{a1})^b \varepsilon$ for the L.A. 9-story building model.

Story	b	
	Ductile Case	BFO Base Case
1	0.90	0.90
2	0.97	1.03
3	0.91	1.01
4	0.82	0.94
5	0.68	0.71
6	0.62	0.51
7	0.43	0.34
8	0.33	0.25
9	0.25	0.20

Also note from Table 3-7 that whereas the values of b increase from the ductile to the BFO base case in the lower (i.e., 1st-5th) stories, they actually decrease in the upper (6th-9th) stories. This is consistent with the θ_i results presented in Chapter 2. There it was demonstrated that, with increasing severity of the connection fracture case, the median and 1-sigma level θ_i (for both the 10/50 and 2/50 earthquake records) increase in the lower stories but decrease (or remain about the same) in the upper stories.

3.5.3 Probability of Collapse given Spectral Acceleration

As detailed in Section 3.3, collapses of the L.A. 9- and 20-story models are taken into account by considering the probability of collapse given S_{a1}, denoted $P_{C=1|S_{a1}}$. With the results for the L.A. earthquake records, $P_{C=1|S_{a1}}$ is estimated via a binary regression of the indicator variable C (equal to 1 for collapse) on S_{a1} (refer to Equation 3-9). The L.A. earthquake records that cause collapse of the L.A. 9- and/or 20-story buildings modeled with ductile and with brittle connections are listed in Table 3-8.

Table 3-8. L.A. earthquake records that cause collapse of the L.A. 9- and/or 20-story models.

Connections Case	Earthquake Records that cause Collapse of …	
	L.A. 9-Story	L.A. 20-Story
Ductile Case	--	LA30
BFO Base Case	--	LA30, LA33, LA34, LA35, LA36, LA37, LA38, LA40
TBF Base Case	LA24, LA30, LA35, LA36, LA38	LA24, LA30, LA31, LA33, LA34, LA35, LA36, LA37, LA38, LA40
TBF Extreme Case	LA24, LA30, LA35, LA36, LA37, LA38	LA04, LA09, LA24, LA28, LA30, LA31, LA32, LA33, LA34, LA35, LA36, LA37, LA38, LA40

As one might expect, the number of collapses increases with increasing severity of the connection fracture cases. Also note the preponderance of simulated earthquake records (i.e., LA31-LA40) among those that cause collapse.

The binary regressions of C on S_{a1} for the L.A. earthquake records yield the estimates of $(s_{a1})_o$ (the value of S_{a1} below which $P_{C=1|S_{a1}}$ is assumed to equal zero) and β (a measure of how quickly $P_{C=1|S_{a1}}$ increases with increasing S_{a1}) that are listed in Table 3-9.[7]

Table 3-9. Binary regression estimates of the parameters $(s_{a1})_o$ and β.

Connections Case	$(s_{a1})_o$		β	
	L.A. 9-story [g]	L.A. 20-story [g]	L.A. 9-story	L.A. 20-story
Ductile Case	--[a]	0.46	--[a]	3.19
BFO Base Case	--[a]	0.25	--[a]	2.71
TBF Base Case	0.55	0.24	1.00	3.54
TBF Extreme Case	0.55	0.17	1.27	2.10

[a] none of the L.A. earthquake records cause "collapse"

[7] The binary regressions were carried out by Nilesh Shome.

Note that for the L.A. 20-story model, $(s_{a1})_o$ decreases with increasing severity of the connections case. Among connections cases with approximately the same value of $(s_{a1})_o$ (i.e., the TBF base case and TBF extreme cases for the L.A. 9-story, and the BFO and TBF base cases for the L.A. 20-story), β increases with increasing severity of the connection fracture case.

Substituting the binary regression estimates of $(s_{a1})_o$ and β into Equation 3-9 for $P_{C=1|S_{a1}}$ results in the estimates of the probability of non-collapse, $P_{C=0|S_{a1}} = 1 - P_{C=1|S_{a1}}$, that are illustrated in Figure 3-5 and Figure 3-6 for the L.A. 9-story and L.A. 20-story models that experience collapse under some of the L.A. earthquake records. Also plotted in the figures are the points on the $P_{C=0|S_{a1}}$ versus S_{a1} curves that correspond to each of the LA01-LA40 earthquake records, distinguishing by filled markers those that cause collapse. Note that the density of filled markers tends to increase with S_{a1}, implying increased probability of collapse.

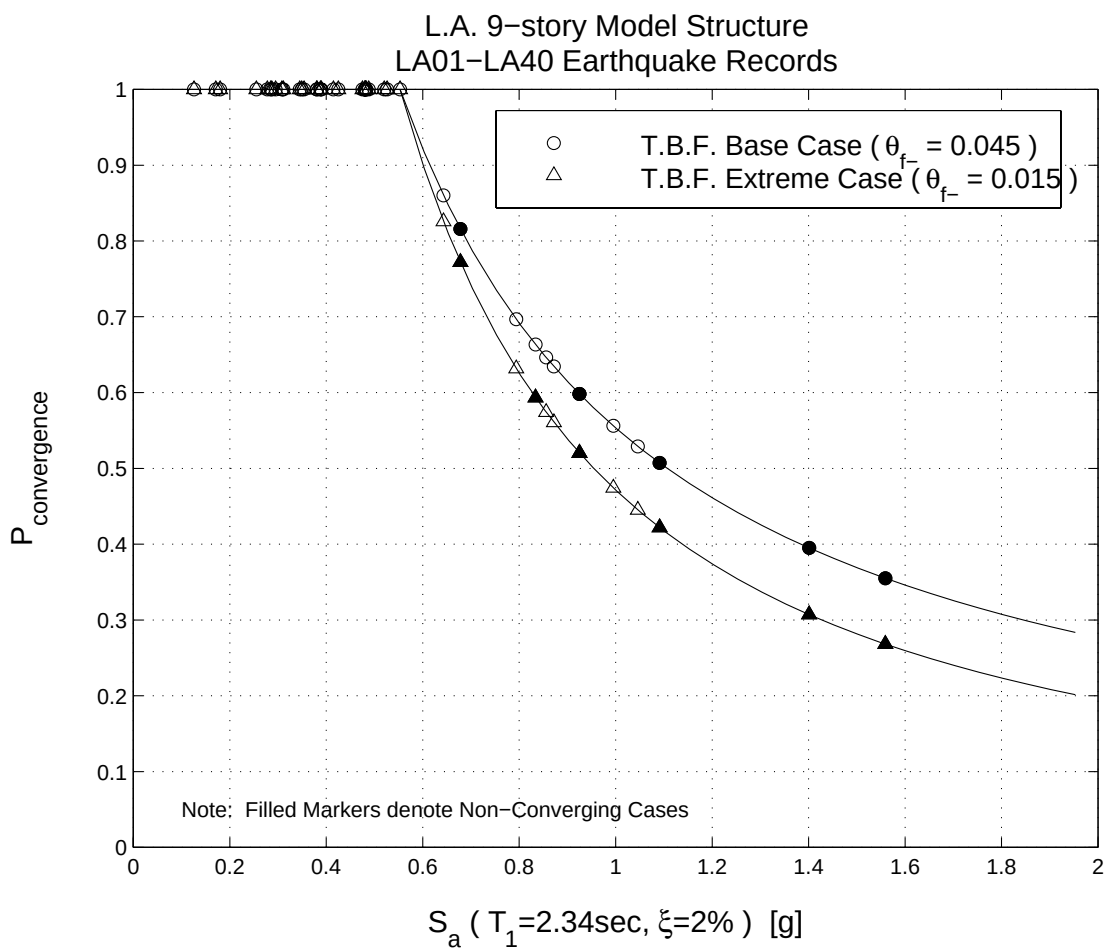

Figure 3-5. Estimated probability of non-collapse versus S_{a1} obtained using binary regression.

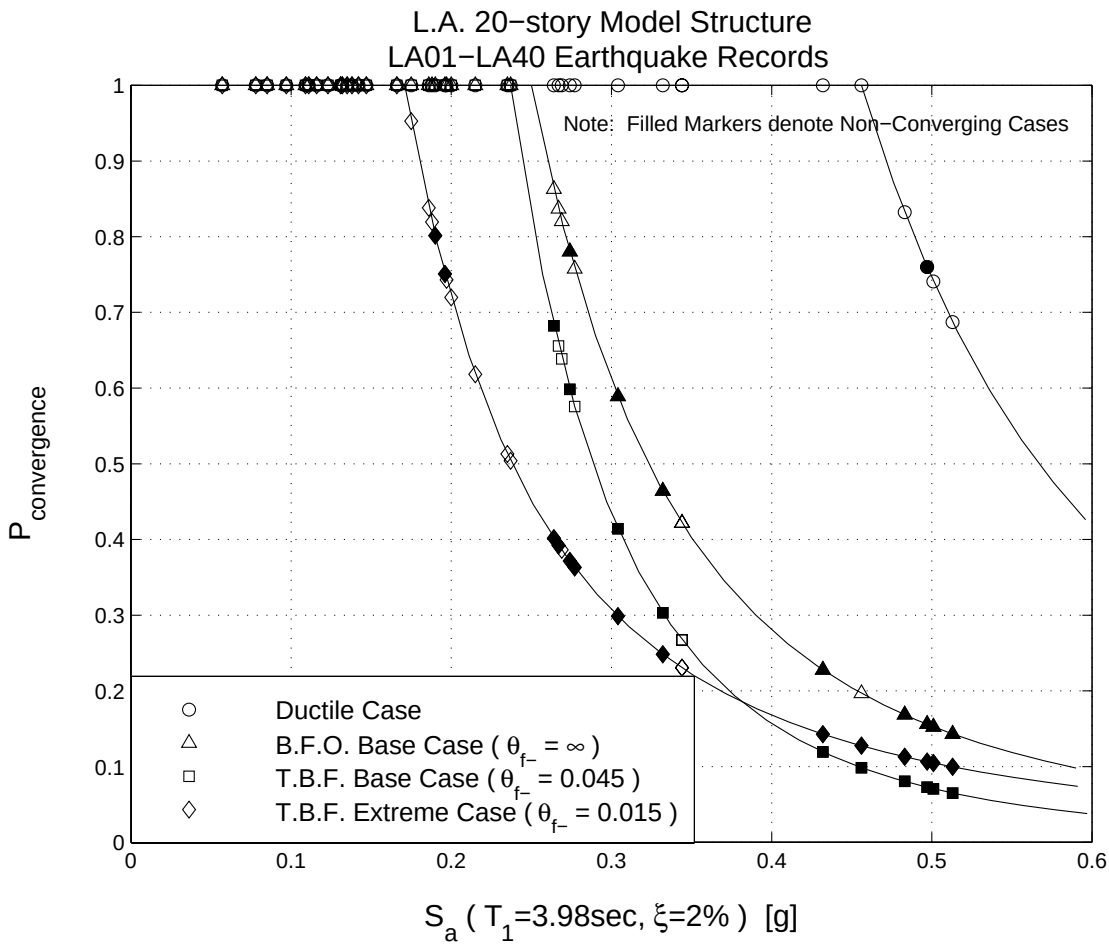

Figure 3-6. Estimated probability of non-collapse versus S_{a1} obtained using binary regression.

3.5.4 Drift Demand Hazard

With the S_{a1} hazard (parameterized by k and k_0), the distribution of $\theta_{\max}$ given S_{a1} barring collapse (parameterized by b, a, and σ),[8] and the probability of collapse given S_{a1} (parameterized by $(s_{a1})_o$ and β), the drift demand hazard $\lambda_{\theta_{\max}}$ is calculated according to Equation 3-8 for the L.A. 9- and 20-story buildings modeled with ductile and brittle connections. The resulting drift demand hazard curves for values of $\theta_{\max}$ ranging from 0.02 to 0.10 radians are plotted in Figure 3-7 and Figure 3-8. Note that for the L.A. 20-story models with brittle connections, the drift demand hazard curves tend to "flatten out" at large values of $\theta_{\max}$ (i.e., greater than about 0.07 radians). The same can be said for the

[8] Recall (from Section 3.4.2) that the median-to-median fit estimates of b, a, and σ (rather than the least-squares regression estimates) are used here in computing the drift demand hazard.

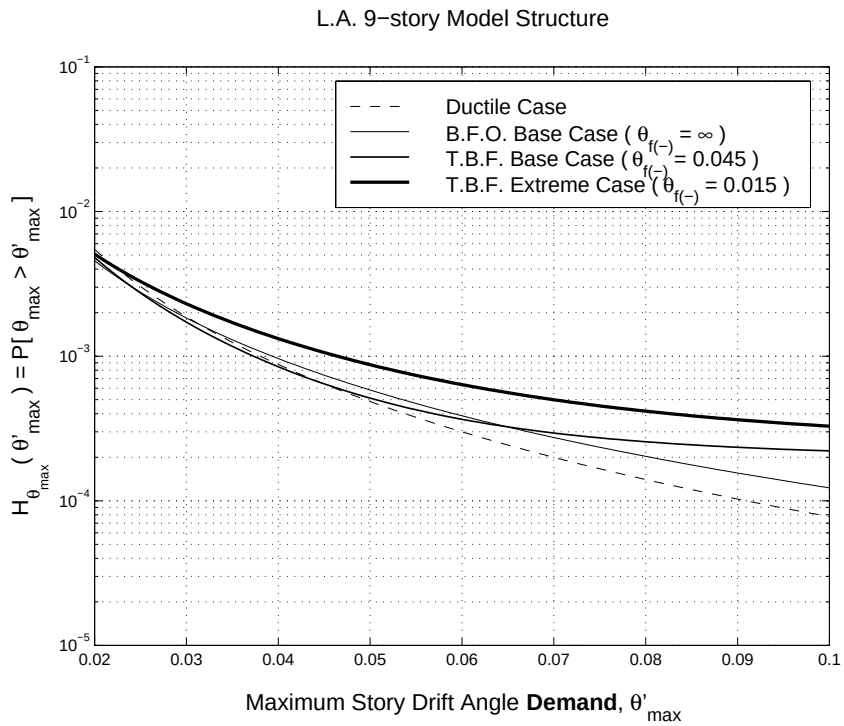

Figure 3-7. Drift demand hazard curves for the L.A. 9-story building modeled with ductile and with brittle connections (for which collapses are observed).

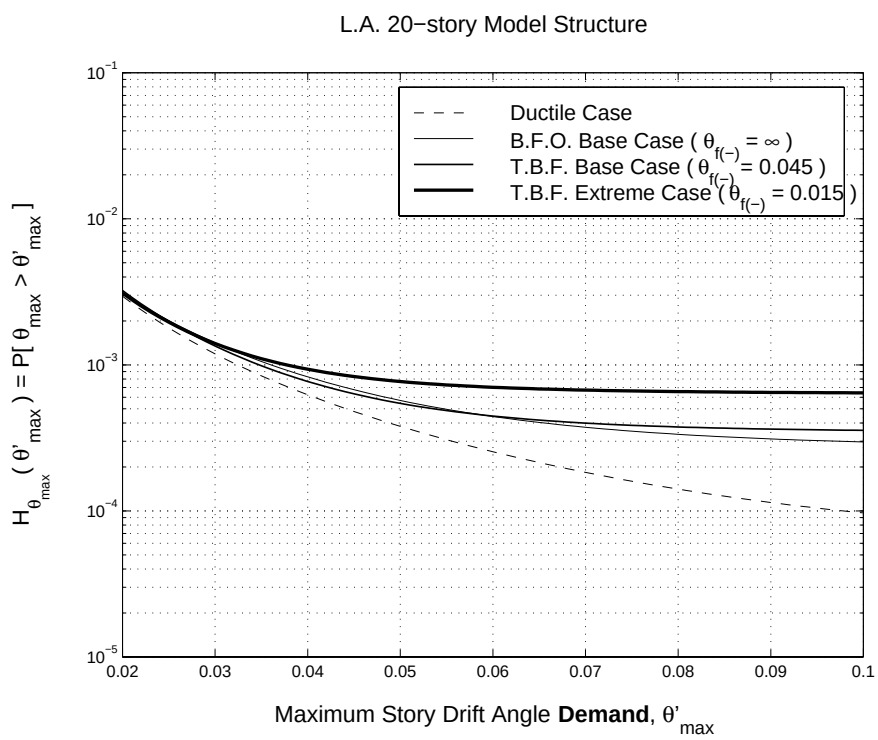

Figure 3-8. Drift demand hazard curves for the L.A. 20-story building modeled with ductile and with brittle connections (for which collapses are observed).

L.A. 9-story models with TBF (base case or extreme) brittle connections, which also experience collapse. As discussed by Shome & Cornell (1999), this "flattening" is a result of the relatively large collapse probabilities at spectral accelerations corresponding to large values of $\theta_{\max}$.

As for the L.A 3-story models, the effect of connection fractures on $\lambda_{\theta_{\max}}$ is more pronounced at higher levels of drift demand. For example, as listed in Table 3-10, the values of $\lambda_{\theta_{\max}}(0.03)$ are nearly the same (i.e., about $2\text{x}10^{-3}$ for the L.A. 9-story and about $1\text{x}10^{-3}$ for the L.A. 20-story) for all of the connections cases considered (ductile through TBF extreme). The values of $\lambda_{\theta_{\max}}(0.08)$, on the other hand, for the TBF extreme case are 3 times larger for the L.A. 9-story and about 5 times larger for the L.A. 20-story than those for the ductile case.

Table 3-10. Mean annual frequencies of $\theta_{\max}$ exceeding 0.03 and 0.08 radians for the L.A. 3-story building models.

Connections Case	$\lambda_{\theta\max}(y)$	
	y = 0.03 rad	y = 0.08 rad
(a) L.A. 9-story		
Ductile Case	$1.9\text{x}10^{-3}$	$1.4\text{x}10^{-4}$
BFO Base Case	$1.8\text{x}10^{-3}$	$2.0\text{x}10^{-4}$
TBF Base Case	$1.7\text{x}10^{-3}$	$2.6\text{x}10^{-4}$
TBF Extreme Case	$2.3\text{x}10^{-3}$	$4.2\text{x}10^{-4}$
(b) L.A. 20-story		
Ductile Case	$1.1\text{x}10^{-3}$	$1.4\text{x}10^{-4}$
BFO Base Case	$1.4\text{x}10^{-3}$	$3.3\text{x}10^{-4}$
TBF Base Case	$1.3\text{x}10^{-3}$	$3.8\text{x}10^{-4}$
TBF Extreme Case	$1.4\text{x}10^{-3}$	$6.6\text{x}10^{-4}$

3.6 Limitations

In addition to the assumptions described in Sections 3.2 and 3.3, the following limitations associated with computing the drift demand hazard curves deserve mention:

(a) The estimates of the parameters a and b computed in this chapter via median-to-median fits should be considered "local" fits of the general relationship between

median $\theta_{\max}$ and S_{a1}. Thus, these estimates of a and b should not be used to predict the median $\theta_{\max}$ for S_{a1} values too far outside the range covered by the L.A. earthquake records (e.g., for the L.A. 9-story models, values of S_{a1} outside, say, 0.3g to 0.7g). Neither should these estimates of a and b be used to predict $\theta_{\max}$ medians too far outside the range of $\theta_{\max}$ values observed (e.g., 0.02rad to 0.05rad, say, for the L.A. 9-story). At larger values of $\theta_{\max}$ (e.g., 0.08rad), these estimates of a and b are likely to result in estimates of the drift demand hazard that are too low, due to an underestimation of the median $\theta_{\max}$ given S_{a1}. The general relationship between median $\theta_{\max}$ and S_{a1} can only be observed by considering a broader range of ground motion intensities. For example, the least-squares regression estimates of a and b in this chapter make use of the full range of S_{a1} and $\theta_{\max}$ data for the L.A. earthquake records (e.g., for the L.A. 9-story building, values of S_{a1} between 0.1g and 1.6g and $\theta_{\max}$ values between 0.01rad and 0.08rad). Using different (than the SAC) sets of earthquake records, a broad range of ground motion intensities is considered via least-squares regression in Chapter 6.

(b) Similarly, the range of applicability of the binary regression estimates of $(s_{a1})_o$ and β, which parameterize the probability of collapse given S_{a1} (i.e., $P_{C=1|S_{a1}}$), is limited to the range of S_{a1} covered by the L.A. earthquake records (e.g., values of S_{a1} less than about 1.6g for the L.A. 9-story models). The accuracy of the estimate of $P_{C=1|S_{a1}}$ is particularly important at relatively large values of $\theta_{\max}$ (e.g., 0.08rad), where the contribution of "collapses" to the drift demand hazard is large and the prediction of the median $\theta_{\max}$ given S_{a1} is outside its range of applicability.

(c) It is important to keep in mind that the analysis models of the buildings do not take into account, for example, potential shear connection or column splice failures. According to FEMA 351, pre-Northridge shear connections are expected to fail at rotations less than 0.08 radians. In a sense, the drift demand hazard curves computed in this chapter are likely lower bounds.

3.7 Conclusions

The drift demand hazard curves (computed via PSDA) for the L.A. 3-, 9-, and 20-story building models provide a more concise summary of the effects of connection fractures that were also investigated in Chapter 2. By either means, it is observed that the effects of connection fractures depend on the drift demand level. At relatively small drift

demand levels (e.g., $\theta_{\max}$=0.03rad), the effects are minimal even if "extreme" (i.e., $\theta_{f\text{-}}$=0.015rad) TBF brittle connection are considered. Note that in the story for which the peak story drift angle is 0.03 radians, it is anticipated that both flanges of the connections may have fractured in the TBF extreme case. In engineering practice, of course, $\theta_{\max}$=0.03rad (i.e., 3% interstory drift) is already considered very large. At larger drift demand levels (e.g., $\theta_{\max}$=0.08rad), the effects on the drift demand hazard, while important, are still perhaps less than one might have anticipated, except maybe in the TBF extreme case.

In the process of computing the drift demand hazard curves (i.e., $\lambda_{\theta_{\max}}$) via PSDA, the median and dispersion of $\theta_{\max}$ given S_{a1}, barring collapse of the model structure, is estimated with the results for the SAC earthquake records. Like $\lambda_{\theta_{\max}}$, the parameters that define the median relationship (i.e., b and a) can be used to quantify the effects of connection fractures given the ground motion intensity (i.e., S_{a1}), but only if no collapses are observed. The drift demand hazard curves prove to be an effective way to also deal with collapses, by accounting for the probability of collapse given the ground motion intensity (i.e., $P_{C=1|S_{a1}}$). Computing $\lambda_{\theta_{\max}}$ circumvents the need to employ "counted" statistics (used in Chapter 2), which cannot be calculated if the number of collapses is too large.

Finally, note that if a limit state is defined by a deterministic $\theta_{\max}$ capacity (e.g., equal to 0.03 or 0.08 radians), then the drift demand hazard $\lambda_{\theta_{\max}}(y)$ at such a capacity is also the MAF of exceeding the limit state (i.e., λ_{LS}). Such "annual limit-state frequencies" may be compared to prescribed absolute standards (rather than comparing the ductile versus brittle connections cases) to assess whether connection fractures push λ_{LS} beyond acceptable limits. In Chapter 4, a procedure for estimating the annual limit-state frequency for a partially-inspected earthquake-damaged SMRF building with fractured beam-column connection is presented.

Table 3-11. Earthquake record-by-record S_{a1} and θ_{max} results for the ductile and brittle connections cases of the L.A. 3-story building.

Earthquake Record	S_{a1} [g]	θ_{max} Ductile [rad]	BFO Base [rad]	TBF Base [rad]	TBF Extreme [rad]
LA01	0.678	0.0206	0.0235	0.0235	0.0235
LA02	1.269	0.0245	0.0218	0.0218	0.0218
LA03	0.882	0.0217	0.0208	0.0208	0.0208
LA04	0.531	0.0140	0.0138	0.0138	0.0138
LA05	0.490	0.0165	0.0163	0.0163	0.0163
LA06	0.415	0.0132	0.0137	0.0137	0.0137
LA07	0.647	0.0177	0.0177	0.0177	0.0177
LA08	0.892	0.0244	0.0299	0.0299	0.0315
LA09	1.084	0.0287	0.0432	0.0432	0.0605
LA10	0.934	0.0271	0.0311	0.0311	0.0359
LA11	0.810	0.0335	0.0351	0.0351	0.0475
LA12	0.628	0.0228	0.0186	0.0186	0.0186
LA13	1.072	0.0294	0.0298	0.0298	0.0308
LA14	1.263	0.0286	0.0338	0.0338	0.0344
LA15	1.208	0.0371	0.0466	0.0466	0.0591
LA16	1.410	0.0407	0.0547	0.0547	0.0667
LA17	0.612	0.0204	0.0203	0.0203	0.0203
LA18	0.873	0.0270	0.0298	0.0298	0.0302
LA19	0.792	0.0203	0.0203	0.0203	0.0203
LA20	1.208	0.0276	0.0284	0.0284	0.0380
LA21	2.698	0.0456	0.0763	0.0817	0.0808
LA22	2.643	0.0590	0.0775	0.0932	0.0992
LA23	0.716	0.0240	0.0248	0.0248	0.0251
LA24	1.453	0.0463	0.0711	0.0867	0.1547
LA25	1.966	0.0544	0.0697	0.0775	0.0875
LA26	2.295	0.0549	0.0685	0.0790	0.0769
LA27	0.996	0.0582	0.0884	0.0908	0.1671
LA28	1.421	0.0491	0.0591	0.0591	0.0739
LA29	0.946	0.0223	0.0204	0.0204	0.0204
LA30	0.874	0.0327	0.0348	0.0348	0.0970
LA31	2.002	0.0359	0.0630	0.0667	0.0846
LA32	2.107	0.0421	0.0557	0.0558	0.0573
LA33	1.787	0.0331	0.0280	0.0280	0.0274
LA34	1.218	0.0288	0.0329	0.0329	0.0539
LA35	1.106	0.0781	0.1037	0.1311	"collapse"
LA36	1.511	0.0659	0.0918	0.0971	0.1571
LA37	1.522	0.0768	0.0850	0.1423	0.2309
LA38	1.821	0.1206	0.1711	"collapse"	"collapse"
LA39	1.002	0.0331	0.0404	0.0404	0.0503
LA40	0.914	0.0757	0.1056	0.1204	0.1359

Table 3-12. Earthquake record-by-record S_{a1} and θ_{max} results for the ductile and brittle connections cases of the L.A. 9-story building.

Earthquake Record	S_{a1} [g]	θ_{max} Ductile [rad]	BFO Base [rad]	TBF Base [rad]	TBF Extreme [rad]
LA01	0.481	0.0229	0.0255	0.0255	0.0330
LA02	0.380	0.0216	0.0210	0.0210	0.0210
LA03	0.520	0.0286	0.0361	0.0361	0.0497
LA04	0.308	0.0242	0.0233	0.0233	0.0233
LA05	0.483	0.0411	0.0488	0.0488	0.0613
LA06	0.287	0.0194	0.0214	0.0214	0.0214
LA07	0.345	0.0185	0.0175	0.0175	0.0175
LA08	0.278	0.0188	0.0187	0.0187	0.0187
LA09	0.425	0.0315	0.0303	0.0303	0.0352
LA10	0.180	0.0227	0.0191	0.0191	0.0191
LA11	0.480	0.0234	0.0217	0.0217	0.0217
LA12	0.171	0.0199	0.0161	0.0161	0.0161
LA13	0.295	0.0230	0.0206	0.0206	0.0206
LA14	0.311	0.0219	0.0193	0.0193	0.0193
LA15	0.255	0.0300	0.0250	0.0250	0.0251
LA16	0.526	0.0412	0.0449	0.0449	0.0761
LA17	0.643	0.0299	0.0326	0.0326	0.0429
LA18	0.488	0.0202	0.0224	0.0224	0.0224
LA19	0.126	0.0216	0.0196	0.0196	0.0196
LA20	0.388	0.0243	0.0282	0.0282	0.0293
LA21	0.553	0.0377	0.0600	0.0600	0.1068
LA22	0.475	0.0450	0.0444	0.0444	0.0547
LA23	0.390	0.0239	0.0227	0.0227	0.0227
LA24	0.925	0.1514	0.1226	"collapse"	"collapse"
LA25	0.415	0.0330	0.0392	0.0392	0.0527
LA26	0.856	0.0417	0.0532	0.0532	0.0847
LA27	1.046	0.0396	0.0385	0.0385	0.1041
LA28	0.794	0.0354	0.0440	0.0440	0.0573
LA29	0.349	0.0265	0.0238	0.0238	0.0238
LA30	0.678	0.0653	0.1059	"collapse"	"collapse"
LA31	0.285	0.0287	0.0351	0.0351	0.0324
LA32	0.381	0.0322	0.0285	0.0285	0.0405
LA33	0.925	0.0383	0.0426	0.0426	0.0477
LA34	0.872	0.0393	0.0416	0.0416	0.0459
LA35	1.401	0.0971	0.1139	"collapse"	"collapse"
LA36	1.559	0.1038	0.1088	"collapse"	"collapse"
LA37	0.834	0.0602	0.0684	0.0773	"collapse"
LA38	1.091	0.0702	0.0813	"collapse"	"collapse"
LA39	0.354	0.0283	0.0273	0.0273	0.0297
LA40	0.995	0.0479	0.0611	0.0611	0.0760

Table 3-13. Earthquake record-by-record S_{a1} and θ_{max} results for the ductile and brittle connections cases of the L.A. 20-story building.

Earthquake Record	S_{a1} [g]	θ_{max} Ductile [rad]	BFO Base [rad]	TBF Base [rad]	TBF Extreme [rad]
LA01	0.147	0.0180	0.0156	0.0156	0.0156
LA02	0.078	0.0127	0.0128	0.0128	0.0128
LA03	0.269	0.0274	0.0241	0.0241	0.0262
LA04	0.267	0.0431	0.0494	0.0494	"collapse"
LA05	0.344	0.0365	0.0396	0.0396	0.0507
LA06	0.197	0.0226	0.0200	0.0200	0.0200
LA07	0.344	0.0223	0.0208	0.0208	0.0213
LA08	0.131	0.0138	0.0151	0.0151	0.0151
LA09	0.196	0.0301	0.0512	0.0512	"collapse"
LA10	0.188	0.0190	0.0276	0.0276	0.0313
LA11	0.109	0.0198	0.0171	0.0171	0.0171
LA12	0.097	0.0117	0.0110	0.0110	0.0110
LA13	0.142	0.0175	0.0159	0.0159	0.0159
LA14	0.166	0.0207	0.0209	0.0209	0.0209
LA15	0.132	0.0147	0.0135	0.0135	0.0135
LA16	0.085	0.0233	0.0193	0.0193	0.0193
LA17	0.123	0.0119	0.0133	0.0133	0.0133
LA18	0.116	0.0228	0.0207	0.0207	0.0207
LA19	0.057	0.0164	0.0154	0.0154	0.0154
LA20	0.111	0.0157	0.0166	0.0166	0.0166
LA21	0.237	0.0251	0.0219	0.0219	0.0219
LA22	0.235	0.0266	0.0233	0.0233	0.0240
LA23	0.175	0.0169	0.0177	0.0177	0.0177
LA24	0.456	0.0424	0.0920	"collapse"	"collapse"
LA25	0.215	0.0279	0.0328	0.0328	0.0392
LA26	0.138	0.0250	0.0280	0.0280	0.0309
LA27	0.200	0.0338	0.0390	0.0390	0.0463
LA28	0.190	0.0430	0.0545	0.0545	"collapse"
LA29	0.186	0.0163	0.0193	0.0193	0.0193
LA30	0.497	"collapse"	"collapse"	"collapse"	"collapse"
LA31	0.264	0.0416	0.0640	"collapse"	"collapse"
LA32	0.277	0.0304	0.0394	0.0394	"collapse"
LA33	0.304	0.0618	"collapse"	"collapse"	"collapse"
LA34	0.274	0.0614	"collapse"	"collapse"	"collapse"
LA35	0.513	0.1158	"collapse"	"collapse"	"collapse"
LA36	0.501	0.1317	"collapse"	"collapse"	"collapse"
LA37	0.432	0.0576	"collapse"	"collapse"	"collapse"
LA38	0.483	0.0913	"collapse"	"collapse"	"collapse"
LA39	0.135	0.0174	0.0201	0.0201	0.0201
LA40	0.332	0.0518	"collapse"	"collapse"	"collapse"

Chapter 4

Annual Limit-State Frequencies for Partially-Inspected Damaged Buildings

4.1. Introduction

In the preceding chapter, PSDA (probabilistic seismic demand analysis) was applied to compute drift demand hazard curves for buildings modeled with and without brittle beam-column connections. Whether ductile or brittle, the building models were analyzed under the assumption that, at the time, the structure was in an undamaged state. Particularly since the 1994 Northridge earthquake, however, the future reliability of damaged SMRF (steel moment-resisting frame) buildings with fractured beam-column connections has also come into question. Of concern is not only whether fractured connections should be repaired before permitting long-term occupancy, but also whether to permit occupancy soon after a damaging earthquake, and before repairs, when the threat of aftershocks arises. Complicating the issue is the expense of inspecting beam-column connections for fractures, which in many cases renders inspection of all the moment-resisting connections in a building uneconomical. As a result, the true state of damage is uncertain, and therefore how many (not to mention which) connections to inspect also becomes an important consideration.

As noted in Chapter 1, drift demand hazard curves like those computed in Chapter 3 can be used to estimate the mean annual frequency of exceeding a seismic-drift limit state, abbreviated as an "annual limit-state frequency." In this chapter, a procedure from estimating an annual limit-state frequency for a partially-inspected SMRF building

damaged by an earthquake is presented. The procedure accounts for the uncertainty, due to incomplete inspection, in the total number and locations of fractured beam-column connections, and can take into account the ground motion hazard due to potential aftershocks. Note that this chapter, in largely similar form, is to be published as a article in *Structural Safety* (Luco *et al.* 2002b).

An annual limit-state frequency for a damaged building estimated by the proposed procedure can be compared to that assuming no damage, or to a prescribed absolute standard, to help decide (for example) whether to permit occupancy soon after the damaging earthquake. This may require use of an aftershock hazard curve. Because uncertainty in the total number of fractured connections in the damaged building (due to incomplete inspection) contributes to the annual limit-state frequency (as explained in this chapter), the estimated annual limit-state frequency can in turn be used to decide, for example, whether to inspect additional connections and thereby reduce the uncertainty in the state of damage.

As an example, the proposed procedure is applied for the SAC (Phase II) 9-story SMRF building designed according to pre-Northridge practices for Los Angeles conditions (i.e., UBC zone 4). In the hypothetical example, the building is located on the Stanford University campus and has been damaged by a rupture of the entire Peninsula segment of the San Andreas fault 10 kilometers away.

4.2. Background

4.2.1 PSDA

The procedure presented in this chapter for a partially-inspected damaged building is an extension of PSDA for a given structure at a designated site (Cornell 1996). For convenience, the PSDA integral (described in Chapter 1) is repeated here in Equation 4-1.

$$\lambda_D(y) = \int \mathrm{P}[D > y \mid IM = x] \; |\, \mathrm{d}\lambda_{IM}(x) \,| \tag{4-1}$$

Recall that $\lambda_D(y)$ denotes the mean annual frequency of D exceeding the value y, where D is the structural (e.g., drift) demand that can be used to define a limit state. Similarly, IM is the ground motion intensity measure (e.g., spectral acceleration at or near the fundamental period of the structure) and $\mathrm{d}\lambda_{IM}(x)$ denotes the differential of the ground

motion hazard (evaluated at x). Refer to Chapter 3 for examples of the implementation of PSDA, including cases in which "collapses" necessitate an alternate form of Equation 4-1 (i.e., Equation 3-8) – the L.A. 9-story building model, which is to be considered in the example of Section 4.5, is one such case, even without pre-existing damage.

4.2.2 Aftershock Ground Motion Hazard

In order to carry out PSDA (and the proposed procedure) for a structure soon after an earthquake, the ground motion hazard curve for the site (i.e., λ_{IM}) should account for the possibility of aftershocks. As illustrated in the example in Section 4.5, this is accomplished by computing the post-earthquake ground motion hazard contributed by the fault segment ruptured by the main-shock (Yeo & Cornell, in preparation, 2002). Specifically, Yeo & Cornell assume that the ruptured fault segment can only contribute to the ground motion hazard because of the potential for aftershocks that originate randomly along the ruptured fault segment. On the other hand, the contribution to the total "aftershock ground motion hazard" from other faults in the vicinity of the site (i.e., the "background hazard") is presumed to be unchanged by the main earthquake. In reality, the aftershock ground motion hazard at a site diminishes with time after the main-shock, eventually returning to the pre-earthquake hazard. Accordingly, the computed aftershock hazard curves depend on the time since the main-shock and the length of the subsequent time window.

4.3. Definitions

4.3.1 Limit State

For this chapter, a limit state is defined by a deterministic structural (e.g., drift) capacity, denoted d_{LS}. In this case, the mean annual frequency of exceeding the limit state for a given (e.g., undamaged or fully-inspected) building is a direct result of PSDA, namely $\lambda_D(d_{LS})$ by Equation 4-1. Estimating an "annual limit-state frequency" for a partially-inspected building for which the state of damage is uncertain, however, calls for the extension of PSDA outlined in Section 4.4. Note that a limit state characterized by a random-valued structural capacity can also be considered with a simple extension of PSDA (e.g., Luco & Cornell 1998).

4.3.2 Damage State Measure

Based on the extensive study of the effects of beam-column connection fractures on seismic drift demands for SMRF buildings that is described in Chapter 2, the proportion (or equivalently the number) of connections with a fractured top-beam-flange is adopted here as a measure of the state of damage. Fractured bottom-beam-flanges (abbreviated here as BFF's) are not counted because their effects on seismic drifts, without fractured top-beam-flanges (TFF's) that generally occur at larger demands (e.g., due to the presence of a slab), were observed to be relatively mild. Unlike the locations of TFF's, for example, the proportion of TFF's is a scalar that can be inferred from the results of partial inspection.

4.4. Procedure

If a damaged building is fully inspected such that the total number and locations of fractured connections are known, then a "standard" PSDA with an analysis model that reflects the known damage can be carried out to estimate an annual limit-state frequency for the fully-inspected damaged building. In contrast, after only partial inspection the total number and locations of fractured connections in a damaged building are still unknown. The same is true when, for example, structural analysis with a ground motion recorded at (or simulated for) the site (SAC95-04 1995) or a damage detection method (Allen *et al.* 2001) is employed in an attempt to predict the total number and locations of fractured connections. Uncertainty in the total number and locations of fractured connections suggests that, in order to estimate an annual limit-state frequency for a damaged building, PSDA should be conducted for a range of possibilities (i.e., various total numbers and locations of fractured connections).

As expressed in Equation 4-2, the proposed procedure arrives at an annual limit-state frequency for a partially-inspected damaged building, denoted λ_{LS}, by integrating over all the possible proportions (0 to 1) of fractured top-beam-flanges among un-inspected connections, denoted F. The integrand in Equation 4-2 is the annual limit-state frequency given that $F=z$, denoted $\lambda_{D|F}(d_{LS}|z)$, weighted by the probability (density) of $F=z$, denoted $f_F(z)$. Note that like Equation 4-1 for PSDA, Equation 4-2 is an application of the total probability theorem.

$$\lambda_{LS} = \int \lambda_{D|F}(d_{LS} \mid z)\ f_F(z)\ dz \tag{4-2}$$

As detailed below, $\lambda_{D|F}(d_{LS}|z)$ is estimated using PSDA, accounting for the uncertainty in the locations of fractured connections via simulation; $f_F(z)$, the probability distribution for the actual but unknown proportion F, is inferred from partial inspection results.

4.4.1 Estimating $\lambda_{D|F}(d_{LS}|z)$ via PSDA

As indicated by Equation 4-2, the proposed procedure entails estimating $\lambda_{D|F}(d_{LS}|z)$, an annual limit-state frequency for a damaged building with a given proportion of fractured un-inspected top-beam-flange connections. Applying PSDA for this purpose requires at least one analysis model of the building with M (already) fractured top-beam-flange connections, where M is directly related to F by Equation 4-3. Note that n denotes the total number of connections in the building, n' is the number of inspected (top-beam-flange) connections, and m' is the number of inspected top-beam-flanges already found to be fractured.

$$M = F(n - n') + m' \tag{4-3}$$

Although partial inspection reveals the locations of some (i.e., m') of these M fractured top-beam-flanges (TFF's), the locations of the other TFF's are undiscovered. In addition, the locations of fractured bottom-beam-flanges (BFF's), which should be considered in conjunction with the TFF's, are (at least partially) unknown. Consequently, there are many candidates for the locations of the M TFF's (and the unspecified number of BFF's) in the building model(s) required to estimate $\lambda_{D|F}(d_{LS}|z)$ via PSDA.

For the proposed procedure, samples of possible locations of the TFF's (and BFF's) in a damaged-building model for a given value of F are selected from the outcomes of nonlinear dynamic analyses of the undamaged-building model that happen to result in exactly M (related to F by Equation 4-3) TFF's. Conveniently, if PSDA is first conducted for the undamaged depiction of a building (e.g., as a basis of comparison), then the requisite nonlinear dynamic analyses provide a suite of damaged-building models, several of which may feature M TFF's. Although the locations of the M TFF's determined in this manner may not agree precisely with partial inspection results, the resulting analysis models are nevertheless representative of a damaged building associated with the corresponding F. Ideally, each damaged building model would have m' TFF's and n'-m' intact top-beam-flanges (not to mention the BFF's) all located precisely where they have been discovered during inspection. However, it is difficult to

maintain perfect consistency with partial inspection results in addition to prescribing realistic locations for the undiscovered TFF's (and BFF's).

Just as the random nature of (pre-yield) connection fractures was accounted for via simulation in the PSDA computations of Chapter 3, the uncertainty in the locations of the un-inspected TFF's (and the BFF's) for a given value of F is accounted for by considering several damaged-building models with the same number of TFF's (i.e., the same M corresponding to F), but different locations of TFF's and BFF's. Specifically, this simulation scheme analyzes different damaged-building models for different earthquake ground motions, thereby combining the variability of structural response due to uncertainty in the locations of fractured connections with that resulting from earthquake record-to-record variability (given the ground motion intensity measure).

In addition to damaged-building analysis models for the given value of F, estimating $\lambda_{D|F}(d_{LS}|z)$ via PSDA for conditions soon after a damaging earthquake requires a ground motion hazard curve that accounts for the fact that an earthquake has recently occurred, and reflects the threat of aftershocks. Even when estimating $\lambda_D(d_{LS})$ for the undamaged depiction of a building as a basis of comparison (e.g., in the example in Section 4.5), an aftershock ground motion hazard curve is employed so that only the effect of (uncertain) damage on an annual limit-state frequency is measured. An increase in an annual limit-state frequency for a building due solely to the elevated ground motion hazard after an earthquake would not likely warrant prohibiting occupancy. Perhaps though, if an annual limit-state frequency for a partially-inspected damaged building is merely to be compared to that assuming no damage, it may be adequate to utilize, in computing both, the pre-earthquake ground motion hazard.

4.4.2 Inferring $f_F(z)$ from Partial Inspection Results

With partial inspection results (i.e., m' fractured top-beam-flanges among n' inspected connections, as defined above for Equation 4-3), a continuous probability density function $f_F(z)$ for the true but unknown proportion of TFF's among un-inspected connections can be inferred. Equation 4-4 for $f_F(z)$ is derived (Benjamin & Cornell 1970) according to rather elementary Bayesian statistics with the assumptions stipulated below.

$$f_F(z) = \frac{(n'+1)!}{m'!(n'-m')!} z^{m'} (1-z)^{n'-m'} \tag{4-4}$$

The probability density function expressed in Equation 4-4 is that of a beta distribution with mean μ_F and variance σ_F^2 given by Equations 4-5 and 4-6. The mode of this distribution is the observed (by partial inspection) proportion of TFF's, m'/n'. Note that as n' increases, the beta distribution for F will approach a normal distribution, so μ_F will approach the mode; this is also evident from Equation 4-5.

$$\mu_F = \frac{m'+1}{n'+2} \tag{4-5}$$

$$\sigma_F^2 = \frac{(m'+1)(n'-m'+1)}{(n'+2)^2(n'+3)} = \frac{\mu_F(1-\mu_F)}{n'+3} \tag{4-6}$$

As expressed in Equation 4-6, the uncertainty in the proportion of TFF's among un-inspected connections (i.e., σ_F^2) decreases with an increase in the number of connections inspected (i.e., n'), if the mean estimate of the proportion (i.e., μ_F) remains constant. In other words, the smaller the inspection sample size (i.e., n'), the less firm is the evidence about F, and the more broadly dispersed is the distribution of likelihood for the possible values of F.

The derivation of Equation 4-4 for $f_F(z)$ assumes that partial inspection represents random sampling from independent Bernoulli trials with replacement. In reality, inspection sampling is done without replacement (i.e., once a connection is inspected it is not inspected again), but the assumption made is adequate if the fraction of connections inspected, n'/n, is not large (e.g., less than 30%). The assumption made also implies that the choice of which connections to inspect has been made at random. "Smarter" choices that are more likely to find a fractured connection would render the procedure presented in this paper conservative because F would be overestimated.

Also assumed in deriving Equation 4-4 for $f_F(z)$ is that before inspection all possible values of F (0 to 1) are equally likely (i.e., no "prior" information). In reality, based on experience from other inspections of damaged buildings, the externally observable damage of the building, or other information, the engineer might have a rough prior estimate of the proportion of TFF's and a subjective uncertainty band. This prior information can be incorporated, in which case the analysis of the inspection data is referred to as "Bayesian updating." The form of Equation 4-4 will be the same if the most convenient (i.e., "natural conjugate") form of representing this prior information is used, namely another beta distribution (Benjamin & Cornell 1970).

Finally, it should be noted that because the number of connections is finite, in reality F is discrete, but in this paper it is treated as continuous. This is primarily because the proportion of TFF's among un-inspected connections (i.e., F) is treated synonymously with the probability of finding a TFF upon inspecting a single connection (or the "long-term" fraction); let this latter parameter be denoted here as p. If inspection truly represents random sampling from independent Bernoulli trials with replacement, one should recognize that even with p known, the proportion F (or number of TFF's among un-inspected connections) would still be random. In this case, F would follow a simple Binomial distribution with parameters n-n' and p. A discrete likelihood distribution for F that accounts for this additional uncertainty (given p) could be obtained via another total probability theorem integration. In fact, the resulting distribution on F is available in closed form (Benjamin & Cornell 1970). The difference between this distribution and that attained by assuming that F is equivalent to p is relatively small, as long as the fraction of connections inspected, n'/n, is not large (e.g., less than 30%). Hence, the simpler of these two approaches (i.e., assuming that F is equivalent to p) is intentionally applied in the procedure presented here.

4.4.3 Integrating to Arrive at λ_{LS}

The convolution of $\lambda_{D|F}(d_{LS}|z)$ and $f_F(z)$ expressed by the integral in Equation 4-2 for λ_{LS} (above) can be evaluated numerically if $\lambda_{D|F}(d_{LS}|z)$ is computed (by PSDA) for many values of the proportion F. Alternatively, an analytical solution of the integral can be found if, for example, a quadratic form is assumed for $\lambda_{D|F}(d_{LS}|z)$. Recognizing that the integration expressed by Equation 4-2 can be interpreted as finding the expectation of the function $\lambda_{D|F}(d_{LS}|z)$, a quadratic form for this function renders λ_{LS} a simple function of the mean and variance of F, as expressed in Equation 4-7.

$$\lambda_{LS} \equiv \int (az^2 + bz + c)\ f_F(z)\ dz \quad = \quad a(\sigma_F^2 + \mu_F^2) + b\mu_F + c \qquad (4\text{-}7)$$

Note that a quadratic form for $\lambda_{D|F}(d_{LS}|z)$ can capture a more than proportional increase in the annual limit-state frequency with increasing F, in which case the uncertainty in F contributes to λ_{LS}. In contrast, a proportional (i.e., linear) relationship between $\lambda_{D|F}(d_{LS}|z)$ and F would render λ_{LS} a function of only the mean of F (since a in Equation 4-7 would equal 0). In that case, λ_{LS} would be independent of the uncertainty in F because larger and smaller than expected values of F would tend to offset each other.

A quadratic formula for $\lambda_{D|F}(d_{LS}|z)$ can be established with PSDA estimates of annual limit-state frequencies for just three assumed values of F (or the corresponding values of M). Specifically, $\lambda_D(d_{LS})$ assuming no damage (i.e., M=0) and $\lambda_{D|F}(d_{LS}|z)$ for two other values of F near the observed proportion of TFF's (i.e., m'/n') can be used to establish the coefficients of a quadratic equation for $\lambda_{D|F}(d_{LS}|z)$. This is true despite the fact that, if at least one TFF has been discovered, M=0 translates to a negative value of F, which is outside the range of observable values. It should also be noted that in using the undamaged model of the building for the M=0 (i.e., no TFF's) case, existing BFF's are not included as they are in the damaged-building models for the other values of M (or F). However, the results of Chapters 2 and 3 suggest that the annual limit-state frequency for a building model with existing BFF's, but no TFF's, might not be dramatically different than that for the entirely undamaged building model considered here.

The expression for λ_{LS} in Equation 4-7 suggests that, all else being equal (i.e., a, b, c and μ_F), the larger the uncertainty in the true proportion of TFF's among un-inspected connections (i.e., σ_F^2), the larger will be the estimated annual limit-state frequency for a partially-inspected damaged building (i.e., λ_{LS}). Such an increase in λ_{LS} (due to an increase in σ_F^2) may serve as a penalty for incomplete inspection and hence an incentive to do more, since σ_F^2 is inversely proportional to the number of connections inspected (for constant μ_F), as rationalized above based on Equation 4-6. Of course, with additional inspections, μ_F (the mean estimate of the true F) will not remain exactly constant. The outcomes of future inspections are themselves uncertain; thus, the estimate μ_F may increase or decrease, affecting further λ_{LS}, as indicated by Equation 4-7.

In practice, a reduction of λ_{LS} as a result of more complete inspection (and the corresponding safety or cost implications) is offset by the significant cost of inspecting additional connections. The two considerations can be weighed in a "pre-posterior" analysis (Benjamin & Cornell 1970) in order to decide (beforehand) on an optimal amount of inspection, or to decide (in a sequential manner) whether to inspect further as new results are discovered. It is perhaps more likely that, in any future application, such an analysis would be used a priori to set generic standards for degree of inspection, perhaps as a function of what is found in a preliminary inspection.

4.5. Example

As an illustration of the proposed procedure, consider the following hypothetical example:

The SAC (Phase II) 9-story perimeter SMRF building designed according to pre-Northridge practices for Los Angeles conditions (i.e., UBC zone 4), but located on the Stanford University campus, is subjected to the ground motion resulting from a rupture of the entire Peninsula segment of the San Adreas fault 10 kilometers away (i.e., the characteristic event of moment magnitude 7.23). During the week after the earthquake, 10 randomly selected moment-resisting connections (of a total of 90) in one of the two north-south 5-bay perimeter SMRF's are inspected, and the top-beam-flange of 1 of the 10 connections is found to be fractured.

An annual limit-state frequency (i.e., the mean annual frequency of exceeding a limit-state) for the partially-inspected damaged building is to be estimated in order to decide whether to permit occupancy of the damaged building within the next year (e.g., before completing repairs). If the estimated annual limit-state frequency is too high relative to either the corresponding annual limit-state frequency assuming no damage or a prescribed absolute standard, a decision to inspect more connections may be made, or it may be decided to absorb the loss of vacating the building.

The structural demand measure (i.e., D) used to define the limit states is the maximum (over all stories) peak (over time) story drift angle (i.e., inter-story drift normalized by story height), also denoted $\theta_{\max}$. Deterministic maximum peak story drift angle capacities (i.e., d_{LS}) of 0.03 and 0.08 (radians) are chosen to represent a local (e.g., a connection losing gravity load carrying ability) and a global (e.g., building collapse) limit state, as recommended in the recent SAC guidelines (FEMA 351, 2000).

4.5.1 $\lambda_D(d_{LS})$ Assuming No Damage

With the aftershock ground motion hazard curve for the Stanford site shown in Figure 4-1 (and described below), and an undamaged analysis model of the SMRF that has been partially inspected, PSDA is conducted to arrive at the structural-drift-demand hazard curve labeled M=0 in Figure 4-2. Read from this curve, the annual limit-state frequencies $\lambda_D(d_{LS}=0.03)$ and $\lambda_D(d_{LS}=0.08)$ (defined above in terms of $\theta_{\max}$) are equal to $1.5\text{x}10^{-2}$ and $1.6\text{x}10^{-3}$, respectively. These two values of the annual limit-state frequencies will serve as a basis of comparison, in addition to being used to establish a quadratic form for $\lambda_{D|F}(d_{LS}|z)$. Note that for the presumably undamaged building prior to the earthquake the corresponding annual limit-state frequencies are $1.5\text{x}10^{-3}$ and $1.3\text{x}10^{-4}$, which reflects the roughly uniform order of magnitude increase in the ground motion hazard at all spectral accelerations due to potential aftershocks, as seen in Figure 4-1.

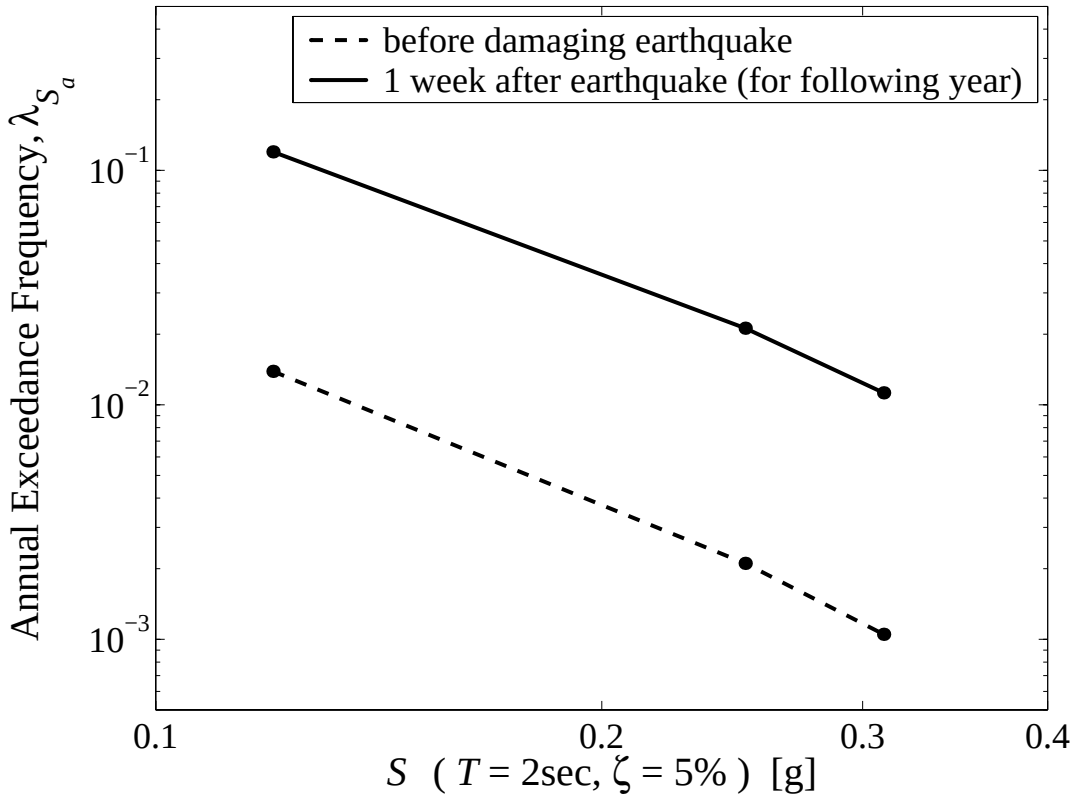

Figure 4-1. Ground motion hazard curves for the Stanford site before and after a rupture of the entire Peninsula segment of the San Andreas fault.

The aftershock ground motion hazard curve depicted in Figure 4-1 assumes that one week has past since the main earthquake (i.e., time for inspection) and accounts for the possibility of aftershocks over the subsequent year, without a repeat of the main-shock. After one year the threat of aftershocks generally decays to an insignificant level. The ground motion hazard before the damaging earthquake, which includes the "background hazard," is also depicted in Figure 4-1 (Woodward-Clyde Consultants 1991). Note that the ground motion intensity measure considered is the 2-second, 5%-damped spectral acceleration; the period of 2 seconds is chosen to be near the fundamental period of the undamaged building model (i.e., T=2.34 sec). Note, too, that an "M1" model of the Los Angeles 9-story building is analyzed here, assuming that top and bottom beam-flange connections fracture at a plastic rotation of 0.015 radians (in addition to pre-yield bottom flange fractures). Refer back to Chapter 2 for more details of this model.

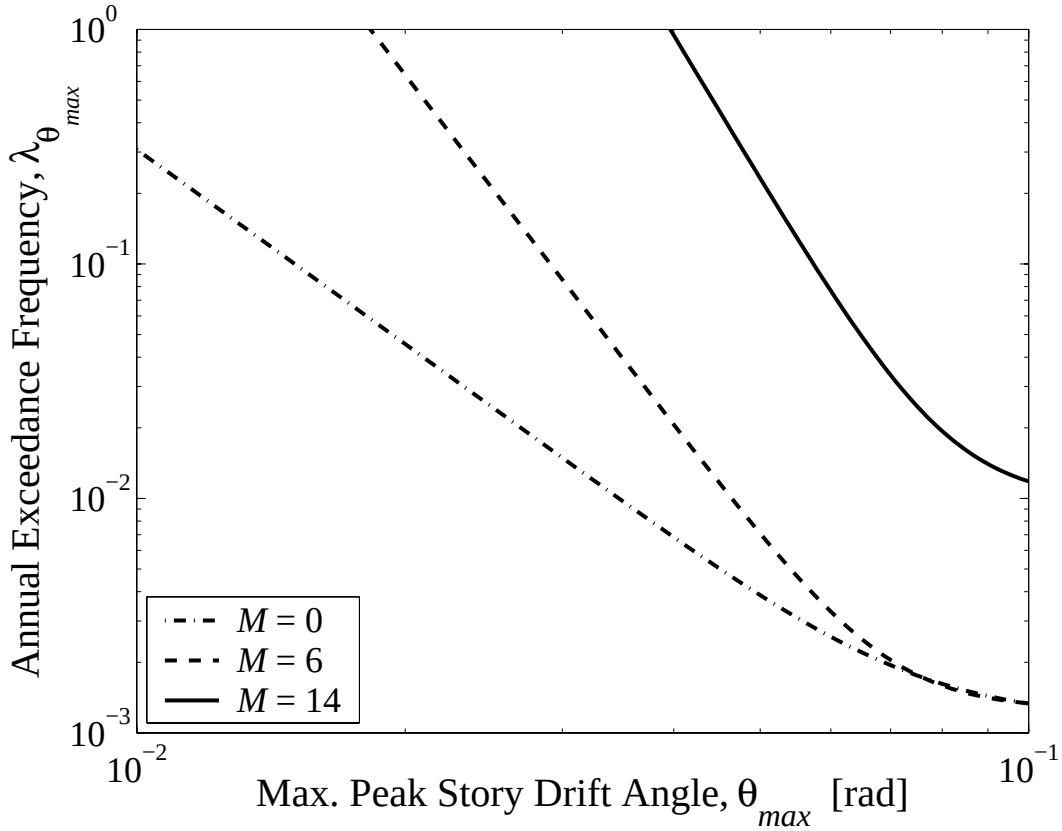

Figure 4-2. Seismic drift demand hazard curves (computed by PSDA) for the building after the main earthquake, assuming no damage (M=0) or several TFF's (M=6 and M=14).

4.5.2 $\lambda_{D|F}(d_{LS}|z)$ for Assumed Damage

From the nonlinear dynamic analysis results for the forty SAC Phase II ground motions for Los Angeles, attained while computing $\lambda_D(d_{LS})$ for the undamaged depiction of the building, samples of the total number and locations of fractured top-beam-flange connections are selected. As illustrated in Figure 4-3, two samples (each) of the locations of TFF's (and BFF's) in a damaged-building model with M=6 and M=14 TFF's are considered. These two values of M translate to F=0.0625 and F=0.1625 (according to Equation 4-3 above), which bracket the observed proportion of TFF's, namely m'/n'=0.10.

As done for the undamaged depiction of the building (in Section 4.5.1), PSDA is conducted for the damaged-building models illustrated in Figure 4-3 to arrive at the two drift demand hazard curves labeled M=6 and M=14 in Figure 4-2. Recall (from

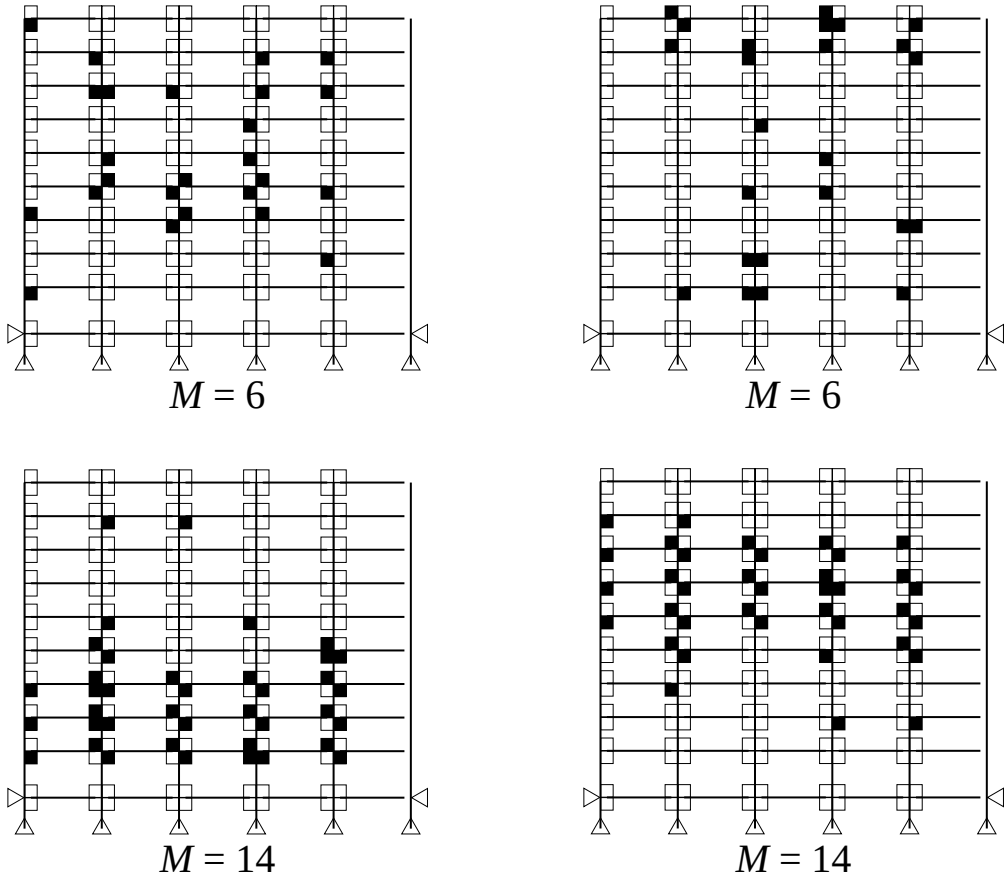

Figure 4-3. Locations of TFF's and BFF's among the moment-resisting connections in the (9-story, 5-bay) damaged-building models for a given M. Note that the beam-column connections along the right-most column line are not moment-resisting, and that the ground floor is laterally restrained.

Section 4.4.1) that the two different patterns of locations of TFF's (and BFF's) for each value of M are intended to represent the many possible locations of TFF's (and BFF's) for a given value of F (or M); a larger set of patterns would be preferable. Again read from Figure 4-2, the "local" and "global" annual limit-state frequencies for the given values of F (or M) are listed in Table 4-1.

As expected, the results in Table 4-1 indicate that the more TFF's (i.e., the larger M or F), the larger the corresponding annual limit-state frequency $\lambda_{D|F}(d_{LS}|z)$. Apparently, $\lambda_{D|F}(d_{LS}|z)$ increases rapidly (i.e., faster than linearly or exponentially) with F (or M). Note that M=0 (i.e., no damage) translates to a negative proportion of TFF's among

Table 4-1. Mean annual frequencies of exceeding the "local" and "global" limit states given the proportion of TFF's among un-inspected connections, F (or the total number of TFF's, M).

M	F (=z)	$\lambda_{D\|F}(d_{LS}\|z)$	
		d_{LS}=0.03	d_{LS}=0.08
0	-0.0125	$1.5\text{x}10^{-2}$	$1.6\text{x}10^{-3}$
6	0.0625	$8.6\text{x}10^{-2}$	$1.6\text{x}10^{-3}$
14	0.1625	$5.9\text{x}10^{0}$	$1.9\text{x}10^{-2}$

un-inspected connections (i.e., $F = -0.125$) because m'=1 TFF has already been discovered. As discussed in Section 4.4.3, even though a negative value of F cannot be observed, the annual limit-state frequencies corresponding to M=0 can nevertheless be used to establish a quadratic formula for $\lambda_{D|F}(d_{LS}|z)$.

Incidentally, the nonlinear dynamic analyses of the damaged-building models with M=6 TFF's resulted in 3 collapses under the 24 selected ground motions, whereas the more damaged M=14 models suffered 10 collapses out of 36 earthquake records. Note that these two subsets of the 40 SAC earthquake records for Los Angeles are picked out because of constraints related to running earthquake records back-to-back (i.e., first for an undamaged structure, then for the damaged one), namely that the two records have the same time step. Recall from Chapter 2 or 3 that the undamaged-building model suffered 6 collapses out of the 40 earthquake records. All of these collapses were accounted for in computing $\lambda_{D|F}(d_{LS}|z)$, but the non-collapse data (i.e., θ_{max} versus spectral acceleration) alone and the regression fits that are also used in computing $\lambda_{D|F}(d_{LS}|z)$ are illustrated in Figure 4-4. Note the significant scatter and the generally increasing drift demands, for a given ground motion level, with increasing number of TFF's.

4.5.3 $f_F(z)$ Inferred from Partial Inspection Results

The partial inspection results, namely m'=1 fractured top-beam-flange (TFF) among n'=10 randomly selected connections, parameterize the probability density function $f_F(z)$ for the proportion of TFF's among un-inspected connections that is given by Equation 4-4 and is illustrated in Figure 4-5 below. Also included in Figure 4-5 are the distributions of F assuming inspection sample sizes of n'=20 and n'=30 but the same observed proportion

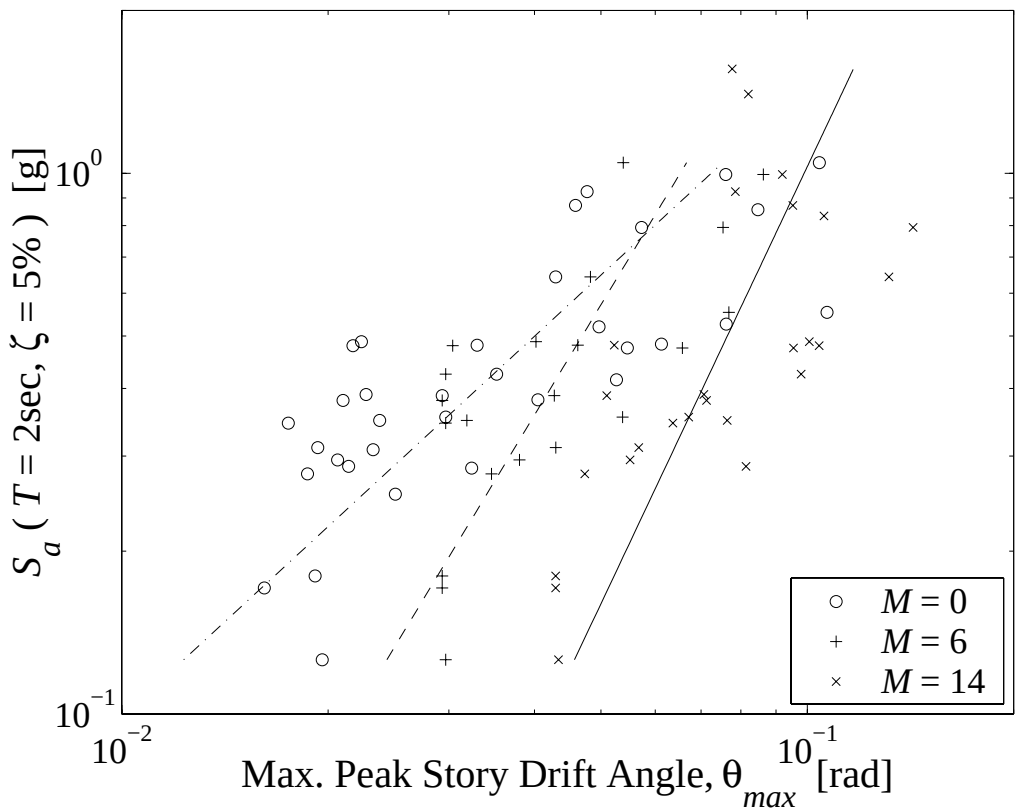

Figure 4-4. Nonlinear dynamic analysis results for those earthquake records that do not cause collapse of the building modeled with three different levels of damage. Along with the ground motion hazard curve depicted in Figure 4-1, these results are used to compute $\lambda_{D|F}(d_{LS}|z)$ via PSDA.

of TFF's, m'/n'=0.10. The reduction of the uncertainty in F with increasing n' (but constant m'/n') is clear.

Applying Equations 4-5 and 4-6, the estimates of the mean and COV (coefficient of variation) of F given the partial inspection results m'=1 and n'=10 are μ_F=0.167 and σ_F/μ_F=0.620 (since σ_F^2=0.011). Note that if more connections are inspected (i.e., n' is increased), μ_F will approach the observed proportion of TFF's (since the shape of the distribution of F approaches a normal distribution and the mode of F is m'/n', as mentioned in Section 4.4.2).

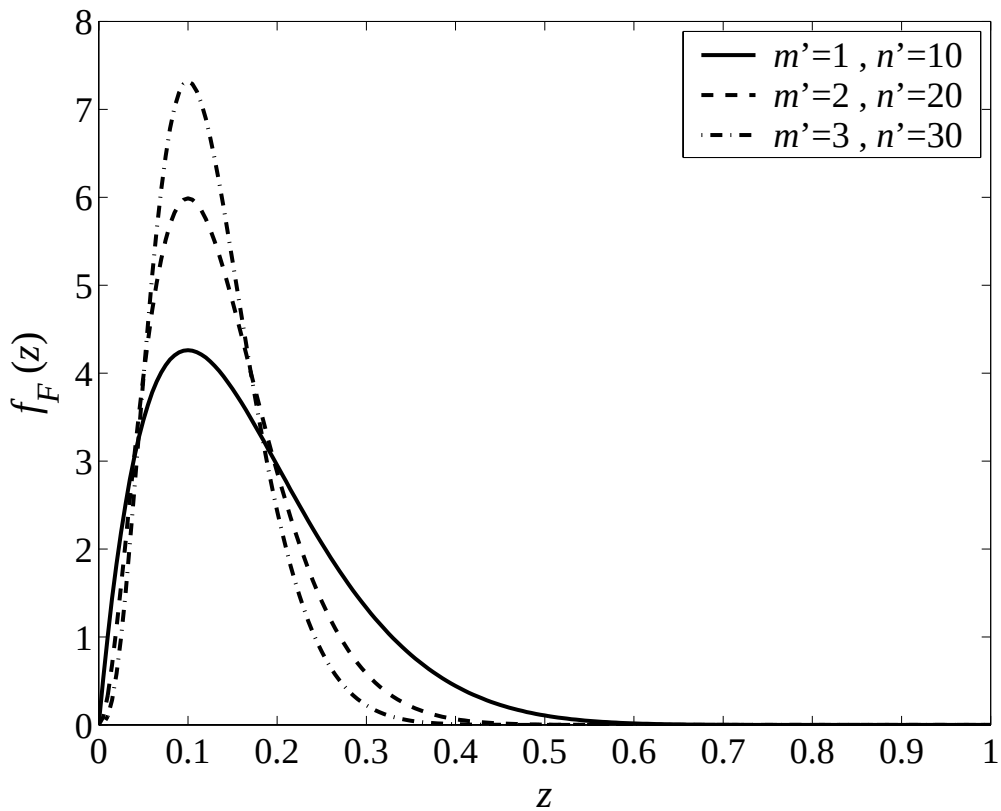

Figure 4-5. Probability density function for the proportion of TFF's among un-inspected connections given partial inspection results (i.e., *m*' and *n*').

4.5.4 λ_{LS} for Partially-Inspected Damaged Building

With the annual limit-state frequencies $\lambda_{D|F}(d_{LS}|z)$ for each of the three assumed values of F (listed in Table 4-1), the coefficients a, b, and c of a quadratic equation for $\lambda_{D|F}(d_{LS}|z)$ are defined. The resulting values of a, b, and c for the "local" and "global" limit states (i.e., $\theta_{\max}$=0.03 and $\theta_{\max}$=0.08) are listed in Table 4-2. Given a, b, and c, and μ_F and σ_F^2, the annual limit-state frequency for the partially-inspected damaged building (i.e., λ_{LS}) is calculated according to Equation 4-7. Again for the "local" and "global" limit states, the resulting values of λ_{LS} equal $9.8\text{x}10^0$ and $3.1\text{x}10^{-2}$, respectively. Compared to $\lambda_D(d_{LS})$ assuming no damage after the main earthquake (i.e., the M=0 results in Table 4-1), λ_{LS} for the partially-inspected damaged building is more than an order of magnitude larger for the "global" limit state and more than two orders of magnitude larger for the "local" limit state.

Table 4-2. Coefficients of the quadratic formulae established for $\lambda_{D|F}(d_{LS}|z)$ with the PSDA estimates of the "local" and "global" annual limit-state frequencies for M=0, 6, and 14 (related to values of F by Equation 4-3 with n=90, n'=10, and m'=1).

Limit State	$\lambda_{D\|F}(d_{LS}\|z) = az^2 + bz + c$		
	a	b	c
d_{LS}=0.03	$3.27\text{x}10^{2}$	$-1.54\text{x}10^{1}$	$-2.29\text{x}10^{-1}$
d_{LS}=0.08	$9.94\text{x}10^{-1}$	$-4.97\text{x}10^{-2}$	$8.23\text{x}10^{-4}$

Note that these values of λ_{LS} for the partially inspected building with m'=1 and n'=10 are larger than those for the case when F=0.1625 (i.e., $5.9\text{x}10^{0}$ and $1.9\text{x}10^{-2}$), even though the observed fraction of TFF's is only m'/n'=0.1. This is due both to the significant weight that, in light of the small number of connections inspected, must be given to the possibility of values of F larger than 0.1625 (as seen in Figure 4-5), and the rapid increase in $\lambda_{D|F}(d_{LS}|z)$ with increasing F (as evidenced by Table 4-1). If, rather than m'=1 of n'=10, m'=2 of n'=20 or m'=3 of n'=30 connections are inspected and found to have a fractured top-beam-flange, the observed fraction of TFF's (i.e., m'/n') would remain the same but the uncertainty in F would be reduced, as illustrated by Figure 4-5 above. Consequently, the estimated annual limit-state frequencies λ_{LS} would be smaller (in accordance with Equation 4-7 above), as shown in Table 4-3. The reduction of λ_{LS} associated with an increase in n' (evidenced by Table 4-3) quantifies the benefits of additional information and forms an explicit justification for inspecting more connections. Practically this benefit must be weighed against the significant cost of conducting these inspections, perhaps via a formal (e.g., a "pre-posterior") decision analysis (as mentioned in Section 4.4.3).

Table 4-3. Annual limit-state frequencies for the damaged building assuming different partial inspection results with the same observed proportion of TFF's.

m'/n'	λ_{LS}	
	d_{LS}=0.03	d_{LS}=0.08
1/10	$9.8\text{x}10^{0}$	$3.1\text{x}10^{-2}$
2/20	$4.7\text{x}10^{0}$	$1.5\text{x}10^{-2}$
3/30	$3.2\text{x}10^{0}$	$1.1\text{x}10^{-2}$

4.6. Conclusions

As illustrated by the example, the proposed procedure estimates an annual limit-state frequency for a partially-inspected damaged building that can be used to decide, for example, whether fractured connections should be repaired before allowing long-term occupancy, or whether to permit occupancy soon after the damaging earthquake (and before any repairs). Whereas the former decision considers the everyday (e.g., pre-earthquake) ground motion hazard, the latter decision should account for the possibility of aftershocks, as reflected in an aftershock hazard curve like the one developed for the example by Yeo & Cornell (in preparation, 2002).

An extension of PSDA, the proposed procedure accounts for the uncertainty induced by incomplete inspection in the state of damage (specifically the proportion of fractured top-beam-flange connections). As a result, the estimated annual limit-state frequency reflects a penalty associated with incomplete inspection, and hence serves as an explicit incentive to inspect more connections. Practically, the cost of inspecting for fractures must also be considered if a decision to inspect more connections is to be made.

The proposed procedure is similar in approach to the level 2 detailed post-earthquake evaluation methodology recommended in the recent SAC guidelines (FEMA 352, 2000), which estimates the probability of earthquake-induced collapse of a damaged building. The most significant difference is that the methodology in the SAC guidelines requires complete inspection of "all fracture-susceptible connections in the building." Another difference is the presumed aftershock ground motion hazard, which is based on a repeat of a main-shock in the SAC guidelines.

While an annual limit-state frequency estimated by the proposed procedure is treated here in a subjectivist manner, it can also be construed as the mean estimate of an annual limit-state frequency, where the uncertainty is induced by that in the true but unknown proportion of fractured top-beam-flanges (among un-inspected connections). This alternate interpretation implies that, for example, the 90% upper confidence bound for an annual limit-state frequency can be determined given the inspection results. Indeed this approach is more consistent with the way the SAC guidelines have been constructed, namely in terms of achieving a specified confidence that an annual limit-state frequency lies below an acceptable value (Cornell *et al.* 2002).

Chapter 5

Ground Motion Intensity Measures for Structural Performance Assessment at Near-Fault Sites

5.1 Introduction

As demonstrated in the preceding two chapters, PSDA can be used to assess the seismic performance of a given structure at a designated site. More precisely, the results of PSDA, namely a seismic demand hazard curve, can be combined with structural capacity information to compute an "annual limit-state frequency" (i.e., the mean annual frequency of exceeding a specified limit state, like the collapse limit state). Denoted here as λ_{LS}, the mean annual frequency of exceeding the limit state *LS* is given by Equation 5-1, which is merely an expansion of Equation 1-2 from Chapter 1. For a definition of each of the terms within the integral, refer back to Chapter 1; recognize, however, that $\mathrm{d}G_{DM|IM}$ denotes the derivative of $G_{DM|IM}$ with respect to *DM*, which is also the probability density function (PDF) for *DM* given *IM*.

$$\lambda_{LS} = \iint_{DM,IM} G_{LS|DM} \,|\, \mathrm{d}G_{DM|IM} \,|\,|\, \mathrm{d}\lambda_{IM} \,| \tag{5-1}$$

As Equation 5-1 is an application of the total probability theorem (e.g., Benjamin & Cornell 1970), formally $G_{LS|DM}$ should be $G_{LS|(DM,IM)}$, but here the latter is presumed to

be functionally independent of *IM* because *LS* is normally defined in terms of *DM* only. Note that in this chapter PSDA and Equation 5-1 for λ_{LS} are referred to synonymously; in truth, Equation 5-1 is a simple extension of PSDA. As mentioned in Chapter 1, PSDA and Equation 5-1 are at the core of recent performance-based seismic guidelines like FEMA 350-353 and the draft ISO Offshore Structures Standard.

In applying PSDA for a structural performance assessment (i.e., computing λ_{LS} via Equation 5-1), the ground motion intensity measure (*IM*) adopted is customarily (as in Chapters 3 and 4) the spectral acceleration at or near the fundamental period of the structure (with a damping ratio of 5%), denoted here as $S_a(T_1)$. In part, this *IM* choice is driven by convenience, as seismic hazard curves in terms of $S_a(T_1)$ are either readily available (e.g., from the U.S. Geological Survey) or commonly computed. Moreover, several studies (e.g., Shome *et al.* 1998) have demonstrated that $S_a(T_1)$ is closely related to inelastic demands (e.g., drift) for moderate-period structures (e.g., around 1 second); consequently, relatively few NDA's (nonlinear dynamic analyses) under different earthquake records are necessary to estimate the conditional distribution of *DM* given $S_a(T_1)$. It is important to note, however, that such studies have predominantly considered "ordinary" (i.e., non-near-source) ground motions.

As reviewed in Chapter 1, near-source ground motions can produce very different nonlinear structural demands than do ordinary ground motions, even for the same level of $S_a(T_1)$. This difference implies that $S_a(T_1)$ may not be as closely related to nonlinear structural demands for near-source ground motions as it is for ordinary ground motions, thereby calling for more NDA's of the given structure under different earthquake records in order to apply PSDA. Furthermore (as explained in this chapter), the results of PSDA may not be accurate for sites susceptible to near-source ground motions if $S_a(T_1)$ is employed. Consequently, several alternative ground motion intensity measure (*IM*'s) are introduced in this chapter that are meant to ensure the accuracy of PSDA at near-fault sites using relatively few NDA's of the structure. For comparing between alternative *IM*'s, the "efficiency" and "sufficiency" of an *IM* are defined. An approach for quantifying these criteria is outlined here, but its implementation is left for Chapter 6. Also in this chapter, other modifications of the customary PSDA approach that result in accurate estimates of λ_{LS} are discussed. Note that parts of this chapter are included in an article that is currently being revised for publication in *Earthquake Spectra* (Luco & Cornell 2002).

5.2 Criteria for Selecting an Appropriate *IM* to be Employed in PSDA

The ground motion intensity measure *IM* in Equation 5-1 serves as a link between seismic hazard curves typically provided by seismologists (i.e., λ_{IM}) and structural analysis conducted by engineers (to estimate $G_{DM|IM}$). Beyond convention or convenience, the selection of an appropriate *IM* to be employed in computing λ_{LS} is driven by the "efficiency" and the "sufficiency" of the *IM*. These two criteria are defined in the subsections below; both are related to the accuracy, or precision, in estimating $G_{DM|IM}$ and hence λ_{LS}. It is important to keep in mind that the efficiency and sufficiency of an *IM* can depend not only on the type of ground motions considered (e.g., near-source versus ordinary), but also on the characteristics of the structure of interest. As pointed out below, consideration must also be given to the computability of the ground motion hazard at a site in terms of the selected *IM*.

5.2.1 "Efficiency" of an *IM*

Recall (e.g., from Chapters 3 and 4) that the conditional (complementary cumulative) distribution of *DM* given *IM*, denoted $G_{DM|IM}$, is customarily estimated with the results of NDA of the given structure for a suite of earthquake records. An efficient *IM* is defined simply (from the perspective of a structural engineer) as one that results in a relatively small variability of *DM* given *IM*, thereby reducing the number of NDA's and earthquake records necessary to estimate $G_{DM|IM}$ with adequate precision, that is, with adequately small uncertainty (Shome & Cornell 1999). A functional relationship between the variability of *DM* given *IM* and the necessary number of NDA's and earthquake records is detailed in Section 5.5.

5.2.2 "Sufficiency" of an *IM*

Also related to the estimation of $G_{DM|IM}$, a sufficient *IM* is defined here as one that renders *DM* conditionally independent, given *IM*, of earthquake magnitude (*M*) and source-to-site distance (*R*). As explained further below, a sufficient *IM* is desirable because it ensures an accurate estimate of $G_{DM|IM}$ and thereby an accurate estimate of λ_{LS} by Equation 5-1. Equation 5-1 for λ_{LS} is merely an application of the total probability theorem, so theoretically the result should be the same regardless of the choice of *IM* (or *DM*). However, (as mentioned above) $G_{DM|IM}$ in Equation 5-1 is normally estimated using NDA results for a limited number of earthquake ground motion records. If *IM* is

not sufficient (i.e., if *DM* is not conditionally independent, given *IM*, of *M* and *R*), then the estimate of $G_{DM|IM}$ must be expected to depend to some degree on the *M*'s and *R*'s of the earthquake records selected. In this (insufficient *IM*) case, unless the distribution of the *M*'s and *R*'s (conditioned on *IM*) of the selected ground motions matches the distribution that appears naturally at the site (as discussed in more detail Section 5.6), the estimate of $G_{DM|IM}$ (and thereby of λ_{LS}) will be somewhat inaccurate. In contrast, if *IM* is sufficient, by definition the $G_{DM|IM}$ estimate will be independent of the *M*'s and *R*'s of the selected ground motions, and therefore λ_{LS} estimated with Equation 5-1 should, in principle, be accurate *regardless* of which earthquake records are used to estimate $G_{DM|IM}$.

As an example demonstrating that the estimate of $G_{DM|IM}$ can depend on the *M*'s of the selected ground motions if *IM* is not sufficient, consider a preview of the results presented in Chapter 6. Summarized in Table 5-1 are *DM* (here $\theta_{\max}$) on *IM* regression results for the "LA9" building model (i.e., an M1+ model of the SAC Los Angeles 9-story) subjected to "ordinary" earthquake records (detailed in Appendix A) with $M < 6.5$ versus those with $M \geq 6.5$. More specifically, the regression coefficient *a* and the dispersion σ of the residuals from a one-parameter fit of the form $\theta_{\max} = a \cdot IM \cdot \varepsilon$ are reported. Recall (e.g., from Chapter 3) that $G_{DM|IM}$ is estimated with such regression results, under the assumption that *DM* is log-normally distributed given *IM*; thus, different regression results will lead to different estimates of $G_{DM|IM}$. From Table 5-1, notice that for the intensity measure denoted as IM_{1E} (defined in Section 5.4.1), which in Chapter 6 is found to be insufficient for the LA9 building model subjected to the ordinary earthquake records, the regression estimate of the parameter *a* using the ordinary

Table 5-1. $\theta_{\max}$ on *IM* regression results for the "LA9" building model demonstrating a dependence on *M* for the relatively insufficient IM_{1E} but not for the relatively sufficient $IM_{1I\&2E}$.

IM	*a*	σ
(a) 29 "ordinary" earthquake records of $M < 6.5$		
IM_{1E}	1.33	0.45
$IM_{1I\&2E}$	1.18	0.28
(b) 30 "ordinary" earthquake records of $M \geq 6.5$		
IM_{1E}	1.13	0.46
$IM_{1I\&2E}$	1.15	0.26

earthquake records with $M < 6.5$ is different from that using the earthquake records with $M \geq 6.5$ (i.e., a=1.33 vs. 1.13). (The two regression estimates of σ for IM_{1E} happen to be approximately equal.) In contrast, for the intensity measure $IM_{1I\&2E}$ (defined in Section 5.4.4), which in Chapter 6 is found to be sufficient (for LA9 subjected to the ordinary earthquake records), the estimates of a and σ are approximately equal for the two subsets of the ordinary earthquake records partitioned by M.

In other words, the $G_{DM|IM}$ estimate depends on whether the $M < 6.5$ or the $M \geq 6.5$ suite of earthquake records is selected if the insufficient IM_{1E} is employed, but not if the sufficient $IM_{1I\&2E}$ is used. (It follows that different combinations of the earthquake records from the two suites would also lead to different estimates of $G_{DM|IM}$ if the insufficient IM_{1E} is employed.) Also for the LA9 building model, in Chapter 6 a difference in the regression estimates of a for a near-source versus an ordinary suite of earthquake records is observed for the insufficient IM_{1E}, but not (to the same extent) for the sufficient $IM_{1I\&2E}$. Those regression results (summarized in Table 6-6) demonstrate a dependence of the estimate of $G_{DM|IM}$ on the R's of the selected ground motions for an insufficient IM.

Regarding the definition of a sufficient IM, note that it should theoretically include conditional (given IM) independence of DM not just from M and R, but from all influential parameters. For example, if near-source directivity effects are of concern, the definition of a sufficient IM should include conditional independence of DM from (in addition to M and R) the directivity parameter $X\cos\theta$ (or $Y\cos\phi$) introduced by Somerville *et al.* (1997b). With the building models and ground motions considered in Chapter 6, however, little evidence is encountered of a conditional (given any of the alternative IM's) dependence of DM on this directivity parameter alone (i.e., without also a dependence on M and/or R). More generally, the definition of sufficiency should at least include those parameters that are taken into account by attenuation relations for IM (e.g., faulting style, soil type, etc.). In the case of soil type, in lieu of demonstrating conditional independence of DM from soil type, the ground motions used to estimate $G_{DM|IM}$ may be (and are in Chapter 6) exclusively selected from those recorded on the same soil type as the designated site.

5.2.3 Computability of Ground Motion Hazard, λ_{IM}

Based on its efficiency and sufficiency alone, note that the ultimate IM is actually DM itself. Of course, directly computing λ_{DM} via PSHA (in place of λ_{IM} in Equation 5-1 for λ_{LS}) would require either a structure-specific attenuation relationship for DM or

extensive ground motion simulation (e.g., Collins *et al.* 1995, or as demonstrated in Chapter 7). In turn, both would call for NDA of the given structure under hundreds of ground motions from an array of *M*'s and *R*'s, which is impractical. This extreme alternative for *IM* emphasizes the need to bear in mind the computability of λ_{IM} in addition to the efficiency and the sufficiency of *IM* in selecting an appropriate intensity measure. Often there is a trade-off between the computability of λ_{IM} and the efficiency and sufficiency of *IM*. For example, $\lambda_{S_a(T_1)}$ is generally available (e.g., from the U.S. Geological Survey), or at least is readily computed (via PSHA), but $S_a(T_1)$ is not always efficient nor sufficient.

5.3 Shortcomings of $S_a(T_1)$ for PSDA Applications

As mentioned in the introduction to this chapter, the ground motion intensity measure customarily considered for computing λ_{LS} via PSDA is $S_a(T_1)$. Several studies (e.g., Shome *et al.* 1998) have demonstrated (e.g., for drift demand measures) that $S_a(T_1)$ is more "efficient" than peak ground acceleration (PGA), for example, presumably because $S_a(T_1)$ is period specific. Nonetheless, recent studies have also demonstrated that $S_a(T_1)$ may not be particularly efficient, nor "sufficient," for some structures (e.g., tall, long period buildings) (Shome & Cornell 1999) or for near-source ground motions.

5.3.1 For Near-Source Ground Motions

Under near-source ground motions, several studies (e.g., those cited in Chapter 1) have demonstrated that inelastic spectral displacements can be significantly larger (and more disperse) than their elastic counterparts, even at periods for which the (predominantly non-near-source ground motion based) "equal displacements rule" (Veletsos & Newmark 1960) is expected to apply. At least for an inelastic single-degree-of-freedom (SDOF) structure of moderate period, this implies that $S_a(T_1)$ may not be as efficient for near-source ground motions as it is for ordinary (i.e., non-near-source) ground motions, which tend to uphold the equal displacements rule. The difference between inelastic and elastic spectral displacements under near-source earthquake records depends roughly on the predominant period of the ground motion (Alavi & Krawinkler 2000). To the extent that this predominant period depends on *M* (Somerville 1998), $S_a(T_1)$ may also be insufficient for near-source ground motions. Furthermore, $S_a(T_1)$ may be insufficient inasmuch as *R* is a proxy for near-source ground motions. For nonlinear multi-degree-of-freedom (MDOF) structures, a few studies (Alavi & Krawinkler 2000,

Mehanny 1999) have demonstrated the inefficiency of $S_a(T_1)$ for near-source ground motions. In an attempt to gain efficiency for near-source ground motions, Deierlein *et al.* (i.e., Mehanny 1999, Cordova *et al.* 2000) have considered a scalar *IM* that combines $S_a(T_1)$ and $S_a(cT_1)$, where $c > 1$ in order to reflect "softening" of an inelastic structure.

5.3.2 For Tall, Long Period Buildings

For tall, long period buildings, the higher modes typically contribute significantly to the seismic inter-story drift response (at least in the elastic range). Thus, as one might expect, $S_a(T_1)$ has been observed to be less efficient (i.e., the variability of *DM* given $S_a(T_1)$ is larger) for tall, long period buildings than it is for a shorter building whose response is dominated by the fundamental mode (Shome & Cornell 1999, Cornell & Luco 1999). Moreover, for tall, long period buildings, $S_a(T_1)$ has been observed to be rather insufficient as well (i.e., given $S_a(T_1)$, *DM* still depends on *M*). Like the observed inefficiency, this insufficiency is presumably due to the fact that $S_a(T_1)$ does not reflect important higher-mode spectral accelerations, or spectral shape, which depends on *M* (e.g., Abrahamson & Silva 1997). Note, in addition, that for soft-soil or near-source ground motions with a predominant period near (for example) the second-mode period of the structure (i.e., T_2), the intensity measure $S_a(T_1)$ may prove particularly inefficient and insufficient. In order to gain efficiency and sufficiency when higher modes of response are important, Shome & Cornell (1999) and Bazzuro (1998) have considered a vector *IM* comprised of $S_a(T_1)$ and the ratio $S_a(T_2)/S_a(T_1)$, as well as a scalar *IM* that combines $S_a(T_1)$ and $S_a(T_2)$.

5.4 Alternative Ground Motion Intensity Measures

Motivated by the shortcomings of $S_a(T_1)$ reviewed above, several alternative *IM*'s that are each intended to be used in PSDA are introduced. All of the *IM*'s considered can be thought of as (multiplicative) modifications of $S_a(T_1)$, which serves as a basis for comparison. Most of the modifications are intended to reflect the contributions of higher modes or the effects of inelasticity on structural demands. Whereas the period-specific $S_a(T_1)$ requires only an estimate of T_1 (usually from an eigenvalue analysis) and an SDOF earthquake time-history analysis, the *IM*'s detailed here are more structure-specific. However, keeping in mind the computability of the ground motion hazard λ_{IM}, the space of possible *IM*'s is intentionally limited to measures that can be computed from only (i) modal vibration properties of the given model structure (e.g., T_1 and T_2), (ii) a nonlinear

static-pushover (NSP for short) curve for the model structure, and (iii) elastic or inelastic spectral displacements for the ground motion. Note that these are routinely attainable pieces of information about a structure and ground motions.

The *IM*'s introduced here are meant to be related to peak (over time) structural drift demands. Specifically, the *DM*'s considered are:

(i) θ_i, the peak i^{th} story drift angle (i.e., inter-story drift divided by story height)

(ii) θ_{ave}, the average (over the height of a building) peak story drift angle

(iii) $\theta_{\max}$, the maximum (over the height of a building) peak story drift angle

Although $\theta_{\max}$ is assumed to be the *DM* of interest in introducing the alternative *IM*'s, the same equations apply for the other *DM*'s considered as well. The differences among the *DM*'s are reflected in the modal participation factors, which are detailed in Section 5.4.8.

5.4.1 Elastic-First-Mode Ground Motion Intensity Measure, IM_{1E}

Inspired by modal analysis, the ground motion intensity measure IM_{1E} is simply the first-mode elastic estimate of $\theta_{\max}$. Like $S_a(T_1)$, IM_{1E} involves only the elastic first-mode vibration properties of the model structure and an SDOF time-history analysis for the ground motion. As expressed in Equation 5-2, IM_{1E} is the product of $|PF_1^{[1]}|$, the model structure's first-mode participation factor for $\theta_{\max}$ (refer to Section 5.4.8 for details), and $S_d(T_1,\zeta_1)$, the first-mode spectral displacement for the ground motion. Note that the damping ratio ζ_1 for the first mode is not necessarily equal to 5%, as assumed for $S_a(T_1)$.

$$IM_{1E} \quad = \quad |PF_1^{[1]}|\, S_d(T_1,\zeta_1) \qquad \tilde{\propto} \quad S_a(T_1) \tag{5-2}$$

Under the assumptions that (i) spectral displacement and acceleration are related by the period of interest (i.e., $S_d=(T/2\pi)^2 \cdot S_a$), and (ii) spectral accelerations for different damping ratios but the same period are proportional (which is a rough approximation), IM_{1E} is proportional to $S_a(T_1)$ and the two are equivalent in terms of efficiency and sufficiency. In what follows, IM_{1E} replaces $S_a(T_1)$ as the basis for comparison.

5.4.2 Inelastic-First-Mode Ground Motion Intensity Measure, IM_{1I}

Given that the *DM* of interest is nonlinear structural drift, it is logical to consider an inelastic spectral displacement as the intensity measure, particularly for near-source ground motions under which the effects of inelasticity on spectral displacements can be

substantial (as cited in Section 5.3). As expressed in Equation 5-3, IM_{1I} is the inelastic spectral displacement $S_d^I(T_1,\zeta_1,d_y)$ multiplied by the same first-mode participation factor for $\theta_{\max}$, $|PF_1^{[1]}|$, that is applied in Equation 5-2 for IM_{1E}. Also shown in Equation 5-3, IM_{1I} can be written as IM_{1E} multiplied by the ratio of $S_d^I(T_1,\zeta_1,d_y)$ to the corresponding elastic spectral displacement $S_d(T_1,\zeta_1)$.

$$IM_{1I} = |PF_1^{[1]}|\, S_d^I(T_1,\zeta_1,d_y) = \frac{S_d^I(T_1,\zeta_1,d_y)}{S_d(T_1,\zeta_1)}\, IM_{1E} \tag{5-3}$$

In Equation 5-3 and below, $S_d^I(T_1,\zeta_1,d_y)$ denotes the spectral displacement of an elastic-perfectly-plastic (EPP) oscillator with period T_1, damping ratio ζ_1, and yield-displacement d_y. As explained below in Section 5.4.9, d_y can be determined via a NSP of the model structure of interest.

5.4.3 Elastic-First-and-Second-Mode Ground Motion Intensity Measure, $IM_{1E\&2E}$

Whereas IM_{1E} and IM_{1I} reflect only the fundamental mode of structural response, the ground motion intensity measure $IM_{1E\&2E}$ is the estimate of $\theta_{\max}$ using the first two modes and the square-root-of-sum-of-squares (SRSS) rule of modal combination, as expressed in Equation 5-4. At least in the event of elastic response, $IM_{1E\&2E}$ is an improved estimate of $\theta_{\max}$ if higher modes contribute significantly to the structural response (e.g., for tall, long period structures).

$$\begin{aligned} IM_{1E\&2E} &= \sqrt{[PF_1^{[2]} S_d(T_1,\zeta_1)]^2 + [PF_2^{[2]} S_d(T_2,\zeta_2)]^2} \\ &= \sqrt{1+R_{2E/1E}^2}\left|\frac{PF_1^{[2]}}{PF_1^{[1]}}\right| IM_{1E} \quad \text{where } R_{2E/1E} = \frac{PF_2^{[2]} S_d(T_2,\zeta_2)}{PF_1^{[2]} S_d(T_1,\zeta_1)} \end{aligned} \tag{5-4}$$

Also noted in Equation 5-4, $IM_{1E\&2E}$ can be written as IM_{1E} multiplied by two modification factors: the first (i.e., the square root term) accounts for the (elastic) contribution of the second mode to $\theta_{\max}$ and thereby reflects the relevant spectral shape, whereas the second (i.e., the absolute value term) adjusts for the fact that the first-mode estimate and the first-two-modes estimate of $\theta_{\max}$ may correspond to different stories. Note that $PF_1^{[2]}$ denotes the first-mode participation factor for the story corresponding to

the first-two-mode SRSS estimate of $\theta_{\max}$, whereas $PF_1^{[1]}$ is that for the story corresponding to the first-mode estimate of $\theta_{\max}$. Refer to Section 5.4.8 for details.

5.4.4 Inelastic-First-Mode and Elastic-Second-Mode Ground Motion Intensity Measure, $IM_{1I\&2E}$

In an attempt to reflect both the contribution of the second mode (in addition to the first) and the effects of nonlinearity, the ground motion intensity measure $IM_{1I\&2E}$ is considered. As expressed in Equation 5-5, $IM_{1I\&2E}$ is equal to $IM_{1E\&2E}$ multiplied by the ratio of $S_d^I(T_1,\zeta_1,d_y)$ to $S_d(T_1,\zeta_1)$ (i.e., the same ratio of inelastic to elastic spectral displacements that is applied for IM_{1I} in Equation 5-3). Note that Equation 5-5 is slightly different than merely substituting $S_d^I(T_1,\zeta_1,d_y)$ for $S_d(T_1,\zeta_1)$ in the elastic SRSS modal combination expressed in Equation 5-4; this latter option was tested, but the efficiency and sufficiency of the intensity measure were found to be about the same in either case. Equation 5-5 for $IM_{1I\&2E}$ is preferred because, similar to Equation 5-4 for $IM_{1E\&2E}$, it can be written as IM_{1I} multiplied by two modification factors.

$$IM_{1I\&2E} = \frac{S_d^I(T_1,\zeta_1,d_y)}{S_d(T_1,\zeta_1)}\, IM_{1E\&2E} = \sqrt{1+R_{2E/1E}^2}\left|\frac{PF_1^{[2]}}{PF_1^{[1]}}\right| IM_{1I} \qquad (5\text{-}5)$$

Note that if $IM_{1I\&2E}$ is approximately equal to $\theta_{\max}$, for example, then Equation 5-5 indicates that the ratio of nonlinear to elastic MDOF drift response (i.e., $\theta_{\max}/IM_{1E\&2E}$) is approximately equal to the ratio of $S_d^I(T_1,\zeta_1,d_y)$ to $S_d(T_1,\zeta_1)$.

5.4.5 "Equivalent"-First-Mode Ground Motion Intensity Measure, IM_{1eq}

To avoid inelastic SDOF time-history analysis, the inelastic spectral displacement required for IM_{1I} and $IM_{1I\&2E}$ can be replaced by the spectral displacement of an "equivalent" elastic SDOF oscillator, denoted $S_d^{eq}(T_1,\zeta_1,d_y)$. Doing so for IM_{1I} results in the ground motion intensity measure IM_{1eq}, as expressed in Equation 5-6.

$$IM_{1eq} = |PF_1^{[1]}|\, S_d^{eq}(T_1,\zeta_1,d_y) = \frac{S_d^{eq}(T_1,\zeta_1,d_y)}{S_d(T_1,\zeta_1)}\, IM_{1E} \qquad (5\text{-}6)$$

The period and damping of the equivalent elastic oscillator can be (and are in Chapter 6) established using the empirical formulas developed by Iwan (1980). These formulas are functions of ductility, which can be approximated by $S_d(T_1,\zeta_1)/d_y$. Alternatively, the period and damping of the equivalent elastic oscillator could be established by a procedure resembling the Capacity Spectrum Method (Freeman *et al.* 1975), for example.

5.4.6 "Effective"-First-Mode Ground Motion Intensity Measure, IM_{1eff}

Another *IM* that attempts to capture the effects of inelasticity by considering the elastic spectrum at an "effective" period longer than T_1 (reflecting a reduction in stiffness) has been proposed by Deierlein *et al.* (i.e., Mehanny 1999, Cordova *et al.* 2000). As noted at the far right of Equation 5-7, the proposed *IM* is a function of both $S_a(T_1)$ and $S_a(cT_1)$, where $c > 1$. By optimizing the efficiency of the proposed *IM* for a specific set of model structures and earthquake records, Cordova *et al.* (2000) have calibrated c and α to equal 2 and 1/2, respectively.

$$IM_{1eff} = \sqrt{\frac{S_d(2T_1,\zeta_1)}{2S_d(T_1,\zeta_1)}}\ IM_{1E} \quad \tilde{\propto} \quad S_a(T_1)\left[\frac{S_a(cT_1)}{S_a(T_1)}\right]^{\alpha} \text{ where } c = 2\,,\ \alpha = \frac{1}{2} \qquad (5\text{-}7)$$

Also expressed in Equation 5-7, IM_{1eff} is approximately (because ζ_1 may be different than 5%, and S_a and $(2\pi/T)^2 \cdot S_d$ are only approximately equal) proportional to the ground motion intensity measure proposed by Deierlein *et al.*, but is formulated here as a modification of IM_{1E} that involves only spectral displacements. Note that the factor of 2 introduced in front of $S_d(T_1,\zeta_1)$ renders the modification factor equal to one if spectral displacement increases proportionally with period (i.e., as it would in the "constant-velocity" realm of a spectrum).

5.4.7 Vector-Valued Ground Motion Intensity Measures

It should be noted that the basic components of the scalar modifications of $S_a(T_1)$ introduced above (e.g., $S_d^I(T_1,\zeta_1,d_y)/S_d(T_1,\zeta_1)$ and $S_a(T_1)$ for IM_{1I}) could instead be considered as separate elements of a vector-valued *IM*. Employing a vector-valued *IM*, however, requires certain extensions to conventional PSHA (Bazzurro & Cornell 2002). Moreover, the scalar *IM*'s considered here are easier to interpret, particularly because their units are the same as those for the *DM* of interest, namely radians for drift angles such as $\theta_{\max}$.

5.4.8 Definition of Participation Factors

The participation factors $PF_j^{[k]}$, where $1 \le j \le k$, that are used in calculating the alternative *IM*'s introduced above are defined here. First, recall that θ_i denotes the peak drift angle for the ith story of a building model subjected to a particular earthquake ground motion record. The jth–mode participation factor for θ_i is defined here as

$$PF_j(\theta_i) = \Gamma_j \frac{\phi_{j,i} - \phi_{j,i-1}}{h_i} \tag{5-8}$$

where $\phi_{j,i}$ is the element of the jth modal vector that corresponds to the upper floor of the ith story (i.e., the ith floor), and h_i is the height of the ith story (in the same units used for spectral displacement). Γ_j, which is also commonly referred to as a participation factor, is given (Chopra 1995) by

$$\Gamma_j = \frac{\sum_{i=1:n} \phi_{j,i} m_i}{\sum_{i=1:n} \phi_{j,i}^2 m_i} \tag{5-9}$$

where n is the total number of stories (or floors) in the building model and m_i is the mass of the ith floor.

Averaging the absolute values of $PF_j(\theta_i)$ from Equation 5-8 over the n stories of a building, the jth–mode participation factor for θ_{ave} is defined as

$$PF_j(\theta_{\text{ave}}) = \frac{\Gamma_j}{n} \sum_{i=1:n} \frac{|\phi_{j,i} - \phi_{j,i-1}|}{h_i} \tag{5-10}$$

Note that $PF_j(\theta_i)$ and $PF_j(\theta_{\text{ave}})$ are abbreviated as $PF_j^{[k]}$ in Equations 5-2 to 5-7 for the alternative *IM*'s. As described next, however, only the participation factor for $\theta_{\max}$ depends on k (the number of modes considered).

With $PF_j(\theta_i)$ defined according to Equation 5-8, the (elastic) SRSS estimate of θ_i using the first k modes is expressed as

$$\theta_i^{[k]} = \sqrt{\sum_{j=1:k} [PF_j(\theta_i) \cdot S_d(T_j, \zeta_j)]^2} \tag{5-11}$$

where $S_d(T_j,\zeta_j)$ is the spectral displacement of the SDOF oscillator that represents the jth mode. For a specified k, the largest $\theta_i^{[k]}$ (among all the stories, i=1:n) is adopted here as the SRSS estimate of $\theta_{\max}$, denoted $\theta_{\max}^{[k]}$. Clearly, $\theta_{\max}^{[k]}$ corresponds to a particular story, denoted $i^{[k]}$ (which, incidentally, does not necessarily match the story corresponding to the observed $\theta_{\max}$). Associated with story $i^{[k]}$ are the participation factors $PF_j(\theta_{\max}^{[k]})$, which are formally defined in Equation 5-12.

$$PF_j(\theta_{\max}^{[k]}) = PF_j(\theta_{i^{[k]}}) \qquad \text{where} \qquad i^{[k]} = \arg\max_{i=1:n} \theta_i^{[k]} \tag{5-12}$$

Note that with k>1, $PF_j(\theta_{\max}^{[k]})$ is different for different earthquake records, as it depends on the values of $S_d(T_j,\zeta_j)$ for each of the k modes (or in other words, the spectral shape). With k=1, on the other hand, Equation 5-12 simplifies to

$$PF_j(\theta_{\max}^{[1]}) = \Gamma_j \max_{i=1:n}\left[\frac{\phi_{j,i} - \phi_{j,i-1}}{h_i}\right] \tag{5-13}$$

which is independent of the earthquake record. Finally, note that $PF_j(\theta_{\max}^{[k]})$ is abbreviated as $PF_j^{[k]}$ in Equations 5-2 to 5-7 for the alternative *IM*'s.

5.4.9 Definition of Yield Displacement

As mentioned above, the yield displacement d_y in $S_d^I(T_1,\zeta_1,d_y)$ or $S_d^{eq}(T_1,\zeta_1,d_y)$, which are used in calculating IM_{1I} and $IM_{1I\&2E}$ or IM_{1eq} (respectively), can be determined via a NSP (nonlinear static-pushover) of the model structure under consideration. The approach is described here generally, but is illustrated in Figure 5-1 for the "LA9" building model (detailed in Chapter 6).

Since d_y is the yield displacement of an SDOF oscillator that represents the first mode of the model structure (i.e., T_1 and ζ_1), a "first-mode lateral load pattern" is applied during the NSP conducted to estimate d_y. A first-mode load pattern is that which, in the elastic range, results in the first-mode deflected shape of the model structure. Derived from (elastic) modal analysis, the first-mode lateral load applied at the ith floor of a building model, denoted F_i, is given by

$$F_i = \frac{m_i\phi_{1,i}}{\sum_{i=1:n} m_i\phi_{1,i}} V_b \tag{5-14}$$

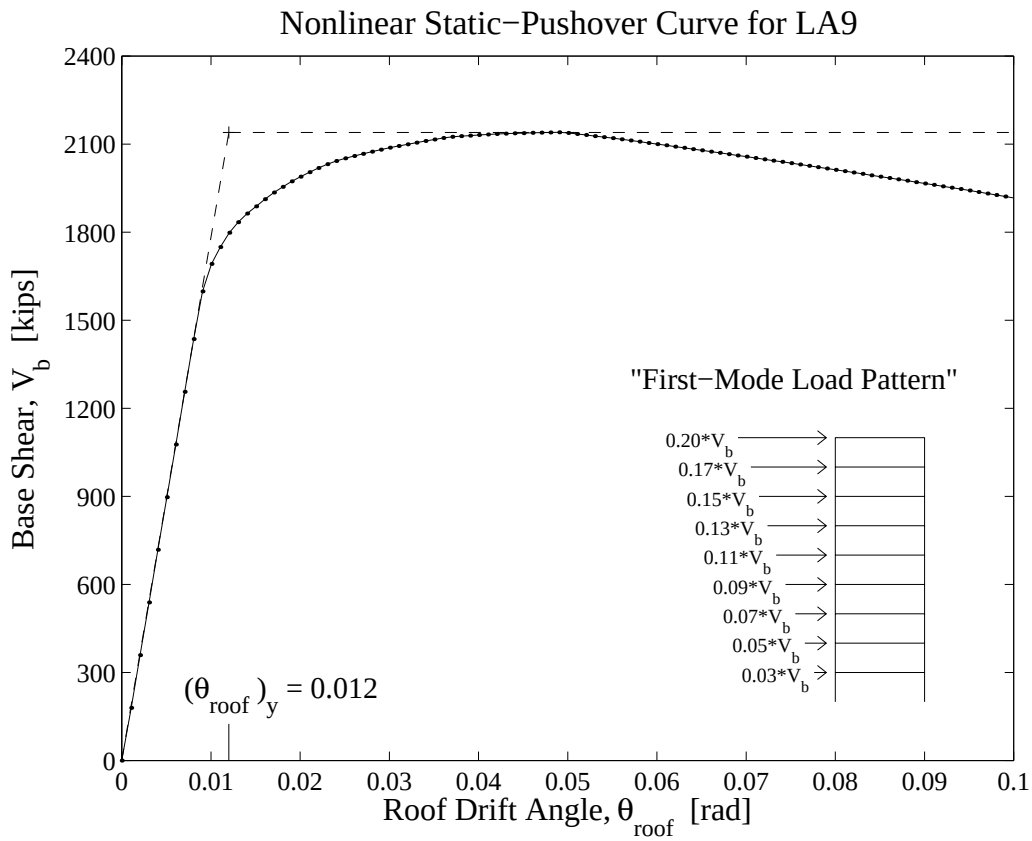

Figure 5-1. Illustration of procedure for estimating d_y via NSP.

where m_i, $\phi_{1,i}$, and n are defined in the previous subsection for Equations 5-8 and 5-9, and V_b is the base shear (i.e., sum of F_i for i=1:n).

For $S_d^I(T_1,\zeta_1,d_y)$, an EPP idealization of the V_b versus θ_{roof} (i.e, roof drift angle) curve resulting from the NSP of the building model (i.e., applying the first-mode lateral load pattern defined by F_i) is used to estimate d_y. The elastic slope of the bilinear depiction follows the elastic points of the NSP curve (which, by the way, can be used to establish T_1 because a first-mode load pattern is applied). The perfectly-plastic slope passes through the peak V_b on the NSP curve (e.g., for θ_{roof} between 0 and 0.10). The intersection of the two lines provides an estimate of $(\theta_{\text{roof}})_y$, the yield displacement in θ_{roof} terms. This yield displacement is translated to d_y according to elastic modal analysis by

$$d_y = \frac{(\theta_{\text{roof}})_y}{\Gamma_1 \dfrac{\phi_{1,n}}{\sum_{i=1:n} h_i}} \tag{5-15}$$

where Γ_1, $\phi_{1,n}$, and h_i are defined in the previous subsection for Equation 5-8. Note that the denominator in Equation 5-15 is equal to the first-mode participation factor for θ_{roof}. For the example illustrated in Figure 5-1, the values of d_y estimated by the above approach is 33cm.

As demonstrated briefly in Chapter 6, instead of an EPP idealization of the NSP curve, a bilinear (e.g., with negative strain-hardening) or trilinear backbone can be fit instead. In any case, Equation 5-15 is used to translate the transition points in θ_{roof} terms to the appropriate spectral displacement value. Note that for the transition point between the second and third segments of a trilinear model, elastic modal analysis assumptions do not hold; potential implications of this discrepancy are discussed in Chapter 6.

5.5 Approach for Quantifying the Efficiency and Sufficiency of an *IM*

Recall that $G_{DM|IM}$ in Equation 5-1 for λ_{LS} is normally estimated for a given structure using *DM* results from NDA under a suite of earthquake ground motions. Specifically, $G_{DM|IM}$ can be estimated via a regression of the *DM* results on the corresponding values of *IM*, together with an assumed type of probability distribution for *DM* given *IM*; this approach was demonstrated in Chapter 3. In this case, the efficiency of *IM* is gauged by the degree of scatter about the regression fit (of *DM* on *IM*), whereas the sufficiency of *IM* is gauged by the extent to which, after regressing on *IM*, the residual *DM* is statistically independent of *M* and *R*. In short, like $G_{DM|IM}$, the efficiency and sufficiency of an *IM* can be quantified via regression analysis.

For most of the results presented in Chapter 6, a one-parameter log-log linear regression of *DM* (specifically θ_i, θ_{ave}, or θ_{max}) on *IM* is utilized in assessing the efficiency and sufficiency of each alternative *IM*. The regression model is expressed in Equation 5-16, where *a* is the parameter (or coefficient) to be estimated and $\varepsilon_{DM|IM}$ is the (random) error in *DM* given *IM*.

$$DM = a \cdot IM \cdot (\varepsilon_{DM|IM}) \Leftrightarrow \ln(DM / IM) = \ln(a) + \ln(\varepsilon_{DM|IM}) \tag{5-16}$$

Note that a log-log scale is employed primarily because with it the variability of *DM* given *IM* is observed to be roughly uniform over the range of *IM* values (here and in (Shome & Cornell 1999), for example). In other words, it is anticipated that the standard deviation of $\ln(\varepsilon_{DM|IM})$, hereafter denoted simply as σ, will be approximately constant, which is an assumption of standard linear regression analysis (i.e., homoscedasticity). Furthermore, $\ln(\varepsilon_{DM|IM})$ (or *DM* given *IM*) is observed to be approximately lognormally distributed, so the log-log scale makes it possible to take advantage of normality assumptions (e.g., in quantifying the statistical significance of differences among estimates of *a* and of σ).

The one-parameter model expressed in Equation 5-16 is utilized instead of the standard two-parameter log-log linear regression model used in Chapter 3 (which includes an exponent on *IM*) for several reasons. In general, for peak drift angles from 0% to 10%, the one-parameter model is observed in Chapter 6 to be adequate for regressing *DM* on each of the alternative *IM*'s investigated. That is, the nonlinear regression model employing an exponent on *IM* is generally not necessary, except for some cases in which the simple intensity measure IM_{1E} is employed. For these cases, the two-parameter model used in Chapter 3 is also considered in Chapter 6. In contrast to the two-parameter model, the one-parameter model is attractive in that the coefficient *a* can be interpreted as the bias of *IM* in estimating *DM*. Moreover, the one-parameter regression analysis amounts to merely calculating the "median" (strictly the geometric mean, or the exponential of the mean of the natural logarithm) of the ratio *DM*/*IM* as the least-squares estimate of *a*, and the "dispersion" (strictly the standard deviation of the natural logarithm) of *DM*/*IM* in order to estimate σ.

As alluded to above, σ (i.e., the dispersion of *DM* given *IM*) serves as a measure of the efficiency of *IM* (regardless of the regression model). This is because, based on the simplest notions of statistics, σ is directly related to the number of earthquake records and NDA's, denoted *n*, that is necessary to estimate *a* with adequate precision (e.g., $\sigma_{\ln(a)} \leq 0.10$). This relationship is expressed in Equation 5-17 (e.g., Benjamin & Cornell 1970). Note that $\sigma_{\ln(a)}$ is actually the dispersion *of the regression estimate* of *a*, which could more formally be denoted as $\sigma_{\ln(\hat{a})}$.

$$n = (\sigma / \sigma_{\ln(a)})^2 \tag{5-17}$$

According to Equation 5-17, if a particular choice of one *IM* over another reduces σ from, for example, 0.3 to 0.2, then *n* will be roughly halved, doubling the efficiency.

Using the one-parameter regression model expressed in Equation 5-16 also simplifies the procedure for quantifying the sufficiency of *IM*. Generally, *IM* can be regarded as sufficient if the coefficients on *M* and *R* estimated from a regression of *DM* on *IM*, *M*, and *R* are not statistically significant; here and in Chapter 6, this condition is simplified (in an approximate way) by considering *M* and *R one at a time*. Beginning with the one-parameter model for the regression of *DM* on *IM*, a regression of *DM* on *IM* and *M* (or *R*) can be accomplished with a standard univariate linear regression (i.e., $y = \beta_0 + \beta_1 x + \varepsilon$), as expressed in Equations 5-18a (or 5-18b). Similar to the notation used in Equation 5-16 above, *a'* and *c* are the regression parameters to be estimated and $\varepsilon_{DM|(IM,M)}$ (or $\varepsilon_{DM|(IM,R)}$) is the random error in *DM* given *IM* and *M* (or *R*). Note that the assumed log-linear dependencies on *M* and on ln(*R*) are consistent with the first order terms in standard attenuation relations (e.g., Abrahamson & Silva 1997).

$$\ln(DM / IM) = \ln a' + c \cdot M + \ln \varepsilon_{DM|(IM,M)} \tag{5-18a}$$

$$\ln(DM / IM) = \ln a' + c \cdot \ln R + \ln \varepsilon_{DM|(IM,R)} \tag{5-18b}$$

According to the one-parameter regression model expressed in Equation 5-16, ln(*DM*/*IM*) is within a constant of $\ln(\varepsilon_{DM|IM})$, hence Equations 5-18a and 5-18b can be rewritten as Equations 5-19a and 5-19b, respectively.

$$\ln \varepsilon_{DM|IM} = \ln a'' + c \cdot M + \ln \varepsilon_{DM|(IM,M)} \tag{5-19a}$$

$$\ln \varepsilon_{DM|IM} = \ln a'' + c \cdot \ln R + \ln \varepsilon_{DM|(IM,R)} \tag{5-19b}$$

Equations 5-19a and 5-19b reveal that the coefficient *c* on *M* or ln(*R*) can conveniently be estimated via a standard linear regression of the observed values of $\ln(\varepsilon_{DM|IM})$ (i.e., the "residuals") on the corresponding values of *M* or ln(*R*). These equations are only valid, though, if the one-parameter model expressed in Equation 5-16 is adopted for regressing *DM* on *IM*. Otherwise, $\ln(\varepsilon_{DM|IM})$ must be regressed on the residuals from an additional regression of *M* or ln(*R*) on *IM*.

The statistical significance of the regression estimate of the coefficient *c* on *M* or ln(*R*), and thereby the sufficiency of *IM*, can be quantified by the *p*–value for the *c* estimate (which is commonly reported by linear regression software). The *p*–value is

defined as the probability of finding an estimate of c at least as large (in absolute value) as that observed if, in fact, the true value of c is 0 (e.g., Benjamin & Cornell 1970). Hence, a small p–value (e.g., less than about 0.05) suggests that the estimated coefficient c on M or $\ln(R)$ is statistically significant, and therefore that IM is insufficient.

5.6 Other PSDA-Based Approaches for Computing λ_{LS} Accurately

In order to accurately estimate λ_{LS} even if IM is insufficient and a limited number of earthquake records are used to estimate $G_{DM|IM}$, the dependence on M and R can be accounted for explicitly. Analogous to Equation 5-1, λ_{LS} can be expressed as an application of the total probability theorem that integrates over not only DM and IM, but over M and R as well, as in Equation 5-20.

$$\lambda_{LS} = \int_{DM}\int_{IM}\int_{M}\int_{R} G_{LS|DM} \,|\, \mathrm{d}G_{DM|(IM,M,R)} \,|\,|\, \mathrm{d}G_{(M,R)|IM} \,|\,|\, \mathrm{d}\lambda_{IM} \,| \tag{5-20}$$

Also analogous to Equation 5-1, note that $G_{LS|DM}$ replaces $G_{LS|(DM,IM,M,R)}$ because the latter is presumed to be functionally independent of IM, M, and R since LS is normally defined in terms of DM only. Unlike Equation 5-1, Equation 5-20 for λ_{LS} is expected to be accurate regardless of whether or not IM is sufficient, and regardless of which earthquake records are selected to estimate $G_{DM|(IM,M,R)}$ (Shome & Cornell 1999).[1] Clearly this accuracy comes at the expense of having to integrate, over M and R, the product of (i) $G_{DM|(IM,M,R)}$, which calls for, in its estimation, a multidimensional regression of DM on IM, M, and R, and (ii) $\mathrm{d}G_{(M,R)|IM}$, which is the result of a disaggregation of λ_{IM} for each value of IM (Bazzurro & Cornell 1999). It should be noted that $\mathrm{d}G_{(M,R)|IM}$ is a site-dependent distribution; that is, different events (i.e., M's and R's) typically dominate the IM hazard (i.e., λ_{IM}) at different sites. If IM is sufficient, however, by definition $\mathrm{d}G_{(M,R)|IM}$ is functionally independent of M and R and hence Equation 5-20 simplifies to Equation 5-1 while maintaining its accuracy.

Although it has been affirmed that a sufficient IM ensures the accuracy of Equation 5-1 for λ_{LS}, employing a sufficient IM is not the only way to achieve this accuracy; two other means are discussed briefly here. As mentioned above, the conditional (on IM) distribution of the M's and R's of the earthquake records selected to estimate $G_{DM|IM}$ may match (closely enough) the distribution that appears naturally at the site, namely

[1] Essentially, it is assumed that computing λ_{LS} via PSHA, although impractical, is accurate.

$\mathrm{d}G_{(M,R)|IM}$. Using (to estimate $G_{DM|IM}$) a suite of earthquake records that is consistent with $\mathrm{d}G_{(M,R)|IM}$ has the effect of carrying out the integration over *M* and *R* in Equation 5-20, thereby resulting in an accurate estimate of λ_{LS} with Equation 5-1 even if *IM* is insufficient. In practice, though, it would be very difficult to select a suite of earthquake records that is consistent with $\mathrm{d}G_{(M,R)|IM}$ unless the same events dominate the hazard at all *IM* levels. When the suite of earthquake records used to estimate $G_{DM|IM}$ is *not* consistent with $\mathrm{d}G_{(M,R)|IM}$, a weighted regression of *DM* on *IM* that adjusts (approximately) for this inconsistency can be conducted in order to estimate $G_{DM|IM}$. Such a scheme has been applied by Shome & Cornell (1999, pg. 208) and Bazzurro (1998, pg. 285) in order to adjust for the conditional distribution of $S_a(T_2)$ given $S_a(T_1)$; the same approach can be followed for *M* (or *R*) given *IM*. This weighted regression scheme also has the effect of carrying out the integration over *M* and *R* in Equation 5-20; thus, it also results in an accurate estimate of λ_{LS} with Equation 5-1 even if *IM* is insufficient. Note that among all of the alternatives discussed for estimating λ_{LS} with confident accuracy, only the use of a sufficient *IM* manages to do so without concern about the nature of the site seismicity (i.e., $\mathrm{d}G_{(M,R)|IM}$ from disaggregation of λ_{IM}).

5.7 Summary

Although PSDA can be modified to ensure it accuracy with any ground motion intensity measure (as explained in the preceding section), two criteria for the *IM* employed in PSDA are defined in this chapter that together ensure the accuracy of PSDA using relatively few nonlinear dynamic analyses (NDA's) of the given structure. Referred to as the "efficiency" and "sufficiency" of an *IM*, these two criteria can be used to objectively compare alternative intensity measures, as will be demonstrated in Chapter 6. In this chapter, an approach for quantifying these two criteria is detailed. Like PSDA itself, the efficiency and sufficiency of an *IM* can be quantified via (i) nonlinear dynamic analysis of the structure under a suite of earthquake records, and (ii) linear regression analysis. Of course, the computability of the ground motion hazard at a site in terms of a candidate *IM* is also an important consideration.

Motivated by the shortcomings of traditional intensity measures like $S_a(T_1)$, several new scalar *IM*'s are introduced in this chapter that are each meant to ensure the accuracy of PSDA at near-fault (and "ordinary") sites using relatively few NDA's of the structure. All of these new *IM*'s can be written as multiplicative modifications of $S_a(T_1)$ that take into account the contribution of the second mode to the response of a structure and/or the

effects of inelasticity. Keeping in mind that PSDA makes use of the ground motion hazard at a site expressed in terms of *IM*, the space of alternative *IM*'s is intentionally limited to measures that can be computed from only (i) modal vibration properties of the given model structure, (ii) a nonlinear static-pushover curve for the model structure, and (iii) elastic or inelastic spectral displacements for the ground motion. The efficiency and sufficiency of these alternative *IM*'s relative to $S_a(T_1)$ is evaluated in the following chapter.

Chapter 6

Evaluation of Alternative Intensity Measures for Near-Source and Ordinary Earthquake Ground Motions

6.1 Introduction

In Chapter 5, several criteria are identified for evaluating alternative ground motion intensity measures (*IM*'s) that are each intended to be used in a performance assessment (i.e., PSDA) for a structure at a site susceptible to near-source and/or ordinary ground motions. In particular, the "efficiency" and "sufficiency" of an *IM* are defined. An efficient *IM* is defined simply (from the perspective of a structural engineer) as one that results in a relatively small variability of structural demand given the level of ground motion (i.e., *IM*). The primary advantage of an efficient *IM* is that it reduces the number of NDA's (nonlinear dynamic analyses) and earthquake records necessary to estimate, with adequate precision, the conditional distribution of structural demand given *IM* that is pivotal to PSDA. A sufficient *IM*, on the other hand, is defined as one that renders structural demand conditionally independent, given *IM*, of earthquake magnitude and source-to-site distance. As explained in detail in Chapter 5, a sufficient *IM* is desirable because it ensures the accuracy of the PSDA integral (i.e., Equation 1-1). A third criterion deserving of consideration is the computability of the seismic hazard at a site in terms of *IM*. For the conventional *IM* of spectral acceleration, for example, a seismic hazard curve at a site is often available from the U.S. Geological Survey.

Also in Chapter 5, several alternative (e.g., to the conventional spectral acceleration) ground motion intensity measures are introduced that are meant to ensure the accuracy (and precision) of the PSDA approach at near-fault sites. In this chapter, the efficiency and sufficiency of each of these alternative *IM*'s is quantified (using the approach outlined in Chapter 5) with respect to the structural drift demands for each of three different SMRF building models under a suite of near-source and a suite of ordinary earthquake records. The SMRF building models considered are ductile representations of both the exterior MRF and interior gravity frames of the SAC buildings designed for Los Angeles conditions. The near-source and ordinary suites of earthquake records are compiled from the PEER Strong Motion Database (Silva 1999). Note that parts of this chapter are included in an article that is currently being revised for publication in *Earthquake Spectra* (Luco & Cornell 2002).

6.2 Earthquake Ground Motion Records

Both ordinary and near-source earthquake ground motion records (described in more detail in Appendix A) are considered in this chapter. The suite of ordinary earthquake records consists of ground motions with closest distances to the rupture surface (i.e., R) between 30 and 46 kilometers. The suite of near-source earthquake records, on the other hand, is restricted to ground motions with R less than 16 kilometers, motivated by the SEAOC Blue Book (1999). Furthermore, the near-source suite is restricted to "forward-directivity" earthquake records, whereas the ordinary suite excludes such earthquake records. Here a forward-directivity earthquake record is defined as one for which the rupture directivity modification factor for average $S_a(T)$, developed by Somerville *et al.* (1997a), is greater than one (at T = 1, 2, *and* 4 seconds, which are near the T_1's of the three building models considered). Because forward-directivity is generally manifested as a "pulse-like" ground motion perpendicular to the fault, the strike-normal component of each of the near-source earthquake records is considered. Likewise, in order to be consistent, the strike-normal components of the ordinary earthquake records are considered.

The ordinary and near-source suites of earthquake records are selected from the PEER Strong Motion Database (Silva 1999). In addition to the constraints based on R and forward-directivity, all of the earthquake records selected also satisfy the following criteria: (i) earthquake moment magnitude (i.e., M) greater than or equal to 6.0 (and less than or equal to 7.4), (ii) recorded on "stiff soil" or "very dense soil and soft rock" (e.g.,

FEMA 273 (1997) site classes D or C, respectively), and (iii) processed record with a maximum (between two horizontal components) high-pass filter corner-frequency less than or equal to 0.25 hertz.[1] Listed in Appendix A, the 31 near-source earthquake records selected are from the Imperial Valley earthquake of 1979, the Superstition Hills earthquake of 1987, the Northridge earthquake of 1994, and the Loma Prieta earthquake of 1989. It is interesting to note that not all of these near-source earthquake records are clearly "pulse-like" (a subjective description), even though they are (objectively) identified as "forward-directivity" ground motions with R<16km. The 59 earthquake records selected for the ordinary suite are also listed in Appendix A. Note that a 60th ordinary earthquake record (from the Coalinga earthquake of 1983, station code H-C04) that meets the criteria above is excluded for reasons discussed in Section 6.4.1. Additional near-source and ordinary ground motions from the recent (1999) large magnitude (M>7) earthquakes in Taiwan (Chi-Chi) and Turkey (Duzce and Kocaeli) have not yet been included.

To augment the near-source suite, 6 additional "pulse-like" earthquake records from Somerville *et al.* (1997b, 1998) via Alavi & Krawinkler (2000) are also considered (again refer to Appendix A for a list). These supplemental ground motions were not originally recorded on "stiff soil" or "very dense soil and soft rock," but most of them were modified by Somerville *et al.* to reflect stiff soil conditions. Due to this difference, the results for the 6 supplemental pulse-like earthquake records are considered separately. Note that another 6 of the 15 pulse-like earthquake records considered by Alavi & Krawinkler are among the 31 in the near-source suite.

In order to investigate higher levels of nonlinear response, the near-source earthquake records considered are scaled as a suite (i.e., all earthquake records scaled by the same constant) by a factor of two. Correspondingly, the ordinary earthquake records are scaled as a suite by a factor of eight. This factor is chosen such that the "1-sigma level" (refer back to Chapter 2 for a definition) elastic spectral displacements at the fundamental periods and damping ratios of the three building models (described in the next section) are approximately the same for the ordinary and near-source earthquake records.

[1] As detailed in Appendix A, the high-pass filter corner-frequency is greater than 0.15 hertz for only 10% or so of the near-source earthquake records, but about 75% of the ordinary earthquake records.

6.3 Building Models

The structures considered in this chapter (as well as in Chapters 2 and 3) are the 3-story, 9-story, and 20-story steel moment-resisting frame (SMRF) buildings designed for Los Angeles conditions by consulting structural engineers as part of the SAC Steel Project (Phase II). The designs were carried out according to pre-Northridge earthquake practices (i.e., 1994 Uniform Building Code). Only the perimeter frames of each building are moment resisting; the interior frames are intended to support gravity loads only. Detailed descriptions of the SAC buildings can be found in Appendix B and in FEMA 355C (2000).

Under the assumption of a rigid diaphragm, a two-dimensional centerline model of each of the three (relatively symmetric) buildings is created for nonlinear analysis using DRAIN-2DX (Prakash *et al.* 1993). Unlike the "M1" analysis models considered in Chapters 2-4, here each model accounts for both the perimeter MRF's and the interior gravity frames. The nonlinear analyses take into account *P*-Δ effects, *M-P* interaction, and plastic hinging (with 3% strain hardening) at beam-ends, column-ends, and column-splices; the connections are modeled as ductile, akin to post-Northridge connection design. Rather than modeling the shear connections (e.g., in the gravity frames) as "pins," they are each attributed stiffness and strength properties reasonably close to those observed in laboratory tests carried out by Liu & Astaneh-Asl (2000). The analysis models considered in this chapter are similar to the "M1+" models in Chapter 2, except that a full interior gravity frame is modeled rather than an equivalent frame. Refer to Appendix B for more details.

The periods and damping ratios for the first two modes of each of the three buildings models, as well as the yield displacement d_y associated with the first mode (as defined in Chapter 5), are listed in Table 6-1.

Table 6-1. First- and second-mode properties of the three SMRF building models.

Building model	First mode			Second mode	
	T_1 (sec)	ζ_1	d_y (cm)	T_2 (sec)	ζ_2
LA3	0.98	0.020	12	0.30	0.016
LA9	2.23	0.020	33	0.82	0.011
LA20	3.96	0.021	41	1.35	0.012

Along with the participation factors (described in detail in Chapter 5), the information in Table 6-1 is used to calculate the *IM*'s introduced above. For convenience in calculating the *IM*'s, however, the damping ratios ζ_1 and ζ_2 are set equal to 0.02 for all three building models. Note that for brevity, the Los Angeles 3-, 9-, and 20-story building models are hereafter referred to as LA3, LA9, and LA20.

6.4 Results with Respect to $\theta_{\max}$

Using the regression analysis approach detailed in Chapter 5, here the efficiency and sufficiency (as well as the bias) of each of the *IM*'s investigated are quantified with respect to $\theta_{\max}$, the maximum peak story drift angle. First, pair-wise comparisons of the alternative *IM*'s are made for the most pertinent building model (i.e., LA3, LA9, or LA20) and suite(s) of earthquake records (i.e., ordinary and/or near-source). For the first few pair-wise *IM* comparisons, the regression of $\theta_{\max}$ on *IM* is illustrated with a figure. The figure depicts the data and the regression fit, and lists the regression estimates for the coefficient *a* and for σ; the number of data points, *n*, is also listed. Although $\theta_{\max}$ is the dependent variable in the regression of $\theta_{\max}$ on *IM*, it is plotted as the abscissa, as per a traditional force (in this case *IM*) versus deformation (here $\theta_{\max}$) plot. Recall that *a* is a measure of the bias of the ground motion intensity measure *IM* in estimating $\theta_{\max}$, and σ is a measure of the efficiency of *IM*. The regression of the observed $\varepsilon_{\theta_{\max}|IM}$ residuals (also denoted as $\varepsilon|IM$) on *M* or *R*, which is conducted in order to measure the sufficiency of *IM*, is also illustrated with a figure. Noted in the figure are the regression estimate of the coefficient *c*, the *p*–value for the estimate of *c*, and the regression estimate of the variability of $\varepsilon_{\theta_{\max}|(IM,M)}$ or $\varepsilon_{\theta_{\max}|(IM,R)}$ (also denoted simply as σ). Recall that a small *p*–value (e.g., less than about 0.05) suggests that the estimated coefficient *c* on *M* or *R* is statistically significant and hence that *IM* is insufficient. In all of the figures, each of the $\theta_{\max}$ versus *IM* data points is plotted as the number (within a circle) of the story in which $\theta_{\max}$ occurs. In addition to the pair-wise *IM* comparisons, the regression analysis results for the "primary" intensity measures IM_{1E}, IM_{1I}, $IM_{1E\&2E}$, and $IM_{1I\&2E}$ are summarized in a table for every combination of the three building models and two suites of earthquake records.

6.4.1 $IM_{1E\&2E}$ vs. IM_{1E} for LA20 under Ordinary Ground Motions

As cited in Chapter 5, recent studies have demonstrated that $S_a(T_1)$, or equivalently IM_{1E}, can be relatively inefficient and insufficient when considering tall, long period

building models for which higher modes contribute significantly to the response (at least in the elastic range). This shortcoming of IM_{1E}, as well as the relative efficiency and sufficiency of $IM_{1E\&2E}$ (which accounts for the second mode), are demonstrated here with the LA20 building model subjected to the ordinary earthquake records. First, as a basis of comparison, the regression analysis results assuming elastic building response are presented for IM_{1E}, $IM_{1E\&2E}$, and $IM_{1E\&2E\&3E}$ (i.e., an SRSS of the first three elastic modes). In effect, these elastic results are merely a check of the SRSS rule of modal combination. Subsequently, the inelastic (i.e., ductile) response of the building model is considered. Note that in the inelastic case, 2 of the 59 ordinary earthquake records (which, recall, have been scaled up by a factor of 8) are excluded because they cause "collapse" of the LA20 building model.

6.4.1.1 Assuming Elastic Building Response

The regression analysis results for the LA20 building model subjected to the ordinary earthquake records, assuming elastic building response, are summarized in Table 6-2. As expected, the larger the number of elastic modes that are taken into account by the ground motion intensity measure (e.g., $IM_{1E\&2E}$ versus IM_{1E}), the less biased (i.e., smaller a) and more efficient (i.e. smaller σ) is the IM. Moreover, only when the second mode is taken into account (i.e., $IM_{1E\&2E}$ or $IM_{1E\&2E\&3E}$) is the ground motion intensity measure sufficient (i.e., p–value>0.05) with respect to both M and R. An explanation of the insufficiency of IM_{1E} with respect to M for elastic building response is reasoned below in the summary of the inelastic results.

Table 6-2. Regression analysis results for LA20 subjected to 59 "ordinary" earthquake records, *assuming elastic building response*. In effect, the results compare the bias, efficiency, and sufficiency of the SRSS rule of modal combination with one, two, or three modes.

IM	$\theta_{\max}$ on IM		$\varepsilon \mid IM$ on M			$\varepsilon \mid IM$ on R		
	a	σ	c	p-value	σ	c	p-value	σ
IM_{1E}	1.94	0.47	-0.86	0.00	0.40	0.26	0.61	0.48
$IM_{1E\,\&\,2E}$	1.37	0.20	-0.16	0.07	0.20	-0.21	0.33	0.20
$IM_{1E\,\&\,2E\,\&\,3E}$	1.30	0.17	-0.12	0.12	0.17	-0.20	0.29	0.17

Note that the results in Table 6-2 for $IM_{1E\&2E}$ are not much different than those for $IM_{1E\&2E\&3E}$, which is one of the reasons (the other being simplicity) that the third mode is not systematically included in the ground motion intensity measure investigated in this dissertation. In fact, only for 5 of the 59 ordinary earthquake records is $IM_{1E\&2E\&3E}$ more than 10% larger than $IM_{1E\&2E}$. The 60th earthquake record that was excluded from the ordinary set (as mentioned in Section 6.2) was left out because its third-mode contribution to $\theta_{\max}$ (for LA20) is unusually large (i.e., 75% of $IM_{1E\&2E}$). Both $IM_{1E\&2E\&3E}$ and $IM_{1E\&2E}$ are somewhat biased low ($a \approx 1.3-1.4$), but both are relatively efficient ($\sigma \approx 0.2$) and sufficient ($p-\text{value} \geq 0.07$). One reason why, on average, even $IM_{1E\&2E\&3E}$ under-estimates $\theta_{\max}$ (i.e., is biased low) is that a damping ratio of 2% is assumed for all modes, even though the true damping ratios for the second and third modes are smaller (i.e., 1.2% and 1.4%, respectively). It is helpful to keep these elastic results in mind when examining the analogous results for nonlinear building response, presented next.

6.4.1.2 Considering Inelastic Building Response

As described generically above, the regression of $\theta_{\max}$ (considering inelastic building response) on IM_{1E} is illustrated in Figure 6-1. First note the broad range of $\theta_{\max}$ values, from less than 0.01 radians (effectively elastic) to almost 0.07 radians, a story ductility of about 7. The estimated regression coefficient (a=1.59) indicates that IM_{1E} is biased low. In fact, IM_{1E} under-estimates $\theta_{\max}$ for most of the ground motions, as evidenced by the fact that most of the data points in Figure 6-1 lie below the one-to-one dashed line. At least in the elastic range, it is not surprising that IM_{1E} is biased low, for it does not take into account the contributions to $\theta_{\max}$ from higher modes. Meanwhile, the comparatively large scatter about the regression fit in Figure 6-1 (quantified by $\sigma = 0.44$) indicates that IM_{1E} is relatively inefficient as well. Recall (as explained in Chapter 5) that a σ of 0.44 implies that at least 20 earthquake records must be considered in order to estimate a with less than 10% variability (i.e., $\sigma_{\ln(a)} \leq 0.10$). To the extent that σ reflects the earthquake record-to-record variability of spectral shape (e.g., the $S_d(T_2,\zeta_2)$ to $S_d(T_1,\zeta_1)$ ratio), the inefficiency of IM_{1E} is also (like the bias) due in part to the fact that IM_{1E} does not take into account higher modes.

Notice also from Figure 6-1 that the residuals about the regression fit (i.e., the observed values of $\varepsilon_{\theta_{\max}|IM_{1E}}$) appear to be negatively correlated with IM_{1E} (i.e., $\varepsilon_{\theta_{\max}|IM_{1E}} > 1$ for smaller values of IM_{1E}, and vice-versa, since by definition the

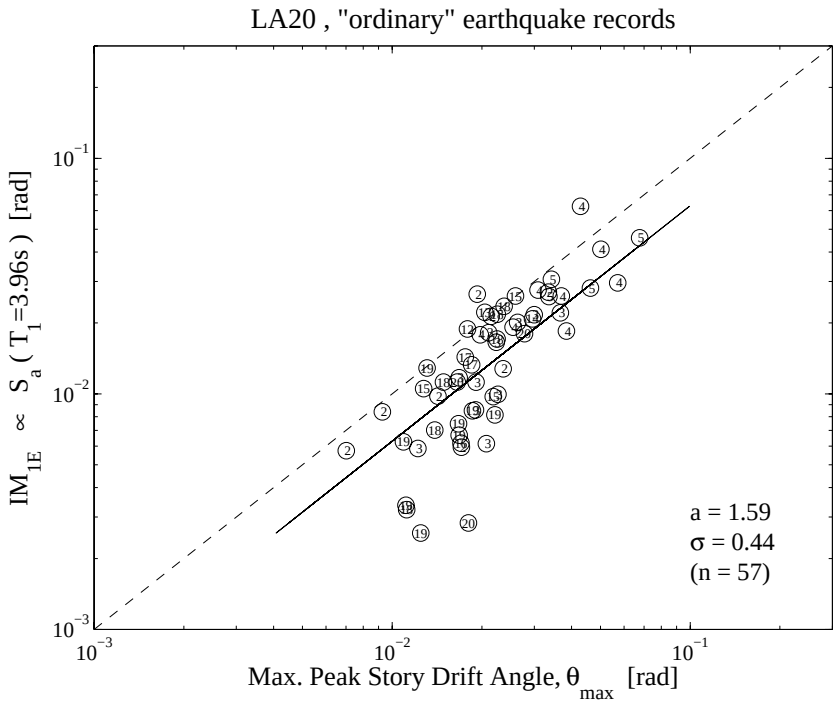

Figure 6-1. Regression of θ_{max}, for LA20 subjected to "ordinary" earthquake records, on the ground motion intensity measure IM_{1E}, in order to quantify the bias (a) and efficiency (σ) of IM_{1E}.

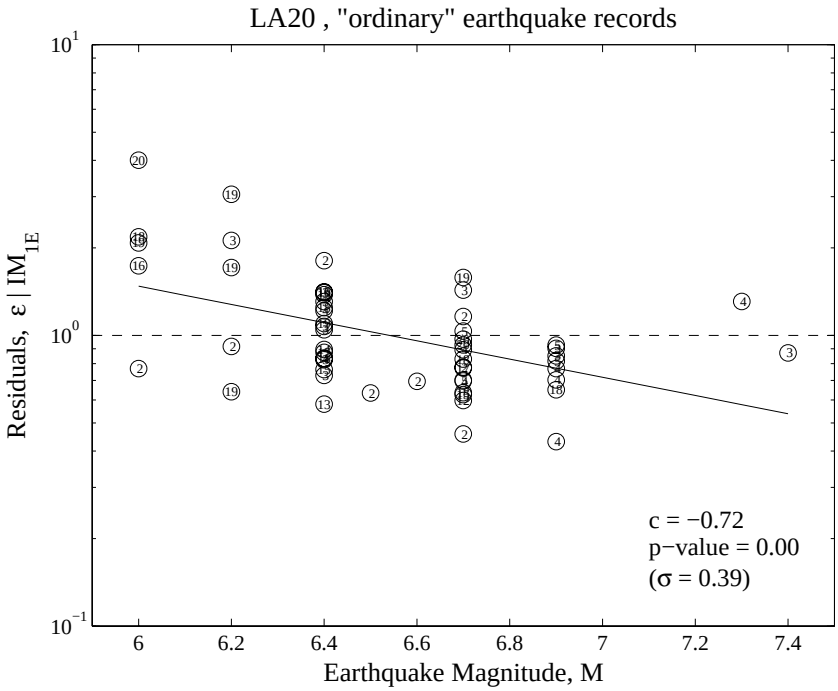

Figure 6-2. Regression of $\varepsilon|IM_{1E}$ (residuals from Figure 6-1) on M, in order to quantify the sufficiency (p–value) of IM_{1E} with respect to M.

median $\varepsilon_{\theta_{\max}|IM_{1E}}$ is 1). In turn, IM_{1E} is expected to be positively correlated with M, since the range of R is relatively narrow (i.e., 30 to 46 km). Accordingly, a negative correlation between $\varepsilon_{\theta_{\max}|IM_{1E}}$ and M is expected, which would imply that IM_{1E} is insufficient; this is confirmed by Figure 6-2, which shows a significant (p–value $\cong 0$) negative ($c = -0.72$) dependence of $\varepsilon_{\theta_{\max}|IM_{1E}}$ on M. Although not shown here with a figure (but summarized below in Table 6-6), a mild (p–value=0.06) positive ($c = 0.92$) dependence of $\varepsilon_{\theta_{\max}|IM_{1E}}$ on R is also observed, further suggesting that IM_{1E} is insufficient.

Because the response of the LA20 building model to each of the smaller magnitude (M) earthquake records is roughly elastic, the relatively large values of $\varepsilon_{\theta_{\max}|IM_{1E}}$ observed in Figure 6-2 at smaller values of M can be explained by the fact that IM_{1E} does not take into account higher modes. First note that, due to their relatively weak low-frequency content, for smaller M earthquake ground motions the ratio of the spectral displacement at a relatively short period (e.g., corresponding to a higher mode) to that at a longer period (e.g., T_1 for LA20) is on average relatively large (Abrahamson & Silva 1997). Thus, smaller M earthquake records will tend to excite the higher modes relatively more (than larger M earthquake records), resulting in relatively large values of $\varepsilon_{\theta_{\max}|IM_{1E}}$ because IM_{1E} only considers the first mode. This relatively large contribution of higher modes for smaller M earthquake ground motions is consistent with (or perhaps compounded by) the observation for such earthquake records that $\theta_{\max}$ tends to occur in the upper stories (as noted in Figure 6-2), where (for example) the second-mode participation factor is relatively large.

In contrast to IM_{1E}, recall that the intensity measure $IM_{1E\&2E}$ takes into account the contribution to $\theta_{\max}$ from the second mode (in addition to the first mode). As evidenced by Figure 6-3, $IM_{1E\&2E}$ manages to capture much of the higher-mode contribution that resulted in large $\varepsilon_{\theta_{\max}|IM_{1E}}$ residuals in (or near) the elastic range in Figure 6-1. Accordingly, the estimated regression coefficient (a=1.11) indicates that $IM_{1E\&2E}$ is only slightly biased in estimating $\theta_{\max}$, and the relatively small scatter about the regression fit (quantified by $\sigma = 0.25$) indicates that $IM_{1E\&2E}$ is substantially more efficient than IM_{1E}. Furthermore, the $\varepsilon_{\theta_{\max}|IM_{1E\&2E}}$ residuals about the regression fit are more uniformly distributed over the range of $\theta_{\max}$ than are the $\varepsilon_{\theta_{\max}|IM_{1E}}$ residuals. In fact, as shown in Figure 6-4, $\varepsilon_{\theta_{\max}|IM_{1E\&2E}}$ is not significantly dependent on M ($p-\text{value} = 0.87$). Although not shown here with a figure, the residuals are also practically independent of R as well ($p-\text{value} = 0.19$), suggesting that $IM_{1E\&2E}$ is practically sufficient. It should be mentioned that if a two-parameter regression fit is employed, even IM_{1E} is found to be relatively efficient ($\sigma = 0.28$) and sufficient ($p-\text{value} = 0.59$ for M and 0.55 for R); of course, a two-parameter model does not provide a single measure of bias.

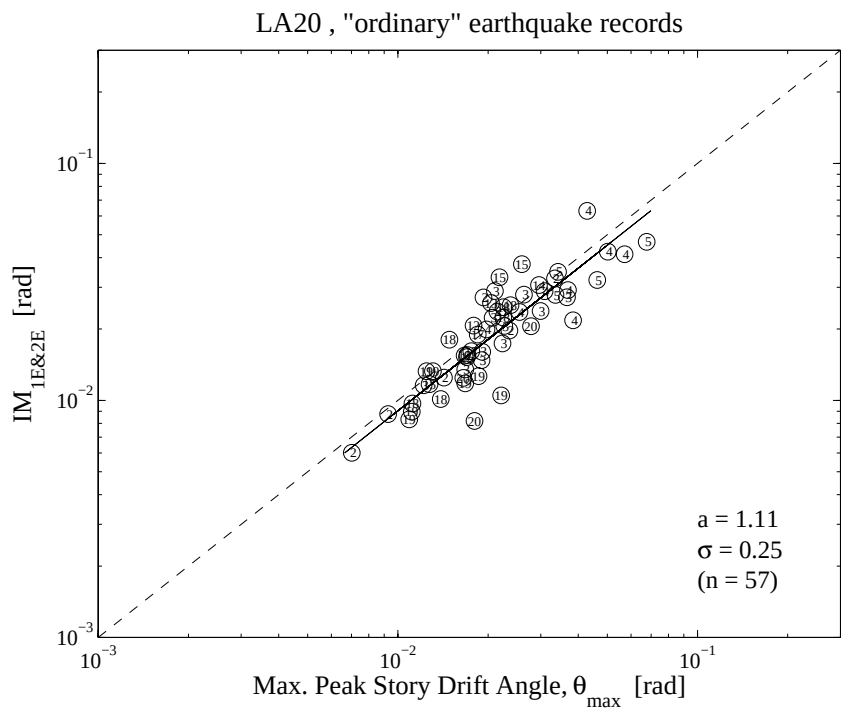

Figure 6-3. Regression of $\theta_{\max}$, for LA20 subjected to "ordinary" earthquake records, on the ground motion intensity measure $IM_{1E\&2E}$, in order to quantify the bias (a) and efficiency (σ) of $IM_{1E\&2E}$.

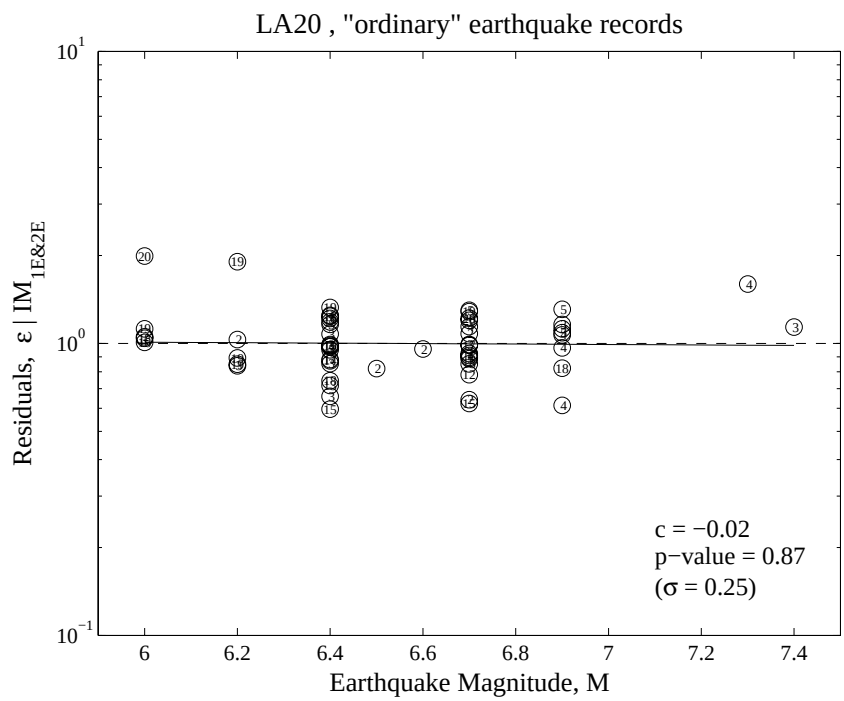

Figure 6-4. Regression of $\varepsilon|IM_{1E\&2E}$ (residuals from Figure 6-3) on M, in order to quantify the sufficiency (p–value) of $IM_{1E\&2E}$ with respect to M.

6.4.2 IM_{1I} vs. IM_{1E} for LA3 under Near-Source Ground Motions

As explained in Chapter 5, it is suspected that $S_a(T_1)$, or equivalently IM_{1E}, may also be relatively inefficient and insufficient when considering the inelastic response of moderate-period structures to near-source ground motions. This shortcoming of IM_{1E}, as well as the relative efficiency and sufficiency of IM_{1I} (which accounts for inelasticity), are demonstrated here with the LA3 building model subjected to the 31 near-source earthquake records. As a basis of comparison for the inelastic results to follow, first the regression analysis results assuming elastic building response are summarized.

6.4.2.1 Assuming Elastic Building Response

Assuming elastic building response, the $\theta_{\max}$ on IM_{1E} and on $IM_{1E\&2E}$ regression analysis results for the LA3 building model subjected to the 31 near-source earthquake records are summarized in Table 6-3. Based on the fact that IM_{1E} is essentially unbiased ($a = 1.05$), very efficient ($\sigma = 0.09$), and also sufficient ($p-\text{value} \geq 0.05$ for M and R), it is evident that the elastic response of LA3 is first-mode dominated. Consequently, the regression results for $IM_{1E\&2E}$ are not much different than those for IM_{1E}.

Table 6-3. Regression analysis results for LA3 subjected to 31 near-source earthquake records, *assuming elastic building response*. In effect, the results compare the bias, efficiency, and sufficiency of the SRSS rule of modal combination with one or two modes.

IM	$\theta_{\max}$ on IM		$\varepsilon\,\|IM$ on M			$\varepsilon\,\|IM$ on R		
	a	σ	c	p-value	σ	c	p-value	σ
IM_{1E}	1.05	0.09	-0.29	0.05	0.09	0.02	0.21	0.09
$IM_{1E\,\&\,2E}$	1.04	0.06	-0.17	0.06	0.05	0.01	0.41	0.06

The fact that σ is less than 0.10, recall, implies that the elastic response of LA3 to just one earthquake record is enough to estimate a with less than 10% variability (i.e., $\sigma_{\ln(a)} < 0.10$). Given that the regression estimates of a are nearly equal to one, it may even be adequate to assume that IM_{1E} (or $IM_{1E\&2E}$) is unbiased (i.e., $a = 1$).

6.4.2.2 Considering Inelastic Building Response

Considering inelastic building response, the regression of $\theta_{\max}$ on IM_{1E} is illustrated in Figure 6-5. The estimated regression coefficient ($a = 1.02$) indicates that IM_{1E} is essentially unbiased, and the rather small scatter about the regression fit (quantified by $\sigma = 0.29$) indicates that IM_{1E} is fairly efficient. Note that the data points for the 6 supplemental "pulse-like" earthquake records (symbolized as diamonds), which are not included in the regression analysis, do appear to lie within the scatter of the data for the other 31 near-source earthquake records. The fact that IM_{1E} is essentially unbiased and relatively efficient is not surprising insofar as the response of the LA3 building model is dominated by its first mode (at least in the elastic range). Nevertheless, it does not follow that IM_{1E} is sufficient. As shown in Figure 6-6, a somewhat mild (p–value=0.05) negative (c=–0.11) dependence of the $\varepsilon_{\theta_{\max}|IM_{1E}}$ residuals on R is observed. The values of $\varepsilon_{\theta_{\max}|IM_{1E}}$ for the 6 supplemental pulse-like earthquake records (not included in the regression analysis) appear to support the observed negative dependence. To the degree that ground motions at smaller R are more likely to be strongly pulse-like and therefore are more likely to induce large inelastic displacements relative to IM_{1E} (i.e., large values of $\varepsilon_{\theta_{\max}|IM_{1E}}$), the negative dependence of $\varepsilon_{\theta_{\max}|IM_{1E}}$ on R is expected. Bear in mind that the dependence on R observed here may be somewhat mild because all of the ground motions considered are near-source (i.e., R<16km).

Although not shown here with a figure, a somewhat significant (p–value=0.02) negative (c=–1.13) dependence of $\varepsilon_{\theta_{\max}|IM_{1E}}$ on M is also observed. However, note that of the 31 near-source earthquake records, 14 are from the M=6.5 Imperial Valley earthquake (of 1979), 16 are from the M=6.7 Northridge (1994) and Superstition Hills (1987) earthquakes, and 1 is from the M=6.9 Loma Prieta earthquake (1989), as listed in Appendix A. Due to the small number of distinct earthquake events over a narrow range of M, the results of the regression of $\varepsilon_{\theta_{\max}|IM_{1E}}$ on M may be suspect. Furthermore, the results for the 6 supplemental pulse-like earthquake records (including 1 from each of the M=6.2 Morgan Hill (1984) and M=7.3 Landers (1992) earthquakes) do not support the observed negative dependence on M. Nevertheless, whether due to a dependence on R or M, the regression analysis results suggest that IM_{1E} is relatively insufficient. Note that if a two-parameter regression model is employed, IM_{1E} is still found to be insufficient with respect to R (p–value $\cong 0$), but not M (p–value=0.07), and relatively efficient (σ=0.28).

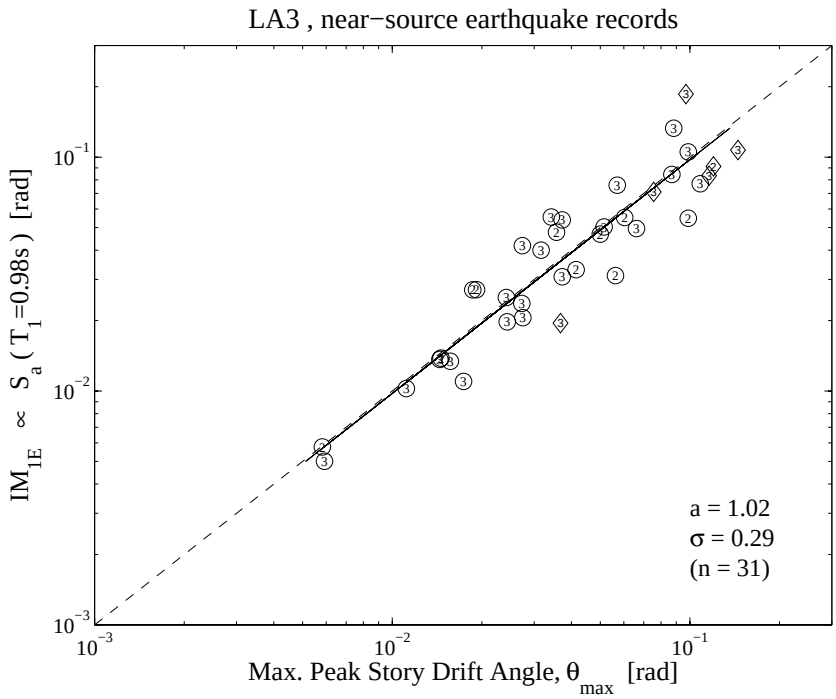

Figure 6-5. Regression of $\theta_{\max}$, for LA3 subjected to near-source earthquake records, on the ground motion intensity measure IM_{1E}, in order to quantify the bias (a) and efficiency (σ) of IM_{1E}.

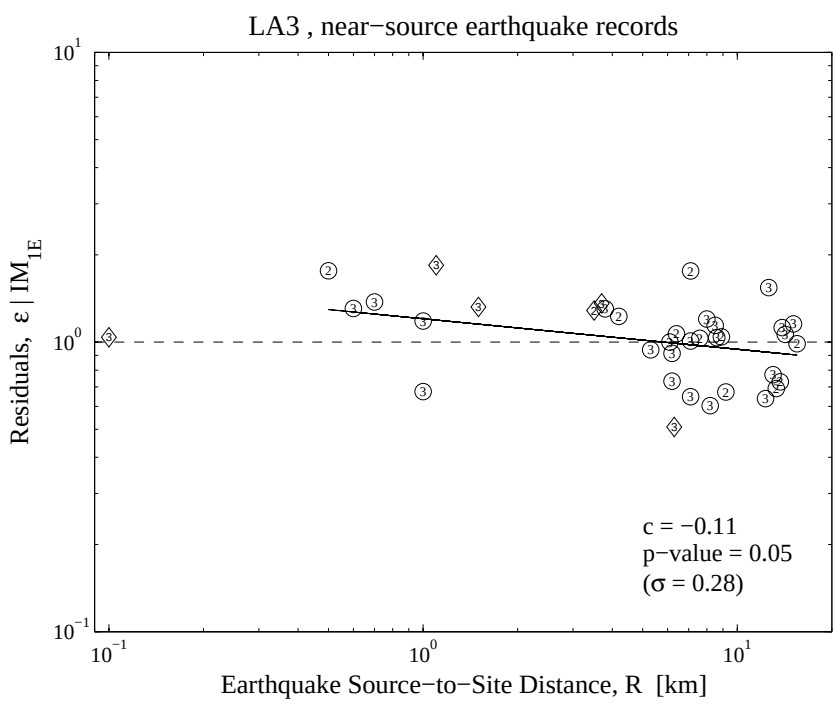

Figure 6-6. Regression of $\varepsilon|IM_{1E}$ (residuals from Figure 6-5) on R, in order to quantify the sufficiency (p–value) of IM_{1E} with respect to R.

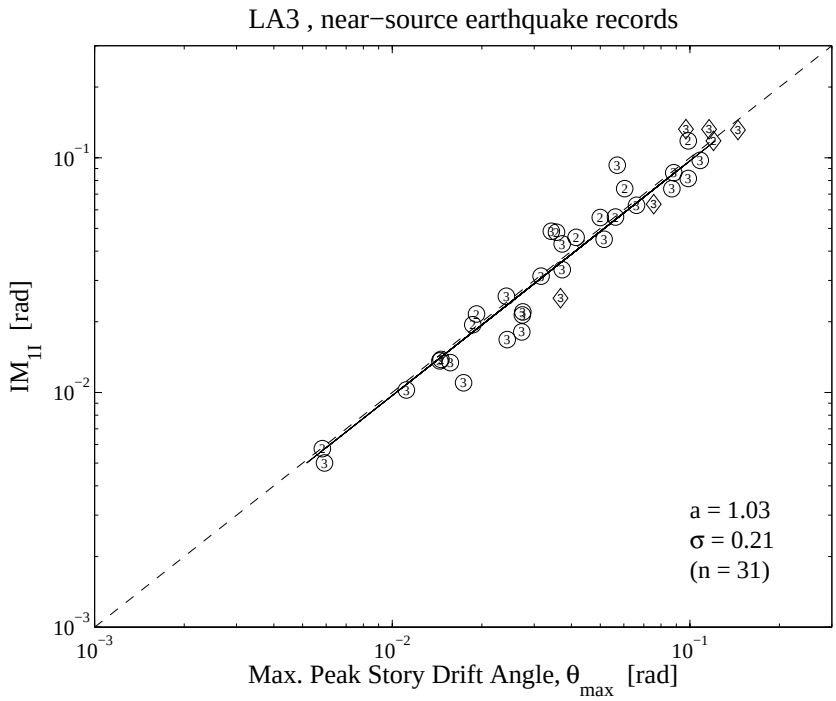

Figure 6-7. Regression of θ_{max}, for LA3 subjected to near-source earthquake records, on the ground motion intensity measure IM_{1I}, in order to quantify the bias (a) and efficiency (σ) of IM_{1I}.

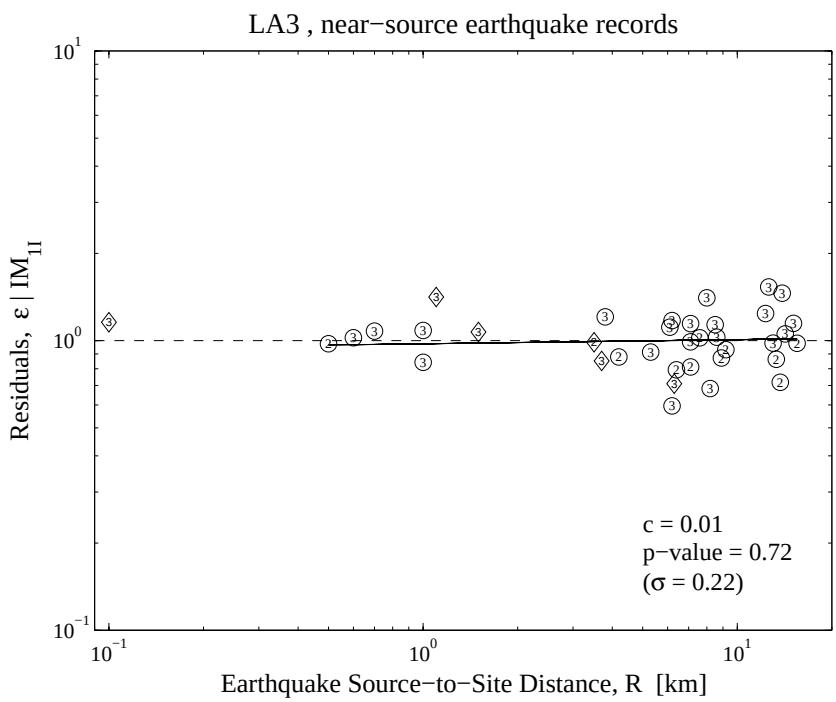

Figure 6-8. Regression of $\varepsilon|IM_{1I}$ (residuals from Figure 6-7) on R, in order to quantify the sufficiency (p–value) of IM_{1I} with respect to R.

Unlike IM_{1E}, recall that the intensity measure IM_{1I} takes into account the effects of inelasticity. The regression of $\theta_{\max}$ on IM_{1I} is illustrated in Figure 6-7. As for IM_{1E}, the estimated regression coefficient (a=1.03) indicates that IM_{1I} is essentially unbiased. The small scatter about the regression fit (quantified by σ=0.21) indicates that IM_{1I} is even more efficient than IM_{1E}. Moreover, Figure 6-8 shows that the $\varepsilon_{\theta_{\max}|IM_{1I}}$ residuals are not significantly dependent on R (p–value=0.72); although not shown here with a figure, the residuals are also observed to be practically independent of M as well (p–value=0.14), suggesting that IM_{1I} is relatively sufficient. Note that the data for the 6 supplemental pulse-like earthquake records further supports the observations that IM_{1I} is essentially unbiased, more efficient than IM_{1E}, and relatively sufficient.

6.4.3 $IM_{1I\&2E}$ vs. IM_{1E} for LA9 under Ordinary and Near-Source Ground Motions

In the preceding subsections, it has been demonstrated that (i) an intensity measure that takes into account higher modes, like $IM_{1E\&2E}$, can be more efficient and sufficient than IM_{1E} if higher modes contribute significantly to the structural response (e.g., LA20), and (ii) an intensity measure that takes into account inelasticity, like IM_{1I}, can be more efficient and sufficient than IM_{1E} if inelasticity significantly affects the response, as it does under near-source ground motions for a moderate period structure (e.g., LA3). Here the relative (compared to IM_{1E}) efficiency and sufficiency of $IM_{1I\&2E}$, which takes into account both the second mode and inelasticity, are demonstrated with the LA9 building model subjected both to the ordinary and to the near-source earthquake records. Following the pattern of the preceding subsections, the regression analysis results assuming elastic building response are investigated as a basis of comparison before considering the inelastic building results.

6.4.3.1 Assuming Elastic Building Response

The regression analysis results for the LA9 building model subjected to the ordinary and the near-source earthquake records, assuming elastic building response, are summarized in Table 6-4. As expected (and as observed for LA20), the larger the number of elastic modes that are taken into account in the ground motion intensity measure (e.g., $IM_{1E\&2E}$ versus IM_{1E}), the less biased (i.e., smaller a) and more efficient (i.e. smaller σ) is the IM. Moreover, for the near-source ground motions, only when the second mode is taken into account (i.e., $IM_{1E\&2E}$ or $IM_{1E\&2E\&3E}$) is the intensity measure

Table 6-4. Regression analysis results for LA9 subjected to "ordinary" and near-source earthquake records, *assuming elastic building response*. In effect, the results compare the bias, efficiency, and sufficiency of the SRSS rule of modal combination with one, two, or three modes.

IM	$\theta_{\max}$ on *IM*		$\varepsilon \mid IM$ on *M*			$\varepsilon \mid IM$ on *R*		
	a	σ	c	p-value	σ	c	p-value	σ
(a) 59 "ordinary" earthquake records								
IM_{1E}	1.60	0.41	-0.20	0.27	0.41	-0.33	0.46	0.41
$IM_{1E\,\&\,2E}$	1.29	0.22	-0.11	0.26	0.22	-0.05	0.84	0.22
$IM_{1E\,\&\,2E\,\&\,3E}$	1.21	0.13	-0.06	0.31	0.13	-0.07	0.63	0.13
(b) 31 near-source earthquake records								
IM_{1E}	1.41	0.33	1.32	0.01	0.30	0.07	0.29	0.33
$IM_{1E\,\&\,2E}$	1.22	0.13	0.39	0.07	0.13	0.01	0.63	0.14
$IM_{1E\,\&\,2E\,\&\,3E}$	1.19	0.10	0.31	0.07	0.10	0.00	0.89	0.11

sufficient (i.e., p–value>0.05) with respect to both M and R. The observed insufficiency of IM_{1E} with respect to M under the near-source ground motions could potentially be due to a dependence of the predominant period of near-source ground motions on magnitude (e.g., Somerville 1998). Obviously the effects of a magnitude-dependent predominant period cannot be fully captured by IM_{1E} alone; as a result, $\varepsilon_{\theta_{\max}|IM_{1E}}$ may depend significantly on M, indicating that IM_{1E} is insufficient.

As for the LA20 building model, the third mode is not systematically included in the ground motion intensity measures investigated for the LA9 building model. This is justified by the fact that the results (in Table 6-2) for $IM_{1E\&2E}$ are similar to those for $IM_{1E\&2E\&3E}$, perhaps with the exception of the efficiency of the two intensity measures for the ordinary earthquake records (i.e., $\sigma = 0.22$ versus 0.13). Both $IM_{1E\&2E\&3E}$ and $IM_{1E\&2E}$, however, are sufficient (p–value>0.05) and somewhat biased low (a=1.2 to 1.3) for both the ordinary and near-source ground motions. Once again, it is helpful to keep these elastic results in mind when examining the analogous results for nonlinear building response, presented next.

6.4.3.2 Considering Inelastic Building Response

Before considering the inelastic response of the LA9 building model, note that for the first-mode dominated LA3 building model, $IM_{1I\&2E}$ is essentially equivalent to IM_{1I}; for the relatively long period LA20 building model, $IM_{1I\&2E}$ is expected to be (according to the "equal displacements rule") comparable to $IM_{1E\&2E}$ (perhaps even for near-source ground motions). The regression analysis results for the LA3 and LA20 building models, which for the most part confirm these expectations, are summarized in Table 6-6 of Section 6.4.4.

The LA9 regression analysis results for both IM_{1E} and $IM_{1I\&2E}$ are summarized in Table 6-5. For both the ordinary and near-source ground motions, the regression estimates of the coefficient a (all approximately 1.2 or larger) indicate that both intensity measures are somewhat biased low in estimating $\theta_{\max}$. Note, however, that $IM_{1I\&2E}$ is less biased (i.e., a closer to 1) than IM_{1E}, particularly for the near-source ground motions. Also note that whereas the regression estimates of a are somewhat different for the ordinary versus near-source ground motions when IM_{1E} is employed (i.e., a=1.22 vs. 1.38), they are more similar for $IM_{1I\&2E}$ (i.e., a=1.17 vs. 1.23). As discussed in Chapter 5, this bias similarity is related to the sufficiency of $IM_{1I\&2E}$ relative to IM_{1E}. Moreover, the regression estimates of σ reveal that $IM_{1I\&2E}$ is significantly more efficient than IM_{1E} for both the ordinary ($\sigma = 0.27$ vs. 0.46) and near-source ($\sigma = 0.20$ vs. 0.35) earthquake

Table 6-5. Regression analysis results, for LA9 subjected to "ordinary" and near-source earthquake records, comparing the bias, efficiency, and sufficiency of the ground motion intensity measures $IM_{1I\&2E}$ and IM_{1E}.

IM	$\theta_{\max}$ on IM		$\varepsilon \mid IM$ on M			$\varepsilon \mid IM$ on R		
	a	σ	c	p-value	σ	c	p-value	σ
(a) 59 "ordinary" earthquake records								
IM_{1E}	1.22	0.46	-0.46	0.02	0.44	0.53	0.29	0.46
$IM_{1I\&2E}$	1.17	0.27	-0.08	0.51	0.27	0.36	0.22	0.27
(b) 31 near-source earthquake records								
IM_{1E}	1.38	0.35	-0.58	0.31	0.35	-0.03	0.61	0.35
$IM_{1I\&2E}$	1.23	0.20	-0.36	0.26	0.19	-0.02	0.68	0.20

records. Based on the regression estimates of σ, only about 1/3 the number of (ordinary or near-source) earthquake records are needed to estimate the regression coefficient a with $\sigma_{\ln(a)} \leq 0.10$ when $IM_{1I\&2E}$ is employed in lieu of IM_{1E}.

Also listed in Table 6-5, the p–values suggest that whereas IM_{1E} is rather insufficient for the ordinary earthquake records, $IM_{1I\&2E}$ is relatively sufficient. For the near-source earthquake records, both IM_{1E} and $IM_{1I\&2E}$ are found to be acceptably sufficient. Note that the insufficiency of IM_{1E} for the ordinary earthquake records is due to a somewhat significant (p–value=0.02) negative (c= –0.46) dependence of $\varepsilon_{\theta_{\max}|IM_{1E}}$ on M, as was observed (in Section 6.4.1) for the LA20 building model. For the LA9 building model, however, merely taking into account the elastic contributions to $\theta_{\max}$ from the first two modes (i.e., $IM_{1E\&2E}$) does not achieve a sufficient intensity measure as it did for the LA20 building model (refer to Table 6-6 below). Evidently, the effects of inelasticity, in addition to the second mode, must be taken into account in order to achieve a sufficient intensity measure (i.e., $IM_{1I\&2E}$) for the moderate height LA9 building model.

It should be noted that if a two-parameter regression model is employed, IM_{1E} is found to be insufficient with respect to M (p–value =0.02) for the near-source ground motions, but still somewhat efficient ($\sigma = 0.32$). Unlike the one-parameter results presented in Table 6-5, however, the two-parameter results indicate that IM_{1E} is efficient ($\sigma = 0.26$) and sufficient (p–value=0.11 for M and 0.90 for R) for the ordinary ground motions. Of course, a two-parameter model does not provide a single measure of bias.

6.4.4 Summary of Results for IM_{1E}, $IM_{1E\&2E}$, IM_{1I}, and $IM_{1I\&2E}$

The regression analysis results for the four "primary" intensity measures IM_{1E}, $IM_{1E\&2E}$, IM_{1I}, and $IM_{1I\&2E}$ are summarized in Table 6-6 for every combination of the three building models (LA3, LA9, and LA20) and two sets of earthquake records (ordinary and near-source). While only some of the results listed in the table are described in detail in the subsections above, additional results from the table are referred to in the following subsections.

Table 6-6. Summary of regression analysis results comparing the bias, efficiency, and sufficiency of the four "primary" intensity measures for every combination of the two sets of ground motions and three building models considered.

IM	$\theta_{\max}$ on *IM*		$\varepsilon \mid IM$ on *M*			$\varepsilon \mid IM$ on *R*		
	a	σ	c	p-value	σ	c	p-value	σ
(a) LA3 subjected to 59 "ordinary" earthquake records								
IM_{1E}	0.84	0.28	-0.28	0.02	0.27	-0.03	0.92	0.28
$IM_{1E\,\&\,2E}$	0.83	0.27	-0.26	0.03	0.26	-0.06	0.85	0.27
IM_{1I}	1.01	0.25	-0.05	0.63	0.25	-0.11	0.70	0.25
$IM_{1I\,\&\,2E}$	0.99	0.24	-0.03	0.78	0.24	-0.13	0.62	0.24
(b) LA3 subjected to 31 near-source earthquake records								
IM_{1E}	1.02	0.29	-1.13	0.02	0.27	-0.11	0.05	0.28
$IM_{1E\,\&\,2E}$	1.01	0.28	-1.01	0.02	0.26	-0.12	0.02	0.26
IM_{1I}	1.03	0.21	-0.51	0.14	0.21	0.01	0.72	0.22
$IM_{1I\,\&\,2E}$	1.01	0.19	-0.40	0.21	0.19	0.00	0.95	0.20
(c) LA9 subjected to 59 "ordinary" earthquake records								
IM_{1E}	1.22	0.46	-0.46	0.02	0.44	0.53	0.29	0.46
$IM_{1E\,\&\,2E}$	0.99	0.32	-0.37	0.01	0.31	0.82	0.02	0.31
IM_{1I}	1.44	0.37	-0.17	0.29	0.37	0.07	0.85	0.37
$IM_{1I\,\&\,2E}$	1.17	0.27	-0.08	0.51	0.27	0.36	0.22	0.27
(d) LA9 subjected to 31 near-source earthquake records								
IM_{1E}	1.38	0.35	-0.58	0.31	0.35	-0.03	0.61	0.35
$IM_{1E\,\&\,2E}$	1.19	0.31	-1.51	0.00	0.27	-0.09	0.13	0.31
IM_{1I}	1.43	0.25	0.57	0.16	0.24	0.04	0.41	0.25
$IM_{1I\,\&\,2E}$	1.23	0.20	-0.36	0.26	0.19	-0.02	0.68	0.20
(e) LA20 subjected to 57 "ordinary" earthquake records								
IM_{1E}	1.59	0.44	-0.72	0.00	0.39	0.92	0.06	0.43
$IM_{1E\,\&\,2E}$	1.11	0.25	-0.02	0.87	0.25	0.36	0.19	0.24
IM_{1I}	1.81	0.41	-0.64	0.00	0.36	0.87	0.05	0.40
$IM_{1I\,\&\,2E}$	1.26	0.29	0.07	0.60	0.29	0.31	0.33	0.29
(f) LA20 subjected to 30 near-source earthquake records								
IM_{1E}	1.70	0.37	0.69	0.26	0.36	-0.05	0.48	0.37
$IM_{1E\,\&\,2E}$	1.50	0.32	-0.14	0.79	0.33	-0.08	0.18	0.31
IM_{1I}	1.92	0.31	0.78	0.12	0.30	-0.10	0.07	0.29
$IM_{1I\,\&\,2E}$	1.69	0.28	-0.05	0.92	0.29	-0.13	0.01	0.25

6.4.5 IM_{1eq} vs. IM_{1I} for LA3 under Ordinary and Near-Source Ground Motions

As detailed in Chapter 5, IM_{1eq} is an "equivalent" elastic approximation of IM_{1I} (i.e., one that avoids nonlinear SDOF time-history analysis). Here, the efficiency and sufficiency (as well as the bias) of IM_{1eq} relative to IM_{1I} are demonstrated for the LA3 building model. Whereas above IM_{1I} was compared with IM_{1E} for the LA3 building model subjected to only the near-source earthquake records, here both the ordinary and near-source earthquake records are considered.

The regression analysis results for both IM_{1eq} and IM_{1I} are summarized in Table 6-7. For both the ordinary and near-source ground motions, the regression estimates of the coefficient a indicate that, whereas IM_{1I} is essentially unbiased in estimating $\theta_{\max}$ (a≈1.0), IM_{1eq} is slightly biased (a≈1.1). Nevertheless, the regression estimates of σ indicate that IM_{1eq} is nearly as efficient as IM_{1I}, for both the ordinary (σ=0.28 vs. 0.25) and near-source (σ=0.22 vs. 0.21) ground motions. The p–values, however, suggest that whereas IM_{1I} is practically sufficient for the near-source earthquake records (as discussed in Section 6.4.2), IM_{1eq} is somewhat insufficient; for the ordinary earthquake records, both IM_{1eq} and IM_{1I} are evidently sufficient.

Table 6-7. Regression analysis results, for LA3 subjected to "ordinary" and near-source earthquake records, comparing the bias, efficiency, and sufficiency of the ground motion intensity measures IM_{1eq} and IM_{1I}.

IM	$\theta_{\max}$ on IM		$\varepsilon\|IM$ on M			$\varepsilon\|IM$ on R		
	a	σ	c	p-value	σ	c	p-value	σ
(a) 59 "ordinary" earthquake records								
IM_{1I}	1.01	0.25	-0.05	0.63	0.25	-0.11	0.70	0.25
IM_{1eq}	1.13	0.28	0.01	0.95	0.28	0.23	0.45	0.28
(b) 31 near-source earthquake records								
IM_{1I}	1.03	0.21	-0.51	0.14	0.21	0.01	0.72	0.22
IM_{1eq}	1.13	0.22	-0.71	0.04	0.21	-0.07	0.09	0.21

The reason why IM_{1eq} is insufficient for the near-source but not the ordinary ground motions probably lies in the details of how the equivalent period and damping ratio for $S_d^{eq}(T_1,\zeta_1,d_y)$ are established. Recall that in determining the equivalent period and damping ratio, $\mu=S_d^I(T_1,\zeta_1,d_y)/d_y$ is approximated with $S_d(T_1,\zeta_1)/d_y$. However, as

demonstrated in Chapter 1 (for example), $S_d^I(T_1,\zeta_1,d_y)$ can be considerably larger than $S_d(T_1,\zeta_1)$ under near-source ground motions for moderate values of T_1 (e.g., T_1=0.98sec for LA3), and this difference between $S_d^I(T_1,\zeta_1,d_y)$ and $S_d(T_1,\zeta_1)$ may depend on M and/or R. For the LA3 building model, this implies that IM_{1eq} may be insufficient for near-source ground motions. For ordinary ground motions, in contrast, IM_{1eq} may be sufficient because the "equal displacements rule" is more applicable – that is, $S_d^I(T_1,\zeta_1,d_y)$ is a closer to $S_d(T_1,\zeta_1)$. Particularly for near-source ground motions, μ can be estimated more accurately by updating it with each new calculation of $S_d^{eq}(T_1,\zeta_1,d_y)$ (i.e., computing IM_{1eq} iteratively), but this would make it considerably more difficult to compute $\lambda_{IM_{1eq}}$, as discussed briefly at the conclusion of this chapter. Moreover, note that the empirical equations used to determine the equivalent period and damping ratio (as a function of μ) were based predominantly on ordinary earthquake records (Iwan 1980); as a result, the effects of inelasticity under near-source ground motions may not be captured properly by $S_d^{eq}(T_1,\zeta_1,d_y)$.

6.4.6 IM_{1eff} vs. IM_{1I} for LA3 under Ordinary and Near-Source Ground Motions

Like IM_{1eq}, IM_{1eff} can be considered an approximation of IM_{1I}. However, IM_{1eff} involves only the elastic spectral displacements at T_1 and at a single period longer than T_1 (meant to reflect a reduction in stiffness due to inelasticity). As for IM_{1eq} in the previous subsection, here the efficiency and sufficiency (as well as the bias) of IM_{1eff} relative to IM_{1I} are demonstrated for the LA3 building model subjected to the ordinary and near-source earthquake records.

The regression analysis results for both IM_{1eff} and IM_{1I} are summarized in Table 6-8. For both the ordinary and near-source ground motions, the regression estimates of the coefficient a indicate that, like IM_{1I}, IM_{1eff} is essentially unbiased in estimating $\theta_{\max}$ (i.e., $a\approx1.0$). The regression estimates of σ indicate that IM_{1eff} is also nearly as efficient as IM_{1I}, although more-so for the near-source than the ordinary ground motions. Again like IM_{1I}, the p–values suggest that IM_{1eff} is practically sufficient for the near-source ground motions. However, while IM_{1I} is also sufficient for the ordinary ground motions, IM_{1eff} is evidently somewhat insufficient due to a mild (p–value=0.05) negative (c= –0.25) dependence of $\varepsilon_{\theta_{\max}|IM_{1eff}}$ on M.

The relatively large values of $\varepsilon_{\theta_{\max}|IM_{1eff}}$ for smaller values of M that are implied by the negative dependence observed for the ordinary earthquake records may be explained by a known deficiency of IM_{1eff} in the realm of elastic response. Recall (from Chapter 5) that

Table 6-8. Regression analysis results, for LA3 subjected to "ordinary" and near-source earthquake records, comparing the bias, efficiency, and sufficiency of the ground motion intensity measures IM_{1eff} and IM_{1I}.

IM	$\theta_{\max}$ on IM		$\varepsilon \mid IM$ on M			$\varepsilon \mid IM$ on R		
	a	σ	c	p-value	σ	c	p-value	σ
(a) 59 "ordinary" earthquake records								
IM_{1I}	1.01	0.25	-0.05	0.63	0.25	-0.11	0.70	0.25
IM_{1eff}	0.98	0.30	-0.25	0.05	0.29	-0.04	0.90	0.30
(b) 31 near-source earthquake records								
IM_{1I}	1.03	0.21	-0.51	0.14	0.21	0.01	0.72	0.22
IM_{1eff}	0.97	0.23	-0.05	0.89	0.23	-0.06	0.15	0.22

IM_{1eff} is the product of IM_{1E} and a modification factor that reflects the ratio of the spectral displacement at $2T_1$ to that at T_1. In the event of elastic response, IM_{1E} alone is nearly unbiased in estimating $\theta_{\max}$ for a first-mode dominated building model like LA3 (e.g., refer to Table 6-6). However, for the smaller M earthquake records that most often result in elastic response, IM_{1eff} on average under-estimates $\theta_{\max}$ because the ratio of $S_d(2T_1,\zeta_1)$ to $S_d(T_1,\zeta_1)$ is typically relatively small for such ground motions (Abrahamson & Silva 1997). In other words, relatively large values of $\varepsilon_{\theta_{\max}|IM_{1eff}}$ are expected for smaller values of M. For the near-source earthquake records, recall that a dependence on M is difficult to observe due to the narrow range of M (i.e., 6.5 to 6.9).

6.4.7 $IM_{1I\&2E}$ with an EPP vs. Negative-Strain-Hardening Backbone Curve for LA20 under Ordinary and Near-Source Ground Motions

As reported above in Table 6-6, the only case in which $IM_{1I\&2E}$ is insufficient is for the LA20 building model subjected to the near-source earthquake records (p–value=0.01 with respect to R). Also for LA20, but subjected to the ordinary earthquake records, note (from Table 6-6) that $IM_{1I\&2E}$ is slightly less efficient ($\sigma = 0.29$ vs. 0.25) and more biased (a=1.26 vs. 1.11) than $IM_{1E\&2E}$. These deficiencies of $IM_{1I\&2E}$ may be due to the fact that the spectral displacement of an EPP (elastic-perfectly-plastic) oscillator is included in $IM_{1I\&2E}$, even though the NSP (nonlinear static pushover) curve for LA20 is far from EPP. Here the efficiency and sufficiency (as well as the bias) of a ground motion intensity measure that is similar to $IM_{1I\&2E}$, but that includes the spectral

displacement of a bilinear oscillator with negative strain hardening, are demonstrated for the LA20 building model subjected to the ordinary and near-source earthquake records.

The first-mode NSP curve for the LA20 building model is illustrated in Figure 6-9. Also depicted in the figure is the bilinear backbone curve with –8% strain hardening that is assumed for the inelastic spectral displacement in the intensity measure denoted here as $IM_{1B\&2E}$. The regression analysis result for both $IM_{1B\&2E}$ and $IM_{1I\&2E}$ are summarized in Table 6-9. Note that in addition to the two ordinary earthquake records (scaled by a factor of eight) and one near-source earthquake record (scaled by a factor of 2) that cause collapse of the LA20 building model, a third ordinary earthquake record is excluded because the inelastic spectral displacement of the bilinear oscillator with negative strain hardening also becomes unstable and hence $IM_{1B\&2E}$ is effectively infinite. The difference between the regression analysis results for $IM_{1I\&2E}$ with and without this third ordinary earthquake record is insignificant (e.g., compare Table 6-6 and Table 6-9).

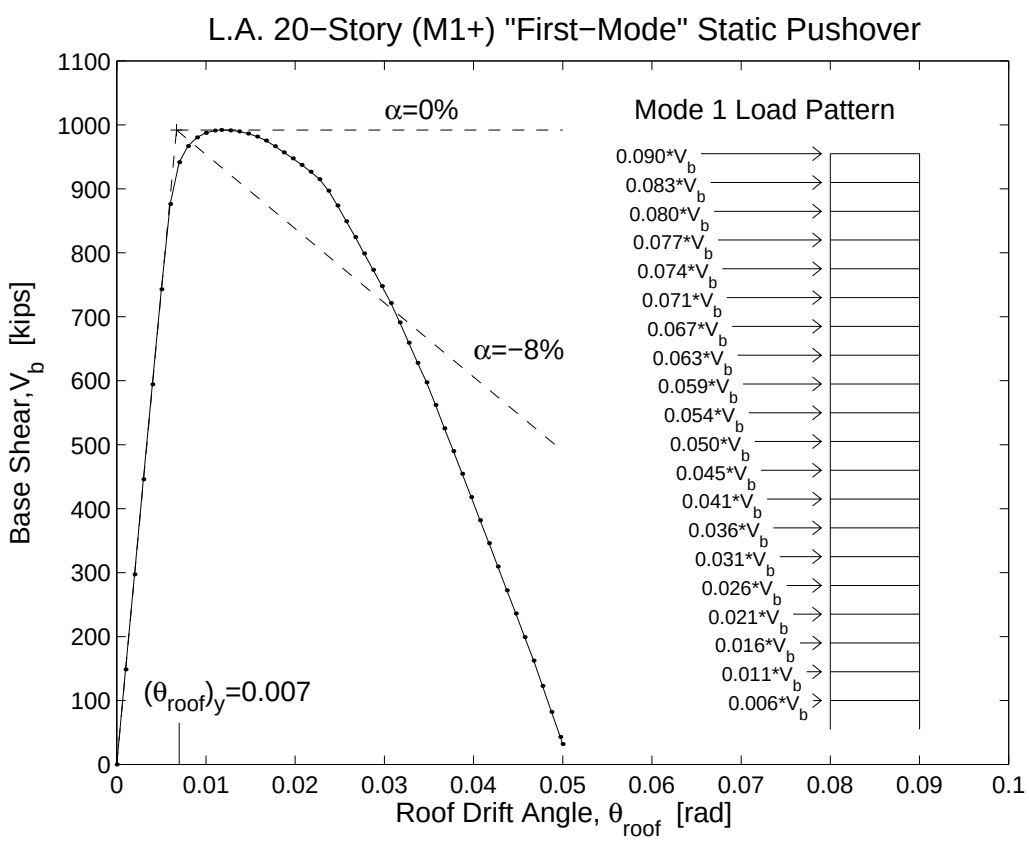

Figure 6-9. First-mode nonlinear static pushover curve for the LA20 building model and the assumed elastic-perfectly-plastic versus bilinear-with-negative-strain-hardening backbone curves.

Table 6-9. Regression analysis results, for LA20 subjected to ordinary and near-source earthquake records, comparing the bias, efficiency, and sufficiency of the ground motion intensity measures $IM_{1B\&2E}$ and $IM_{1I\&2E}$.

IM	$\theta_{\max}$ on *IM*		$\varepsilon\,\|IM$ on *M*			$\varepsilon\,\|IM$ on *R*		
	a	σ	c	p-value	σ	c	p-value	σ
(a) 56 "ordinary" earthquake records								
$IM_{1I\,\&\,2E}$	1.28	0.28	0.11	0.39	0.28	0.20	0.53	0.28
$IM_{1B\,\&\,2E}$	1.16	0.31	-0.17	0.23	0.30	0.42	0.22	0.30
(b) 30 near-source earthquake records								
$IM_{1I\,\&\,2E}$	1.69	0.28	-0.05	0.92	0.29	-0.13	0.01	0.25
$IM_{1B\,\&\,2E}$	1.40	0.28	0.79	0.08	0.27	-0.07	0.14	0.27

For both the ordinary and near-source earthquake records, $IM_{1B\&2E}$ is somewhat less biased than $IM_{1I\&2E}$, but the efficiency of the two intensity measures is practically the same (i.e., $\sigma \approx 0.3$ in all cases). The main advantage of $IM_{1B\&2E}$ is that it is sufficient ($p-\text{value} > 0.05$) for both sets of earthquake records, whereas $IM_{1I\&2E}$ is insufficient with respect to *R* for the near-source ground motions ($p-\text{value} = 0.01$). Also note that the difference between the regression estimates of *a* for the ordinary and near-source earthquake records is smaller for $IM_{1B\&2E}$ ($a = 1.16$ vs. 1.40) than for $IM_{1I\&2E}$ ($a = 1.28$ vs. 1.69). Note (e.g., from Table 6-6) that although the bias, efficiency, sufficiency of $IM_{1E\&2E}$ are about the same as those for $IM_{1B\&2E}$, the differences between the regression estimates of *a* and σ are greater for $IM_{1E\&2E}$ than for $IM_{1B\&2E}$. This suggests that, overall, $IM_{1B\&2E}$ may be more sufficient that $IM_{1E\&2E}$.

In addition to the bilinear backbone curve with negative strain hardening that is considered within $IM_{1B\&2E}$, a trilinear backbone curve (i.e., elastic-perfectly-plastic followed by negative-strain-hardening) that traces the LA20 static pushover curve has also been considered. However, the inelastic spectral displacement of this trilinear oscillator was only different than that of the corresponding EPP oscillator (which is included in $IM_{1I\&2E}$) under a few ground motions; hence, the regression analysis results for an intensity measure that includes a "trilinear" inelastic spectral displacement were practically the same as those for $IM_{1I\&2E}$.

6.4.8 Summary of Results for IM_{1eq}, IM_{1eff}, and $IM_{1B\&2E}$

Introduced as surrogates for IM_{1I} that can be computed without performing inelastic SDOF time-history analysis, the ground motion intensity measures IM_{1eq} and IM_{1eff} are found to be nearly as efficient and roughly as biased as IM_{1I} (in estimating $\theta_{\max}$) for the LA3 building model subjected to ordinary and to near-source earthquake records. However, whereas IM_{1I} is demonstrated to be relatively sufficient in these cases, IM_{1eq} and IM_{1eff} are found to be insufficient with respect to earthquake magnitude for, respectively, the near-source and ordinary ground motions. Analogous to $IM_{1I\&2E}$, note that IM_{1eq} and IM_{1eff} can be expanded to include the elastic second-mode contribution for tall, long period building models like LA9 and LA20.

In an attempt to remedy the insufficiency of $IM_{1I\&2E}$ observed for the LA20 building model subjected to near-source earthquake records (refer to Table 6-6), a similar intensity measure, denoted $IM_{1B\&2E}$, is considered that includes the spectral displacement of a bilinear (rather than EPP) oscillator with negative strain hardening. The bilinear backbone curve considered is more consistent with the NSP curve for the LA20 building model. Hence, $IM_{1B\&2E}$ is observed to be about as efficient and less biased than $IM_{1I\&2E}$ for the LA20 building model subjected to near-source and ordinary earthquake records; perhaps more importantly, $IM_{1B\&2E}$ is also found to be sufficient for both sets of records.

6.5 Results with Respect to θ_{ave}

As a comparison to the results with respect to $\theta_{\max}$ presented in the preceding section, here the efficiency and sufficiency (as well as the bias) of IM_{1E} and $IM_{1I\&2E}$ are quantified with respect to θ_{ave}, the average peak story drift angle, for one of the model buildings (namely LA9). Recall (from Chapter 5) that the participation factors used in calculating IM_{1E} or $IM_{1I\&2E}$ are different when considering θ_{ave} versus $\theta_{\max}$; hence, the values of IM_{1E} and $IM_{1I\&2E}$ in this section are different than those in the preceding section. Conceptually, however, each of the two intensity measures is the same regardless of whether θ_{ave} or $\theta_{\max}$ is the structural demand measure of interest.

6.5.1 $IM_{1I\&2E}$ vs. IM_{1E} for LA9 under Ordinary and Near-Source Ground Motions

The θ_{ave} on IM_{1E} and on $IM_{1I\&2E}$ regression analysis results for the LA9 building model subjected to the near-source and ordinary ground motions are summarized in

Table 6-10. First, note that $IM_{1I\&2E}$ is essentially unbiased (a=1.02) for both the ordinary and near-source sets of earthquake records. Although IM_{1E} is also essentially unbiased for the ordinary set (a=1.02), it is slightly biased for the near-source set (a=1.12). Recall (as discussed in Chapter 5) that a difference in the bias for the near-source versus ordinary earthquake records suggests that the intensity measure is insufficient (presumably with respect to R).

Table 6-10. Regression analysis results, for LA9 subjected to ordinary and near-source earthquake records, comparing the bias, efficiency, and sufficiency of the intensity measures $IM_{1I\&2E}$ and IM_{1E} with respect to θ_{ave}.

IM	θ_{ave} on IM		$\varepsilon \mid IM$ on M			$\varepsilon \mid IM$ on R		
	a	σ	c	p-value	σ	c	p-value	σ
(a) 59 "ordinary" earthquake records								
IM_{1E}	1.02	0.38	-0.39	0.02	0.36	0.48	0.25	0.38
$IM_{1I\&2E}$	1.02	0.23	-0.05	0.60	0.23	0.16	0.53	0.23
(b) 31 near-source earthquake records								
IM_{1E}	1.12	0.31	-0.47	0.36	0.31	-0.01	0.80	0.31
$IM_{1I\&2E}$	1.02	0.15	0.12	0.65	0.15	0.02	0.40	0.15

Moreover, the p–values listed in Table 6-10 indicate that IM_{1E} is insufficient with respect to M for the ordinary earthquake records (p–value=0.02). By taking into account the effects of inelasticity and the contribution of the second mode, however, $IM_{1I\&2E}$ is sufficient for both the ordinary and near-source earthquake records. In addition, $IM_{1I\&2E}$ is significantly more efficient than IM_{1E} for both the ordinary set ($\sigma = 0.23$ vs. 0.38) and the near-source set ($\sigma = 0.15$ vs. 0.31) of earthquake records. Based on these regression estimates of σ, three to four times fewer earthquake records are needed to estimate the regression coefficient a with $\sigma_{\ln(a)} \leq 0.10$ if $IM_{1I\&2E}$ is employed in lieu of IM_{1E}.

6.5.2 Summary of Results for $IM_{1I\&2E}$

As previously demonstrated with respect to $\theta_{\max}$, $IM_{1I\&2E}$ is found here (with respect to θ_{ave}) to be more efficient and sufficient, and less biased, than IM_{1E} for the LA9 building model subjected to ordinary or near-source ground motions. Unlike for $\theta_{\max}$, $IM_{1I\&2E}$ is found to be essentially unbiased with respect to θ_{ave}. Whereas $IM_{1I\&2E}$ is found

to be sufficient in all cases, IM_{1E} is insufficient with respect to M for the ordinary earthquake records regardless of whether θ_{ave} or θ_{max} is the structural demand measure of interest.

6.6 Results with Respect to θ_i

Instead of considering as the structural demand measure a statistic across peak story drift angles (e.g., θ_{max} or θ_{ave}), here the efficiency and bias (but not sufficiency) of IM_{1E} and $IM_{1I\&2E}$ are quantified with respect to each individual peak story drift angle, denoted θ_i. Note that the values of IM_{1E} or $IM_{1I\&2E}$ are different for each θ_i (and also different than those for θ_{ave} or θ_{max}) due to differences in the corresponding participation factors (detailed in Chapter 5). Conceptually, though, each of the intensity measures is the same regardless of whether θ_i, θ_{ave}, or θ_{max} is the structural demand measure of interest. As in the preceding section for θ_{ave}, here the θ_i results for the LA9 building model subjected to the ordinary and near-source earthquake records are considered.

6.6.1 $IM_{1I\&2E}$ vs. IM_{1E} for LA9 under Ordinary and Near-Source Ground Motions

The regressions of θ_i on IM_{1E} for the ordinary earthquake records are illustrated in Figure 6-10, where the regression estimates of a and σ are also recorded for each of the nine stories of the LA9 building model. The bias of IM_{1E} ranges (monotonically) from a=0.74 (i.e., biased high) at the bottom story to a=1.67 (i.e., biased low) at the top story. At the bottom and top stories, IM_{1E} is also relatively inefficient ($\sigma = 0.45$ and 0.55, respectively), whereas at the middle stories it is comparatively efficient (with a minimum $\sigma = 0.30$ at the third story). Lastly, note that the θ_i versus IM_{1E} data do not follow well the one-parameter (i.e., a) regression fits, particularly at the bottom and top stories. The residuals about the regression fits are generally large (i.e., greater than one) for lower levels of θ_i (or IM_{1E}), and vice-versa, suggesting that IM_{1E} may be insufficient (as it is with respect to θ_{max}). At the upper stories, the large residuals for lower, presumably elastic, levels of θ_i are likely due to the contributions of higher modes, which are most significant at the upper stories. The small (i.e., less than one) residuals for higher levels of θ_i, on the other hand, are likely a result of inelasticity. Both of these effects are reflected in the intensity measure $IM_{1I\&2E}$, considered next.

The regressions of θ_i on $IM_{1I\&2E}$ and the resulting estimates of a and σ are illustrated in Figure 6-11 for the ordinary earthquake records. Like IM_{1E}, $IM_{1I\&2E}$ is most biased at

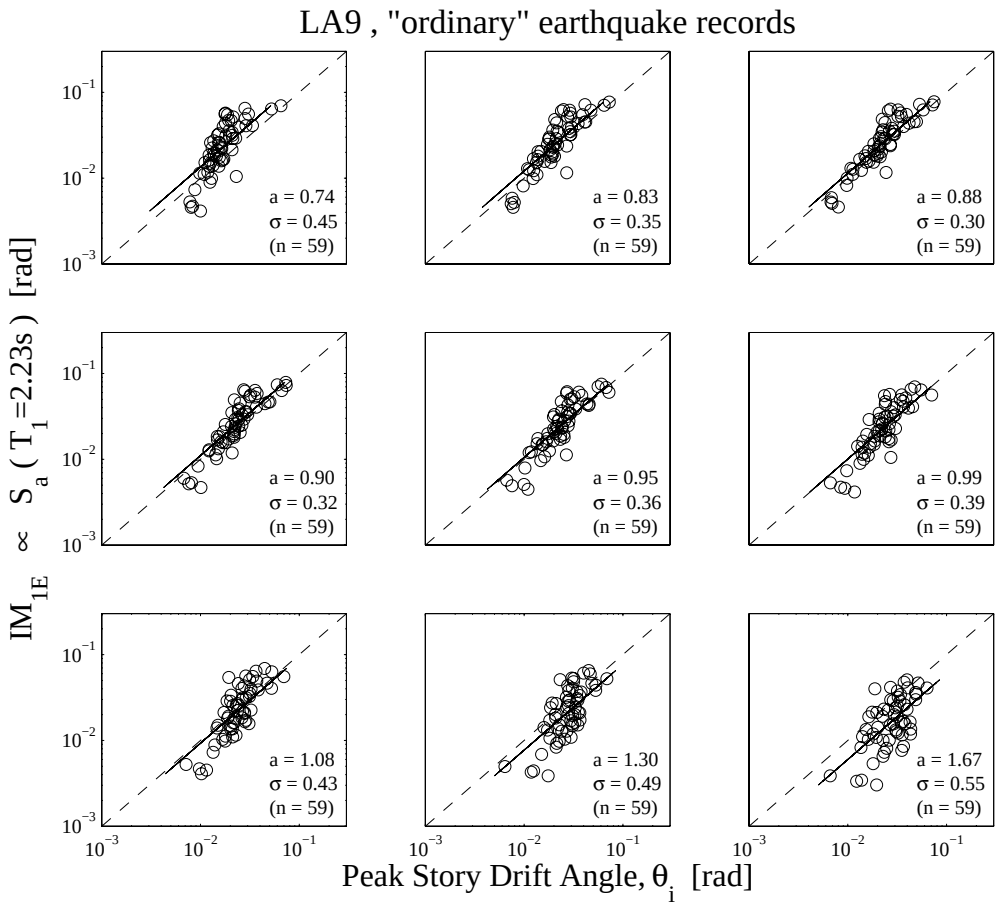

Figure 6-10. Regressions of θ_i, for LA9 subjected to "ordinary" earthquake records, on the ground motion intensity measure IM_{1E}, in order to quantify the bias (a) and efficiency (σ) of IM_{1E} for each story (ordered top-left to bottom-right).

the bottom (a=0.77) and top (a=1.24) stories; however, the bias of $IM_{1I\&2E}$ is significantly smaller (relative to IM_{1E}) at the top two stories (i.e., a=1.04 vs. 1.30 at the eighth and a=1.24 vs. 1.67 at the ninth). At all stories, $IM_{1I\&2E}$ is more efficient than IM_{1E}, with the biggest difference at the top story (i.e., $\sigma = 0.33$ vs. 0.55). It also appears that the θ_i versus $IM_{1I\&2E}$ data follows better the one-parameter regression fits, suggesting that $IM_{1I\&2E}$ is more sufficient than IM_{1E} (as is the case with respect to $\theta_{\max}$). Still, note that the residuals for higher levels of θ_i at the upper stories appear to be systematically small. This may be due to the "base isolating" effect of inelasticity in the lower stories that is not reflected in $IM_{1I\&2E}$ because the same inelastic spectral displacement is used at all stories.

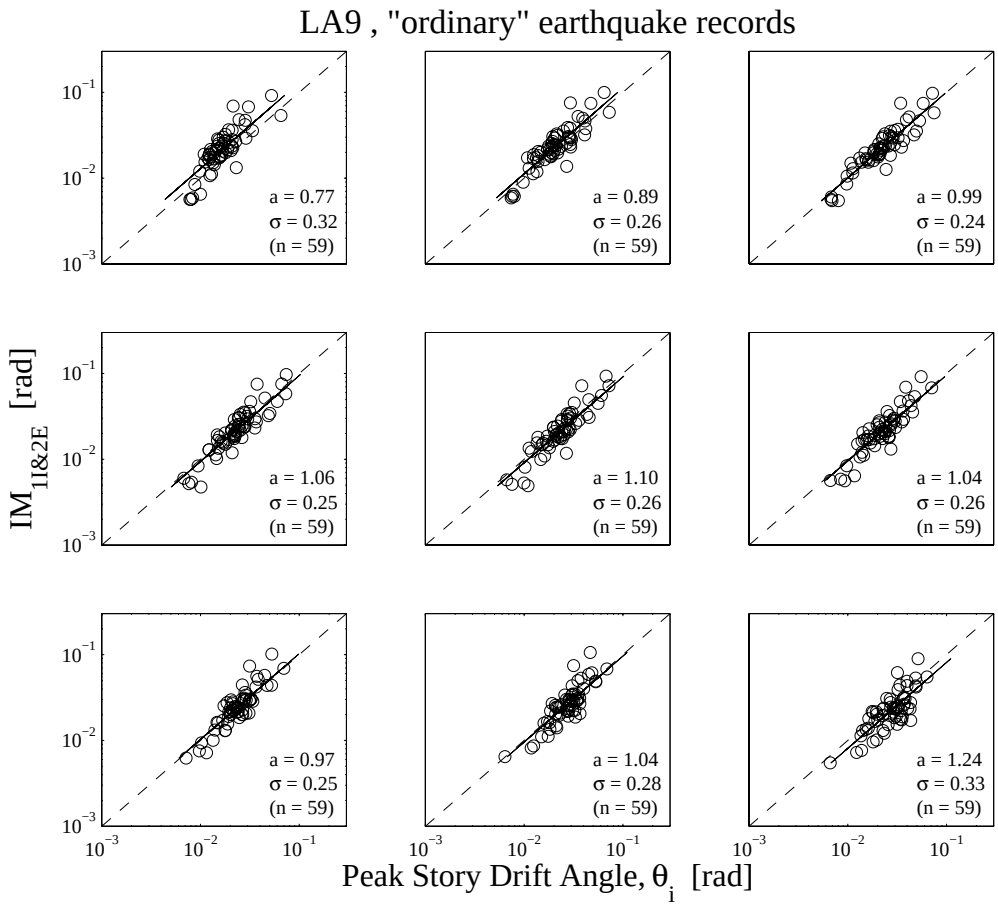

Figure 6-11. Regressions of θ_i, for LA9 subjected to "ordinary" earthquake records, on the ground motion intensity measure $IM_{1I\&2E}$, in order to quantify the bias (a) and efficiency (σ) of $IM_{1I\&2E}$ for each story (ordered top-left to bottom-right).

For the near-source earthquake records, the regressions of θ_i on IM_{1E} (and the resulting estimates of a and σ) are illustrated in Figure 6-12. Overall, the bias of IM_{1E} is smaller for the near-source earthquake records (a=0.95 to 1.22) than for the ordinary earthquake records (a=0.74 to 1.67), but still it is largest at the top story where the (elastic) contribution of higher modes is largest. The efficiency of IM_{1E} for the near-source ground motions is about the same as it is for the ordinary ground motions, and the largest regression estimate of σ is still at the top story ($\sigma = 0.62$). Unlike for the ordinary earthquake records, the θ_i versus IM_{1E} data appears to be reasonably well fit by

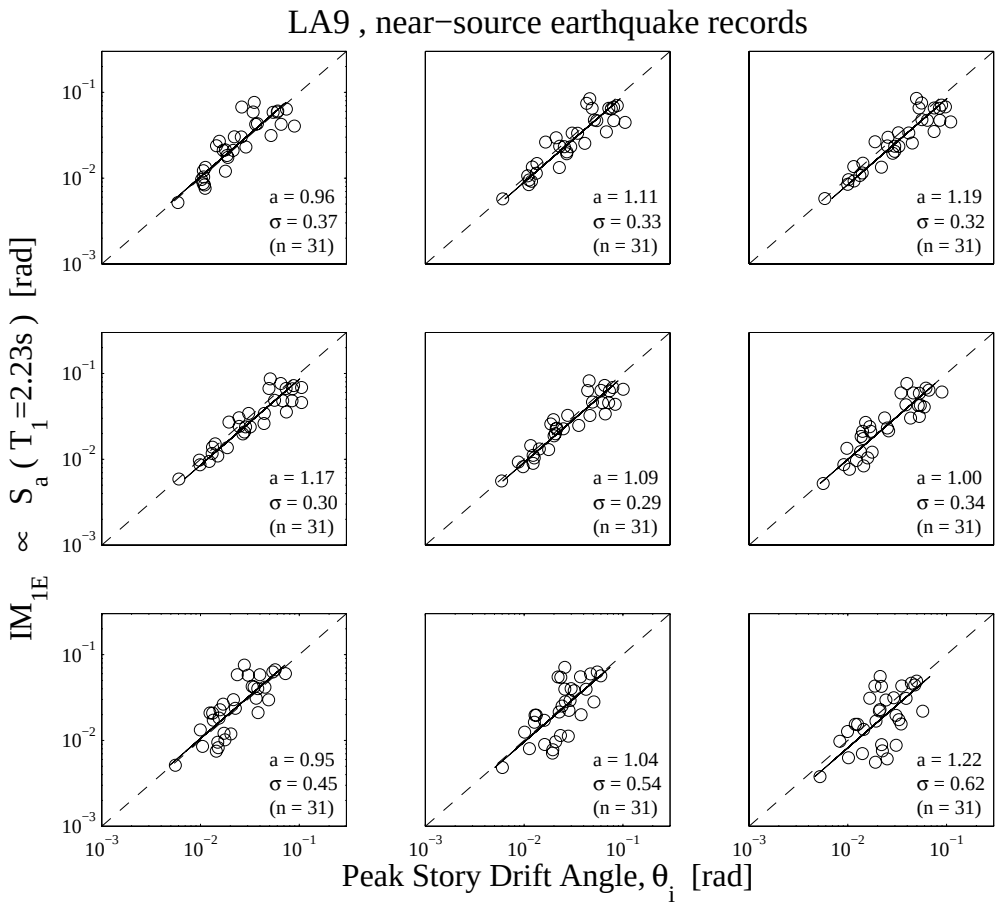

Figure 6-12. Regressions of θ_i, for LA9 subjected to near-source earthquake records, on the ground motion intensity measure IM_{1E}, in order to quantify the bias (a) and efficiency (σ) of IM_{1E} for each story (ordered top-left to bottom-right).

the log-log linear regression (except perhaps at the top three stories). However, the residuals do appear to be larger in magnitude (i.e., more different than one) at higher levels of θ_i (i.e., non-homoskedastic).

The corresponding regressions of θ_i on $IM_{1I\&2E}$ for the near-source earthquake records are illustrated in Figure 6-13. Overall, the bias of $IM_{1I\&2E}$ for the near-source ground motions (a=0.81 to 1.20) is similar to that for the ordinary ground motions (a=0.77 to 1.24), although there are story-by-story differences. At all stories, $IM_{1I\&2E}$ is more efficient than IM_{1E}, with the regression estimates of σ ranging from 0.18 to 0.46 rather than 0.29 to 0.62. Except perhaps at the top three stories, the θ_i versus $IM_{1I\&2E}$ data also appears to be nearly homoskedastic with respect to the log-log linear regression fits.

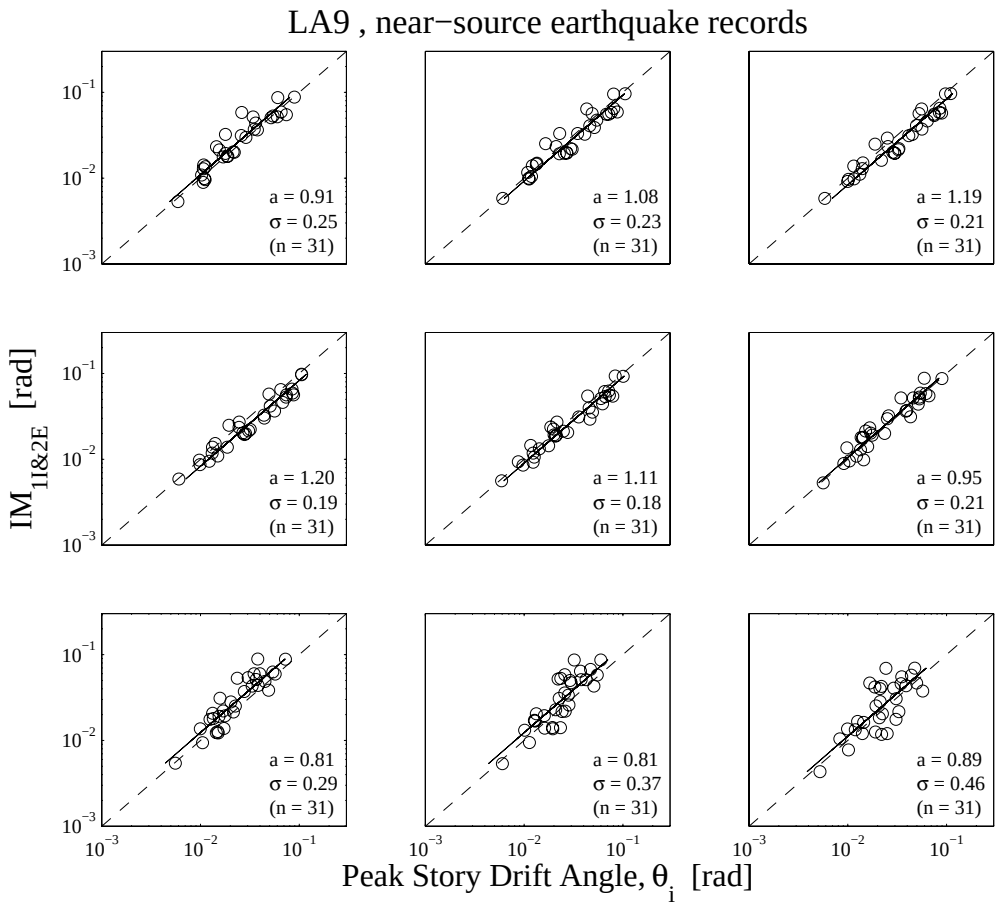

Figure 6-13. Regressions of θ_i, for LA9 subjected to near-source earthquake records, on the ground motion intensity measure $IM_{1I\&2E}$, in order to quantify the bias (a) and efficiency (σ) of $IM_{1I\&2E}$ for each story (ordered top-left to bottom-right).

6.6.2 Summary of Results for $IM_{1I\&2E}$

As previously demonstrated with respect to $\theta_{\max}$ and θ_{ave}, $IM_{1I\&2E}$ is found here (with respect to θ_i) to be more efficient than IM_{1E} for the LA9 building model subjected to ordinary or near-source ground motions. Furthermore, $IM_{1I\&2E}$ is found to be only mildly biased with respect to θ_i (i.e., a between approximately 0.8 and 1.2), whereas IM_{1E} is significantly biased low in some cases (e.g., $a \approx 1.7$). The differences in the bias and efficiency of $IM_{1I\&2E}$ versus IM_{1E} are typically most profound at the top and bottom stories, where the contributions of higher modes and/or the effects of inelasticity are most

significant. Although the sufficiency of each of the intensity measures with respect to θ_i is not explicitly tested here, the fact that the bias of $IM_{1I\&2E}$ is similar for the ordinary and near-source earthquake records suggests that it is sufficient. The homoskedasticity of the θ_i versus $IM_{1I\&2E}$ data with respect to the regression fits also serves as evidence of the sufficiency of $IM_{1I\&2E}$. Neither of these observations hold true for IM_{1E}, however. With respect to either $\theta_{\max}$ or θ_{ave}, recall that $IM_{1I\&2E}$ is found to be sufficient in all of the LA9 cases, but IM_{1E} is observed to be insufficient (with respect to earthquake magnitude) for the ordinary ground motions.

6.7 Conclusions (bearing in mind the computability of λ_{IM})

As mentioned in Chapter 5, the only perfectly efficient and sufficient (not to mention unbiased) ground motion intensity measure is *DM* itself. Defining *IM* equal to *DM* would entirely eliminate the need to estimate the complementary cumulative conditional distribution of *DM* given *IM* (i.e., $G_{DM|IM}$) and to integrate over *IM* in order to compute the annual limit-state frequency λ_{LS} via PSDA (i.e., as expressed in Equation 5-1, for example). However, directly computing the *DM* hazard λ_{DM} via PSHA would require a structure-specific attenuation relation for *DM*, which in turn would require hundreds (if not thousands) of relatively time-consuming NDA's of the model structure under ground motions from an array of *M*'s and *R*'s. Because the alternative *IM*'s evaluated in this chapter can each be computed via relatively expeditious SDOF earthquake time-history analyses (once given the modal vibration properties and a NSP curve for the structure), it is more practical to compute λ_{IM} than λ_{DM}. Obviously, though, none of the alternative *IM*'s are as efficient and sufficient as *DM*. An analogous trade-off between the efficiency and sufficiency of *IM* and the computability of the ground motion hazard λ_{IM} is also apparent amongst the other alternative *IM*'s.

For the most part (as summarized in Table 6-6), IM_{1E} is relatively inefficient and insufficient in comparison to the other alternative ground motion intensity measures. As a result, a relatively large number of NDA's and site-specific seismicity information (i.e., $\mathrm{d}G_{(M,R)|IM_{1E}}$, as explained in Chapter 5) would in general be necessary to estimate $G_{DM|IM_{1E}}$ accurately. In favor of IM_{1E}, however, the ground motion hazard $\lambda_{IM_{1E}}$ can be computed via a common PSHA that makes use of an existing attenuation relation for spectral acceleration (since $S_a(T_1)$ is effectively proportional to IM_{1E}). In a sense, the computation of $\lambda_{IM_{1E}}$ can take advantage of the hundreds of SDOF earthquake time-history analyses that were carried out in developing the attenuation relation. Note also

that $\lambda_{S_a(T_1)}$ and thereby $\lambda_{IM_{1E}}$ may already be available for the designated site (e.g., from the U.S. Geological Survey).

In contrast to IM_{1E}, for the most part $IM_{1I\&2E}$ is found to be relatively efficient and sufficient (again, as summarized in Table 6-6). For the tall, long period LA20 building model that is sensitive to P-Δ effects, though, a bilinear oscillator with negative strain hardening (for example) should be used to compute the first-mode inelastic spectral displacement in $IM_{1I\&2E}$ instead of an EPP (elastic-perfectly-plastic) oscillator (refer to Table 6-9). This bilinear version of $IM_{1I\&2E}$ is found to be sufficient with respect to M and R, although a difference in the bias of $IM_{1I\&2E}$ for the ordinary versus near-source ground motions may indicate some form of insufficiency for the LA20. In any case, the relative efficiency and sufficiency of $IM_{1I\&2E}$ for all three of the model building considered indicates that $G_{DM|IM_{1I\&2E}}$ can be estimated with relatively few NDA's and without site-specific seismicity information. However, as attenuation relations for inelastic spectral displacement are not yet available, computing the ground motion hazard $\lambda_{IM_{1I\&2E}}$ (or $\lambda_{IM_{1I}}$ for that matter) via PSHA currently requires hundreds of inelastic SDOF time-history analyses. Otherwise, conceptually there is little difference between computing $\lambda_{IM_{1I\&2E}}$ (or $\lambda_{IM_{1I}}$) and $\lambda_{IM_{1E}}$, and neither involves the hundreds of NDA's of the given MDOF structure that would be necessary to directly compute λ_{DM} via PSHA. Perhaps in the near future, attenuation relations for inelastic spectral displacement will be developed, facilitating a PSHA for $IM_{1I\&2E}$ (or IM_{1I}). Note, incidentally, that in addition to being relatively efficient and sufficient, $IM_{1I\&2E}$ (or IM_{1I}) is unbiased for the LA3 building model. In general, such an unbiased and efficient intensity measure might be treated as an approximate DM, an option pursued further in Chapter 7.

Although the intensity measure $IM_{1E\&2E}$ is found to be relatively efficient and sufficient for the LA20 building model (even in comparison to $IM_{1I\&2E}$), it is relatively inefficient and insufficient for the LA3 and LA9 building models (as evidenced by Table 6-6). In computing the ground motion hazard via PSHA, though, the advantage of $IM_{1E\&2E}$ is that existing attenuation relations for $S_a(T_1)$ and $S_a(T_2)$ can be combined in order to approximate an attenuation relation for $IM_{1E\&2E}$. With an attenuation relation for $IM_{1E\&2E}$, the ground motion hazard $\lambda_{IM_{1E\&2E}}$ can be computed in the same manner as $\lambda_{IM_{1E}}$ (i.e., without hundreds of SDOF earthquake time-history analyses). Because of the many possible pairs of modal periods and participation factors, the PSHA carried out to compute $\lambda_{IM_{1E\&2E}}$ must, of course, be structure specific. Nonetheless, one can easily envision a software package or even a U.S. Geological Survey website capable of addressing this problem easily.

Analogous to $IM_{1E\&2E}$, the intensity measure IM_{1eq} is merely a (complicated) function of elastic spectral displacements. In fact, IM_{1eq} was introduced as a surrogate for IM_{1I} that could conceivably take advantage of existing attenuation relations for elastic spectral accelerations to compute, in an approximate manner, the ground motion hazard $\lambda_{IM_{1eq}}$ via PSHA. Alternatively, the same elastic response spectra data that is used in developing existing attenuation relations can be used to form an attenuation relation for IM_{1eq}, without re-running hundreds of SDOF time-history analyses; this is true even if IM_{1eq} is computed iteratively (an option mentioned in Section 6.4.5 with the results for IM_{1eq}). In turn, such an attenuation relation for IM_{1eq} can be used to compute $\lambda_{IM_{1eq}}$ more accurately. (Note that the same can be done for $IM_{1E\&2E}$, since it too involves only elastic spectral displacements.) Although IM_{1eq} is found (in Section 6.4.5) to be about as efficient as IM_{1I} for the first-mode dominated LA3 building model, a disadvantage of IM_{1eq} is that it is relatively insufficient for the near-source earthquake records.

Also somewhat similar to $IM_{1E\&2E}$, the intensity measure IM_{1eff} is (approximately) a function of $S_a(T_1)$ and $S_a(2T_1)$. Like IM_{1eq}, IM_{1eff} was in fact introduced as a surrogate to IM_{1I} that can take advantage of existing attenuation relations for elastic spectral accelerations in computing the ground motion hazard $\lambda_{IM_{1eff}}$ via PSHA. Since IM_{1eff} is a log-log linear combination of $S_a(T_1)$ and $S_a(2T_1)$, given an estimate of the correlation between $S_a(T_1)$ and $S_a(2T_1)$ (Inoue & Cornell 1990) an attenuation relation (median and dispersion) for IM_{1eff} can be easily derived from those for spectral acceleration (Cordova *et al.* 2000). Thus, $\lambda_{IM_{1eff}}$ can be estimated nearly as readily as $\lambda_{IM_{1E}}$. However, IM_{1eff} is found (in Section 6.4.6) to be relatively insufficient for the LA3 building model subjected to the ordinary earthquake records. As for IM_{1eq}, apparently the advantage of IM_{1eff} in terms of the computability of its hazard is tempered by its inefficiency and/or insufficiency.

Of all the alternative ground motion intensity measures evaluated in this chapter, the only two for which λ_{IM} cannot be computed (or estimated) by taking advantage of existing attenuation relations for spectral acceleration, or at least the same response spectra data used to develop these relations, are $IM_{1I\&2E}$ and IM_{1I}. Given that $IM_{1I\&2E}$ is found here to be relatively efficient and sufficient for both ordinary and near-source ground motions, developing an attenuation relation for $IM_{1I\&2E}$ appears to be the best way to move forward. In the near-source region, where $IM_{1I\&2E}$ is particularly effective but the existing ground motion data is relatively sparse, simulated earthquake records might be used to develop such an attenuation relation.

Without using an attenuation relation, in the following chapter a simulation-based approach for computing the ground motion hazard in terms of any *IM* is demonstrated for

a site susceptible to near-source and ordinary ground motions. Using simulated earthquake records, the ground motion hazard at the site is computed in terms of IM_{1E} and $IM_{1I\&2E}$, in particular, as well as in terms of a structural demand measure (*DM*) from nonlinear dynamic analysis of a building at the site (i.e., λ_{DM}). This "exact" λ_{DM} is then used to judge the accuracy of PSDA using the conventional IM_{1E} versus $IM_{1I\&2E}$, which incorporates the contribution of a higher mode of structural response and the effects of inelasticity.

Chapter 7

Demonstration of PSDA at a Near-Fault Site Using Simulated Earthquake Records

7.1 Introduction

As demonstrated in Chapter 6, the alternative ground motion intensity measures (*IM*'s) introduced in Chapter 5 are typically more "efficient" and "sufficient" than spectral acceleration (at or near the fundamental period of the structure of interest), which is customarily employed as the *IM* in a structural performance assessment (i.e., PSDA). This is particularly true for near-source ground motions and/or tall, long period buildings. Unlike for spectral acceleration, however, the ground motion hazard at a site in terms of the alternative *IM*'s is not currently available or readily computable. Particularly for intensity measures like IM_{1I} or $IM_{1I\&2E}$ (defined in Chapter 5) that incorporate an inelastic spectral displacement, new attenuation relations need to be developed in order to compute the ground motion hazard in terms of these *IM*'s via PSHA. While attenuation relations for inelastic spectral displacement that are applicable near a fault are potentially an area of future research, in the meantime an alternate approach to PSHA that does not employ an attenuation relation is demonstrated in this chapter. The alternate approach can be used to compute the ground motion hazard at site in terms of any *IM*.

The approach demonstrated in this chapter for computing the ground motion hazard at a near-fault site makes use of (i) the mean annual rates of recurrence for "characteristic events" on local faults that are estimated by the U.S.G.S. Working Group on California

Earthquake Probabilities (1999), and (ii) earthquake records at the site that are simulated for such events by Mai (2002) with a stochastic finite-source rupture model.[1] The simulated earthquake records for each characteristic event reflect the randomness associated with several aspects of fault rupture, so the conditional (given the characteristic event) probability distribution of (any) *IM* can be estimated from the values of *IM* for the simulated earthquake records. With conditional distributions of *IM* and the mean annual rates of recurrence for the characteristic events considered, the ground motion hazard at the site can be computed. Note that non-characteristic events (i.e., event of smaller magnitude) are not considered here, but their contribution to the ground motion hazard at a site could also be computed via a similar approach. At high levels of ground motion, though, the contribution of non-characteristic events to the ground motion hazard may be comparatively small.

The simulation-based approach demonstrated in this chapter for computing the ground motion hazard at a site in terms of any *IM* can also be used to compute a structural demand hazard curve. However, doing so requires that the structural demand be computed via NDA (nonlinear dynamic analysis) of the given structure for all of the simulated earthquake records. This method of computing a structural demand hazard curve is somewhat similar in concept to that developed by Collins *et al.* (1995); it also calls for many more NDA's than does PSDA, which makes use of an *IM* hazard curve. Nevertheless, here the "direct" computation of a drift demand hazard curve via the simulation-based approach provides an "exact" result to compare with the results of PSDA using alternative *IM*'s.

In this chapter, the ground motion hazard in terms of the intensity measures IM_{1E} and $IM_{1I\&2E}$ (defined in Chapter 5) is computed via the simulation-based approach for a University of California at Berkeley (UCB) site located near the Hayward-Rogers Creek (HRC) Fault system. Employing the resulting IM_{1E} and $IM_{1I\&2E}$ hazard curves, drift demand hazard curves for the SAC L.A. 9-story SMRF building hypothetically located at the near-fault site are computed via PSDA. These drift demand hazard curves are compared with that computed directly via the simulation-based approach in order to illustrate the benefits of employing an efficient and sufficient *IM* (like $IM_{1I\&2E}$ in comparison to IM_{1E}) in PSDA.

[1] Incidentally, note that simulated earthquake records like the ones employed here may also prove useful, due to the limited number of recorded near-source ground motions, for developing new attenuation relations that are applicable in the near-field.

7.2 Characteristic Events on the HRC Fault System

A schematic representation of the HRC Fault system (and the nearby UCB site) is depicted in Figure 7-1. Although there are several other earthquake fault systems in the San Francisco Bay Region that pose a threat (e.g., San Andreas), the HRC Fault system is the closest to the UCB site (3.6 km) and it is the only one likely to induce directivity effects there. Hence, the HRC Fault system is the only one considered in this chapter.

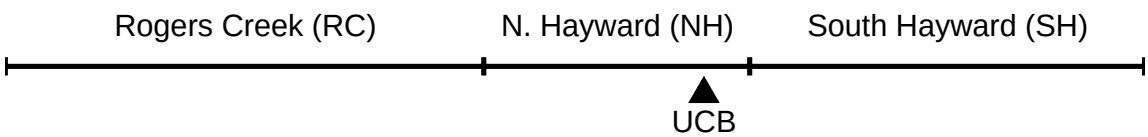

Figure 7-1. Schematic representation of HRC Fault system and UCB site (map view).

The three segments of the HRC Fault system shown in Figure 7-1 (i.e., RC, NH, and SH) are delimited by the 1999 U.S.G.S. Working Group on California Earthquake Probabilities (hereafter referred to as WG99). The characteristic events considered in this chapter, referred to as "rupture sources" by WG99, are earthquakes that rupture one or more of these three fault segments (e.g., RC+NH). The WG99 estimates of the mean annual rates of recurrence for the six possible contiguous HRC rupture sources are listed in Table 7-1. The areas of the rupture sources are also listed in the table. Note that WG99 also defined a seventh HRC rupture source, referred to as a "floating earthquake," that is disregarded here. The estimated mean annual rate of recurrence for the floating earthquake is as small as that for the SH+NH+RC rupture source (i.e., 0.22×10^{-3}/year),

Table 7-1. Mean annual recurrence rates and rupture areas for six potential rupture sources, or "characteristic events," on the HRC Fault system, from WG99.

Rupture Source	Mean Rate [1/yr]	Area [km^2]
RC	3.49×10^{-3}	63 x 12
SH	2.69×10^{-3}	52 x 12
NH	2.58×10^{-3}	35 x 12
SH+NH	1.91×10^{-3}	87 x 12
NH+RC	0.51×10^{-3}	98 x 12
SH+NH+RC	0.22×10^{-3}	150 x 12

but its moment magnitude (6.9) is significantly smaller than the mean magnitude for the SH+NH+RC rupture source (as detailed below).

7.3 Simulated Earthquake Records at a UCB Site

For each of the rupture sources listed above in Table 7-1, a stochastic fault-rupture model that is suitable for generating near-field (and far-field) ground motions is used to simulate 30 earthquake records at the UCB site (Mai 2002). The input for the kinematic rupture model includes (i) the spatial distribution of slip on the fault plane, (ii) the slip velocity time function (uniform over the fault plane), which is assumed to be a simple boxcar function of length τ_r, the rise time, and (iii) the rupture propagation velocity, denoted v_r, expressed as a percentage of the local shear wave velocity. The location of the hypocenter on the fault plane is also input. As detailed in the subsections below, the spatial distribution of slip and the rise time depend (stochastically) on the seismic moment prescribed for each rupture simulation, or equivalently on the moment magnitude M_w. In turn, M_w is a random function of the area of the rupture source (listed in Table 7-1). Independently of M_w, the location of the hypocenter on the rupture plane is also randomized. The rupture velocity, however, is deterministically specified as 85% of the local shear wave velocity.[2]

It is important to note that, for the applications demonstrated in this chapter, the simulated earthquake records have been scaled up by a factor of two.[3] Without scaling, the inelastic spectral displacement that is a part of $IM_{1I\&2E}$ is in fact elastic (i.e., it does not surpass the elastic limit d_y) for many of the simulated earthquake records. Even for the other unscaled earthquake records, the "equal displacements rule" (Veletsos & Newmark 1960) tends to apply, such that the inelastic spectral displacement is about the same as its elastic counterpart. Scaling the earthquake records by a factor of two, on the other hand, makes it possible to demonstrate the benefits of employing (in PSDA) a ground motion intensity measure that incorporates an inelastic spectral displacement. Perhaps scaling of the earthquake records can be interpreted as considering a structure that has been designed according to a governing drift limit twice as large as that used to design the SAC L.A. 9-story SMRF building.

---

[2] A deterministic rupture velocity seems reasonable because (i) the variability of v_r (as a percentage of local shear wave velocity) is presumably small, and (ii) in a brief check, the sensitivity of the simulated earthquake records to variations in v_r is observed to be mild.

[3] Recall that the recorded "near-source" ground motions considered in Chapter 6 are also scaled up by a factor of two.

7.3.1 Earthquake Moment Magnitude given Rupture Source Area

Following the assumptions of WG99, the earthquake moment magnitude (i.e., M_w) for each rupture simulation is drawn from a normal (i.e., Gaussian) probability distribution of M_w given A, the area of the rupture source. The mean M_w for each of the six HRC rupture sources (of area given in Table 7-1)[4] is listed in Table 7-2, and the standard deviation of M_w given A is assumed to equal 0.12 (both from WG99).

Table 7-2. Mean M_w for each of the HRC rupture sources (of area given in Table 7-1), from WG99.

Rupture Source	Mean M_w
RC	7.06
SH	6.88
NH	6.63
SH+NH	7.08
NH+RC	7.21
SH+NH+RC	7.37

7.3.2 Spatial Distribution of Slip on Rupture Plane given Seismic Moment

As detailed in (Mai 2002), the spatial distribution of slip on the rupture plane for each simulation is generated as a random field with correlation lengths that depend on the seismic moment, or equivalently on M_w. Of course, the mean slip (i.e., spatial average) is also directly related to seismic moment. It is important to randomize the spatial distribution of slip because it can have a profound effect on the nature of nearby ground motions. For example, large slip "asperities" between the hypocenter and a nearby site can result in pulse-like ground motions (e.g., Aagaard *et al.* 2001).

7.3.3 Rise Time given Seismic Moment

Assumed to be uniform over the rupture plane, the slip rise time τ_r is drawn from a lognormal distribution given the seismic moment (or equivalently the value of M_w). The median τ_r is taken to be the average of two equations derived by Somerville *et al.* (1999) for τ_r as a function of M_w. Based on the data used by Somerville *et al.* to develop these

[4] Note that the (epistemic) uncertainty in the area of each rupture source is ignored in this study.

equations, the dispersion of τ_r given M_w is estimated as 0.40. According to Somerville (2001), the rise time is strongly correlated with the period of a pulse-like ground motion.

7.3.4 Location of Hypocenter

Like the spatial distribution of slip and the rise time, the location of the hypocenter on a rupture plane can significantly affect the ground motions at a nearby site, due to the effects of rupture directivity. Thus, the location of the hypocenter is randomized according to the (independent) probability distributions of the depth and along-strike position that are illustrated in Figure 7-2 (Mai 2002).

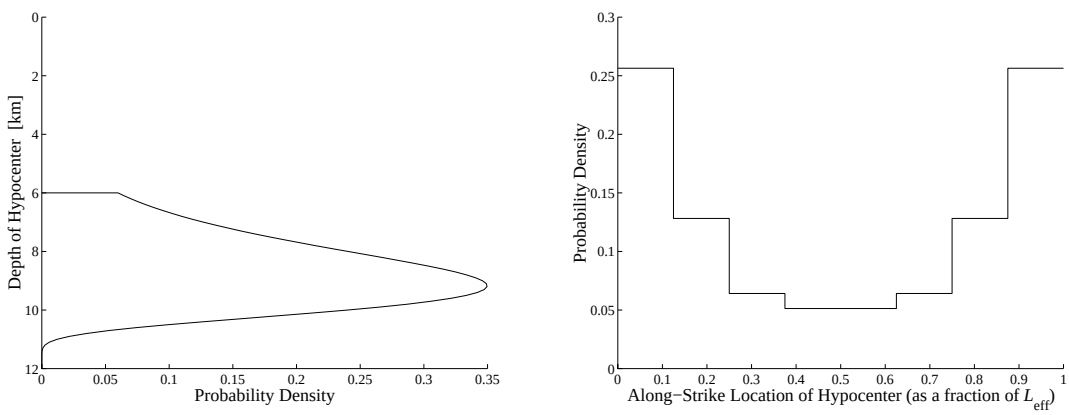

Figure 7-2. Probability distributions for the **(a)** depth and **(b)** along-strike position of the hypocenter.

The distribution of the depth of the hypocenter shown in Figure 7-2a corresponds to a lognormal distribution of the distance from the bottom of the rupture area to the hypocenter. The median of the lognormal distribution is 3.3km, which corresponds to a depth about three-quarters the width of the rupture area, and the standard deviation of the natural logarithm is set equal to 0.40. However, the lognormal distribution is truncated (and renormalized) at a distance corresponding to one-half the width of the rupture area (i.e., 12km for the HRC rupture sources).

Independently from the depth of the hypocenter, the along-strike position of the hypocenter is drawn from the probability distribution illustrated in Figure 7-2b. Note that the effective length of the rupture plane L_{eff} is less than the full length (Mai & Beroza 2000); the extra area (split evenly among the two ends of the fault plane) is left as a buffer in which the hypocenter cannot be located. Clearly the assumed distribution of

along-strike hypocenter position assigns more probability to unilateral (rather than bilateral) rupture.

7.4 Ground Motion Hazard at the UCB Site

As detailed above, the simulated earthquake records for each rupture source (or characteristic event of given area) reflect the randomness associated with various aspects of fault rupture. Consequently, these simulated earthquake records can be used to estimate, for each rupture source, the probability of exceeding a particular level of ground motion. Weighting these exceedance probabilities by the mean annual recurrence rate for each rupture source and summing over the rupture sources yields an estimate of the ground motion hazard, as expressed mathematically in Equation 7-1.

$$\lambda_{IM}(x) = \sum_i G_{IM|RS_i}(x)\, \nu_{RS_i} \tag{7-1}$$

Note that, like the PSDA integral expressed in Equation 1-1, Equation 7-1 is an application of the total probability theorem. The ground motion hazard $\lambda_{IM}(x)$, recall, is strictly the mean annual frequency of *IM* exceeding the value *x*. The term ν_{RS_i} denotes the mean annual rate (or frequency) of recurrence for the rupture source RS_i; for the six HRC rupture sources considered in this chapter, ν_{RS_i} has been estimated by WG99 (as listed in Table 7-1). Lastly, the term $G_{IM|RS_i}(x)$ denotes the probability of *IM* exceeding the value *x* given an earthquake from RS_i. Here, this conditional exceedance probability is estimated from the values of *IM* for the 30 earthquake records simulated for each rupture source. Recall (from Section 7-3) that the simulated earthquake records considered here have been scaled up by a factor of two.

For each of the six HRC rupture sources, normal probability plots of the logarithms of the *IM* data (from the 30 simulated earthquake records) are provided in Figure 7-3 for IM_{1E} and Figure 7-4 for $IM_{1I\&2E}$. Recall that the calculation of IM_{1E} and $IM_{1I\&2E}$ involves the dynamic analysis of only SDOF oscillators. The fact that the data are roughly linear in the normal probability plots suggests that it is reasonable to assume a lognormal distribution of *IM* given RS_i.[5] In this case, $G_{IM|RS_i}(x)$ can be computed according to

[5] For the three rupture sources that include the RC fault segment (i.e., RC, NH+RC, and SH+NH+RC), in particular, note that a divergence of the data from the lognormal assumption is observed. Apparently, the lognormal distributions overestimate the values of *IM* corresponding to low exceedance probabilities, a phenomenon referred to here as "bounding."

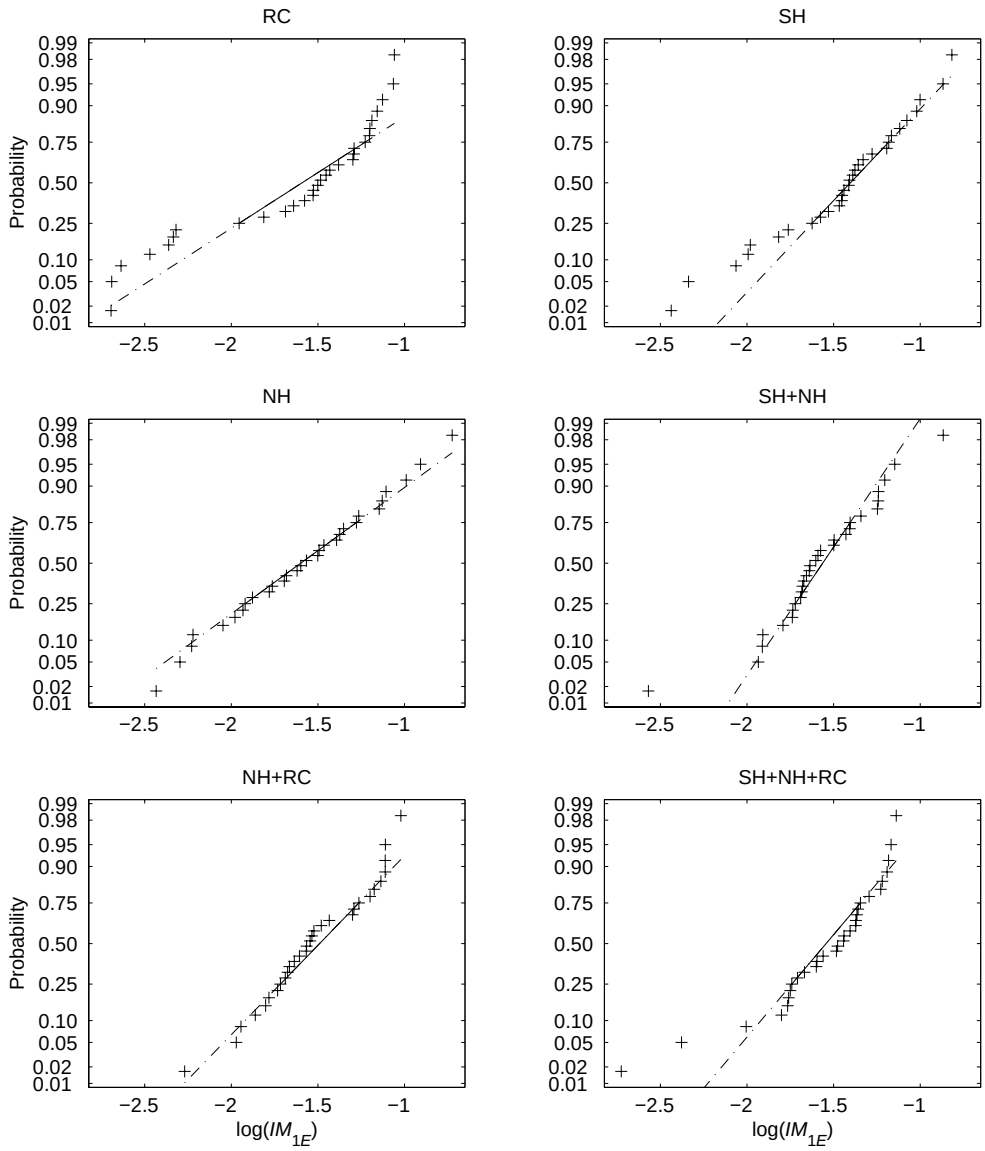

Figure 7-3. Normal probability plots of the log(IM_{1E}) data from the 30 earthquake records simulated for each of the six HRC rupture sources (and scaled up by a factor of two).

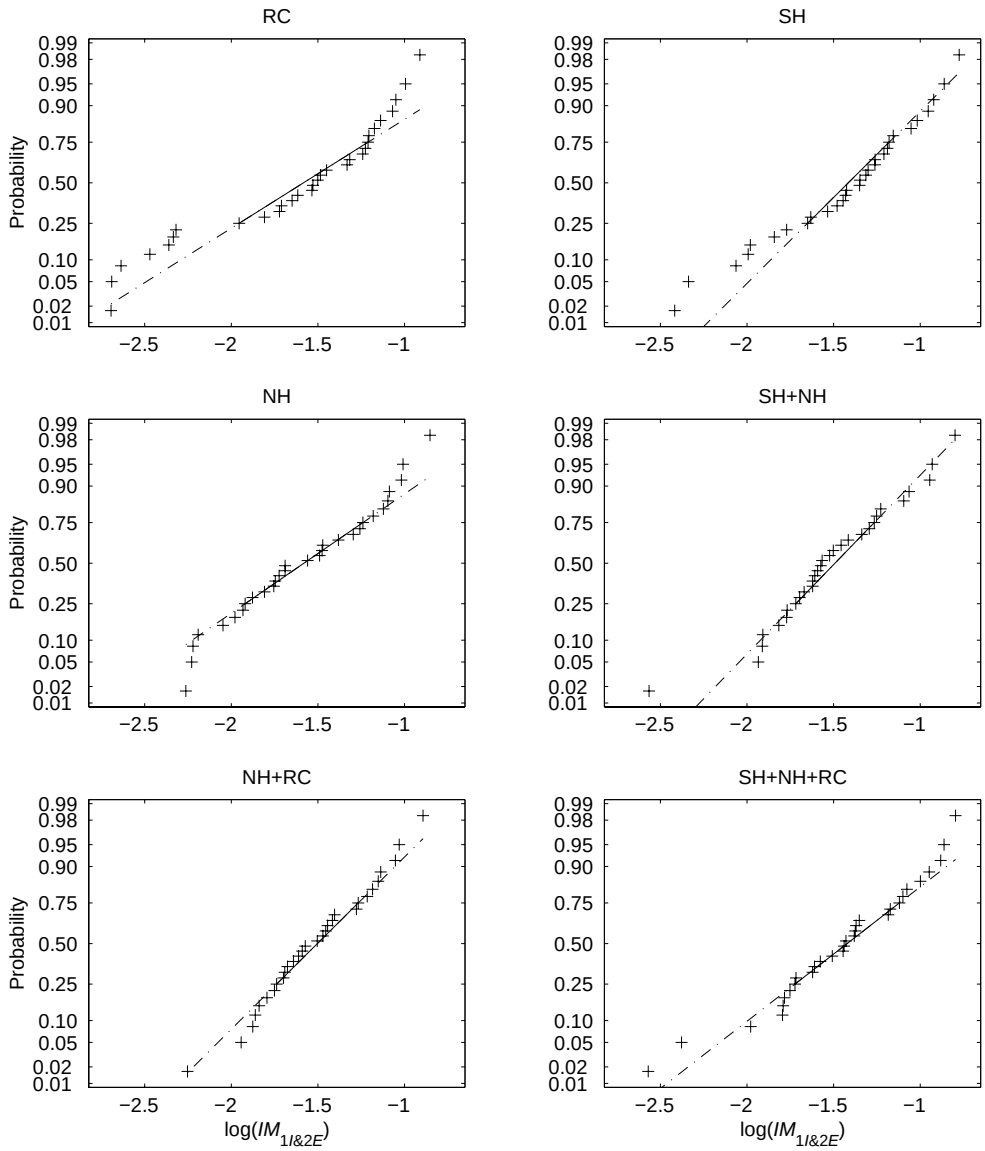

Figure 7-4. Normal probability plots of the log($IM_{1I\&2E}$) data from the 30 earthquake records simulated for each of the six HRC rupture sources (and scaled up by a factor of two).

Equation 7-2, where $\eta_{IM|RS_i}$ and $\sigma_{\ln IM|RS_i}$ are the median and dispersion[6] of *IM* given RS_i.

$$G_{IM|RS_i}(x) = 1 - \Phi\left[\frac{\ln x - \ln \eta_{IM|RS_i}}{\sigma_{\ln IM|RS_i}}\right] \tag{7-2}$$

Calculated from the same *IM* data plotted in Figure 7-3 and Figure 7-4, the median and dispersion of *IM* given RS_i are listed in Table 7-3 for IM_{1E} and $IM_{1I\&2E}$. Note that, for reasons explained below, the median $IM_{1I\&2E}$ for each rupture source is systematically larger than the median IM_{1E}; except for the NH rupture source, the dispersion of $IM_{1I\&2E}$ is also systematically larger than the dispersion of IM_{1E} for each rupture source. Although the RC and SH rupture sources apparently pose the weakest and strongest threats (i.e., smallest and largest medians), respectively, it is difficult to make fine distinctions among the six rupture sources. With only 30 data points for each rupture source, the observed dispersions translate into relatively imprecise estimates of the medians. For the RC rupture source, for example, the dispersion of each median estimate is about $1.2/\sqrt{30} = 0.22$ (i.e., each median has been estimated within only about ±22% due to the large uncertainty).

Table 7-3. Median and dispersion of IM_{1E} and of $IM_{1I\&2E}$ from the 30 earthquake records simulated for each HRC rupture source (and scaled up by a factor of two).

		Median		Dispersion	
i	RS_i	IM_{1E} [rad]	$IM_{1I\&2E}$ [rad]	IM_{1E}	$IM_{1I\&2E}$
1	RC	0.0222	0.0227	1.21	1.25
2	SH	0.0343	0.0364	0.92	0.97
3	NH	0.0256	0.0259	0.99	0.95
4	SH+NH	0.0266	0.0305	0.72	0.84
5	NH+RC	0.0299	0.0305	0.70	0.72
6	SH+NH+RC	0.0281	0.0348	0.82	0.97

[6] Recall that the median is strictly the geometric mean, or the exponential of the average of the natural logarithms of the data, and the dispersion refers to the standard deviation of the natural logarithms of the data.

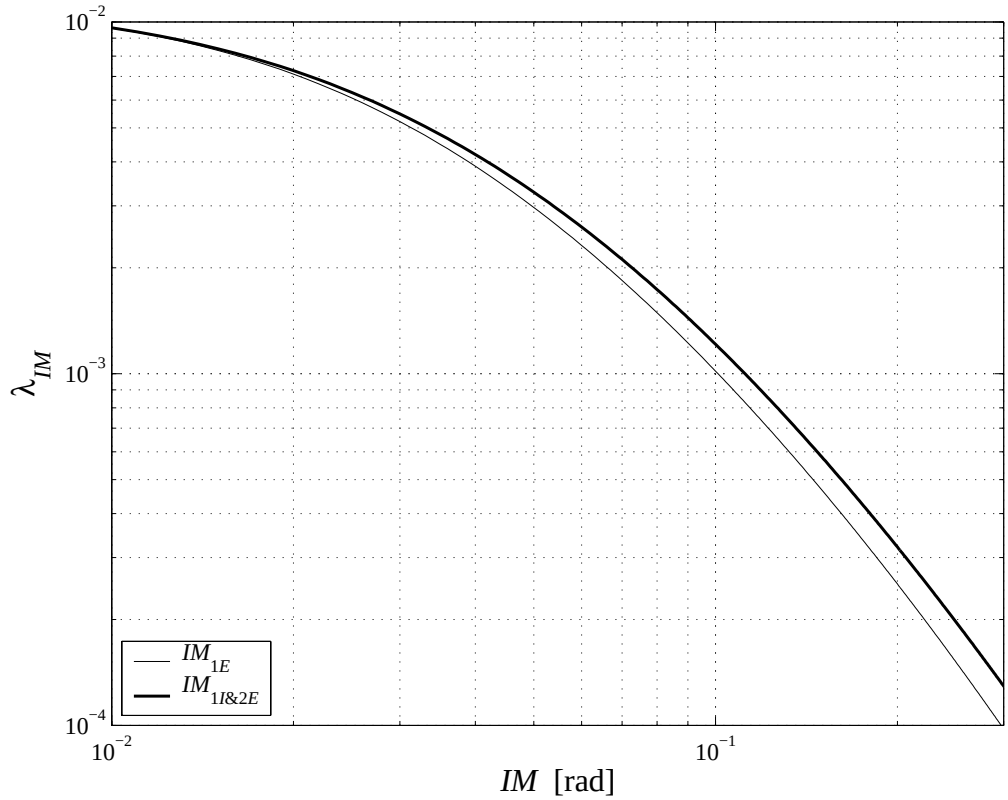

Figure 7-5. Ground motion hazard in terms of IM_{1E} and $IM_{1I\&2E}$ at the UCB site computed using the earthquake records simulated for six "characteristic events" on the HRC Fault system (rather than via PSHA). Recall that the simulated earthquake records have been scaled up by a factor of two.

Substituting into Equation 7-1 the medians and dispersion listed in Table 7-3, the ground motion hazard at the UCB site in terms of IM_{1E} and of $IM_{1I\&2E}$ is computed, as illustrated in Figure 7-5. Since both ground motion intensity measures are estimates of $\theta_{\max}$ (in units of radians), their hazard curves can be plotted concurrently. Note that at relatively small values of the *IM*'s (i.e., 0.01 to 0.02 radians), the ground motion hazard in terms of IM_{1E} and $IM_{1I\&2E}$ are nearly identical. This is because the values of IM_{1E} and $IM_{1I\&2E}$ are approximately equal in this range. Recall that $IM_{1I\&2E}$ is elastic (like IM_{1E}) at low ground motion intensity levels (i.e., at spectral displacements less than the yield displacement specified for $IM_{1I\&2E}$). In addition, the second mode contribution to $IM_{1I\&2E}$ happens to be insignificant because the maximum frequency included in the ground motion simulations is only 1.6hz (a limitation discussed further at the conclusion of this chapter). In effect, for this situation $IM_{1I\&2E}$ is approximately equal to IM_{1I}. Thus, the

fact that the median $IM_{1I\&2E}$ given RS_i is systematically larger than the median IM_{1E} given RS_i (in Table 7-3) indicates that the inelastic spectral displacements for the simulated earthquake records are, on average, larger than their elastic counterparts. This difference is also reflected in Figure 7-5, where for larger values of the *IM*'s (i.e., greater than about 0.02 radians) the ground motion hazard in terms of $IM_{1I\&2E}$ is larger than the hazard in terms of IM_{1E}.

7.5 Drift Demand Hazard for the LA9 Building Model at the UCB Site

As demonstrated above, the simulation-based approach presented in this chapter can be used to compute the ground motion hazard at a site in terms of any intensity measure (e.g., $IM_{1I\&2E}$ or IM_{1E}). In fact, the same approach can be used to compute a structural demand (e.g., $\theta_{\max}$) hazard curve, as demonstrated here for the LA9 building model[7] hypothetically located at the UCB site. Of course, applying the simulation-based approach to compute the $\theta_{\max}$ hazard requires that NDA of the full MDOF model of the building be carried out for all of the simulated earthquake records (which, recall, have been scaled up by a factor of two). In contrast, PSDA only requires NDA (of the MDOF building model) under a relatively small number of earthquake records, because it also makes use of the *IM* hazard at the site and the relationship between *IM* and $\theta_{\max}$, which has comparatively small dispersion. As demonstrated below, though, the precision and accuracy of a PSDA estimate of the $\theta_{\max}$ hazard depends on the efficiency and sufficiency of the intensity measure employed (e.g., $IM_{1I\&2E}$ versus IM_{1E}).

7.5.1 Simulation-Based Approach

The same approach used to compute the ground motion hazard curves illustrated in Figure 7-5 is followed here to compute a drift demand (i.e., $\theta_{\max}$) hazard curve for the LA9 building model at the UCB site. In doing so, $\theta_{\max}$ is computed via NDA of the LA9 building model for all of the simulated earthquake records (180 in total). The median and dispersion of $\theta_{\max}$ from the 30 earthquake records simulated for each of the six HRC rupture sources are listed in Table 7-4. Note (by comparing with Table 7-3) that the median $\theta_{\max}$ for each rupture source is systematically larger than the median $IM_{1I\&2E}$ (and median IM_{1E}); the dispersion of $\theta_{\max}$ for each rupture source is about the same as the dispersion of $IM_{1I\&2E}$ (i.e., neither systematically larger nor smaller). As for $IM_{1I\&2E}$ and

[7] The LA9 building model, which is described in detail in Appendix B, is one of the building models considered in Chapter 6.

IM_{1E}, note that the more distant RC segment, rupturing alone, causes lower median $\theta_{\max}$ than any of the other rupture sources. Given the observed dispersions in $\theta_{\max}$, however, the uncertainty in the estimates of the medians (and their differences among rupture sources) is relatively large for this sample size (i.e., dispersions of the median estimates as large as $1.29/\sqrt{30} = 0.24$).

Table 7-4. Median and dispersion of $\theta_{\max}$ for the LA9 building model subjected to the 30 earthquake records simulated for each of the HRC rupture sources (and scaled up by a factor of two).

i	RS_i	$\theta_{\max}$ Median [rad]	$\theta_{\max}$ Dispersion
1	RC	0.0247	1.29
2	SH	0.0445	1.04
3	NH	0.0311	0.97
4	SH+NH	0.0366	0.81
5	NH+RC	0.0378	0.70
6	SH+NH+RC	0.0421	0.99

Assuming that $\theta_{\max}$ given RS_i is lognormally distributed (with median and dispersion listed in Table 7-4)[8] and applying Equation 7-1 (with $\theta_{\max}$ substituted for *IM*), the $\theta_{\max}$ demand hazard illustrated in Figure 7-6 is computed. This drift demand hazard curve is considered to be "exact" and will be compared (in the following subsection) with the results of PSDA. Also shown in Figure 7-6 are the ground motion hazard curves in terms of $IM_{1I\&2E}$ and IM_{1E}. Note that the hazard curve for $\theta_{\max}$ is larger than that for $IM_{1I\&2E}$ or for IM_{1E}, even in the elastic range (i.e., around 0.01 radians). This difference is due to both the bias of each *IM* in estimating $\theta_{\max}$, and the dispersion of $\theta_{\max}$ given *IM*. As demonstrated in the next subsection, PSDA accounts for this bias and dispersion.

[8] The lognormal assumption for $\theta_{\max}$ given RS_i has been confirmed with normal probability plots, as it was for *IM* given RS_i (in Figure 7-3 and Figure 7-4). In fact, the normal probability plots for $\theta_{\max}$ are quite similar to those for $IM_{1I\&2E}$, including the observed "bounding."

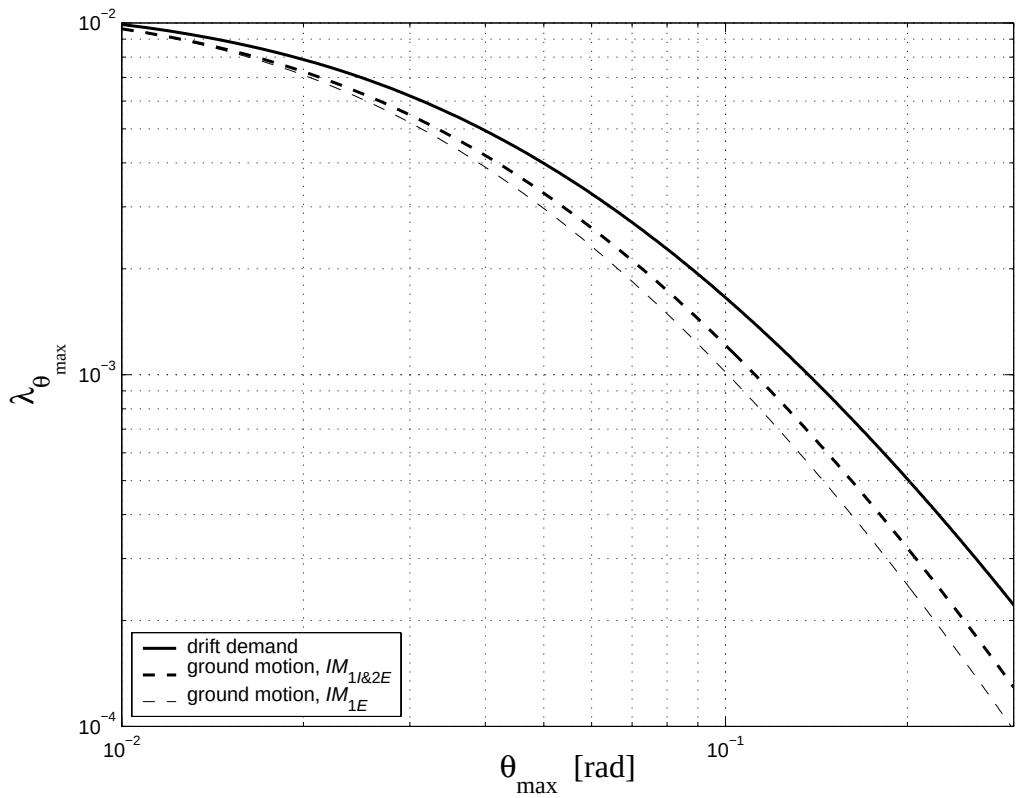

Figure 7-6. "Exact" drift demand (i.e., $\theta_{\max}$) hazard for the LA9 building model at the UCB site, compared with the ground motion hazard at the UCB site (from Figure 7-5). Recall that the simulated earthquake records used to compute these hazard curves have been scaled up by a factor of two.

7.5.2 PSDA Approach

For convenience, the integral used to compute a $\theta_{\max}$ hazard curve via PSDA (e.g., Equation 3-1) is repeated here in Equation 7-3.

$$\lambda_{\theta_{\max}}(y) = \int G_{\theta_{\max}|IM}(y \mid x) \; |\, \mathrm{d}\lambda_{IM}(x) \,| \tag{7-3}$$

For the UCB site considered in this chapter, the ground motion hazard λ_{IM} was computed in Section 7.4 via the simulation-based approach (as depicted in Figure 7-5 in terms of IM_{1E} and $IM_{1I\&2E}$). Using the same approach, the "exact" drift demand hazard $\lambda_{\theta_{\max}}$ for the LA9 building model at the UCB site was also computed (in the preceding subsection). In doing so, $\theta_{\max}$ from NDA of the LA9 building model (in addition to IM_{1E}

and $IM_{1I\&2E}$) has been computed for all 180 of the simulated earthquake records. Computing $\lambda_{\theta_{\max}}$ via PSDA entails estimating the conditional complementary cumulative probability $G_{\theta_{\max}|IM}$ with only a subset of these $\theta_{\max}$ results (and the corresponding values of IM_{1E} and $IM_{1I\&2E}$). As demonstrated below, the efficiency and sufficiency of the *IM* employed (i.e., IM_{1E} versus $IM_{1I\&2E}$) affects the precision and accuracy of the estimate of $G_{\theta_{\max}|IM}$, and hence that of $\lambda_{\theta_{\max}}$.

7.5.2.1 Estimation of $G_{\theta_{\max}|IM}(y \mid x)$

Recall (e.g., from Chapter 3) that $G_{\theta_{\max}|IM}(y \mid x)$ is customarily calculated by assuming that $\theta_{\max}$ given *IM* is lognormally distributed. The requisite median and dispersion of $\theta_{\max}$ given *IM*, which are denoted simply as $\eta(x)$ and σ, are estimated via a (log-log linear) regression of $\theta_{\max}$ on *IM*. Because σ is relatively small (e.g., compared to the dispersions of $\theta_{\max}$ given RS_i listed in Table 7-4), a relatively small number of data points (i.e., earthquake records) is necessary to estimate $\eta(x)$ with adequate precision. As an example, the regressions of $\theta_{\max}$ on IM_{1E} and on $IM_{1I\&2E}$ are illustrated for the LA9 building model in Figure 7-7 using only the data for the 30 earthquake records simulated for the SH+NH+RC rupture source. In contrast, 180 (i.e., 6 sets of 30) NDA's of the MDOF building model were used (in Section 7.5.1) in the simulation-based approach. Note that the same one-parameter regression model described in Chapter 5 is utilized here. That is,

$$\theta_{\max} = a \cdot IM \cdot \varepsilon_{\theta_{\max}|IM} \quad \Leftrightarrow \quad \ln(\theta_{\max}) = \ln(a) + \ln(IM) + \ln(\varepsilon_{\theta_{\max}|IM}) \qquad (7\text{-}4)$$

where a is the regression coefficient (also referred to as the bias of *IM* in estimating $\theta_{\max}$) and $\varepsilon_{\theta_{\max}|IM}$ is the random error with (by definition) median 1 and dispersion σ. Since $\theta_{\max}$ given *IM* is assumed to be lognormally distributed, by design $\varepsilon_{\theta_{\max}|IM}$ is also lognormal.

7.5.2.2 Evaluation of the efficiency and sufficiency of IM_{1E} versus $IM_{1I\&2E}$

As demonstrated in Chapter 6, recall that the results of a regression of $\theta_{\max}$ on *IM* can also be used to quantify the efficiency and sufficiency of *IM*. The dispersion of $\theta_{\max}$ given *IM* (i.e., σ) serves as a measure of the efficiency of *IM* (because σ is inversely related to the number of earthquake records and NDA's necessary to estimate a with adequate precision). Consistent with the findings in Chapter 6, the regressions illustrated

in Figure 7-7 suggest that $IM_{1I\&2E}$ is much more efficient than IM_{1E} (for the LA9 building model subjected to the SH+NH+RC simulated earthquake records). When $IM_{1I\&2E}$ is employed, the σ of 0.17 implies that as few as 3 earthquake records (and NDA's) are necessary to estimate a with less than 10% variability (i.e., $\sigma_{\ln(a)} \leq 0.10$), whereas at least 20 earthquake records are necessary when IM_{1E} is employed, since σ equals 0.44. Note that because 30 earthquake records have been used in this example, the regression estimates of a computed here are rather precise.

Secondly, the residuals from a regression of $\theta_{\max}$ on IM (i.e., the observed values of $\varepsilon_{\theta_{\max}|IM}$) can be used to assess the sufficiency of IM. Continuing with the case of the LA9 building model subjected to the 30 SH+NH+RC simulated earthquake records, the sufficiency (with respect to Mw)[9] of $IM_{1I\&2E}$ is compared to that of IM_{1E} in Figure 7-8. The figure illustrates the regressions of the $\theta_{\max}$ residuals from Figure 7-7 on the corresponding values of M_{w}. Recall (from Chapter 5) that a small p-value (e.g., less than about 0.05) suggests that the regression estimate of the coefficient c is statistically significant and hence that IM is insufficient with respect to M_{w} (i.e., given IM, $\theta_{\max}$ still depends on M_{w}). Again consistent with the findings in Chapter 6, $IM_{1I\&2E}$ is observed in Figure 7-8 to be sufficient (p-value=0.56) whereas IM_{1E} is found to be insufficient (p-value=0.01).

The insufficiency of IM_{1E} for the LA9 building model can also be demonstrated by comparing regression estimates of a obtained using $\theta_{\max}$ versus IM_{1E} data for different sets of ground motions. Listed in Table 7-5 are the regression results (for $IM_{1I\&2E}$ and for IM_{1E}) the six sets of earthquake records simulated for the HRC rupture sources. Note that because, in each case, 30 earthquake records have been used, the estimates of a are rather precise (i.e., $\sigma_{\ln(a)} < 0.10$). When IM_{1E} is employed, the values of a range from 1.11 (for the RC rupture source) to 1.50 (for the SH+NH+RC rupture source); the values of σ also differ for the RC and SH+NH+RC rupture sources (0.13 versus 0.44), but σ is approximately 0.25 for the other four rupture sources. These differences in a and σ imply that, if IM_{1E} is employed, the estimate of $G_{\theta_{\max}|IM}$, and hence of $\lambda_{\theta_{\max}}$, will depend on which set (or combination) of earthquake records is considered. This dependence is an another indication that IM_{1E} is insufficient, in addition to the fact that IM_{1E} is at least somewhat insufficient with respect to M_{w} for the RC, SH, NH+RC, (p-value=0.06) and SH+NH+RC (p-value=0.01) rupture sources.

---

[9] Note that the sufficiency of each IM with respect R_{close}, the closest distance to the rupture surface, cannot be assessed here because all of the earthquake records simulated at the UCB site for the SH+NH+RC rupture source have the same value of R_{close}.

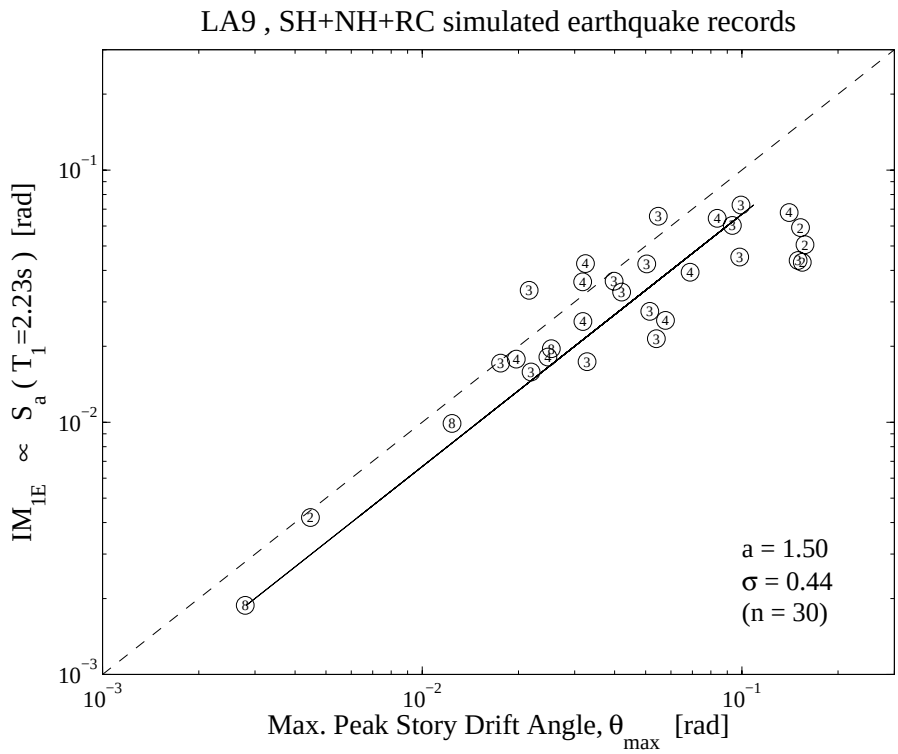

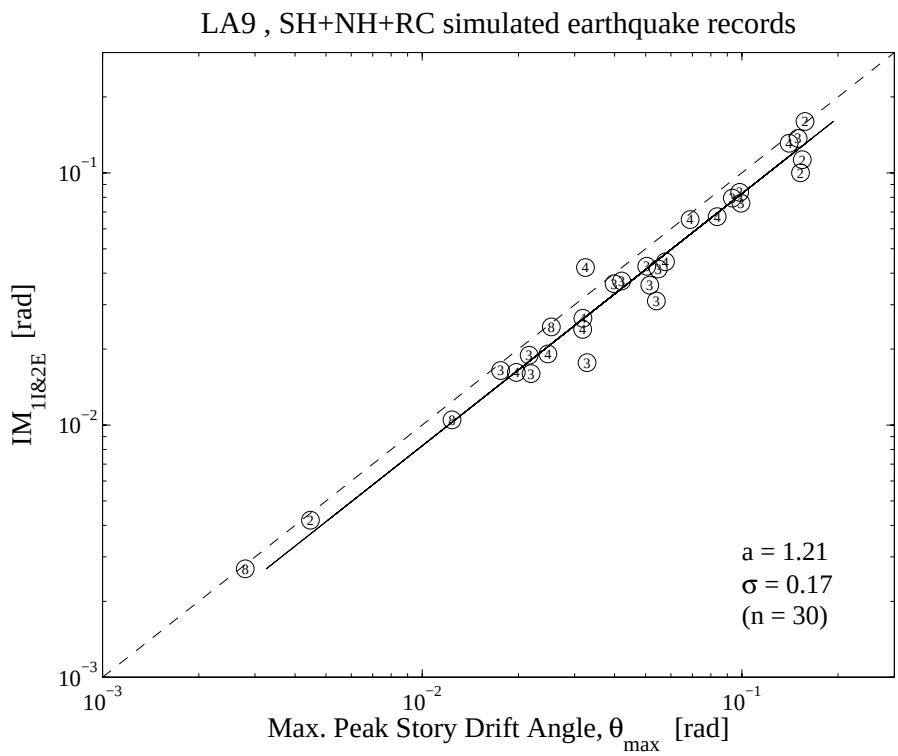

Figure 7-7. Regressions of $\theta_{\max}$ (from NDA of the LA9 building model) on **(a)** IM_{1E} and **(b)** $IM_{1I\&2E}$ for the earthquake records simulated for the SH+NH+RC rupture source (and scaled up by a factor of two).

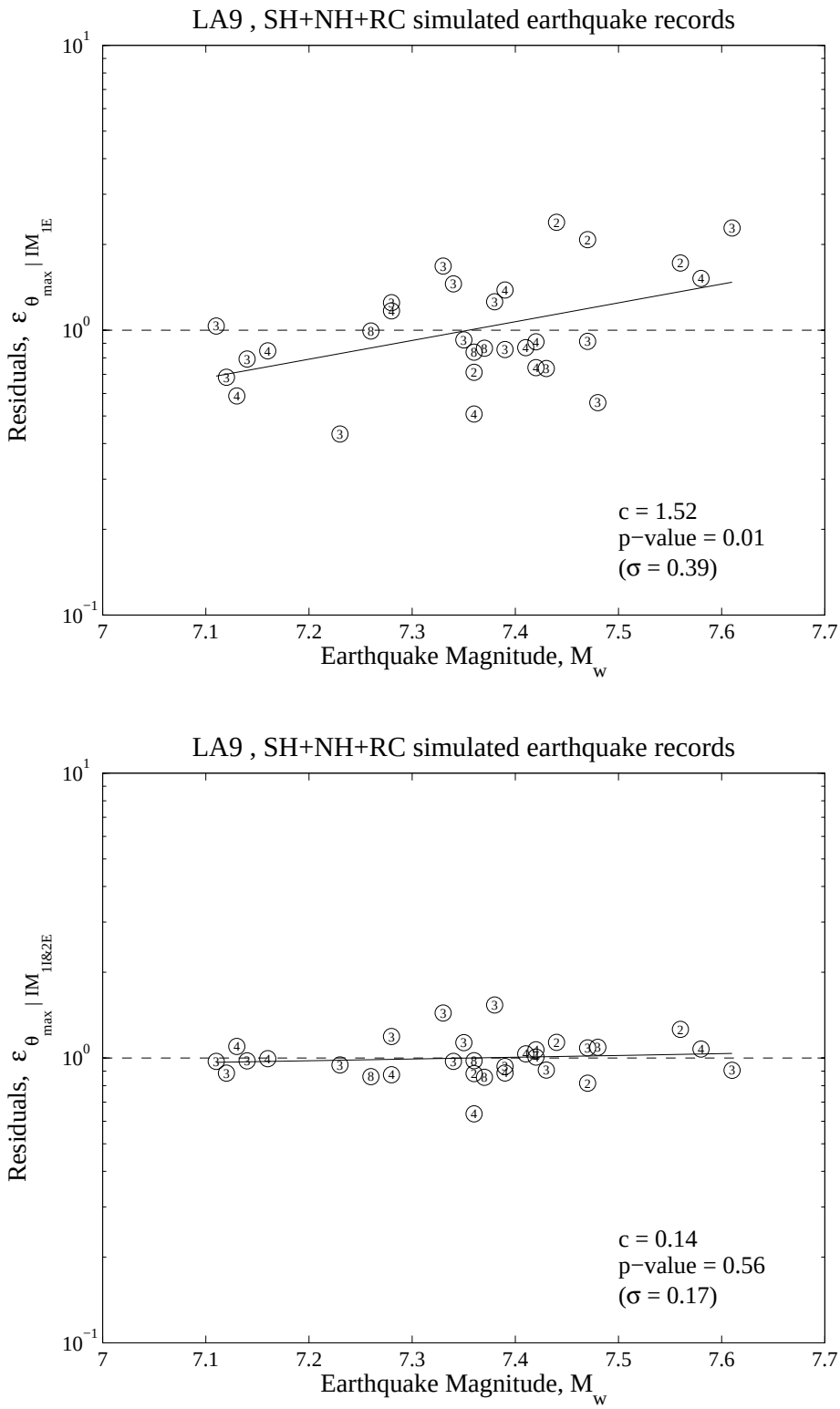

Figure 7-8. Regressions of **(a)** $\varepsilon|IM_{1E}$ and **(b)** $\varepsilon|IM_{1I\&2E}$ (i.e., residuals from Figure 7-7) on M_w, demonstrating the insufficiency of IM_{1E} and the sufficiency of $IM_{1I\&2E}$ with respect to M_w.

In contrast to IM_{1E}, note from Table 7-5 that $IM_{1I\&2E}$ is sufficient for all of the six HRC rupture sources (p-value≥0.30). Furthermore, for all but the RC rupture source, the value of a is approximately 1.2, and the value of σ is about 0.15. Note that the closest distances (R_{close}) from the UCB site to the RC rupture source is 29.1 km, whereas R_{close} is 7.1 km and 3.6 km for the SH and NH rupture sources, respectively. Thus, the difference between the values of a and σ for the RC rupture source and those for the other rupture sources may reflect an insufficiency of $IM_{1I\&2E}$ with respect to R_{close}, or a difference between "near-source" and "ordinary" ground motions.

Table 7-5. Regression of $\theta_{\max}$ on IM_{1E} and on $IM_{1I\&2E}$ results for the LA9 building model using the six different sets of 30 earthquake records simulated for the six HRC rupture sources (and scaled up by a factor of two).

Rupture Source	$\theta_{\max}$ on IM		$\varepsilon \mid IM$ on M		
	a	σ	c	p-value	σ
(a) IM_{1E}					
RC	1.11	0.13	0.35	0.06	0.12
SH	1.30	0.25	0.80	0.06	0.24
NH	1.22	0.25	-0.03	0.93	0.25
SH+NH	1.38	0.27	0.65	0.06	0.25
NH+RC	1.26	0.25	0.40	0.28	0.25
SH+NH+RC	1.50	0.44	1.52	0.01	0.39
(b) $IM_{1I\&2E}$					
RC	1.09	0.12	0.07	0.70	0.12
SH	1.22	0.17	-0.30	0.30	0.17
NH	1.20	0.14	0.05	0.75	0.14
SH+NH	1.20	0.14	-0.13	0.46	0.14
NH+RC	1.24	0.13	-0.08	0.68	0.13
SH+NH+RC	1.21	0.17	0.14	0.56	0.17

Nevertheless, among the near-field rupture sources (i.e., all but RC), the resulting estimates of $G_{\theta_{\max}|IM}$ and ultimately of the drift demand hazard $\lambda_{\theta_{\max}}$ will be (approximately) the same, regardless of which set (or whatever combination) of simulated earthquake records is used. Presumably, these estimates of $\lambda_{\theta_{\max}}$ will also be accurate, as investigated below.

7.5.2.3 Computation of $\lambda_{\theta_{\max}}(y)$

With the assumptions made for estimating $G_{\theta_{\max}|IM}$, recall (from Chapter 3) that the PSDA integral for the drift demand hazard $\lambda_{\theta_{\max}}$ (i.e., Equation 7-3) can be evaluated analytically if a log-log linear form is assumed for the ground motion hazard λ_{IM}. Here, because *IM* is assumed to be lognormally distributed for each rupture source (i.e., given RS_i), and because of the assumed relationship between *IM* and $\theta_{\max}$, $\theta_{\max}$ given RS_i is also lognormally distributed, which further simplifies the solution of Equation 7-3 for $\lambda_{\theta_{\max}}$. Based on Equation 7-4 (relating $\theta_{\max}$ to *IM*) the median and dispersion of $\theta_{\max}$ given RS_i are expressed in Equation 7-5 as functions of the median and dispersion of *IM* given RS_i, and of the regression coefficient *a*.

$$\eta_{\theta_{\max}|RS_i} = a \cdot \eta_{IM|RS_i} \tag{7-5a}$$

$$\sigma_{\ln\theta_{\max}|RS_i} = \sqrt{\sigma^2_{\ln\theta_{\max}|IM} + \sigma^2_{\ln IM|RS_i}} \tag{7-5b}$$

Recall that the dispersion of $\theta_{\max}$ given *IM*, $\sigma_{\ln\theta_{\max}|IM}$, is abbreviated as σ in the subsections above. Equation 7-5b for $\sigma_{\ln\theta_{\max}|RS_i}$ assumes that ln(*IM*) and ln($\varepsilon_{\theta_{\max}|IM}$) in Equation 7-4 are independent for each rupture source. The observed correlation coefficients calculated from the *IM* and $\varepsilon_{\theta_{\max}|IM}$ data for each rupture source are less (in absolute value) than 0.38 (with one exception of 0.57), so the assumption of independence seems reasonable. Of course, the effect of correlation can be easily added. In any case, the $\sigma^2_{\ln IM|RS_i}$ term dominates numerically in Equation 7-5b.

With $\theta_{\max}$ given RS_i lognormally distributed, the PSDA integral (i.e., Equation 7-3) simplifies to Equation 7-6 for drift demand hazard, where the fact that $\Phi(-z) = 1 - \Phi(z)$ is applied.

$$\lambda_{\theta_{\max}}(y) = \sum_i \Phi\left[\frac{\ln(a \cdot \eta_{IM|RS_i}) - \ln y}{\sqrt{\sigma^2_{\ln\theta_{\max}|IM} + \sigma^2_{\ln IM|RS_i}}}\right] \nu_{RS_i} \tag{7-6}$$

It is important to note that, because only a single value of *a* and of $\sigma_{\ln\theta_{\max}|IM}$ is (customarily) estimated in applying PSDA, Equation 7-6 employs a common value of *a* and of $\sigma_{\ln\theta_{\max}|IM}$ for all of the rupture sources. If the distinct values of *a* and $\sigma_{\ln\theta_{\max}|IM}$

(i.e., σ) for each rupture source are employed, the result of Equation 7-6 is found to match closely the "exact" drift demand hazard curve computed directly via the simulation-based approach (in Section 7.5.1). The small difference is due to the differences between the estimates of the median and dispersion of $\theta_{\max}$ given RS_i expressed in Equation 7-5 and those computed directly from the $\theta_{\max}$ data for each rupture source.

Using the six different values of a and σ listed in Table 7-5, the resulting drift demand hazard curves computed via PSDA (i.e., Equation 7-6) are shown in Figure 7-9. Also shown in the figure is the "exact" drift demand hazard curve computed via the simulation-based approach. When the insufficient IM_{1E} is employed for PSDA, note that the drift demand hazard curves differ significantly depending on which set of (simulated) earthquake records are used to estimate $G_{\theta_{\max}|IM}$ (by estimating a and σ). For example, the hazard curves computed using the earthquake records simulated for the RC versus the SH+NH+RC rupture sources underestimate and overestimate, respectively, the "exact" drift demand hazard curve. At large drift demands (e.g., $\theta_{\max}$=0.08rad) the RC and SH+NH+RC estimates of the hazard (i.e., mean rates) differ by almost a factor of two; conversely, the $\theta_{\max}$ demands at low levels of hazard (e.g., about $2\text{x}10^{-3}$) differ by about a factor of 1.5. In contrast, when the (more) sufficient $IM_{1I\&2E}$ is employed, the drift demand hazard curves computed via PSDA are approximately the same regardless of which set of (simulated) earthquake records are used to estimate $G_{\theta_{\max}|IM}$. Moreover, the hazard curves computed using the "near-field" earthquake records simulated for the SH, NH, SH+NH, NH+RC, and SH+NH+RC rupture sources are very close to the "exact" hazard curve. The hazard curve computed using the "far-field" earthquake records simulated for the RC rupture source, however, mildly underestimates the "exact" solution (by about 20% in hazard and only 10% in drift). Using the near-field rather than the far-field earthquake records results in a more accurate estimate of the drift demand hazard because the hazard is dominated by the nearby rupture sources (i.e., other than RC).

7.6 Conclusions

In this chapter, an alternate approach to PSHA for computing the ground motion hazard at a site has been demonstrated. Rather than integrating over all the possible magnitudes of earthquakes on a local fault system (and over all the possible locations of fault rupture), the approach demonstrated here sums over a number of possible

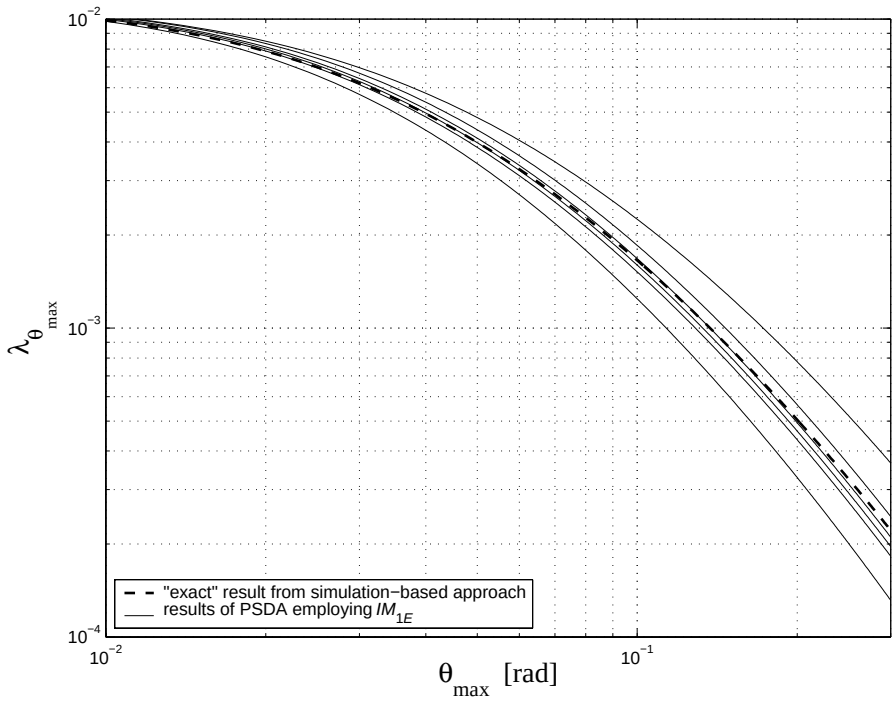

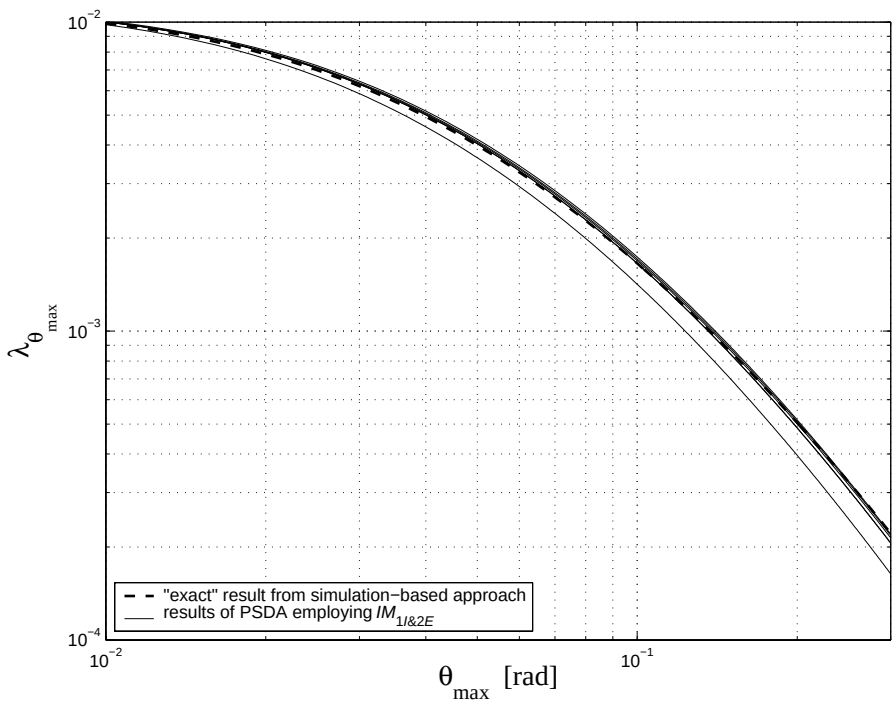

Figure 7-9. Drift demand hazard for LA9 building model at UCB site computed via PSDA using six different sets of (simulated) earthquake records and employing **(a)** IM_{1E} or **(b)** $IM_{1I\&2E}$. Recall that the ground motion hazard (in terms of IM_{1E} or $IM_{1I\&2E}$) has been computed using all of the simulated earthquake records (scaled up by a factor of two).

"characteristic events" (of fixed area). In the San Francisco Bay Region, mean annual rates of recurrence of such events have been estimated by the U.S.G.S. Working Group on California Earthquake Probabilities (1999). To estimate the ground motion at a site, rather than employing an attenuation relation (as in conventional PSHA), the alternate approach uses a stochastic earthquake rupture model of the characteristic events to simulate ground motions. The primary advantage of the simulation-based approach is that the ground motion hazard at a site can be computed in terms of any intensity measure, not just those for which attenuation relations are available. In fact, the approach can be used to directly compute a structural demand (e.g., drift) hazard curve that is "exact"; doing so, however, requires NDA of the given structure under a relatively (compared to PSDA) large number of simulated earthquake records. In this chapter, the "exact" drift demand (i.e., $\theta_{\max}$) hazard curve for the LA9 building model at the UCB site (near the HRC Fault system) is compared with the results of PSDA employing the ground motion intensity measures IM_{1E} and $IM_{1I\&2E}$.

As in Chapter 6, here IM_{1E} is found to be "insufficient" with respect to earthquake magnitude (i.e., given IM_{1E}, $\theta_{\max}$ still depends on M_{w}) when considering the drift response of the LA9 building model. Accordingly, drift demand hazard curves computed via PSDA with IM_{1E} as the intensity measure differ (by as much as 100% in mean rates at larger drifts) depending on which set of (simulated) earthquake records is used. In particular, using "nearby-field" versus "far-field" earthquake records results in different estimates of the drift demand hazard. Moreover, IM_{1E} is found to be quite inefficient in comparison to $IM_{1I\&2E}$. Also consistent with the finding of Chapter 6, $IM_{1I\&2E}$ is found here to be sufficient with respect to M_{w} for the drift response of the LA9 building model. However, here $IM_{1I\&2E}$ may be mildly insufficient with respect to source-to-site distance (R_{close}). While the drift demand hazard curves computed via PSDA with $IM_{1I\&2E}$ as the intensity measure are nearly identical when using different nearby-field sets of the earthquake records, using a far-field set of simulated earthquake records results in a somewhat different hazard curve (by about 10% in hazard or drift). This disparity suggests that the drift demand hazard due to "near-source" versus "ordinary" ground motions may need to be computed separately, if the difference is important practically. The drift demand hazard curves computed via PSDA using the nearby-field sets of (simulated) earthquake records, however, do match closely the "exact" drift demand hazard curve, which is dominated by the nearby-field hazard. This indicates that the drift demand hazard due to nearby-field ground motions, at least, can be computed accurately via PSDA with $IM_{1I\&2E}$ as the intensity measure.

Of course, real-world applications of the simulation-based approach demonstrated for computing the ground motion hazard at a site rely on realistic ground motion simulations that reflect the variabilities inherent in earthquake fault rupture. Although Mai *et al.* (2002) have since developed "pseudo-dynamic" methods for simulating more realistic ground motions, the simulated earthquake records considered in this chapter are deficient in high frequencies. As a result, the structural responses observed are somewhat different in nature than the responses to recorded ground motions. Nevertheless, many of the observations made in Chapter 6 concerning the efficiency and sufficiency of alternative *IM*'s and their effects on the precision and accuracy of a structural performance assessment are confirmed in this chapter using the simulated earthquake records.

Chapter 8

Concluding Remarks

8.1 Overview

In this dissertation, PSDA (Probabilistic Seismic Demand Analysis) is applied, extended, and used as a framework to study (i) the effects of beam-column connection fractures on the seismic performance of SMRF (steel moment-resisting frame) buildings, and (ii) how to account for the effects of "pulse-like" earthquake ground motions on nonlinear structural response in assessing the performance of SMRF buildings at near-fault sites. While specific conclusions for each of these two studies are included in the preceding chapters (i.e., Chapters 2-4 for connection fractures, Chapters 5-7 for near-source effects), links between the two studies are drawn here whilst summarizing some of their limitations and suggesting future topics of research. First, though, in part as a review, some practical implications of the two studies are discussed.

8.2 Practical Implications

8.2.1 Contributions to FEMA 350-353 Design and Evaluation Guidelines

The research presented in the first half of this dissertation concerning the effects of beam-column connection fractures on the seismic performance of SMRF buildings was conducted as part of Phase II of the SAC Steel Project (Cornell & Luco 1999). The SAC Steel Project recently culminated in the FEMA 350-353 (2000) seismic guidelines for SMRF buildings. At the core of these LRFD-like design and evaluation guidelines is the

closed-form PSDA solution (Cornell 1996) employed in Chapter 3. With an extension of PSDA (Cornell *et al.* 2002), the FEMA guidelines provide a procedure that can be used to evaluate the level of confidence that the probability of exceeding the "collapse prevention" or "immediate occupancy" limit state is less than a prescribed threshold. To the best of the author's knowledge, the PSDA evaluations of the three pre-Northridge Los Angeles SMRF buildings reported in Chapter 3 were the first to be carried out for any of the SAC building models (as first reported in Luco & Cornell 1998). Hence, these applications of PSDA have not only provided a concise quantification of the effects of beam-column connection fractures on the seismic performance of the SAC buildings, they have also served as early examples of the PSDA approach adopted in the FEMA guidelines.

In addition to the demonstrations of PSDA, the sensitivity studies detailed in Chapter 2 also ultimately contributed to the recent FEMA guidelines by identifying aspects of beam-column connection fractures that affect most the seismic drift demands, and thereby performance, of SMRF buildings. In particular, the plastic rotation capacity against fracture of the top beam-flange connection, denoted θ_{f-}, (or, more generally, the capacity of the second beam-flange to fracture) is found to be a very influential parameter related to the effects of connection fractures. In contrast, the impacts of the following aspects of *bottom* beam-flange connection fracture are found to be minimal: (i) θ_{f+}, the plastic rotation capacity against fracture, (ii) p, the probability of pre-yield fracture, and (iii) $M_{\mathrm{red+}}$, the post-fracture reduced moment strength in positive bending. These sensitivity results were at hand to guide SAC researchers who, for example, subsequently carried out incremental dynamic analyses in order to estimate maximum story drift angle capacities associated with the global "collapse prevention" limit state (Yun & Foutch 2000).

8.2.2 Future Modeling and Testing of SMRF Beam-Column Connections

As alluded to above, the results of the sensitivity studies reported in Chapter 2 can provide guidance for the modeling of brittle beam-column connection behavior in SMRF buildings. For example, even though the fracture model parameters θ_{f+}, p, and $M_{\mathrm{red+}}$ are likely uncertain and/or random, the observed insensitivity of story drift demands to variations in these parameters suggests that it is unlikely worth the effort to randomize them for structural analysis. The plastic rotation capacity associated with top beam-flange connection fracture (i.e., θ_{f-}), on the other hand, is found to be an influential parameter that might well warrant randomization.

Furthermore, the sensitivity studies of Chapter 2 are useful in focusing future laboratory tests, field investigations, and detailed analytical investigations of beam-column connection fracture. Particularly for the most influential aspects of connection fracture, like θ_{f-}, additional data from such investigations is sorely needed. The observed sensitivity of building response and performance to θ_{f-}, for example, points to the need for additional laboratory experiments that (i) test beam-column connections beyond a single (predominantly bottom) beam-flange fracture, and (ii) include the effects of a slab. Already a few investigators have been motivated to conduct such tests (e.g., Lee *et al.* 2000).

8.2.3 Evaluation of Earthquake-Damaged SMRF Buildings

The significant effects of top-, together with bottom-, beam-flange connection fractures mentioned in the preceding two subsections also led to the decision in Chapter 4 to use the proportion of top-beam-flange connections fractured as a measure of the state of damage for an SMRF building. In Chapter 4, uncertainty in the state of damage after an earthquake event, due to incomplete inspection, is accounted for in assessing the future performance, or safety, of an SMRF building. The proposed procedure is a total-probability-theorem extension of PSDA that involves nonlinear dynamic analyses of the damaged building modeled with a range of proportions of pre-existing fractured connections. By incorporating an aftershock ground motion hazard curve for the building site, the results of the procedure (namely, an annual limit-state frequency) can be used to help decide, for example, whether to permit occupancy soon after the damaging earthquake. Unlike subjective tagging schemes, the proposed procedure provides a quantitative measure of the post-earthquake safety of a damaged building that has been only partially inspected for fractured connections.

Like the rest of the connection fracture research reported in this dissertation, the extension of PSDA described above was also developed as part of Phase II of the SAC Steel Project (Cornell & Luco 1999). Subsequently, a detailed (dubbed "Level 2") procedure for evaluating an earthquake-damaged SMRF building was included in the FEMA 352 guidelines (entitled "Recommended Post-earthquake evaluation and Repair Criteria for Welded Steel Moment-Frame Buildings", 2000). Similar to the procedure outlined and demonstrated in this dissertation, the FEMA 352 approach involves nonlinear dynamic analysis of a damaged building model with pre-existing fractured connections. The "Level 2" procedure also makes use of an aftershock ground motion hazard curve (although it is based simply on a repeat of the main-shock) in order to

probabilistically quantify the safety of a damaged building. However, the FEMA 352 approach does *not* consider any uncertainty in the state of damage, instead requiring complete inspection of "all fracture-susceptible connections in the building." In many cases, though, complete inspection may be uneconomical. As discussed in the future work section below, the trade-off between uncertainty in the state of damage due to incomplete inspection and the significant cost of inspecting connections should be addressed.

8.2.4 Structural Performance Assessment at Near-Fault Sites

Although the research reported in the second half of this dissertation also focuses on SMRF buildings, its broader goal is to ensure the accuracy of PSDA for buildings at near-fault sites. As explained in Chapter 5, PSDA can be imprecise (i.e., uncertain) and/or inaccurate (i.e., biased) if the ground motion intensity measure employed is "inefficient" and/or "insufficient" in estimating nonlinear structural drift demands. An efficient ground motion intensity measure (*IM*) is defined as one that results in a relatively small variability of the structural demand measure (*DM*) of interest, given *IM*, whereas a sufficient *IM* is defined as one that renders *DM* conditionally independent, given *IM*, of earthquake magnitude (*M*) and source-to-site distance (*R*). The conventionally used intensity measure S_{a1} (i.e., the spectral acceleration at approximately the fundamental period and damping of the structure of interest) has been observed to be relatively inefficient and insufficient for near-source ground motions. Hence, one objective of the near-source research presented in this dissertation is to find an intensity measure that, unlike S_{a1}, is efficient and sufficient for near-source (as well as for ordinary) ground motions. Besides the discovery of an efficient and sufficient *IM*, another significant contribution of the near-source research is the approach used to choose between alternative intensity measures intended to ensure the accuracy of PSDA.

8.2.5 Attenuation Relations for New Ground Motion Intensity Measures

In search of a ground motion intensity measure that (unlike S_{a1}) is efficient and sufficient for near-source and ordinary ground motions, several new structure-specific *IM*'s are introduced in Chapter 5 and evaluated in Chapter 6. One of the new intensity measures in particular, denoted $IM_{1I\&2E}$, is found to be relatively efficient and sufficient for both types of ground motions and for three different SMRF buildings (namely a low-, mid-, and high-rise). As detailed in Chapter 5, $IM_{1I\&2E}$ can be written (approximately) as

a multiplicative modification of S_{a1} that further involves (i) the inelastic spectral displacement $S_d(T_1,\zeta_1,d_y)$, for which d_y can be estimated from a NSP (nonlinear static pushover) curve for the building of interest, and (ii) the elastic spectral displacement at the second mode period and damping of the structure. For a mid-rise SMRF building at a near-fault site, the results of PSDA are demonstrated in Chapter 7 to be more accurate and precise if $IM_{1I\&2E}$ is employed in lieu of S_{a1}.

No matter what intensity measure is employed in PSDA, the ground motion hazard at the designated site must be expressed in terms of the selected *IM*. In Chapter 7, a simulation-based approach is demonstrated that can be used to compute the ground motion hazard at a site in terms of any *IM* (and even *DM*); typically, though, the ground motion hazard at a site is computed via PSHA (Probabilistic Seismic Hazard Analysis, Cornell 1968). PSHA makes use of an attenuation relation for the selected *IM*, which readily exists for S_{a1} (e.g., Abrahamson & Silva 1997), but is not yet available for $IM_{1I\&2E}$ [1] – even an attenuation relation for inelastic spectral displacement alone (perhaps normalized by the corresponding elastic value) is not yet readily available. Perhaps, though, the demonstration provided in this dissertation of the efficiency, sufficiency, and in some case unbiased nature of $IM_{1I\&2E}$ in estimating nonlinear structural drift demands may motivate seismologists to develop attenuation relations for inelastic spectral displacements in the future. As suggested by the results in Chapter 7, such attenuation relations could ultimately improve the accuracy of structural performance assessment (via PSDA) at near-fault sites.

8.2.6 Simplified Nonlinear Structural Analysis Procedures

In addition to being relatively efficient and sufficient, in some cases the ground motion intensity measure $IM_{1I\&2E}$ is demonstrated to be virtually unbiased in estimating nonlinear structural drift demands computed via NDA (nonlinear dynamic analysis). More specifically, in Chapter 6 $IM_{1I\&2E}$ is observed (for both ordinary and near-source ground motions) to be practically unbiased in estimating (i) the $\theta_{\max}$ (maximum peak story drift angle) response of a low-rise SMRF building (i.e., "LA3"), and (ii) the θ_{ave} (average peak story drift angle) response of a mid-rise SMRF building (i.e., "LA9"). In cases like these, $IM_{1I\&2E}$ may be thought of as a "predictor" of nonlinear structural drift demand that is computed via a simplified seismic analysis procedure. Simplified seismic

[1] For each of the other ground motion intensity measures introduced in Chapter 5, with the exception of IM_{1I}, an attenuation relation could potentially be built from existing relations for spectral acceleration, or at least using the same response spectra data used to develop those relations.

analysis procedures are an important part of the structural design process, which is one of the reasons why the Applied Technology Council is currently investigating alternative (to NDA) inelastic analysis procedures (i.e., ATC-55 Project: "Evaluation and Improvement of Inelastic Seismic Analysis Procedures"). The procedure for computing $IM_{1I\&2E}$ is certainly an option to be considered, as it requires only (i) modal vibration properties of the given structure (i.e., first- and second-mode periods, damping ratios, and participation factors), (ii) an estimate of the roof drift at which the structure will experience significant yielding, which can be obtained from a nonlinear static-pushover (NSP) curve, and (iii) elastic and inelastic spectral displacements for the given ground motion. These are all routinely attainable pieces of information about a structure and a ground motion that could even be roughly estimated at a preliminary design stage. Hence, aside from employing it in PSDA to assess the seismic performance of a structure, the ground motion intensity measure $IM_{1I\&2E}$ (and perhaps some of the other intensity measures introduced in Chapter 5) could conceivably be used in building design as well.

8.3 Limitations and Future Work

8.3.1 Connection Fracture Sensitivity Studies

As mentioned above, the results of the sensitivity studies detailed in Chapter 2 indicate that the impacts on seismic inter-story drift demands of variations in several aspects of *bottom* beam-flange connection fracture are minimal. It is important to note, however, that these sensitivity studies conducted for various aspects of *bottom* beam-flange fracture did not simultaneously include the effects of *top* beam-flange fracture. Given the significant influence of top, together with bottom, beam-flange fractures, future sensitivity studies centered on the top-and-bottom flange case should be conducted as well. Moreover, the additional effect on structural demands and performance due to column flange/web fractures (considered briefly in Chapter 2) and column splice fractures deserve further attention.

8.3.2 Inspection Guidelines for Earthquake-Damaged SMRF Buildings

As demonstrated in Chapter 4, uncertainty in the post-earthquake state of damage for a partially-inspected SMRF building will typically increase the annual limit-state frequency computed via the proposed extension of PSDA. In this way, the performance assessment will reflect a penalty associated with incomplete inspection that can serve as

an incentive to inspect additional connections. The significant cost of conducting those inspections, however, also needs to be taken into account. The two considerations could conceivably be weighed in a formal "pre-posterior" decision analysis (e.g., Benjamin & Cornell 1970) in order to decide (beforehand) on an optimal amount of inspection, or to decide (in a sequential manner) whether to inspect further as new results are discovered. More practically, with additional research such an analysis could be used to set generic standards for degree of inspection, perhaps as a function of what is found in a preliminary inspection.

8.3.3 PSDA at Sites Susceptible to Both Near-Source and Ordinary Ground Motions

In Chapter 6, the efficiency and sufficiency of several alternative ground motion intensity measures are evaluated for a set of near-source and a set of ordinary earthquake records. As discussed above, this is done in search of an *IM* that ensures the accuracy of PSDA at sites susceptible to near-source or ordinary ground motions. It is important to note, however, that even an *IM* which is efficient and sufficient for near-source and ordinary ground motions, *considered separately*, will not necessarily ensure the accuracy of PSDA for a building at a site susceptible to *both* near-source and ordinary ground motions. In order for the latter to be true, it is also necessary that the bias of the *IM* in estimating *DM*, and to a lesser extent the efficiency of the *IM*, be approximately the same for the near-source versus ordinary ground motions, as demonstrated in Chapter 7. Unlike current practice, in such cases the near-source and ordinary ground motion threats need not be treated separately in assessing the performance of a building susceptible to both types of ground motions.

8.3.4 Additional Evaluations of New Ground Motion Intensity Measures

Besides varying with the kind of ground motions considered (e.g., near-source versus ordinary), it is important to note that the efficiency and sufficiency (not to mention bias) of a ground motion intensity measure can also vary with the structure and the demand measure (i.e., *DM*) considered. Hence, even though $IM_{1I\&2E}$ is found to be relatively efficient and sufficient in estimating seismic drift demands for the SMRF buildings considered in Chapters 6 and 7, it should also be tested for other structures. In order to further investigate the efficiency and bias of $IM_{1I\&2E}$ as a "predictor" of nonlinear drift demands (Luco *et al.* 2002a), additional SMRF building models have already been considered by collaborators in Japan (i.e., Prof. Yasuhiro Mori of Nagoya University and

Prof. Masayoshi Nakashima of Kyoto University). These include "fish-bone" models (Nakashima *et al.* 2002) of SMRF buildings that are much less time-consuming to analyze than full frame models. Another opportunity to further test $IM_{1I\&2E}$ has recently come about within the PEER (Pacific Earthquake Engineering Research) Methodology Testbeds effort, which will evaluate the efficiency (and perhaps sufficiency) of several alternative intensity measures for two buildings and two bridges. Both the Japanese and PEER researchers consider their own sets of earthquake records, and the PEER investigators also consider demand measures, or "engineering demand parameters," other than drift (e.g., floor acceleration, which is closely tied to content damage).

8.3.5 Links between SMRF Connection Fractures and Near-Source Effects

Although the effects of near-source ground motions are obviously not the focus of the SMRF connection fracture research reported in the first half of this dissertation, it is interesting to note that several near-source earthquake records are considered within that research. In fact, fourteen of the forty SAC earthquake records considered for the Los Angeles region overlap with the "near-source" set of ground motions considered in the second half of this dissertation. Unlike for the near-source (and "ordinary") ground motions, though, the strike-normal component of each SAC earthquake record is not considered. Instead, the two horizontal components of each ground motion are rotated away from the strike-normal and strike-parallel orientations by 45 degrees, and both components are considered. As demonstrated by Alavi & Krawinkler (2000), this rotation does not necessarily remove the pulse-like nature of the ground motions.

Despite the significant number of near-source ground motions considered, the PSDA evaluations reported in Chapter 3 (and Chapter 4) employ S_{a1} (i.e., first-mode spectral acceleration) as the ground motion intensity measure. As later demonstrated in Chapter 7, the use of S_{a1} at a site susceptible to near-source ground motions can lead to inaccurate PSDA results. Even at sites exposed only to ordinary ground motions, previous studies (e.g., Shome & Cornell 1999) have demonstrated that employing S_{a1} alone in PSDA can result in inaccurate drift demand hazard curves for tall, long period buildings like the SAC 20-story (and perhaps even 9-story) SMRF building for the Los Angeles region. The drift demand hazard curves computed in Chapter 3 using S_{a1}, however, are only used to make relative comparisons between various cases with beam-column connection fractures and the case of all ductile connections (as anticipated prior to the Northridge earthquake). Likewise, the annual limit-state frequencies computed in Chapter 4 (via an extension of PSDA) are compared for a partially-inspected, earthquake-

damaged building and the once undamaged building. If these drift demand hazard curves or annual limit-state frequencies were to be regarded in an absolute (rather than relative) sense, a ground motion intensity measure other than S_{a1} should be employed in order to ensure the accuracy of the PSDA results. Note that additional limitations of these PSDA applications are listed in a dedicated section of Chapter 3.

Although conceptually there is little difficulty in doing so, the potential for beam-column connection fractures is not considered as part of the research of near-fault effects on SMRF building described in the second half of this dissertation. Instead, ductile connections are assumed, akin to considering post-Northridge building designs that are intended to prevent connection fractures. It is expected that connection fractures could affect the efficiency and/or sufficiency (not to mention bias) of the ground motion intensity measures, introduced in Chapter 5, in an effort to ensure the accuracy of PSDA at near-fault sites. Clearly brittle connection behavior can change the values of the structural demand measures (*DM*'s) used to evaluate the efficiency and sufficiency of the alternative *IM*'s, but perhaps less obvious is the fact that brittle connection behavior can also alter the values of some of the *IM*'s considered. For example, since $IM_{1I\&2E}$ depends on a yield displacement and a backbone curve estimated from a nonlinear static pushover curve for the structure of interest, it is likely to be affected by beam-column connection fractures. In fact, the elastic-perfectly-plastic backbone curve assumed (in most cases) for $IM_{1I\&2E}$ may not be adequate to maintain the efficiency and sufficiency of $IM_{1I\&2E}$ for SMRF buildings with brittle connections. Accounting for the effects of both near-source ground motions and beam-column connection fractures in evaluating the performance of SMRF buildings is certainly a logical topic of future research.

Appendix A

Earthquake Ground Motion Records for Near-Source Research

A.1 Overview

Most of the earthquake ground motion records used for the near-source research (in Chapters 5 and 6) are selected from the PEER Strong Motion Database (Silva 1999). The selected earthquake records comprise three distinct sets based on their closest distances to the rupture surface, R_{close}, as specified in Table A-1. The R_{close}<16km range for the "nearby-field" set is motivated by the SEAOC Blue Book (1999), which defines near-source factors for distances less than 15km. The "intermediate-field" and "far-field" ranges are designed to be of approximately the same width as the nearby-field range. The nearby-field set is so named because the earthquake records in it may or may not exhibit a low frequency, large amplitude pulse that has become synonymous with near-source ground motions and is typically a manifestation of forward rupture directivity (refer to Chapter 1). As detailed below, a "forward-directivity" subset of the nearby-field earthquake records (as well as a "backward-directivity" subset of the far-field earthquake records) is also distinguished. Furthermore, a supplemental set of "pulse-like" earthquake records from Alavi & Krawinkler (2000) is used; some of the pulse-like ground motions considered by Alavi & Krawinkler are among those in the nearby-field set.

Table A-1. Source-to-site distance ranges for earthquake record sets.

Earthquake Record Set	R_{close} Range (km)
"nearby-field"	[0,16)
"intermediate-field"	[16,30)
"far-field"	[30,46)

All of the selected earthquake records also satisfy the following criteria, based on information provided in the database:

(a) earthquake moment magnitude $M_w \geq 6.0$ (and $M_w \leq 7.4$, the largest in the database). Smaller magnitude earthquakes are less likely to generate rupture directivity effects, and are of less engineering interest.

(b) earthquake ground motion recorded on "stiff soil" or "very dense soil and soft rock" (e.g., NEHRP site classes D or C, respectively). In the database, only U.S. Geological Survey (USGS) site classes and/or Geomatrix (GM) geotechnical subsurface characteristics are specified. However, NEHRP (e.g., FEMA 273 1997) site classes D and C coincide approximately with USGS site classes C and B, respectively (refer to http://peer.berkeley.edu/smcat/sites.html), and correlate well with GM classifications D, C, and B (as detailed below). When available, the USGS site classifications are heeded; otherwise, GM D is assumed to correspond to USGS C (stiff soil), whereas GM C and B are assumed to correspond to USGS B (very dense soil and soft rock). The correlation between GM and USGS soil classifications is based on Table A-2, which reports the number (and percentage) of earthquake records in the database of a given GM classification (i.e., A-E) that also have a USGS classification (i.e., A-D). In other words, Table A-2 reports the likely USGS site class given only a GM subsurface characteristic; for example, of the earthquake records classified as GM D (that also have a USGS classification), 74% are classified as USGS C (and 97% as USGS C or B).[1]

[1] Note from Table A-2 that of the earthquake records classified as GM C (that also have a USGS classification), about half are classified as USGS B and the other half as USGS C. In this research, GM C is assumed to correspond to USGS B (very dense soil and soft rock) so as to exclude as many "very dense soil and soft rock" earthquake records as possible from those that are recorded on "stiff soil" (which are of the majority).

Table A-2. Correlation between GM and USGS soil classifications.

GM Classif.	USGS Classification				Total
	A	B	C	D	
A	39 (61%)	22 (34%)	3 (5%)	0 (0%)	64 (100%)
B	3 (4%)	57 (72%)	19 (24%)	0 (0%)	79 (100%)
C	3 (4%)	35 (47%)	36 (49%)	0 (0%)	74 (100%)
D	0 (0%)	68 (23%)	219 (74%)	8 (3%)	295 (100%)
E	0 (0%)	0 (0%)	1 (8%)	11 (92%)	12 (100%)

(c) earthquake record with a maximum (between the two horizontal components) high-pass filter corner-frequency (f_c^{HP}) less than or equal to 0.25 hertz.[2] This constraint is based on the longest elastic period of interest in this research, namely 4 seconds (i.e., approximately the fundamental mode period for the L.A. 20-story model structure). Silva suggests that "the usable bandwidth of the records for the purpose of engineering analysis is within 1/1.25 of the LP frequency and 1.25 of the HP frequency" (refer to http://peer.berkeley.edu/smcat/process.html).[3] Note that the smallest *low-pass filter* corner-frequency for any of the earthquake records selected is 13 hertz, which filters out periods well below the range of interest (i.e., less than at most 0.08 seconds).

The two horizontal components of each (nearby-, intermediate-, or far-field) earthquake record selected from the database are rotated to the strike-normal and strike-parallel orientations using the fault strikes listed in Table 3 of (Somerville *et al.* 1997b). The earthquakes considered by Somerville *et al.* "include all California crustal earthquakes with magnitudes of 6 or larger for which digital strong motion data and faulting mechanism are available." Thus, a few records that satisfy the criteria listed above but are from earthquakes not considered by Somerville *et al.* are also excluded from the sets of earthquake records considered for this research (e.g., 1980 Mammoth Lakes, 1986 Chalfant Valley, 1992 Cape Mendocino). Unless noted otherwise, only the strike-normal component of each earthquake record is considered in this research.

---

[2] A few earthquake records (e.g., the nearby-field Rinaldi Receiving Station, Sylmar Converter Station, and Sylmar Converter Station East recordings of the 1994 Northridge) for which the high-pass filter corner-frequencies are not reported in the database are selected anyway, under the assumption that they were not high-pass filtered (as suggested by http://peer.berkeley.edu/smcat/process.html).

[3] As a result of inelasticity, one might expect the longest "effective" period of interest to be larger than 5 seconds (particularly for the L.A. 20-story model structure). Fortunately, most of the earthquake records for which f_c^{HP} is relatively large are also relatively weak in intensity, and hence do not cause much inelasticity.

It is important to recognize that not all of the earthquake records in the nearby-field set necessarily exhibit the large amplitude, long period pulse in the velocity time history of the strike-normal component that has become synonymous with near-source ground motions. Conversely, the intermediate-field and far-field sets are not certainly void of such "pulse-like" earthquake records. Nevertheless, faced with the subjectivity involved in identifying pulse-like earthquake records, R_{close} alone is used in defining the nearby-field, intermediate-field, and far-field sets.[4] However, as pulse-like ground motions are manifestations of forward rupture directivity, an objectively distinguished "forward-directivity" subset of the nearby-field earthquake records (as well as a "backward-directivity" subset of the far-field earthquake records) is also considered, as detailed below. Still, not all of these forward-directivity earthquake records are necessarily pulse-like, like those considered by Alavi & Krawinkler (2000).

A.2 Nearby-Field, Intermediate-Field, and Far-Field Earthquake Record Sets

Details of the 75 earthquake records in the "nearby-field" set are listed in Table A-3. Note that (the strike-normal components of) 8 of these earthquake records (e.g., NS23) are among the 15 "pulse-like" records considered by Alavi & Krawinkler (2000). Acceleration, velocity, and displacement time-histories of these 8 pulse-like ground motions are presented in Figure A-2 through Figure A-9. The Anderson Dam (downstream) recording of the 1984 Morgan Hill earthquake (i.e., MORGAN\AND) is also considered by Alavi & Krawinkler, but they use the strike-parallel component whereas only the strike-normal component is used in this research. Note from Figure A-10 that the strike-parallel component of the MORGAN\AND earthquake record actually appears to be more pulse-like than the strike-normal component. The other 6 of the 15 pulse-like earthquake records considered by Alavi & Krawinkler are not among those in the nearby-field set because they were not originally recorded on "stiff soil" or "very dense soil and soft rock," as discussed further below (in Section A.1.2). In addition to considering the unscaled nearby-field earthquake records, these records are scaled in amplitude, as a set (i.e., all earthquake records scaled by the same factor), by a factor of two. This scaling is done in order to investigate higher levels of nonlinear response of the building models analyzed in this research.

---

[4] Note that when predicting the behavior of structures in future earthquakes, the distance to a fault is known, but not whether or not a pulse-like ground motion will occur.

Details of the 74 earthquake records in the "intermediate-field" set are listed in Table A-4. These earthquake records serve as a "buffer" between the nearby-field and far-field sets, but have not yet been used in this research.

Details of the 75 earthquake records in the "far-field" set are listed in Table A-5. Without scaling, it is anticipated that the far-field earthquake records will induce little, if any, nonlinearity in the building models. Thus, the far-field earthquake records are scaled as a set by factors of four and eight. These scale factors are chosen so as to match (approximately) the "1-sigma level" elastic spectral displacements (at the fundamental periods of the three building models and 2% damping) for the nearby-field set (unscaled and scaled by a factor of two).

A.2.1 Forward-Directivity and Backward-Directivity Earthquake Record Subsets

As mentioned above, because pulse-like ground motions are manifestations of forward rupture-directivity, a "forward-directivity" subset of the nearby-field earthquake records (as well as a "backward-directivity" subset of the far-field earthquake records) is considered. An objective way to distinguish between ground motions in the forward and backward rupture-directivity regions makes use of the rupture-directivity modification factors developed by Somerville *et al.* (1997b) for empirical spectral acceleration attenuation relations. As a function of two rupture-directivity parameters that depend only the location of the site with respect to the fault geometry and hypocenter location, the modification factors correct for the discrepancies between observed elastic spectral accelerations (at longer periods) and those predicted by existing attenuation relations. As an example, a contour plot of the directivity modification factors for average (of two horizontal components) $S_a(T\text{=2s},\zeta\text{=5\%})$ is shown in Figure A-1 for a simplified fault geometry and hypocenter location based on (a) the strike-slip Imperial Valley earthquake of 1979, and (b) the dip-slip Northridge earthquake of 1994. The "forward-directivity" subset of the nearby-field set is limited to the earthquake records at sites for which the directivity modification factor is greater than one; conversely, the "backward-directivity" subset of the far-field set excludes such earthquake records.

For each earthquake record in the nearby-field and far-field sets[5], the values of the two directivity parameters (obtained from Prof. J.P. Stewart of U.C.L.A.) and the resulting directivity modification factors for average $S_a(T,\zeta\text{=5\%})$ at T=1, 2, and 4 seconds (approximately the fundamental periods of the three building models considered for this

[5] The R_{close} range of applicability for the rupture-directivity model of Somerville *et al.* (1997b) is 0-50km, which includes the range of R_{close} for both the nearby-field and far-field sets of earthquake records.

near-source research) are listed in Table A-6 and Table A-7, respectively. As illustrated in Figure 5 of (Somerville *et al.* 1997b), the directivity parameter X or Y (for strike-slip or dip-slip faults, respectively) is "the fraction of the fault rupture that occurs on the part of the fault that lies between the hypocenter and the site." Likewise, θ or ϕ (for strike-slip or dip-slip faults, respectively) is "the angle between the fault plane and the path from the hypocenter to the site." Note that directivity modification factors are set equal to one for the recordings from earthquakes of magnitude less than 6.5 (e.g., 1987 Whittier Narrows), as suggested by Somerville *et al.* (1997b).

Of the 75 earthquake records in the nearby-field set, 31 have a directivity modification factor greater than one (at all three periods[6]) and hence are classified as "forward-directivity" ground motions. The velocity time histories and directivity parameters (X or Y and θ or ϕ) for these 31 ground motions are listed in Table A-8 (for the strike-slip earthquakes) and Table A-9 (for the dip-slip earthquakes), ranked in decreasing order of the directivity modification factor for average $S_a(T=2\text{s},\zeta=5\%)$. Note that not all of the earthquake records in this "forward-directivity" subset of the nearby-field set are clearly "pulse-like." Also, 2 of the 8 "pulse-like" earthquake records considered by Alavi & Krawinkler (2000) are not among these 31 "forward directivity" earthquake records, namely the Erzincan recording of the 1992 Erzican (Turkey) earthquake and the KJMA recording of the 1995 Kobe (Japan) earthquake. Despite the fact that X is relatively small (i.e., approximately 0.3) for these 2 ground motions and hence their directivity modification factors are less than one, they do appear to be "pulse-like" (see Figure A-4 and Figure A-9).

Of the 75 earthquake records in the far-field set, 15 have directivity modification factors greater than one (at all three periods). The velocity time histories and directivity parameters (X or Y and θ or ϕ) for these 15 ground motions are listed in Table A-10 (for the strike-slip earthquakes) and Table A-11 (for the dip-slip earthquakes), ranked in decreasing order of the directivity modification factor for average $S_a(T=2\text{s},\zeta=5\%)$. Note that a few of these 15 earthquake records might be considered pulse-like, although their amplitudes are relatively small. The remaining 60 earthquake records are classified as "backward-directivity" ground motions; this set of 60 earthquake records is referred to as the "ordinary" set of ground motions.

[6] Note from the directivity modification factors for a given ground motion may be larger than one at some periods and less than one at others; however, in Table A-6 and Table A-7 this is never the case.

A.2.2 Supplemental "Pulse-Like" Earthquake Records

As noted above, 6 of the "pulse-like" earthquake records considered by Alavi & Krawinkler (2000) are not among those selected from the database because they were not originally recorded on "stiff soil" or "very dense soil and soft rock." However, Somerville (*et al.* 1997a, 1998) did modify most of these earthquake records to reflect "stiff soil" conditions. Due to this difference, these 6 supplemental pulse-like earthquake records, listed in Table A-12, are considered separately from those in the nearby-field set.

Table A-3. "Nearby-field" earthquake record set.

Earthquake Location [a]	Year	M_w	Source Mech.	Station	R_{close} [b] (km)	Site Class [c] USGS	Site Class [c] GM	H/F [d]	Max.[e] f_c^{HP} (hz)	Min.[e] f_c^{LP} (hz)	Dir\Filename-Prefix [f]
(1) Imperial Valley	1940	7.0	SS	El Centro Array #9	8.3	C	D	NA	0.20	15	IMPVALL\I-ELC
(2) Parkfield	1966	6.1	SS	Cholame #5	5.3	C	C	NA	0.20	17	PARKF\C05
(3) Parkfield	1966	6.1	SS	Cholame #8	9.2	C	B	NA	0.20	20	PARKF\C08
(4) Imperial Valley	1979	6.5	SS	Aeropuerto Mexicali	8.5	C	D	NA	0.05	--	IMPVALL\H-AEP
(5) Imperial Valley	1979	6.5	SS	Agrarias	12.9	--	D	NA	0.05	--	IMPVALL\H-AGR
(6) Imperial Valley	1979	6.5	SS	Bonds Corner	2.5	C	D	NA	0.10	40	IMPVALL\H-BCR
(7) Imperial Valley	1979	6.5	SS	Brawley Airport	8.5	C	D	NA	0.10	40	IMPVALL\H-BRA
(8) Imperial Valley	1979	6.5	SS	Calexico Fire Station	10.6	C	D	NA	0.20	40	IMPVALL\H-CXO
(9) Imperial Valley	1979	6.5	SS	EC County Center FF	7.6	C	D	NA	0.10	35	IMPVALL\H-ECC
(10) Imperial Valley	1979	6.5	SS	EC Meloland Overpass FF	0.5	C	D	NA	0.10	40	IMPVALL\H-EMO (NS23)
(11) Imperial Valley	1979	6.5	SS	El Centro Array #1	15.5	C	D	NA	0.10	40	IMPVALL\H-E01
(12) Imperial Valley	1979	6.5	SS	El Centro Array #4	4.2	C	D	NA	0.10	40	IMPVALL\H-E04
(13) Imperial Valley	1979	6.5	SS	El Centro Array #5	1.0	C	D	NA	0.10	40	IMPVALL\H-E05
(14) Imperial Valley	1979	6.5	SS	El Centro Array #6	1.0	C	D	NA	0.10	40	IMPVALL\H-E06 (NS21)
(15) Imperial Valley	1979	6.5	SS	El Centro Array #7	0.6	C	D	NA	0.10	40	IMPVALL\H-E07
(16) Imperial Valley	1979	6.5	SS	El Centro Array #8	3.8	C	D	NA	0.10	40	IMPVALL\H-E08
(17) Imperial Valley	1979	6.5	SS	El Centro Array #10	8.6	C	D	NA	0.10	40	IMPVALL\H-E10
(18) Imperial Valley	1979	6.5	SS	El Centro Array #11	12.6	C	D	NA	0.20	40	IMPVALL\H-E11
(19) Imperial Valley	1979	6.5	SS	El Centro Differential Array	5.3	C	D	NA	0.10	40	IMPVALL\H-EDA
(20) Imperial Valley	1979	6.5	SS	Holtville Post Office	7.5	C	D	NA	0.10	40	IMPVALL\H-HVP
(21) Imperial Valley	1979	6.5	SS	SAHOP Casa Flores	11.1	C	C	NA	0.20	--	IMPVALL\H-SHP
(22) Imperial Valley	1979	6.5	SS	Westmorland Fire Sta	15.1	C	D	NA	0.10	40	IMPVALL\H-WSM
(23) Coalinga	1983	6.4	RV/OB	Pleasant Valley P.P. - bldg	8.5	--	D	H	0.20	20	COALINGA\H-PVP
(24) Coalinga	1983	6.4	RV/OB	Pleasant Valley P.P. - yard	8.5	--	D	H	0.20	31	COALINGA\H-PVY
(25) Morgan Hill	1984	6.2	SS	Gilroy Array #2	15.1	C	D	NA	0.20	31	MORGAN\G02
(26) Morgan Hill	1984	6.2	SS	Gilroy Array #3	14.6	C	D	NA	0.10	32	MORGAN\G03
(27) Morgan Hill	1984	6.2	SS	Gilroy Array #4	12.8	C	D	NA	0.10	25	MORGAN\G04
(28) Morgan Hill	1984	6.2	SS	Gilroy Array #7	14.0	C	B	NA	0.10	30	MORGAN\GMR

Table A-3 (continued)

Earthquake Location [a]	Year	M_w	Source Mech.	Station	R_{close} [b] (km)	Site Class [c] USGS	Site Class [c] GM	H/F [d]	Max. [e] f_c^{HP} (hz)	Min. [e] f_c^{LP} (hz)	Dir\Filename-Prefix [f]	
(29) Morgan Hill	1984	6.2	SS	Halls Valley	3.4	C	C	NA	0.20	26	MORGAN\HVR	
(30) Whittier Narrows	1987	6.0	TH	Bell Gardens - Jaboneria #	9.8	C	D	--	0.25	25	WHITTIER\A-JAB	
(31) Whittier Narrows	1987	6.0	TH	LA - E Vernon Ave #	10.8	C	D	--	0.18	25	WHITTIER\A-VER	
(32) Whittier Narrows	1987	6.0	TH	La Habra - Briarcliff #	13.5	C	C	--	0.25	25	WHITTIER\A-BRC	
(33) Whittier Narrows	1987	6.0	TH	West Covina - S Orange #	10.5	C	B	--	0.23	25	WHITTIER\A-SOR	
(34) Superstition Hills (B)	1987	6.7	SS	El Centro Imp. Co. Cent	13.9	C	D	NA	0.10	38	SUPERST\B-ICC	
(35) Superstition Hills (B)	1987	6.7	SS	Westmorland Fire Sta	13.3	C	D	NA	0.10	35	SUPERST\B-WSM	
(36) Loma Prieta	1989	6.9	RV/OB	Capitola	14.5	C	C	--	0.20	40	LOMAP\CAP	
(37) Loma Prieta	1989	6.9	RV/OB	Gilroy - Historic Bldg.	12.7	--	D	F	0.20	38	LOMAP\GOF	
(38) Loma Prieta	1989	6.9	RV/OB	Gilroy Array #2	12.7	C	D	--	0.20	31	LOMAP\G02	
(39) Loma Prieta	1989	6.9	RV/OB	Gilroy Array #3	14.4	C	D	--	0.10	33	LOMAP\G03	
(40) Erzican, TURKEY	1992	6.9	SS	Erzincan	2.0	C	D	NA	0.10	--	ERZIKAN\ERZ	(NF09)
(41) Northridge	1994	6.7	TH	Canoga Park - Topanga Can	15.8	C	D	--	0.05	30	NORTHR\CNP	
(42) Northridge	1994	6.7	TH	Canyon Country - W Lost Cany	13.0	C	D	--	0.10	30	NORTHR\LOS	
(43) Northridge	1994	6.7	TH	Jensen Filter Plant #	6.2	C	D	--	0.20	--	NORTHR\JEN	
(44) Northridge	1994	6.7	TH	Newhall - Fire Sta #	7.1	C	D	--	0.12	23	NORTHR\NWH	(NS31)
(45) Northridge	1994	6.7	TH	Northridge - 17645 Saticoy St	13.3	C	D	--	0.10	30	NORTHR\STC	
(46) Northridge	1994	6.7	TH	Rinaldi Receiving Sta #	7.1	C	C	--	--	--	NORTHR\RRS	(NF13)
(47) Northridge	1994	6.7	TH	Sepulveda VA #	8.9	C	D	--	0.10	--	NORTHR\SPV	(NS33)
(48) Northridge	1994	6.7	TH	Sun Valley - Roscoe Blvd	12.3	C	D	--	0.10	30	NORTHR\RO3	
(49) Northridge	1994	6.7	TH	Sylmar - Converter Sta #	6.2	C	D	--	--	--	NORTHR\SCS	
(50) Northridge	1994	6.7	TH	Sylmar - Converter Sta East #	6.1	C	D	--	--	--	NORTHR\SCE	
(51) Northridge	1994	6.7	TH	Sylmar - Olive View Med FF #	6.4	C	D	--	0.12	23	NORTHR\SYL	(NF15)
(52) Parkfield	1966	6.1	SS	Cholame #12	14.7	B	B	NA	0.20	20	PARKF\C12	
(53) Parkfield	1966	6.1	SS	Temblor pre-1969	9.9	B	A	NA	0.20	15	PARKF\TMB	
(54) Santa Barbara	1978	6.0	RV/OB	Santa Barbara Courthouse	14.0 *	B	D	H	0.10	26	SBARB\SBA	
(55) Imperial Valley	1979	6.5	SS	Parachute Test Site	14.2	B	D	NA	0.10	40	IMPVALL\H-PTS	
(56) Morgan Hill	1984	6.2	SS	Anderson Dam (Downstream)	2.6	B	D	NA	0.10	30	MORGAN\AND	

Table A-3 (continued)

Earthquake Location [a]	Year	M_w	Source Mech.	Station	R_{close} [b] (km)	Site Class [c] USGS	Site Class [c] GM	H/F [d]	Max. [e] f_c^{HP} (hz)	Min. [e] f_c^{LP} (hz)	Dir\Filename-Prefix [f]
(57) Morgan Hill	1984	6.2	SS	Gilroy Array #6	11.8	B	B	NA	0.10	27	MORGAN\G06
(58) N. Palm Springs	1986	6.0	RV/OB	Fun Valley	15.8	B	C	--	0.25	35	PALMSPR\FVR
(59) N. Palm Springs	1986	6.0	RV/OB	Morongo Valley	10.1	B	C	H	0.08	50	PALMSPR\MVH
(60) N. Palm Springs	1986	6.0	RV/OB	North Palm Springs	8.2	B	D	H	0.23	20	PALMSPR\NPS
(61) Whittier Narrows	1987	6.0	TH	Garvey Res. - Control Bldg	12.1	--	B	H	0.20	40	WHITTIER\A-GRV
(62) Superstition Hills (B)	1987	6.7	SS	Parachute Test site	0.7	B	D	NA	0.12	20	SUPERST\B-PTS
(63) Loma Prieta	1989	6.9	RV/OB	Corralitos	5.1	B	B	F	0.20	40	LOMAP\CLS
(64) Loma Prieta	1989	6.9	RV/OB	Gilroy - Gavilan Coll.	11.6	B	B	--	0.20	35	LOMAP\GIL
(65) Loma Prieta	1989	6.9	RV/OB	Saratoga - Aloha Ave	13.0	B	D	--	0.10	38	LOMAP\STG
(66) Loma Prieta	1989	6.9	RV/OB	Saratoga - W Valley Coll.	13.7	B	D	--	0.10	38	LOMAP\WVC
(67) Landers	1992	7.3	SS	Joshua Tree #	11.6	B	C	NA	0.07	23	LANDERS\JOS
(68) Northridge	1994	6.7	TH	Arleta - Nordhoff Fire Sta #	9.2	B	D	--	0.12	23	NORTHR\ARL
(69) Northridge	1994	6.7	TH	LA - UCLA Grounds	14.9	B	--	--	0.08	25	NORTHR\UCL
(70) Northridge	1994	6.7	TH	N. Hollywood - Coldwater Can	14.6	B	C	--	0.10	30	NORTHR\CWC
(71) Northridge	1994	6.7	TH	Newhall - W. Pico Canyon Rd.	7.1	B	C	--	0.10	30	NORTHR\WPI
(72) Northridge	1994	6.7	TH	Pacoima Dam (downstr) #	8.0	--	B	--	0.16	23	NORTHR\PAC
(73) Northridge	1994	6.7	TH	Pacoima Kagel Canyon #	8.2	B	B	--	0.14	23	NORTHR\PKC
(74) Kobe, JAPAN	1995	6.9	SS	KJMA	0.6	B	B	NA	0.05	--	KOBE\KJM (NF17)
(75) Tabas, IRAN	1978	7.4	TH	Tabas	3.0 *	--	C	F	0.05	--	TABAS\TAB

[a] unless noted otherwise, earthquake locations are in California

[b] distances marked with a * are hypocentral instead of closest distances

[c] earthquake recordings on NEHRP site class D are listed first (above dividing line), followed by NEHRP site class C

[d] earthquake recorded on hanging wall (H) or foot wall (F), if applicable

[e] maximum/minimun of two original (i.e., unrotated) horizontal components

[f] ID's noted (in parentheses) for "pulsive" earthquake records (i.e., acc. to Alavi & Krawinkler, 1999)

Table A-4. "Intermediate-field" earthquake record set.

Earthquake Location [a]	Year	M_w	Source Mech.	Station	R_{close} [b] (km)	Site Class [c] USGS	Site Class [c] GM	H/F [d]	Max. [e] f_c^{HP} (hz)	Min. [e] f_c^{LP} (hz)	Dir\Filename-Prefix
(1) San Fernando	1971	6.6	TH	LA - Hollywood Stor Lot	21.2	C	D	--	0.20	35	SFERN\PEL
(2) Imperial Valley	1979	6.5	SS	Calipatria Fire Sta	23.8	C	D	NA	0.10	40	IMPVALL\H-CAL
(3) Imperial Valley	1979	6.5	SS	Chihuahua	28.7	C	D	NA	0.05	--	IMPVALL\H-CHI
(4) Imperial Valley	1979	6.5	SS	El Centro Array #12	18.2	C	D	NA	0.10	40	IMPVALL\H-E12
(5) Imperial Valley	1979	6.5	SS	El Centro Array #13	21.9	C	D	NA	0.20	40	IMPVALL\H-E13
(6) Coalinga	1983	6.4	RV/OB	Cantua Creek School	25.5	--	D	--	0.20	23	COALINGA\H-CAK
(7) Coalinga	1983	6.4	RV/OB	Parkfield - Gold Hill 3E	29.2	--	D	--	0.20	26	COALINGA\H-GH3
(8) Morgan Hill	1984	6.2	SS	Agnews State Hospital	29.4	C	D	NA	0.20	13	MORGAN\AGW
(9) Morgan Hill	1984	6.2	SS	Hollister Diff. Array	28.3	--	D	NA	0.20	23	MORGAN\HDA
(10) Morgan Hill	1984	6.2	SS	Hollister Diff Array #1	28.3	--	D	NA	0.20	30	MORGAN\HD1
(11) Morgan Hill	1984	6.2	SS	Hollister Diff Array #3	28.3	--	D	NA	0.20	30	MORGAN\HD3
(12) Morgan Hill	1984	6.2	SS	Hollister Diff Array #4	28.3	--	D	NA	0.20	30	MORGAN\HD4
(13) Morgan Hill	1984	6.2	SS	Hollister Diff Array #5	28.3	--	D	NA	0.20	30	MORGAN\HD5
(14) N. Palm Springs	1986	6.0	RV/OB	Cabazon	16.3	--	D	F	0.15	40	PALMSPR\CAB
(15) N. Palm Springs	1986	6.0	RV/OB	Palm Springs Airport	16.6	C	D	--	0.20	50	PALMSPR\PSA
(16) Whittier Narrows	1987	6.0	TH	Downey - Co Maint Bldg	18.3	--	D	--	0.25	30	WHITTIER\A-DWN
(17) Whittier Narrows	1987	6.0	TH	LA - 116th St School	22.5	--	D	--	0.20	30	WHITTIER\A-116
(18) Whittier Narrows	1987	6.0	TH	LA - Saturn St #	20.8	C	D	--	0.25	25	WHITTIER\A-STN
(19) Whittier Narrows	1987	6.0	TH	Norwalk - Imp Hwy, S Grnd	17.2	--	D	F	0.15	40	WHITTIER\A-NOR
(20) Superstition Hills(B)	1987	6.7	SS	Brawley	18.2	C	D	NA	0.13	20	SUPERST\B-BRA
(21) Superstition Hills(B)	1987	6.7	SS	Calipatria Fire Station	28.3	C	D	NA	0.23	18	SUPERST\B-CAL
(22) Superstition Hills(B)	1987	6.7	SS	Wildlife Liquef. Array	24.4	--	D	NA	0.10	40	SUPERST\B-IVW
(23) Loma Prieta	1989	6.9	RV/OB	Agnews State Hospital	28.2	C	D	--	0.20	30	LOMAP\AGW
(24) Loma Prieta	1989	6.9	RV/OB	Gilroy Array #4	16.1	C	D	--	0.20	28	LOMAP\G04
(25) Loma Prieta	1989	6.9	RV/OB	Gilroy Array #7	24.2	C	B	--	0.20	35	LOMAP\GMR
(26) Loma Prieta	1989	6.9	RV/OB	Hollister City Hall	28.2	C	D	--	0.10	29	LOMAP\HCH
(27) Loma Prieta	1989	6.9	RV/OB	Hollister Diff. Array	25.8	--	D	--	0.10	33	LOMAP\HDA
(28) Loma Prieta	1989	6.9	RV/OB	Hollister - South & Pine	28.8	--	D	--	0.10	23	LOMAP\HSP

Table A-4 (continued)

Earthquake Location [a]	Year	M_w	Source Mech.	Station	R_{close} [b] (km)	Site Class [c] USGS	Site Class [c] GM	H/F [d]	Max. [e] f_c^{HP} (hz)	Min. [e] f_c^{LP} (hz)	Dir\Filename-Prefix
(29) Loma Prieta	1989	6.9	RV/OB	Sunnyvale - Colton Ave.	28.8	C	D	--	0.10	32	LOMAP\SVL
(30) Loma Prieta	1989	6.9	RV/OB	WAHO	16.9	--	D	--	0.10	--	LOMAP\WAH
(31) Landers	1992	7.3	SS	Yermo Fire Station #	24.9	C	D	NA	0.07	23	LANDERS\YER
(32) Northridge	1994	6.7	TH	Glendale - Las Palmas	25.4	C	C	--	0.13	30	NORTHR\GLP
(33) Northridge	1994	6.7	TH	LA - Fletcher Dr	29.5	C	D	--	0.15	30	NORTHR\FLE
(34) Northridge	1994	6.7	TH	LA - Hollywood Stor FF #	25.5	C	D	--	0.20	23	NORTHR\HOL
(35) Northridge	1994	6.7	TH	LA - N Faring Rd	23.9	C	B	--	0.13	30	NORTHR\FAR
(36) Northridge	1994	6.7	TH	Moorpark - Fire Sta #	28.0	--	D	--	0.16	23	NORTHR\MRP
(37) Kobe, JAPAN	1995	6.9	SS	Abeno	23.8	C	D	NA	0.05	40	KOBE\ABN
(38) Kobe, JAPAN	1995	6.9	SS	Yae	26.3	--	D	NA	0.05	--	KOBE\YAE
(39) Tabas, IRAN	1978	7.4	TH	Dayhook	17.0 *	--	B	H	0.10	--	TABAS\DAY
(40) Imperial Valley	1979	6.5	SS	Cerro Prieto	26.5	B	A	NA	0.10	--	IMPVALL\H-CPE
(41) Imperial Valley	1979	6.5	SS	Superstition Mtn Camera	26.0	B	A	NA	0.10	40	IMPVALL\H-SUP
(42) Coalinga	1983	6.4	RV/OB	Parkfield - Fault Zone 8	29.6	--	B	--	0.20	21	COALINGA\H-Z08
(43) Coalinga	1983	6.4	RV/OB	Parkfield - Fault Zone 11	28.4	--	B	--	0.20	21	COALINGA\H-Z11
(44) Coalinga	1983	6.4	RV/OB	Parkfield - Fault Zone 15	29.9	--	B	--	0.20	20	COALINGA\H-Z15
(45) Morgan Hill	1984	6.2	SS	Corralitos	22.7	B	B	NA	0.20	24	MORGAN\CLS
(46) Morgan Hill	1984	6.2	SS	Gilroy Gavilan Coll.	16.2	B	B	NA	0.10	30	MORGAN\GIL
(47) Loma Prieta	1989	6.9	RV/OB	Anderson Dam (Downstream)	21.4	B	D	--	0.20	40	LOMAP\AND
(48) Loma Prieta	1989	6.9	RV/OB	Anderson Dam (L Abut)	21.4	B	A	--	0.10	32	LOMAP\ADL
(49) Loma Prieta	1989	6.9	RV/OB	Coyote Lake Dam (Downst)	22.3	B	D	F	0.10	29	LOMAP\CLD
(50) Loma Prieta	1989	6.9	RV/OB	Gilroy Array #6	19.9	B	B	--	0.20	31	LOMAP\G06
(51) Loma Prieta	1989	6.9	RV/OB	UCSC	18.1	--	B	H	0.10	--	LOMAP\UC2
(52) Landers	1992	7.3	SS	Coolwater	21.2	B	D	NA	0.10	30	LANDERS\CLW
(53) Landers	1992	7.3	SS	Desert Hot Springs #	23.2	B	D	NA	0.07	23	LANDERS\DSP
(54) Landers	1992	7.3	SS	Morongo Valley	19.3	B	C	NA	--	--	LANDERS\MVH
(55) Landers	1992	7.3	SS	North Palm Springs	24.2	B	D	NA	--	--	LANDERS\NPS
(56) Northridge	1994	6.7	TH	Beverly Hills - 12520 Mulhol	20.8	B	C	--	0.13	30	NORTHR\MU2

Table A-4 (continued)

Earthquake Location [a]	Year	M_w	Source Mech.	Station	R_{close} [b] (km)	Site Class [c] USGS	Site Class [c] GM	H/F [d]	Max.[e] f_c^{HP} (hz)	Min.[e] f_c^{LP} (hz)	Dir\Filename-Prefix
(57) Northridge	1994	6.7	TH	Beverly Hills - 14145 Mulhol	19.6	B	C	--	0.20	30	NORTHR\MUL
(58) Northridge	1994	6.7	TH	Burbank - Howard Rd.	20.0	B	B	--	0.10	30	NORTHR\HOW
(59) Northridge	1994	6.7	TH	Castaic - Old Ridge Route #	22.6	B	B	--	0.12	23	NORTHR\ORR
(60) Northridge	1994	6.7	TH	Hollywood - Willoughby Ave	25.7	B	D	--	0.13	30	NORTHR\WIL
(61) Northridge	1994	6.7	TH	LA - Century City CC North #	25.7	B	D	--	0.14	23	NORTHR\CCN
(62) Northridge	1994	6.7	TH	LA - N Westmoreland	29.0	B	D	--	0.20	30	NORTHR\WST
(63) Northridge	1994	6.7	TH	Lake Hughes #12A #	22.8	B	C	--	0.12	46	NORTHR\H12
(64) Northridge	1994	6.7	TH	Pacific Palisades - Sunset Blvd	26.2	B	B	--	0.05	30	NORTHR\SUN
(65) Northridge	1994	6.7	TH	Santa Monica City Hall #	27.6	B	D	--	0.14	23	NORTHR\STM
(66) Northridge	1994	6.7	TH	Santa Susana Ground #	19.3	B	--	--	--	--	NORTHR\SSU
(67) Northridge	1994	6.7	TH	Sunland - Mt Gleason Ave	17.7	B	C	--	0.05	30	NORTHR\GLE
(68) Northridge	1994	6.7	TH	Tarzana, Cedar Hill #	17.5	--	B	--	0.10	23	NORTHR\TAR
(69) Northridge	1994	6.7	TH	Vasquez Rocks Park #	24.2	B	A	--	0.08	--	NORTHR\VAS
(70) Tabas, IRAN	1978	7.4	TH	Boshrooyeh	26.1	--	C	--	0.04	20	TABAS\BOS
(71) Coalinga	1983	6.4	RV/OB	Parkfield - Fault Zone 12	29.5	--	C	--	0.20	20	COALINGA\H-PRK
(72) Coalinga	1983	6.4	RV/OB	Parkfield - Fault Zone 14	29.9	--	C	--	0.20	23	COALINGA\H-Z14
(73) Coalinga	1983	6.4	RV/OB	Parkfield - Fault Zone 16	28.1	--	C	--	0.20	26	COALINGA\H-Z16
(74) Coalinga	1983	6.4	RV/OB	Parkfield - Vineyard Cany 1E	26.7	--	C	--	0.20	23	COALINGA\H-PV1

[a] unless noted otherwise, earthquake locations are in California

[b] distances marked with a * are hypocentral instead of closest distances

[c] earthquake recordings on NEHRP site class D are listed first (above dividing line), followed by NEHRP site class C

[d] earthquake recorded on hanging wall (H) or foot wall (F), if applicable

[e] maximum/minimun of two original (i.e., unrotated) horizontal components

Table A-5. "Far-field" earthquake record set.

Earthquake Location [a]	Year	M_w	Source Mech.	Station	R_{close} (km)	Site Class [b] USGS	Site Class [b] GM	H/F [c]	Max.[d] f_c^{HP} (hz)	Min.[d] f_c^{LP} (hz)	Dir\Filename-Prefix
(1) San Fernando	1971	6.6	TH	Whittier Narrows Dam	45.1	--	D	--	0.10	20	SFERN\WND
(2) Imperial Valley	1979	6.5	SS	Compuertas	32.6	C	D	NA	0.20	--	IMPVALL\H-CMP
(3) Imperial Valley	1979	6.5	SS	Delta	43.6	C	D	NA	0.05	--	IMPVALL\H-DLT
(4) Imperial Valley	1979	6.5	SS	Niland Fire Station	35.9	C	D	NA	0.10	30	IMPVALL\H-NIL
(5) Imperial Valley	1979	6.5	SS	Plaster City	31.7	C	D	NA	0.10	40	IMPVALL\H-PLS
(6) Coalinga	1983	6.4	RV/OB	Parkfield - Cholame 1E	41.6	--	D	--	0.20	20	COALINGA\H-C01
(7) Coalinga	1983	6.4	RV/OB	Parkfield - Cholame 2WA	42.8	--	D	--	0.20	22	COALINGA\H-C02
(8) Coalinga	1983	6.4	RV/OB	Parkfield - Fault Zone 1	40.4	--	D	--	0.20	20	COALINGA\H-COW
(9) Coalinga	1983	6.4	RV/OB	Parkfield - Fault Zone 2	37.9	--	D	--	0.20	22	COALINGA\H-Z02
(10) Coalinga	1983	6.4	RV/OB	Parkfield - Fault Zone 3	36.4	--	D	--	0.10	22	COALINGA\H-COH
(11) Coalinga	1983	6.4	RV/OB	Parkfield - Fault Zone 10	30.4	--	D	--	0.20	21	COALINGA\H-Z10
(12) Coalinga	1983	6.4	RV/OB	Parkfield - Gold Hill 2E	32.3	--	D	--	0.20	30	COALINGA\H-GH2
(13) Morgan Hill	1984	6.2	SS	Capitola	38.1	C	C	NA	0.20	28	MORGAN\CAP
(14) Morgan Hill	1984	6.2	SS	Hollister City Hall	32.5	C	D	NA	0.20	19	MORGAN\HCH
(15) Morgan Hill	1984	6.2	SS	San Justo Dam (L Abut)	34.9	--	D	NA	0.20	29	MORGAN\SJL
(16) Morgan Hill	1984	6.2	SS	San Justo Dam (R Abut)	34.9	--	D	NA	0.20	23	MORGAN\SJR
(17) N. Palm Springs	1986	6.0	RV/OB	Indio	39.6	--	D	--	0.10	35	PALMSPR\INO
(18) N. Palm Springs	1986	6.0	RV/OB	San Jacinto Vall. Cem	39.6	C	D	--	0.20	31	PALMSPR\H06
(19) Whittier Narrows	1987	6.0	TH	Huntington Beach - Lake St	42.8	--	D	--	0.25	25	WHITTIER\A-HNT
(20) Whittier Narrows	1987	6.0	TH	Northridge - Saticoy St #	39.8	C	D	--	0.23	25	WHITTIER\A-STC
(21) Loma Prieta	1989	6.9	RV/OB	Halls Valley	31.6	C	C	F	0.20	22	LOMAP\HVR
(22) Loma Prieta	1989	6.9	RV/OB	Palo Alto - 1900 Embarc.	36.1	--	D	--	0.20	30	LOMAP\PAE
(23) Loma Prieta	1989	6.9	RV/OB	Palo Alto - SLAC Lab	36.3	C	A	--	0.20	28	LOMAP\SLC
(24) Loma Prieta	1989	6.9	RV/OB	Salinas - John & Work	32.6	C	D	--	0.10	28	LOMAP\SJW
(25) Landers	1992	7.3	SS	Palm Springs Airport #	37.5	C	D	NA	0.07	23	LANDERS\PSA
(26) Northridge	1994	6.7	TH	Anaverde Valley - City R #	38.4	C	D	--	0.20	46	NORTHR\ANA
(27) Northridge	1994	6.7	TH	Camarillo	36.5	C	--	--	0.10	25	NORTHR\CMR
(28) Northridge	1994	6.7	TH	Elizabeth Lake #	37.2	C	D	--	0.16	46	NORTHR\ELI

Table A-5 (continued)

Earthquake Location [a]	Year	M_w	Source Mech.	Station	R_{close} (km)	Site Class [b] USGS	Site Class [b] GM	H/F [c]	Max.[d] f_c^{HP} (hz)	Min.[d] f_c^{LP} (hz)	Dir\Filename-Prefix
(29) Northridge	1994	6.7	TH	LA - Centinela St	30.9	C	D	--	0.20	30	NORTHR\CEN
(30) Northridge	1994	6.7	TH	LA - E Vernon Ave	39.3	C	D	--	0.20	30	NORTHR\VER
(31) Northridge	1994	6.7	TH	LA - Pico & Sentous #	32.7	C	D	--	0.20	46	NORTHR\PIC
(32) Northridge	1994	6.7	TH	LA - Saturn St	30.0	C	D	--	0.10	30	NORTHR\STN
(33) Northridge	1994	6.7	TH	Lake Hughes #1 #	36.3	C	C	--	0.12	23	NORTHR\LH1
(34) Northridge	1994	6.7	TH	Lawndale - Osage Ave	42.4	C	D	--	0.13	30	NORTHR\LOA
(35) Northridge	1994	6.7	TH	Leona Valley #2 #	37.7	C	--	--	0.20	23	NORTHR\LV2
(36) Northridge	1994	6.7	TH	Leona Valley #4 #	38.1	C	--	--	0.20	23	NORTHR\LV4
(37) Northridge	1994	6.7	TH	Leona Valley #5 - Ritter #	38.3	C	C	--	0.20	23	NORTHR\LV5
(38) Northridge	1994	6.7	TH	Leona Valley #6 #	38.5	C	D	--	0.20	23	NORTHR\LV6
(39) Northridge	1994	6.7	TH	Manhattan Beach - Manhattan	42.0	C	C	--	0.23	30	NORTHR\MAN
(40) Northridge	1994	6.7	TH	Palmdale - Hwy 14 & Palmdale #	43.6	C	C	--	0.20	46	NORTHR\PHP
(41) Kobe, JAPAN	1995	6.9	SS	Tadoka	30.5	C	D	NA	0.05	40	KOBE\TDO
(42) Kern County	1952	7.4	RV/OB	Taft Lincoln School	41.0	B	D	F	0.05	13	KERN\TAF
(43) San Fernando	1971	6.6	TH	Pearblossom Pump	38.9	B	B	--	0.20	35	SFERN\PPP
(44) Coalinga	1983	6.4	RV/OB	Parkfield - Fault Zone 4	34.3	--	B	--	0.20	22	COALINGA\H-Z04
(45) Coalinga	1983	6.4	RV/OB	Parkfield - Fault Zone 6	32.8	--	B	--	0.20	24	COALINGA\H-Z06
(46) Coalinga	1983	6.4	RV/OB	Parkfield - Fault Zone 9	31.9	--	B	--	0.20	23	COALINGA\H-Z09
(47) Coalinga	1983	6.4	RV/OB	Parkfield - Gold Hill 2W	36.6	--	B	--	0.20	20	COALINGA\H-PG2
(48) Coalinga	1983	6.4	RV/OB	Parkfield - Gold Hill 3W	38.8	--	B	--	0.20	30	COALINGA\H-PG3
(49) Coalinga	1983	6.4	RV/OB	Parkfield - Gold Hill 4W	41.0	--	B	--	0.20	30	COALINGA\H-PG4
(50) Coalinga	1983	6.4	RV/OB	Parkfield - Gold Hill 5W	43.7	--	B	--	0.20	26	COALINGA\H-PG5
(51) Coalinga	1983	6.4	RV/OB	Parkfield - Vineyard Cany 4W	34.6	--	B	--	0.20	27	COALINGA\H-VC4
(52) Morgan Hill	1984	6.2	SS	San Juan Bautista	30.3	B	D	NA	0.10	21	MORGAN\SJB
(53) Whittier Narrows	1987	6.0	TH	Panorama City - Roscoe #	33.0	B	D	--	0.25	24	WHITTIER\A-RO2
(54) Loma Prieta	1989	6.9	RV/OB	Fremont - Emerson Court	43.4	--	B	--	0.10	31	LOMAP\FMS
(55) Loma Prieta	1989	6.9	RV/OB	Fremont - Mission San Jose	43.0	B	B	--	0.20	24	LOMAP\FRE
(56) Loma Prieta	1989	6.9	RV/OB	SAGO South - Surface	34.7	B	B	--	0.10	25	LOMAP\SG3

Table A-5 (continued)

Earthquake Location [a]	Year	M_w	Source Mech.	Station	R_{close} (km)	Site Class [b] USGS	Site Class [b] GM	H/F [c]	Max.[d] f_c^{HP} (hz)	Min.[d] f_c^{LP} (hz)	Dir\Filename-Prefix
(57) Loma Prieta	1989	6.9	RV/OB	Woodside	39.9	B	B	--	0.10	25	LOMAP\WDS
(58) Landers	1992	7.3	SS	Barstow #	36.1	B	D	NA	0.07	23	LANDERS\BRS
(59) Northridge	1994	6.7	TH	Alhambra - Fremont School	35.7	B	D	--	0.12	25	NORTHR\ALH
(60) Northridge	1994	6.7	TH	Inglewood - Union Oil #	44.7	B	D	--	0.16	23	NORTHR\ING
(61) Northridge	1994	6.7	TH	LA - 116th St School #	41.9	B	D	--	0.16	23	NORTHR\116
(62) Northridge	1994	6.7	TH	LA - Baldwin Hills #	31.3	B	B	--	0.16	23	NORTHR\BLD
(63) Northridge	1994	6.7	TH	LA - City Terrace #	37.0	--	B	--	0.20	46	NORTHR\LAC
(64) Northridge	1994	6.7	TH	LA - Cypress Ave	32.8	B	C	--	0.20	30	NORTHR\CYP
(65) Northridge	1994	6.7	TH	LA - Temple & Hope #	32.3	B	B	--	0.20	46	NORTHR\TEM
(66) Northridge	1994	6.7	TH	LA - Univ. Hospital #	34.6	B	B	--	0.20	46	NORTHR\UNI
(67) Northridge	1994	6.7	TH	LA - W 15th St	32.4	B	C	--	0.13	30	NORTHR\W15
(68) Northridge	1994	6.7	TH	Lake Hughes #4 - Camp Mend #	32.3	--	B	--	0.12	23	NORTHR\LH4
(69) Northridge	1994	6.7	TH	Lake Hughes #4B - Camp Mend #	32.3	B	B	--	0.12	23	NORTHR\L4B
(70) Northridge	1994	6.7	TH	Playa Del Rey - Saran	34.2	B	D	--	0.10	30	NORTHR\SAR
(71) Coalinga	1983	6.4	RV/OB	Parkfield - Cholame 3W	43.9	--	C	--	0.20	21	COALINGA\H-C03
(72) Coalinga	1983	6.4	RV/OB	Parkfield - Cholame 4W	44.7	--	C	--	0.20	21	COALINGA\H-C04
(73) Coalinga	1983	6.4	RV/OB	Parkfield - Fault Zone 7	31.0	--	C	--	0.20	30	COALINGA\H-Z07
(74) Coalinga	1983	6.4	RV/OB	Parkfield - Vineyard Cany 2W	30.7	--	C	--	0.20	30	COALINGA\H-VC2
(75) Coalinga	1983	6.4	RV/OB	Parkfield - Vineyard Cany 6W	41.0	--	C	--	0.20	25	COALINGA\H-VC6

[a] unless noted otherwise, earthquake locations are in California

[b] earthquake recordings on NEHRP site class D are listed first (above dividing line), followed by NEHRP site class C

[c] earthquake recorded on hanging wall (H) or foot wall (F), if applicable

[d] maximum/minimun of two original (i.e., unrotated) horizontal components

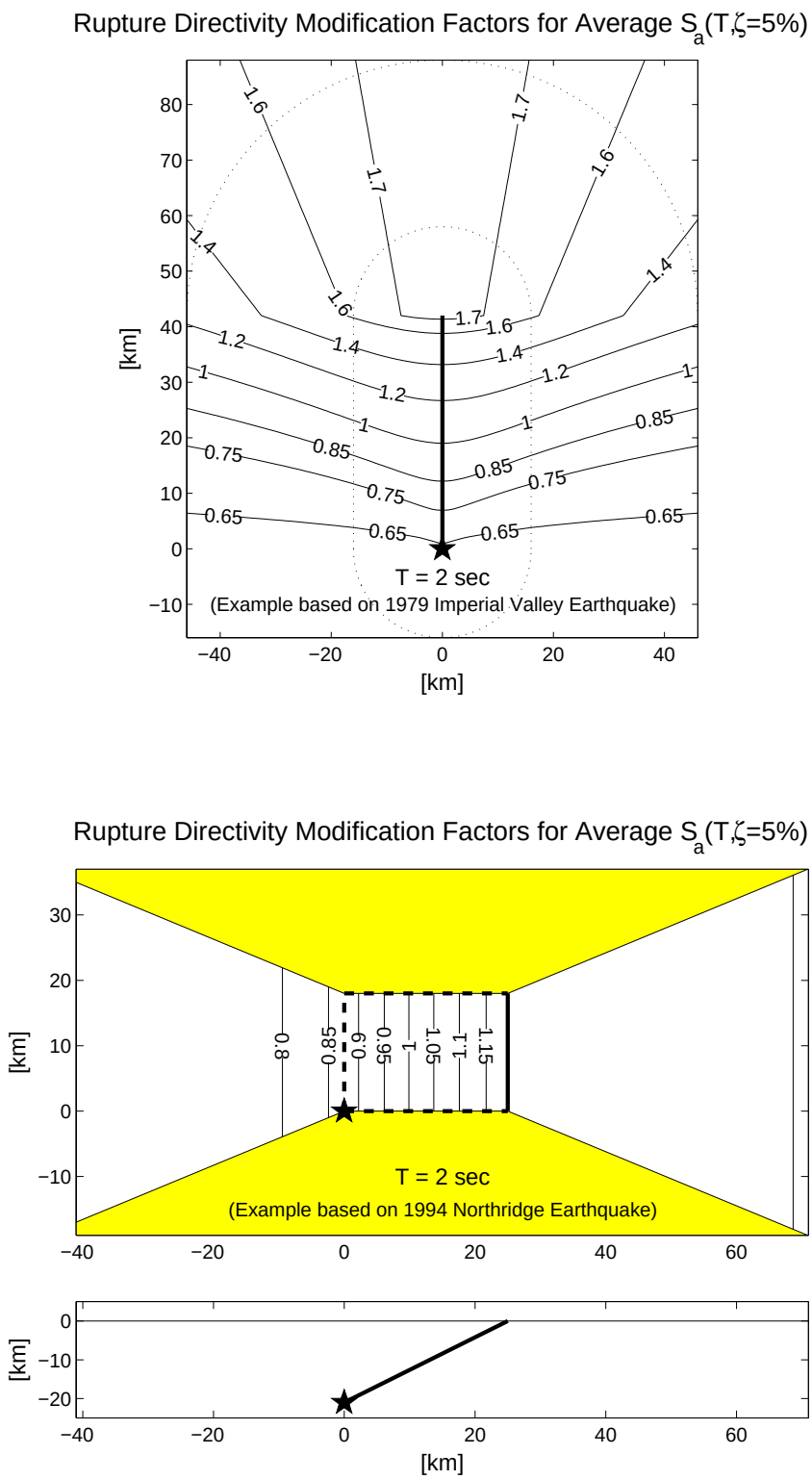

Figure A-1. Contour plot of directivity modification factor for simplified fault geometry and hypocenter location based on **(a)** the strike-slip Imperial Valley earthquake of 1979, and **(b)** the dip-slip Northridge earthquake of 1994.

Table A-6. Directivity parameters and modification factors for the nearby-field earthquake records ("forward-directivity" earthquake records in bold).

Earthquake Record Dir/Filename	X or Y [a]	θ or ϕ [a] [degrees]	Directivity Modification Factor [b] T = 1s	T = 2s	T = 4s	
(1) Impvall/I-ELC.fn	0.150	19.170	0.876	0.733	0.612	
(2) Parkf/C05.fn	0.671	7.922	1.000	1.000	1.000	
(3) Parkf/C08.fn	0.681	16.480	1.000	1.000	1.000	
(4) Impvall/H-AEP.fn	0.030	19.890	0.835	0.655	0.512	
(5) Impvall/H-AGR.fn	0.080	13.260	0.853	0.688	0.554	
(6) Impvall/H-BCR.fn	0.128	25.530	0.867	0.714	0.588	
(7) Impvall/H-BRA.fn	**0.812**	**13.340**	**1.153**	**1.400**	**1.696**	
(8) Impvall/H-CXO.fn	0.295	40.610	0.907	0.796	0.697	
(9) Impvall/H-ECC.fn	**0.672**	**15.450**	**1.085**	**1.215**	**1.356**	
(10) Impvall/H-EMO.fn	**0.550**	**1.000**	**1.041**	**1.102**	**1.163**	**(NS23)**
(11) Impvall/H-E01.fn	**0.697**	**38.210**	**1.040**	**1.099**	**1.159**	
(12) Impvall/H-E04.fn	**0.631**	**15.630**	**1.067**	**1.167**	**1.273**	
(13) Impvall/H-E05.fn	**0.690**	**8.430**	**1.102**	**1.258**	**1.432**	
(14) Impvall/H-E06.fn	**0.670**	**2.650**	**1.095**	**1.241**	**1.403**	**(NS21)**
(15) Impvall/H-E07.fn	**0.663**	**0.370**	**1.092**	**1.233**	**1.389**	
(16) Impvall/H-E08.fn	**0.660**	**8.070**	**1.088**	**1.222**	**1.368**	
(17) Impvall/H-E10.fn	**0.637**	**17.420**	**1.067**	**1.167**	**1.274**	
(18) Impvall/H-E11.fn	**0.614**	**26.520**	**1.041**	**1.101**	**1.162**	
(19) Impvall/H-EDA.fn	**0.650**	**11.180**	**1.081**	**1.202**	**1.335**	
(20) Impvall/H-HVP.fn	0.450	22.520	0.984	0.964	0.942	
(21) Impvall/H-SHP.fn	0.107	66.270	0.840	0.664	0.524	
(22) Impvall/H-WSM.fn	**0.812**	**4.980**	**1.162**	**1.427**	**1.747**	
(23) Coalinga/H-PVP.fn	0.330	37.000	1.000	1.000	1.000	
(24) Coalinga/H-PVY.fn	0.540	13.000	1.000	1.000	1.000	
(25) Morgan/G02.fn	0.938	7.370	1.000	1.000	1.000	
(26) Morgan/G03.fn	0.938	4.670	1.000	1.000	1.000	
(27) Morgan/G04.fn	0.938	1.850	1.000	1.000	1.000	
(28) Morgan/GMR.fn	0.938	10.440	1.000	1.000	1.000	
(29) Morgan/HVR.fn	0.062	9.350	1.000	1.000	1.000	
(30) Whittier/A-JAB.fn	0.500	29.000	1.000	1.000	1.000	
(31) Whittier/A-VER.fn	0.500	33.464	1.000	1.000	1.000	
(32) Whittier/A-BRC.fn	NA	NA	1.000	1.000	1.000	
(33) Whittier/A-SOR.fn	NA	NA	1.000	1.000	1.000	
(34) Superst/B-ICC.fn	**0.900**	**6.300**	**1.205**	**1.554**	**1.998**	
(35) Superst/B-WSM.fn	**0.721**	**44.610**	**1.025**	**1.062**	**1.098**	
(36) Lomap/CAP.fn	0.015	86.500	0.901	0.783	0.680	
(37) Lomap/GOF.fn	0.500	31.120	0.973	0.936	0.901	
(38) Lomap/G02.fn	0.500	25.620	0.977	0.945	0.915	
(39) Lomap/G03.fn	0.500	27.330	0.975	0.942	0.911	
(40) Erzikan/ERZ.fn	0.330	9.650	0.947	0.880	0.817	(NF09)
(41) Northr/CNP.fn	0.427	59.667	0.936	0.857	0.784	
(42) Northr/LOS.fn	**0.852**	**5.296**	**1.048**	**1.116**	**1.189**	
(43) Northr/JEN.fn	**0.852**	**16.023**	**1.043**	**1.102**	**1.166**	
(44) Northr/NWH.fn	**0.852**	**6.008**	**1.048**	**1.115**	**1.188**	**(NS31)**

Table A-6 (continued)

Earthquake Record Dir/Filename	X or Y [a]	θ or ϕ [a] [degrees]	Directivity Modification Factor [b] T = 1s	T = 2s	T = 4s	
(45) Northr/STC.fn	0.577	46.299	0.967	0.925	0.884	
(46) Northr/RRS.fn	**0.852**	**20.609**	**1.039**	**1.092**	**1.150**	**(NF13)**
(47) Northr/SPV.fn	**0.786**	**28.620**	**1.019**	**1.044**	**1.071**	**(NS33)**
(48) Northr/RO3.fn	**0.779**	**29.164**	**1.017**	**1.040**	**1.064**	
(49) Northr/SCS.fn	**0.852**	**16.227**	**1.042**	**1.102**	**1.165**	
(50) Northr/SCE.fn	**0.852**	**14.942**	**1.043**	**1.104**	**1.169**	
(51) Northr/SYL.fn	**0.852**	**8.379**	**1.047**	**1.113**	**1.185**	**(NF15)**
(52) Parkf/C12.fn	0.685	26.300	1.000	1.000	1.000	
(53) Parkf/TMB.fn	0.664	9.470	1.000	1.000	1.000	
(54) Sbarb/SBA.fn	0.001	65.859	1.000	1.000	1.000	
(55) Impvall/H-PTS.fn	**0.812**	**10.200**	**1.157**	**1.413**	**1.720**	
(56) Morgan/AND.fn	0.567	7.000	1.000	1.000	1.000	
(57) Morgan/G06.fn	0.938	4.290	1.000	1.000	1.000	
(58) Palmspr/FVR.fn	0.606	33.877	1.000	1.000	1.000	
(59) Palmspr/MVH.fn	0.246	72.531	1.000	1.000	1.000	
(60) Palmspr/NPS.fn	0.636	14.405	1.000	1.000	1.000	
(61) Whittier/A-GRV.fn	0.500	58.473	1.000	1.000	1.000	
(62) Superst/B-PTS.fn	**0.710**	**11.000**	**1.108**	**1.276**	**1.465**	
(63) Lomap/CLS.fn	0.124	44.030	0.916	0.812	0.721	
(64) Lomap/GIL.fn	0.500	23.210	0.978	0.948	0.920	
(65) Lomap/STG.fn	0.500	22.760	0.978	0.949	0.921	
(66) Lomap/WVC.fn	**0.600**	**11.000**	**1.001**	**1.001**	**1.002**	
(67) Landers/JOS.fn	0.100	45.000	0.850	0.683	0.548	
(68) Northr/ARL.fn	**0.812**	**26.584**	**1.026**	**1.060**	**1.097**	
(69) Northr/UCL.fn	0.236	75.134	0.911	0.803	0.707	
(70) Northr/CWC.fn	0.704	35.238	0.998	0.995	0.993	
(71) Northr/WPI.fn	**0.852**	**13.624**	**1.044**	**1.106**	**1.173**	
(72) Northr/PAC.fn	**0.852**	**3.029**	**1.049**	**1.117**	**1.191**	
(73) Northr/PKC.fn	**0.852**	**8.640**	**1.047**	**1.113**	**1.184**	
(74) Kobe/KJM.fn	0.298	11.190	0.934	0.852	0.776	(NF17)
(75) Tabas/TAB.fn	0.263	2.990	0.944	0.874	0.808	

[a] directivity parameters provided by (Stewart 2000)

[b] for average $S_a(T, \zeta=5\%)$

Table A-7. Directivity parameters and modification factors for the far-field earthquake records ("forward-directivity" earthquake records in bold).

Earthquake Record Dir/Filename	X or Y [a]	θ or ϕ [a] [degrees]	Directivity Modification Factor [b] T = 1s	T = 2s	T = 4s
(1) Sfern/WND.fn	**0.771**	**27.259**	**1.018**	**1.042**	**1.068**
(2) Impvall/H-CMP.fn	0.148	37.000	0.868	0.716	0.590
(3) Impvall/H-DLT.fn	0.162	81.560	0.834	0.652	0.509
(4) Impvall/H-NIL.fn	**0.812**	**22.530**	**1.133**	**1.345**	**1.592**
(5) Impvall/H-PLS.fn	**0.812**	**34.410**	**1.096**	**1.242**	**1.404**
(6) Coalinga/H-C01.fn	0.501	52.757	1.000	1.000	1.000
(7) Coalinga/H-C02.fn	0.501	53.095	1.000	1.000	1.000
(8) Coalinga/H-COW.fn	0.501	52.699	1.000	1.000	1.000
(9) Coalinga/H-Z02.fn	0.501	52.276	1.000	1.000	1.000
(10) Coalinga/H-COH.fn	0.501	51.976	1.000	1.000	1.000
(11) Coalinga/H-Z10.fn	0.501	50.946	1.000	1.000	1.000
(12) Coalinga/H-GH2.fn	0.501	50.897	1.000	1.000	1.000
(13) Morgan/CAP.fn	1.000	30.000	1.000	1.000	1.000
(14) Morgan/HCH.fn	0.938	0.910	1.000	1.000	1.000
(15) Morgan/SJL.fn	1.000	18.000	1.000	1.000	1.000
(16) Morgan/SJR.fn	1.000	18.000	1.000	1.000	1.000
(17) Palmspr/INO.fn	0.636	11.564	1.000	1.000	1.000
(18) Palmspr/H06.fn	0.636	28.497	1.000	1.000	1.000
(19) Whittier/A-HNT.fn	0.500	10.383	1.000	1.000	1.000
(20) Whittier/A-STC.fn	NA	NA	1.000	1.000	1.000
(21) Lomap/HVR.fn	0.220	75.940	0.910	0.800	0.704
(22) Lomap/PAE.fn	0.500	22.100	0.979	0.950	0.922
(23) Lomap/SLC.fn	0.500	17.690	0.981	0.955	0.930
(24) Lomap/SJW.fn	0.500	24.500	0.977	0.947	0.917
(25) Landers/PSA.fn	0.128	16.650	0.869	0.719	0.594
(26) Northr/ANA.fn	**0.852**	**21.276**	**1.038**	**1.091**	**1.147**
(27) Northr/CMR.fn	0.148	73.745	0.908	0.796	0.699
(28) Northr/ELI.fn	**0.852**	**20.733**	**1.039**	**1.092**	**1.149**
(29) Northr/CEN.fn	0.006	89.662	0.901	0.783	0.680
(30) Northr/VER.fn	0.375	64.124	0.928	0.838	0.757
(31) Northr/PIC.fn	0.437	58.808	0.938	0.860	0.789
(32) Northr/STN.fn	0.307	69.690	0.918	0.818	0.729
(33) Northr/LH1.fn	**0.852**	**20.255**	**1.039**	**1.093**	**1.151**
(34) Northr/LOA.fn	0.148	81.383	0.905	0.790	0.690
(35) Northr/LV2.fn	**0.852**	**20.927**	**1.038**	**1.092**	**1.148**
(36) Northr/LV4.fn	**0.852**	**21.025**	**1.038**	**1.091**	**1.148**
(37) Northr/LV5.fn	**0.852**	**21.085**	**1.038**	**1.091**	**1.148**
(38) Northr/LV6.fn	**0.852**	**21.212**	**1.038**	**1.091**	**1.147**
(39) Northr/MAN.fn	0.148	77.546	0.906	0.793	0.694
(40) Northr/PHP.fn	**0.852**	**22.248**	**1.037**	**1.088**	**1.143**
(41) Kobe/TDO.fn	0.296	62.870	0.874	0.728	0.606
(42) Kern/TAF.fn	0.565	37.005	0.977	0.945	0.915
(43) Sfern/PPP.fn	0.229	78.891	0.908	0.797	0.700
(44) Coalinga/H-Z04.fn	0.501	51.661	1.000	1.000	1.000

Table A-7 (continued)

Earthquake Record Dir/Filename	X or Y [a]	θ or ϕ [a] [degrees]	Directivity Modification Factor [b] T = 1s	T = 2s	T = 4s
(45) Coalinga/H-Z06.fn	0.501	51.307	1.000	1.000	1.000
(46) Coalinga/H-Z09.fn	0.501	51.022	1.000	1.000	1.000
(47) Coalinga/H-PG2.fn	0.501	52.241	1.000	1.000	1.000
(48) Coalinga/H-PG3.fn	0.501	52.814	1.000	1.000	1.000
(49) Coalinga/H-PG4.fn	0.501	53.342	1.000	1.000	1.000
(50) Coalinga/H-PG5.fn	0.501	53.897	1.000	1.000	1.000
(51) Coalinga/H-VC4.fn	0.501	51.522	1.000	1.000	1.000
(52) Morgan/SJB.fn	1.000	18.000	1.000	1.000	1.000
(53) Whittier/A-RO2.fn	NA	NA	1.000	1.000	1.000
(54) Lomap/FMS.fn	0.500	47.500	0.957	0.901	0.849
(55) Lomap/FRE.fn	0.500	48.380	0.956	0.899	0.846
(56) Lomap/SG3.fn	0.400	2.000	0.968	0.925	0.885
(57) Lomap/WDS.fn	0.500	14.300	0.982	0.958	0.935
(58) Landers/BRS.fn	**0.605**	**25.020**	**1.041**	**1.100**	**1.160**
(59) Northr/ALH.fn	**0.745**	**31.880**	**1.009**	**1.020**	**1.031**
(60) Northr/ING.fn	0.036	88.154	0.901	0.783	0.680
(61) Northr/116.fn	0.064	86.477	0.902	0.784	0.682
(62) Northr/BLD.fn	0.159	80.536	0.905	0.791	0.692
(63) Northr/LAC.fn	0.650	39.817	0.985	0.964	0.945
(64) Northr/CYP.fn	0.680	37.216	0.992	0.982	0.971
(65) Northr/TEM.fn	0.545	49.136	0.960	0.909	0.860
(66) Northr/UNI.fn	0.645	40.248	0.984	0.962	0.940
(67) Northr/W15.fn	0.408	61.318	0.933	0.849	0.773
(68) Northr/LH4.fn	**0.852**	**18.558**	**1.041**	**1.097**	**1.158**
(69) Northr/L4B.fn	**0.852**	**18.558**	**1.041**	**1.097**	**1.158**
(70) Northr/SAR.fn	0.134	83.623	0.904	0.788	0.686
(71) Coalinga/H-C03.fn	0.501	53.318	1.000	1.000	1.000
(72) Coalinga/H-C04.fn	0.501	53.522	1.000	1.000	1.000
(73) Coalinga/H-Z07.fn	0.501	50.746	1.000	1.000	1.000
(74) Coalinga/H-VC2.fn	0.501	50.337	1.000	1.000	1.000
(75) Coalinga/H-VC6.fn	0.501	53.099	1.000	1.000	1.000

[a] directivity parameters provided by (Stewart 2000)

[b] for average $S_a(T, \zeta=5\%)$

Table A-8. Strike-slip, "forward-directivity" earthquake records of the nearby-field set ranked according to their directivity modification factors.

Rank [a]	Ground Velocity Time History	X [b]	θ [b] [degrees]
1/31	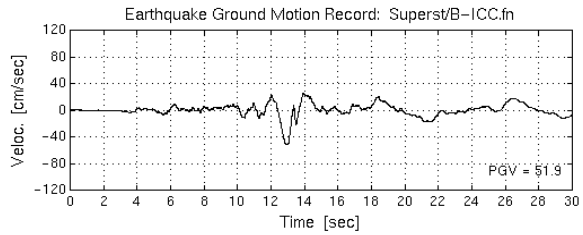	0.90	6.3
2/31	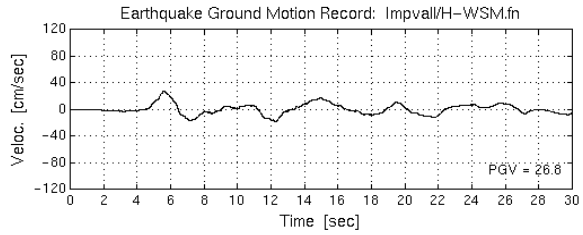	0.81	5.0
3/31	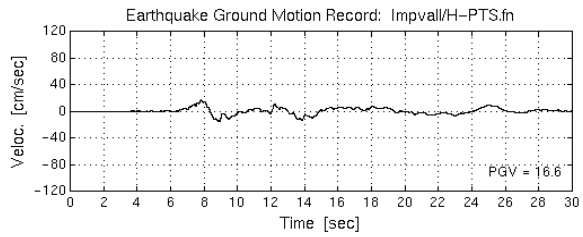	0.81	10.2
4/31	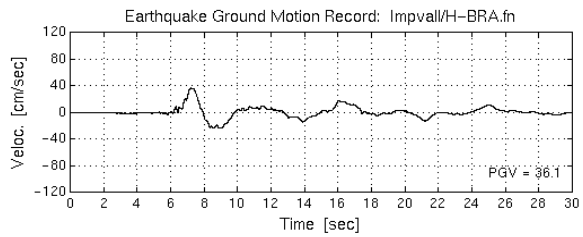	0.81	13.3
5/31	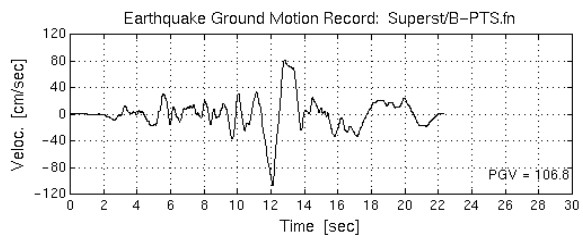	0.71	11.0
6/31	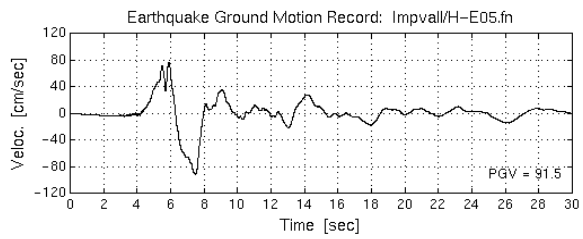	0.69	8.4

Table A-8 (continued)

Rank [a]	Ground Velocity Time History	X [b]	θ [b] [degrees]
7/31	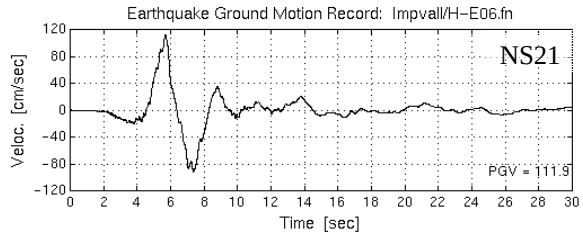	0.67	2.7
8/31	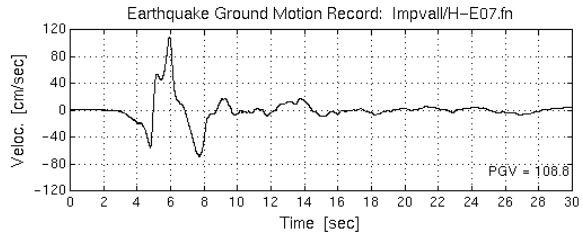	0.66	0.4
9/31	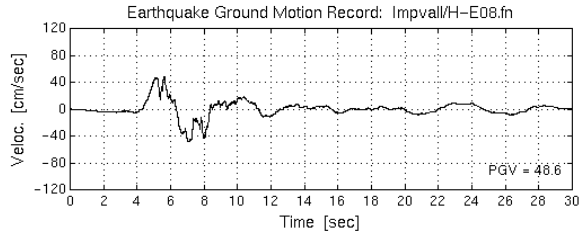	0.66	8.1
10/31	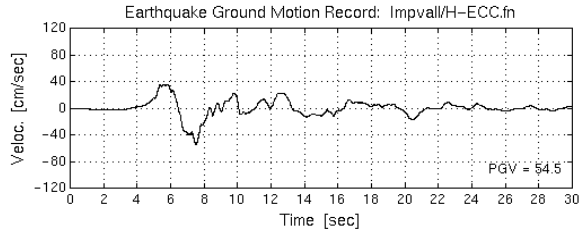	0.67	15.5
11/31	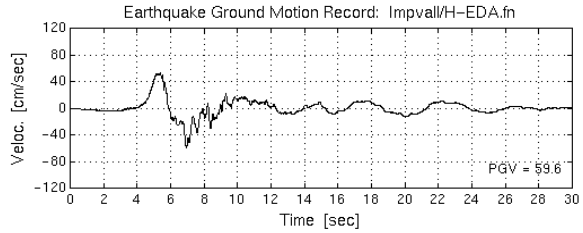	0.65	11.2
12/31	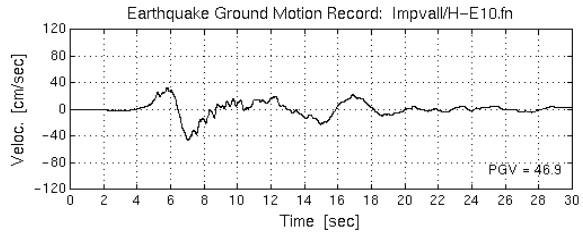	0.64	17.4

Table A-8 (continued)

Rank [a]	Ground Velocity Time History	X [b]	θ [b] [degrees]
13/31	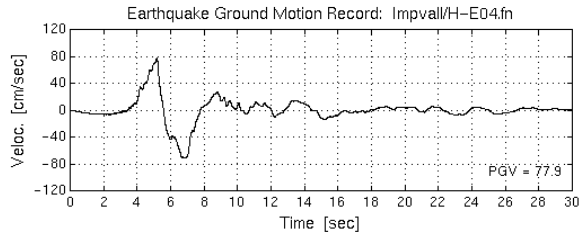	0.63	15.6
23/31	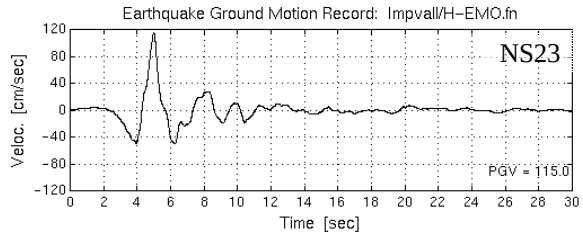	0.55	1.0
24/31	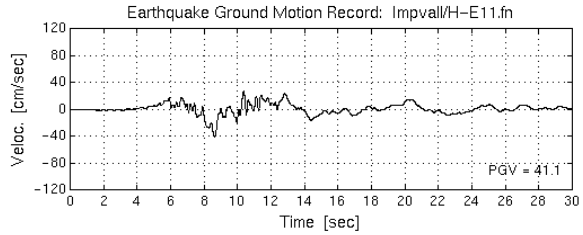	0.61	26.5
25/31	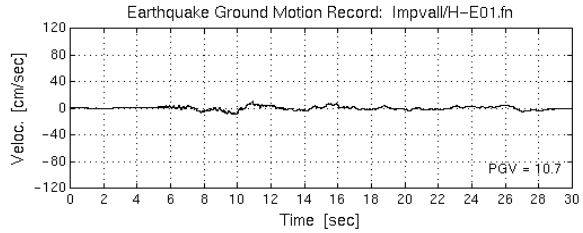	0.70	38.2
27/31	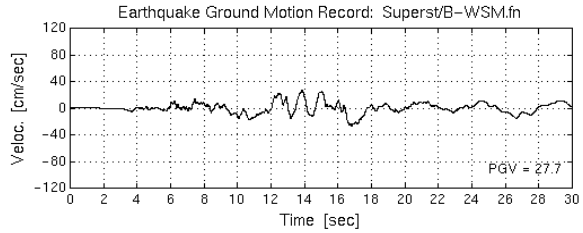	0.72	44.6

[a] from largest to smallest directivity modification factor for average S_a (T=2s, ζ=5%)

[b] directivity parameters provided by (Stewart 2000)

Table A-9. Dip-slip, "forward-directivity" earthquake records of the nearby-field set ranked according to their directivity modification factors.

Rank [a]	Ground Velocity Time History	Y [b]	ϕ [b] [degrees]
14/31	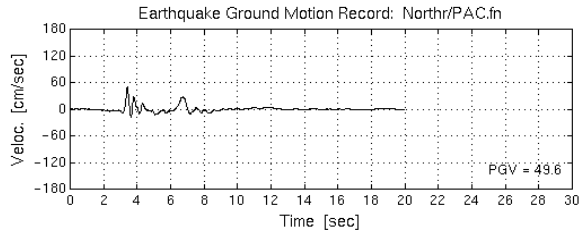	0.85	3.0
15/31	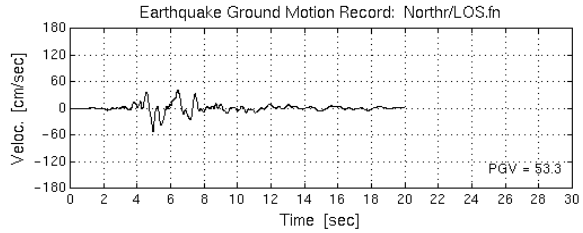	0.85	5.3
16/31	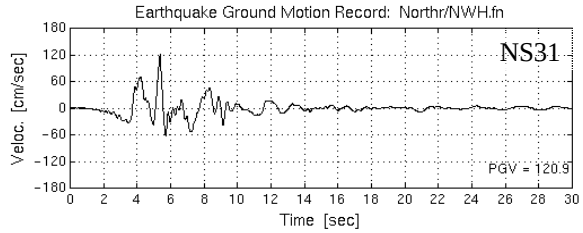	0.85	6.0
17/31	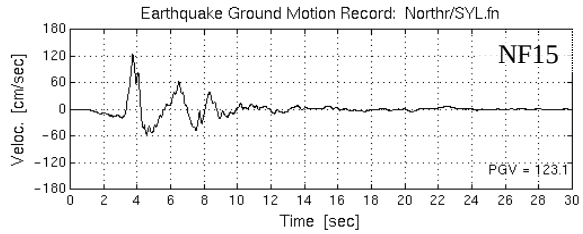	0.85	8.4
18/31	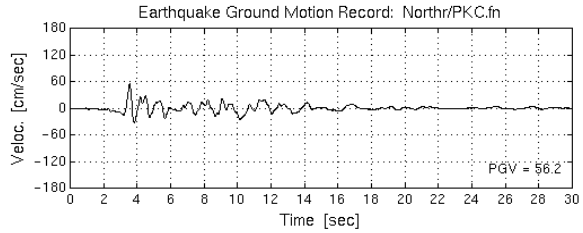	0.85	8.6
19/31	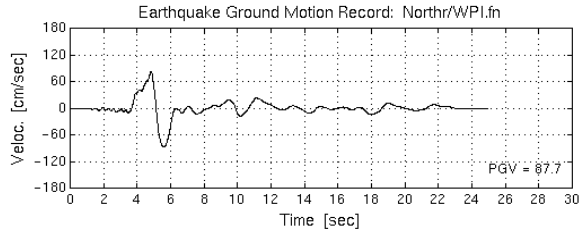	0.85	13.6

Table A-9 (continued)

Rank [a]	Ground Velocity Time History	Y [b]	ϕ [b] [degrees]
20/31	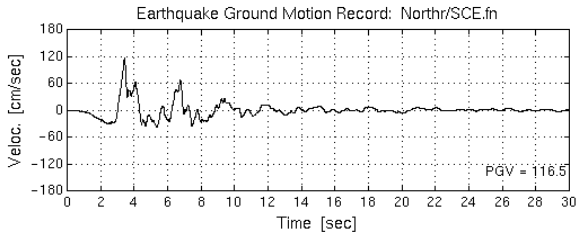	0.85	14.9
21/31	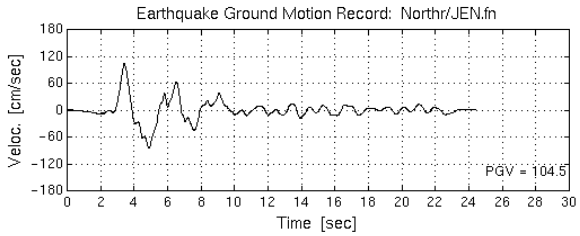	0.85	16.0
22/31	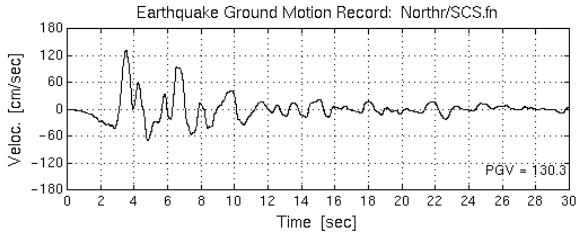	0.85	16.2
26/31	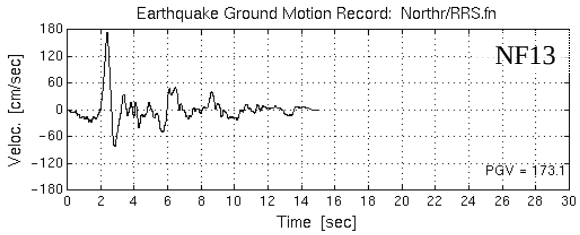	0.85	20.6
28/31	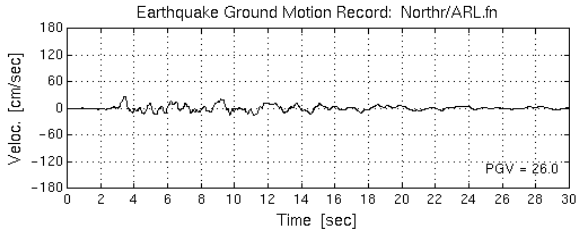	0.81	26.6
29/31	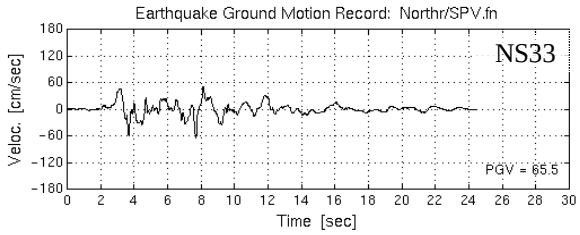	0.79	28.6

Table A-9 (continued)

Rank [a]	Ground Velocity Time History	Y [b]	ϕ [b] [degrees]
30/31	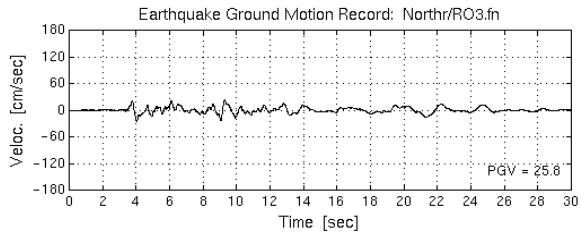	0.78	29.2
31/31	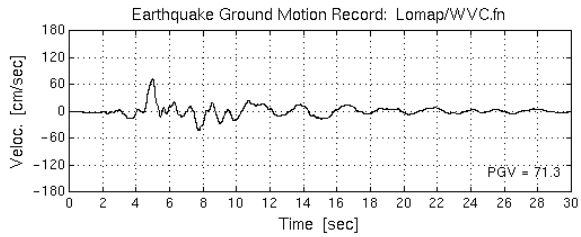	0.60	11.0

[a] from largest to smallest directivity modification factor for average S_a (T=2s, ζ=5%)

[b] directivity parameters provided by (Stewart 2000)

Table A-10. Strike-slip, "forward-directivity" earthquake records of the far-field set ranked according to their directivity modification factors.

Rank [a]	Ground Velocity Time History	X	θ [degrees]
1/15	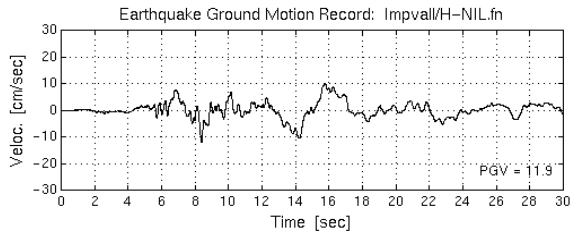	0.81	22.5
2/15	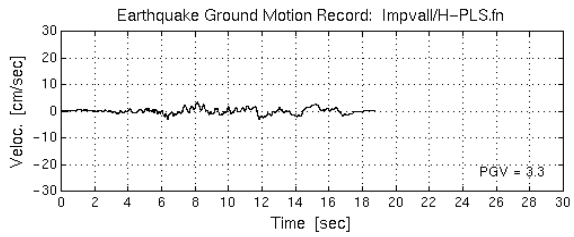	0.81	34.4
3/15	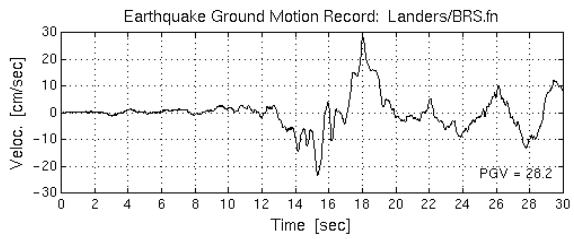	0.61	25.0

[a] from largest to smallest rupture directivity modification factor for average S_a (T =2s, ζ=5%)

Table A-11. Dip-slip, "forward-directivity" earthquake records of the far-field set ranked according to their directivity modification factors.

Rank [a]	Ground Velocity Time History	*Y*	ϕ [degrees]
4/15	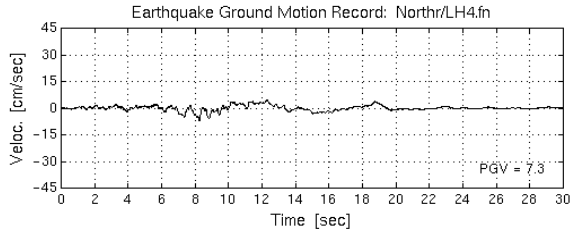	0.85	18.6
5/15	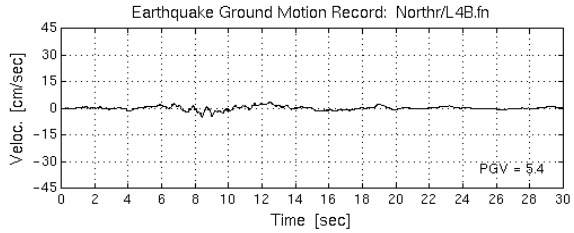	0.85	18.6
6/15	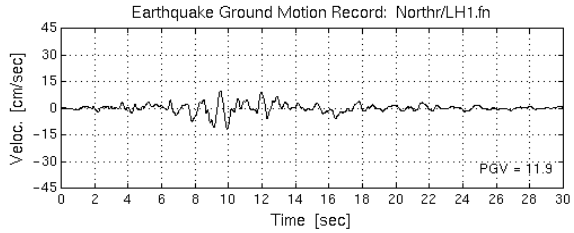	0.85	20.3
7/15	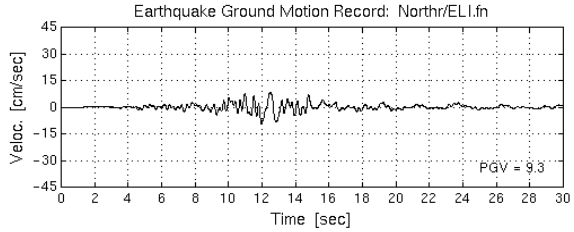	0.85	20.7
8/15	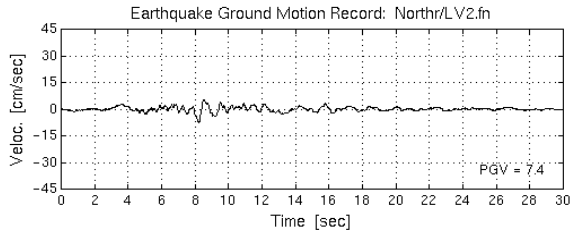	0.85	20.9
9/15	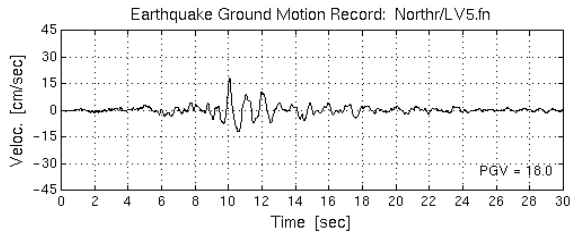	0.85	21.0

Table A-11 (continued)

Rank [a]	Ground Velocity Time History	Y	ϕ [degrees]
10/15	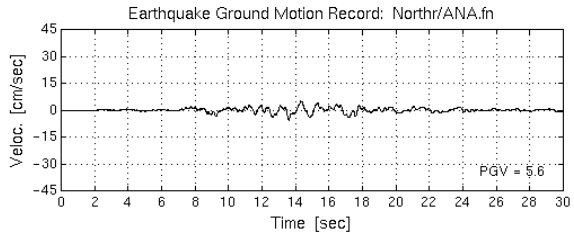	0.85	21.1
11/15	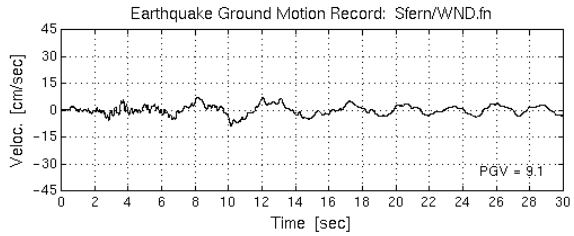	0.85	21.2
12/15	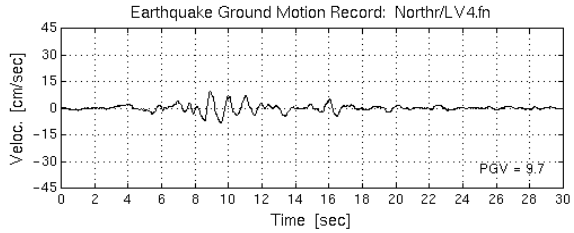	0.85	21.3
13/15	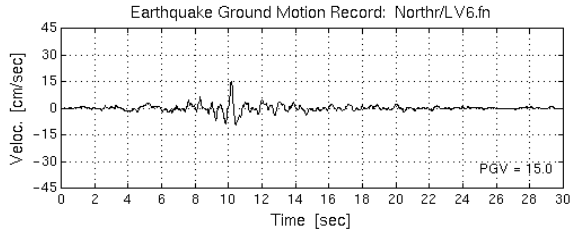	0.85	22.2
14/15	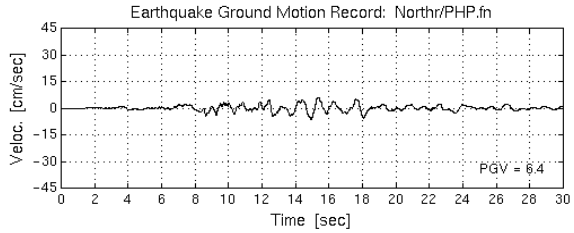	0.77	27.3
15/15	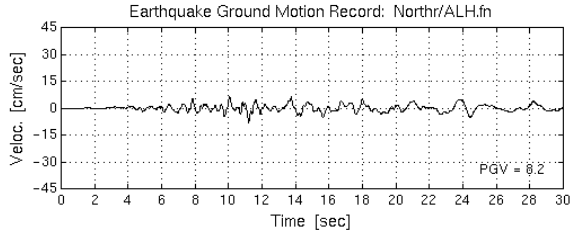	0.75	31.9

[a] from largest to smallest rupture directivity modification factor for average S_a (T =2s, ζ=5%)

Table A-12. Supplemental "pulse-like" earthquake records (from Somerville).

Earthquake Location [a]	Year	M_w	Source Mechan.	Station	R_{close} [b] (km)	Site Class [b]	ID
(1) Loma Prieta	1989	6.9	RV/OB	Los Gatos (LGPC)	3.5	"stiff soil" [c]	NF03
(2) Loma Prieta	1989	6.9	RV/OB	Lexington Dam	6.3	"stiff soil" [c]	NF05
(3) Landers	1992	7.3	SS	Lucerne	1.1	"stiff soil" [c]	NF11
(4) Kobe, JAPAN	1995	6.9	SS	Takatori	1.5	"soil"	NF19
(5) Kobe, JAPAN	1995	6.9	SS	Port Island	3.7	"soil"	NS25
(6) Morgan Hill	1984	6.2	SS	Coyote Lake Dam	0.1	"stiff soil" [c]	NS29

[a] unless noted otherwise, earthquake locations are in California

[b] closest distances and site classes from (Alavi & Krawinkler, 1999)

[c] modified from rock by (Somerville, 1997b; Somerville, 1998)

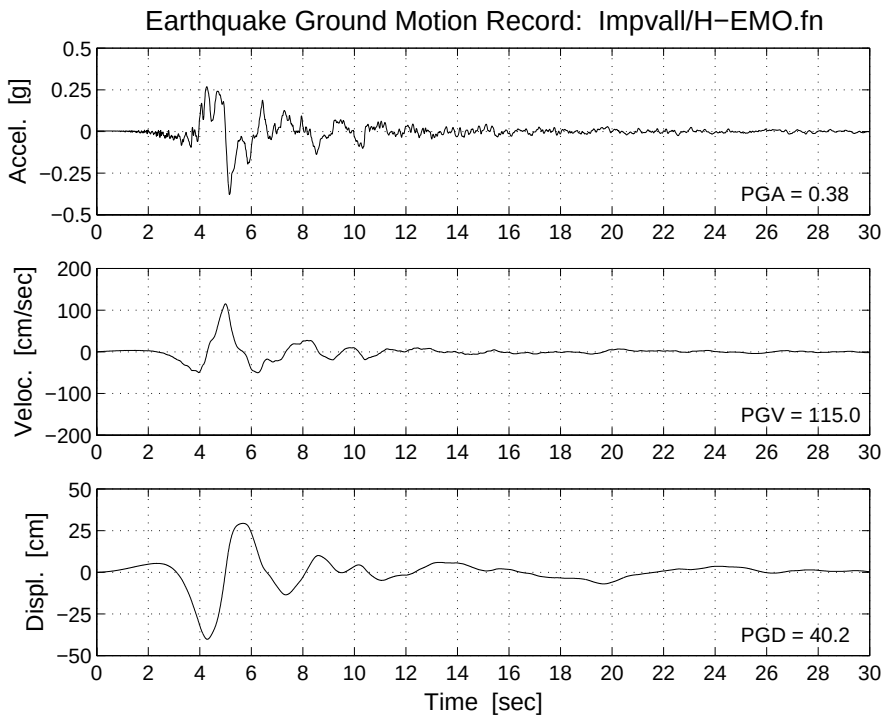

Figure A-2. Time histories for the "pulse-like" NS23 ground motion (i.e., strike-normal component of IMPVALL\H-EMO from nearby-field set).

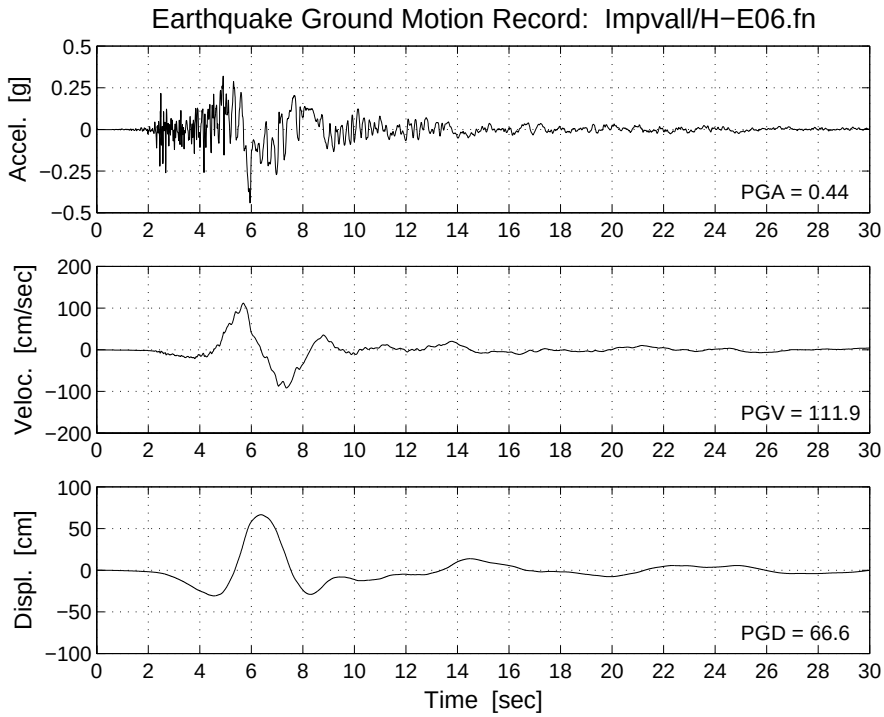

Figure A-3. Time histories for the "pulse-like" NS21 ground motion (i.e., strike-normal component of IMPVALL\H-E06 from nearby-field set).

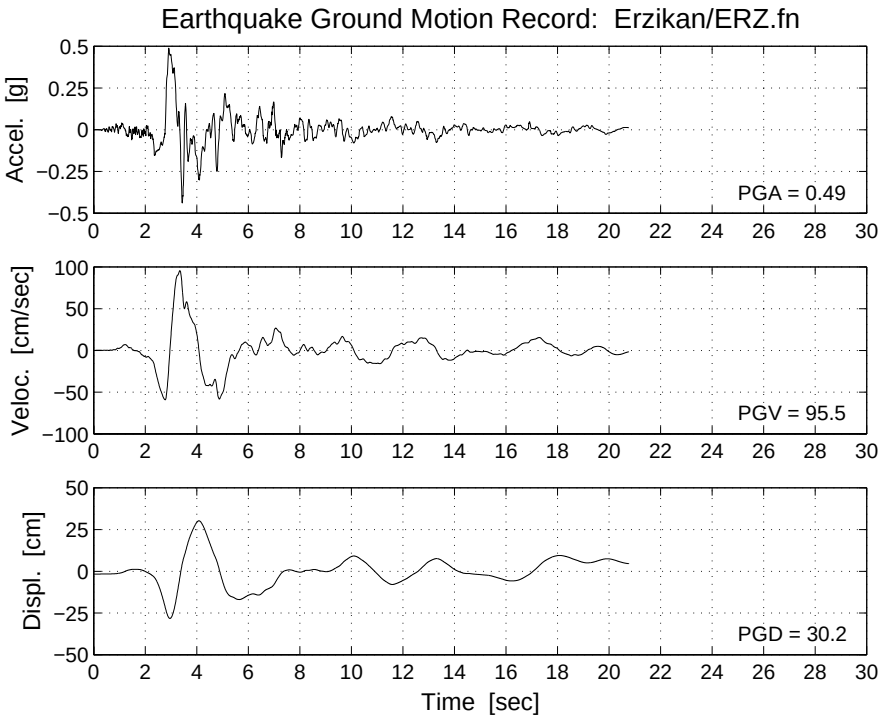

Figure A-4. Time histories for the "pulse-like" NF09 ground motion (i.e., strike-normal component of ERZIKAN\ERZ from nearby-field set).

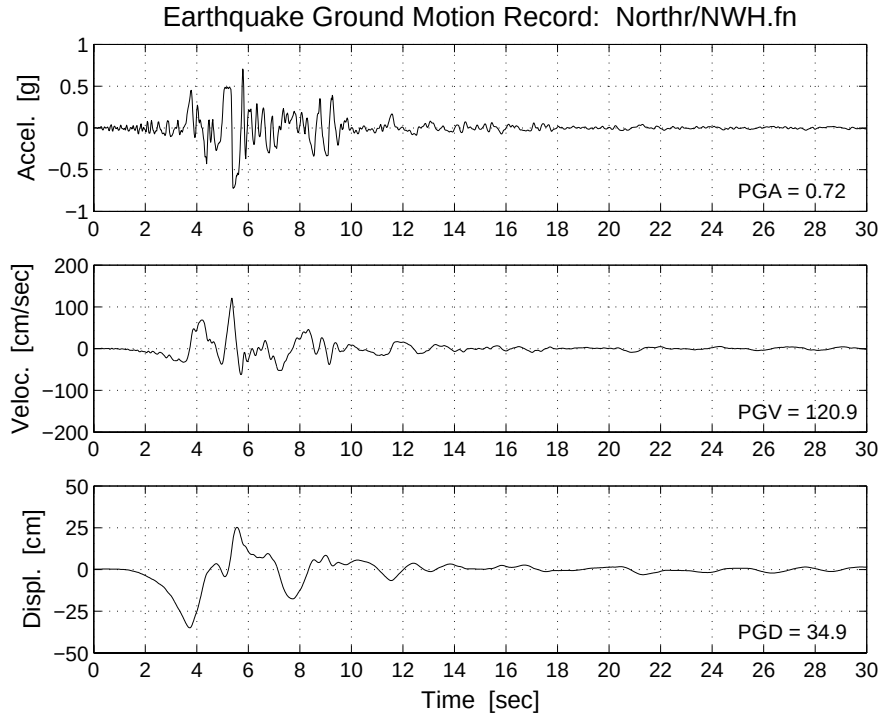

Figure A-5. Time histories for the "pulse-like" NS31 ground motion (i.e., strike-normal component of NORTHR\NWH from nearby-field set).

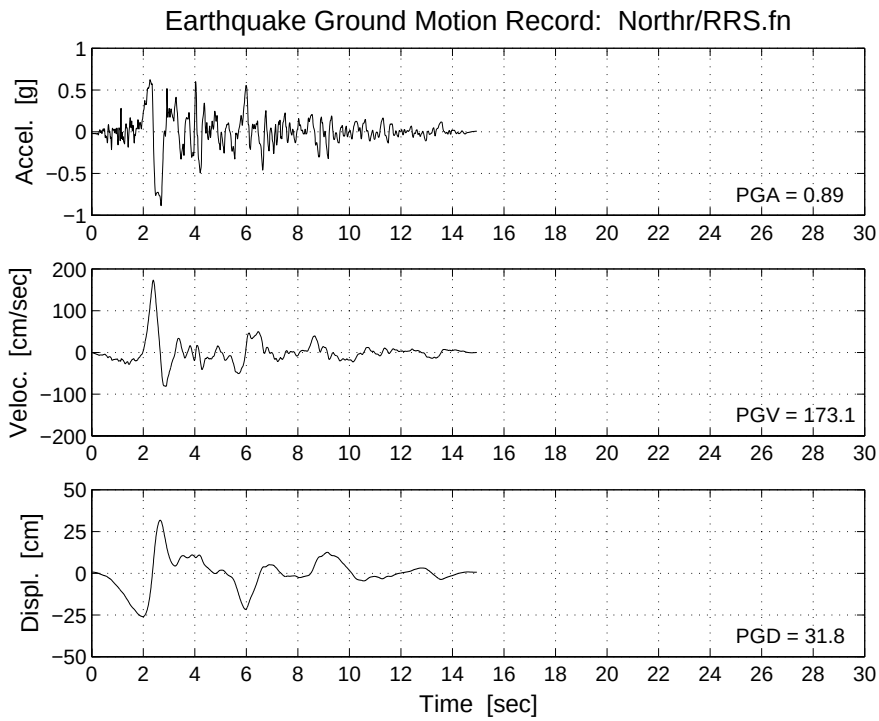

Figure A-6. Time histories for the "pulse-like" NF13 ground motion (i.e., strike-normal component of NORTHR\RRS from nearby-field set).

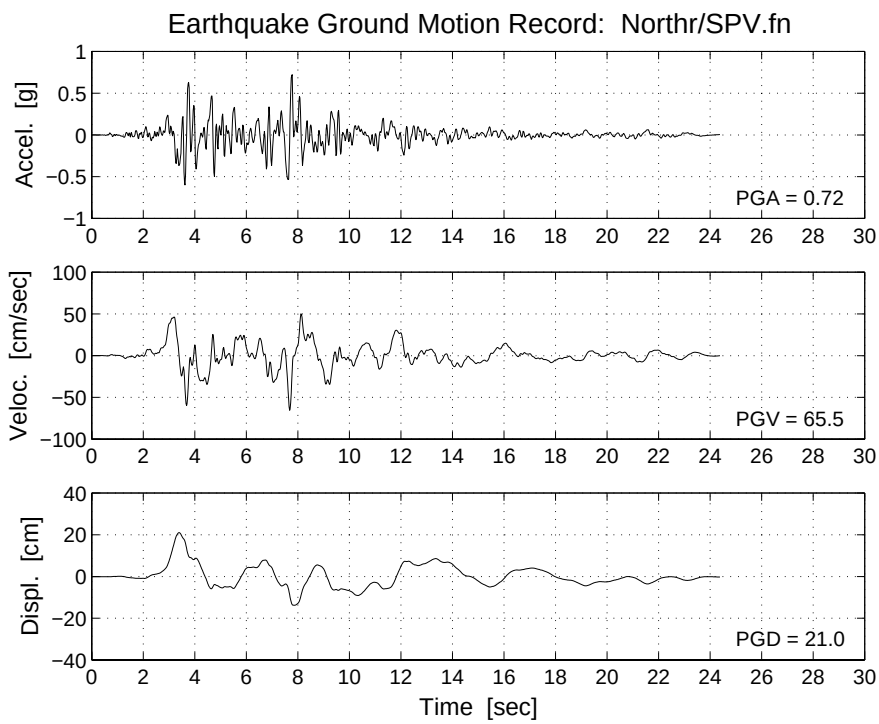

Figure A-7. Time histories for the "pulse-like" NS33 ground motion (i.e., strike-normal component of NORTHR\SPV from nearby-field set).

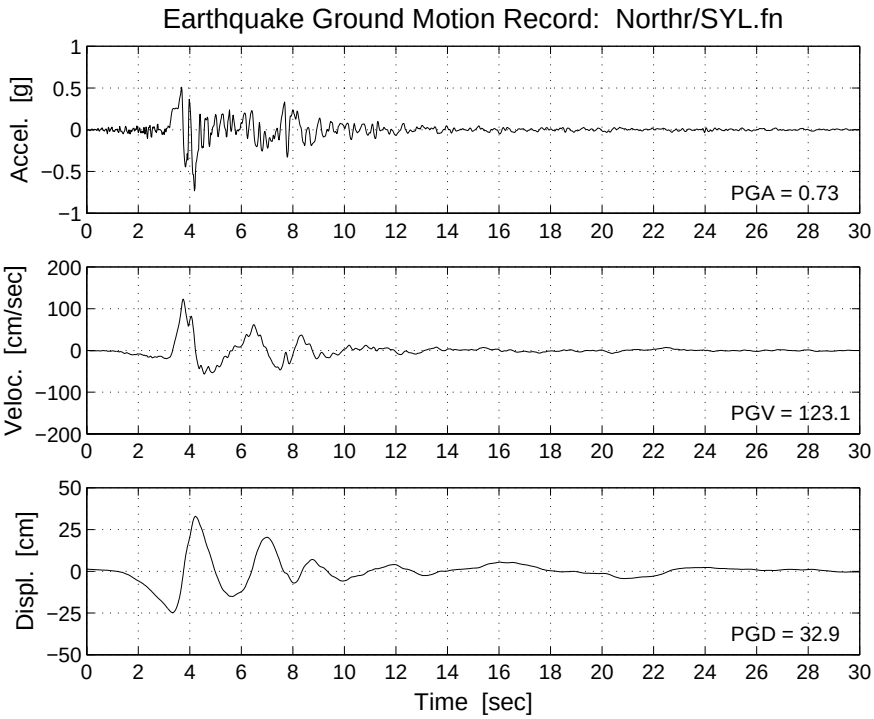

Figure A-8. Time histories for the "pulse-like" NF15 ground motion (i.e., strike-normal component of NORTHR\SYL from nearby-field set).

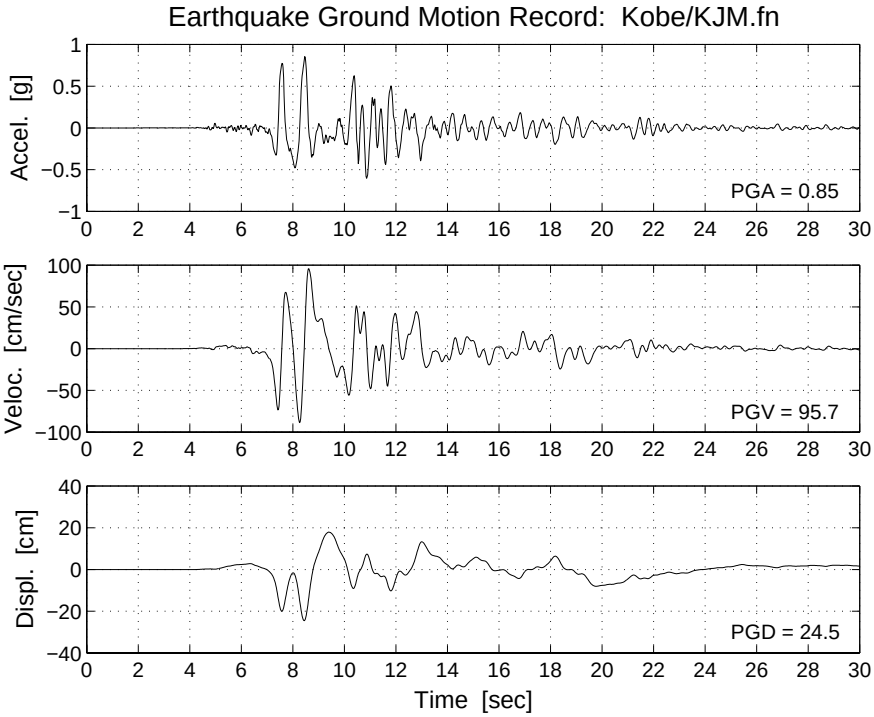

Figure A-9. Time histories for the "pulse-like" NF17 ground motion (i.e., strike-normal component of KOBE\KJM from nearby-field set).

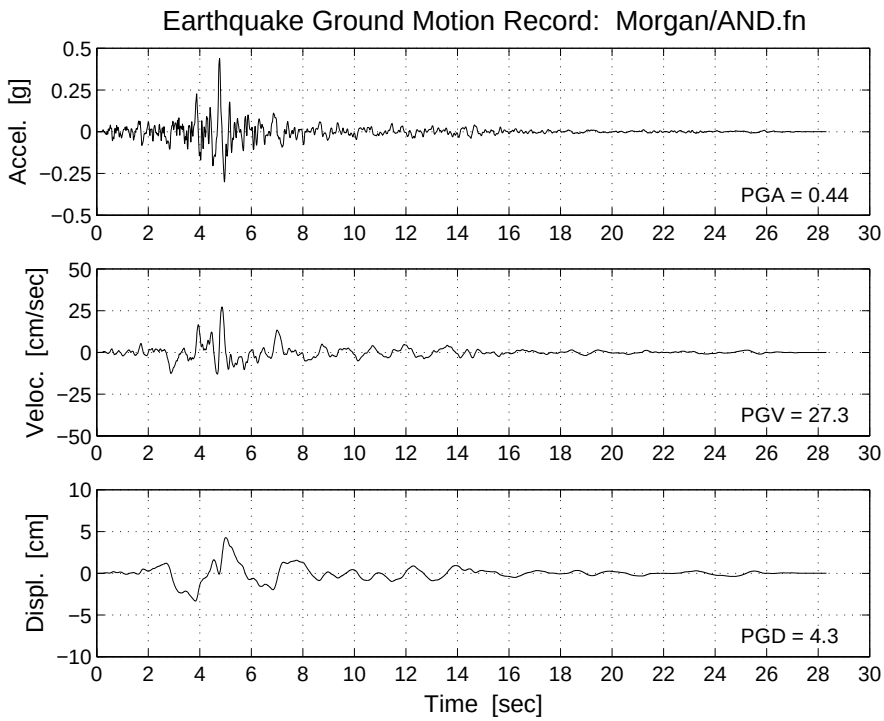

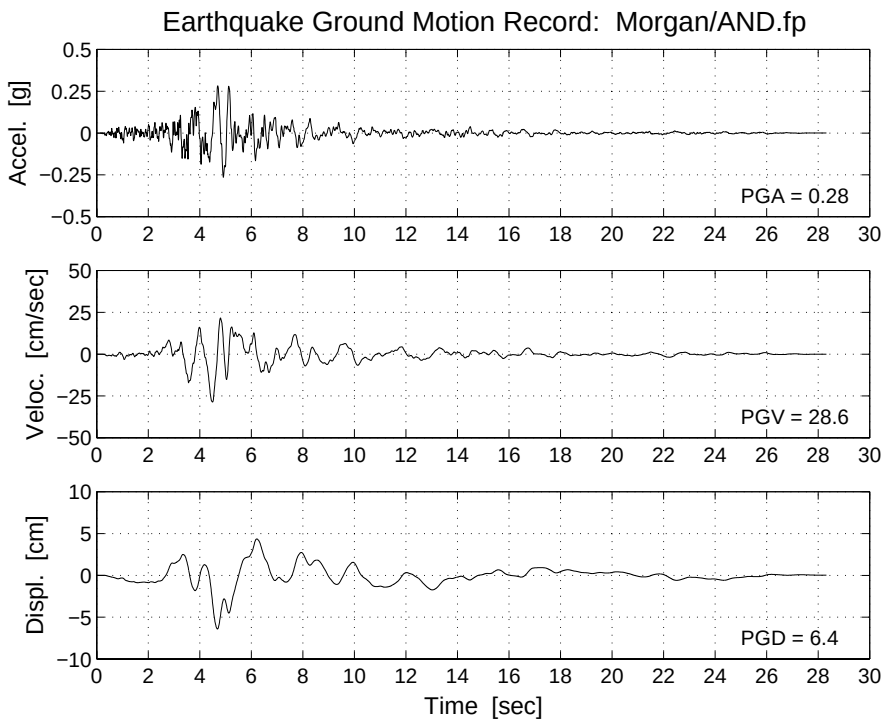

Figure A-10. Time histories for the **(a)** strike-normal (.fn) and **(b)** strike-parallel (.fp) component of the MORGAN\AND ground motion.

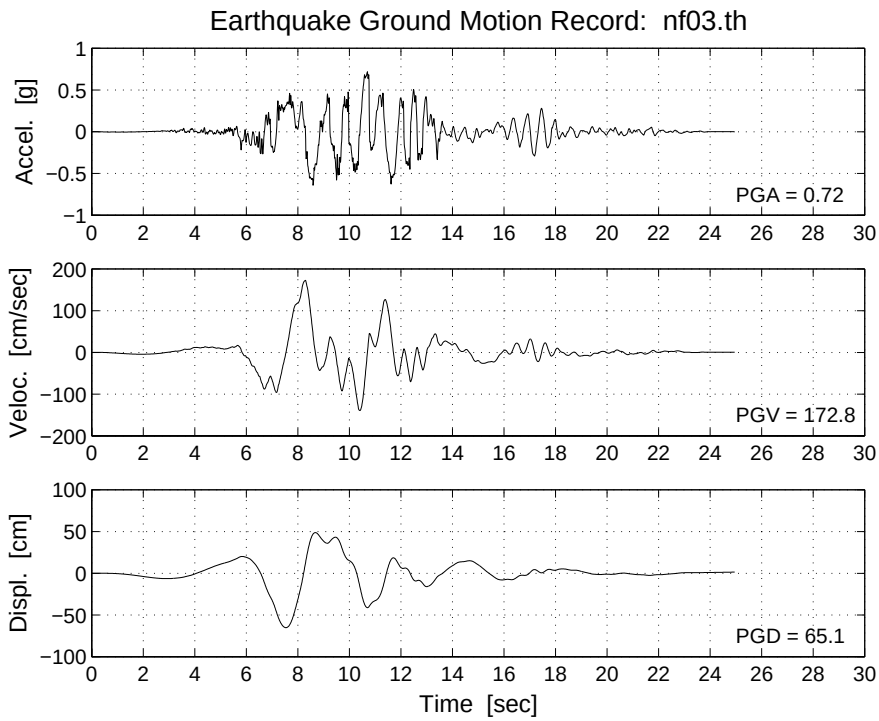

Figure A-11. Time histories for the "pulse-like" NF03 ground motion (i.e., strike-normal component of Loma Prieta-Los Gatos from Somerville).

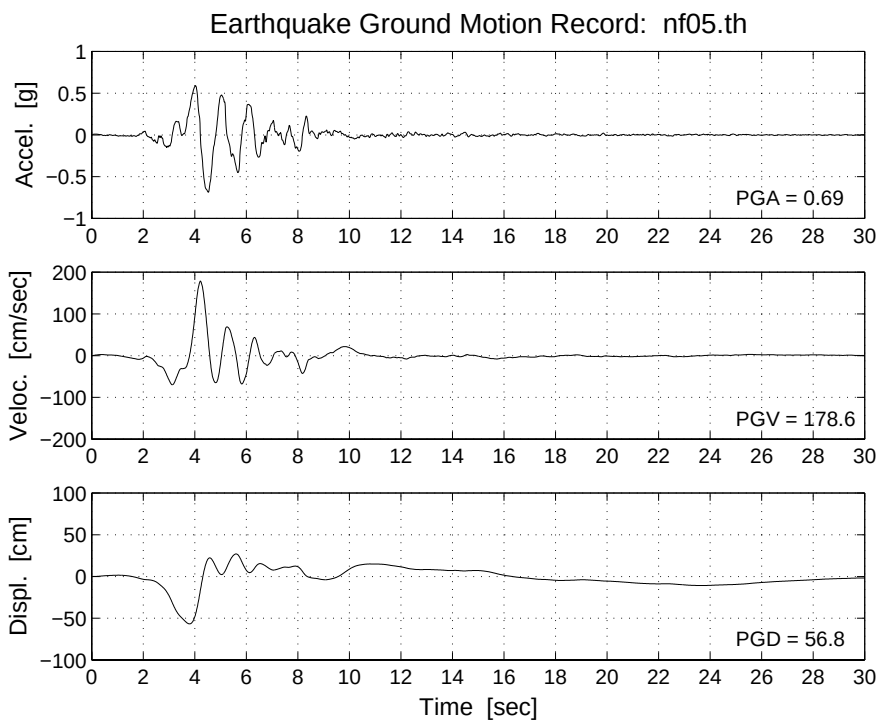

Figure A-12. Time histories for the "pulse-like" NF05 ground motion (i.e., strike-normal component of Loma Prieta-Lexington Dam from Somerville).

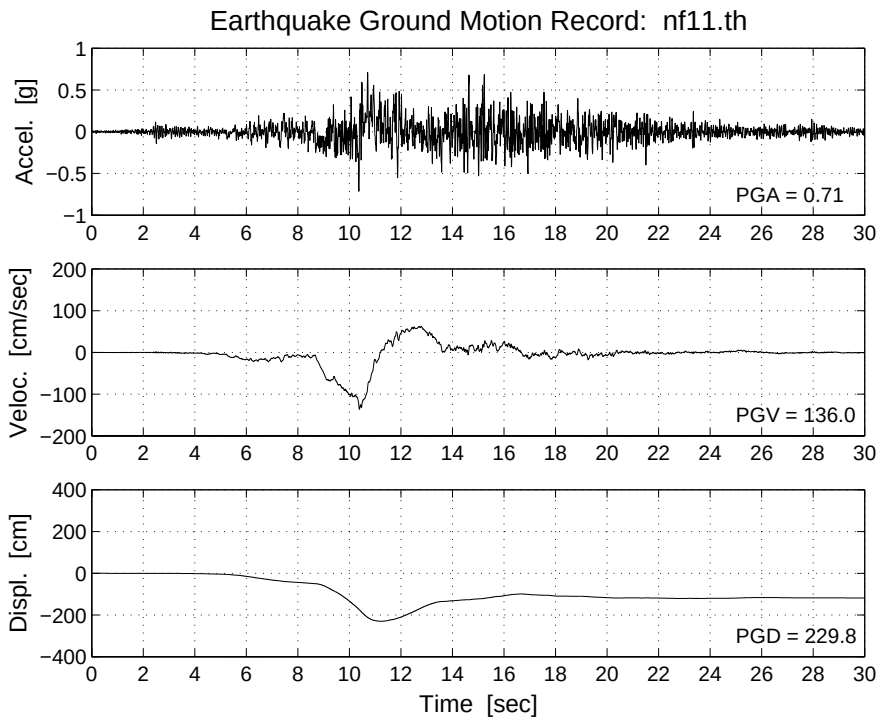

Figure A-13. Time histories for the "pulse-like" NF11 ground motion (i.e., strike-normal component of Landers-Lucerne from Somerville).

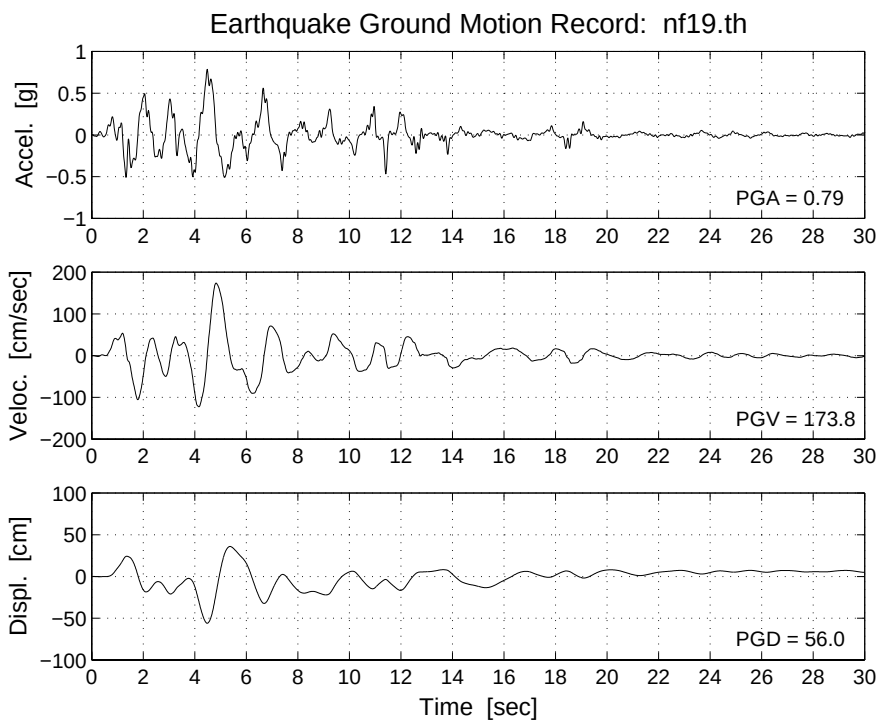

Figure A-14. Time histories for the "pulse-like" NF19 ground motion (i.e., strike-normal component of Kobe-Takatori from Somerville).

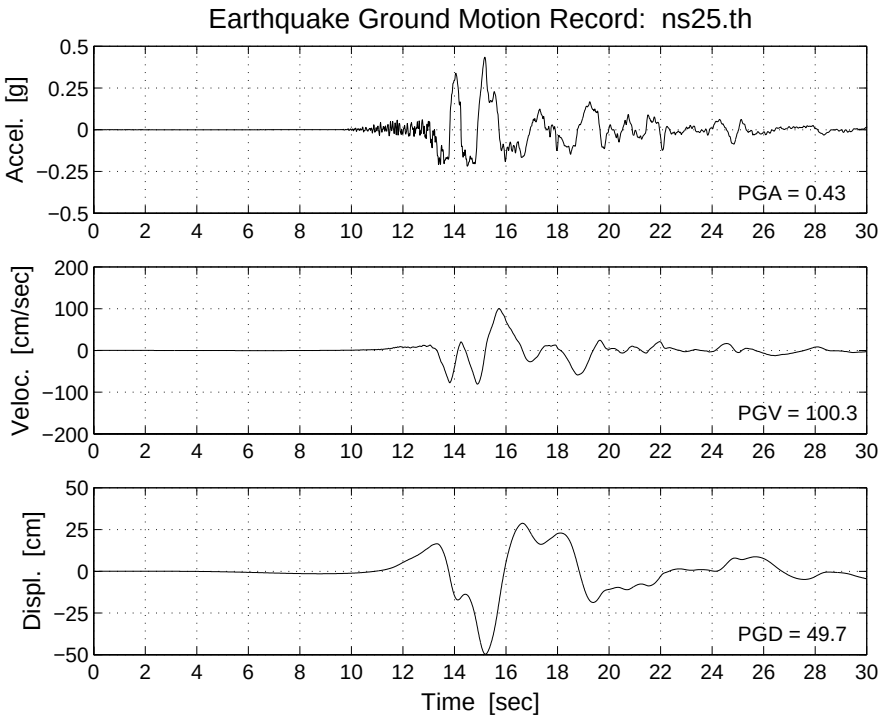

Figure A-15. Time histories for the "pulse-like" NS25 ground motion (i.e., strike-normal component of Kobe-Port Island from Somerville).

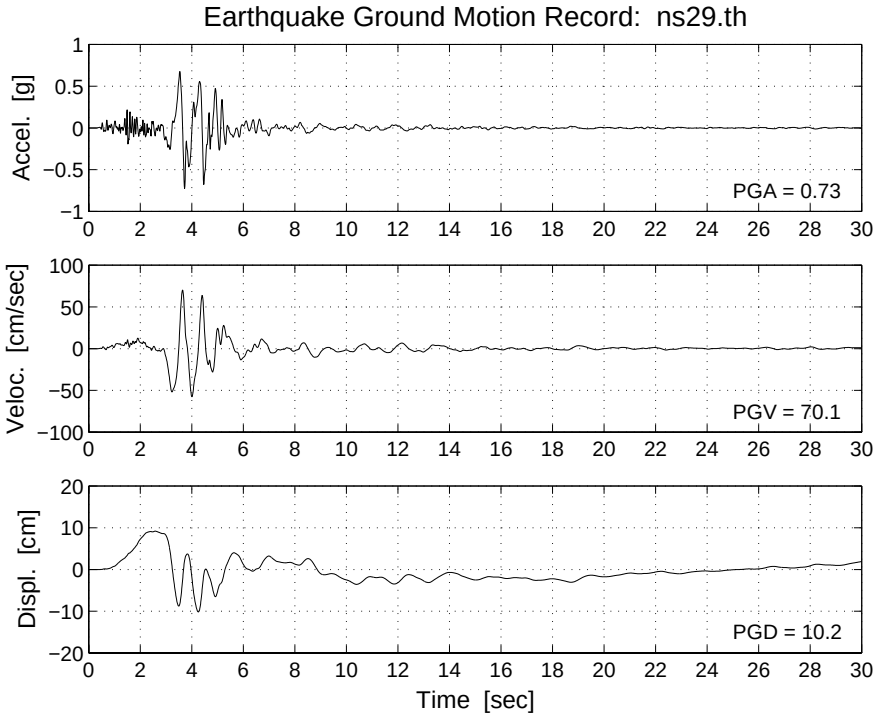

Figure A-16. Time histories for the "pulse-like" NS29 ground motion (i.e., strike-normal component of Morgan Hill-Coyote Lake Dam from Somerville).

Appendix B

Building Models for Near-Source Research

B.1 Overview

The structures used in this dissertation to investigate the effects of near-source ground motions (in Chapters 5-7) are the 3-story, 9-story, and 20-story steel moment-resisting frame (SMRF) buildings designed for Los Angeles conditions by consulting structural engineers (Brandow & Johnston Associates) as part of the SAC Steel Project (Phase II). More specifically, the building designs carried out according to pre-Northridge earthquake practices (i.e., UBC, 1994) are considered. Of course, these three building designs were originally used to investigate the effects of beam-column connection fractures (in Chapters 2-4), along with six other buildings described in FEMA355C (2000). In this appendix, only the three buildings (and their models) considered in the near-source research are detailed. Typical floor plans and north-south elevations are provided in Figure B-3 through Figure B-12. Note that only the perimeter frames of each building are moment-resisting; the interior frames are intended to support gravity loads only. For brevity, the Los Angeles 3-, 9-, and 20-story building designs are referred to below as LA3, LA9, and LA20.

B.2 Analysis Models

Under the assumption of a rigid diaphragm, a two-dimensional centerline model of each of the three (relatively symmetric) buildings is created for nonlinear analysis using DRAIN-2DX (Prakash *et al.* 1993). From each building, one of the two (identical) north-south perimeter moment-resisting frames (MRFs) and half of the north-south interior gravity frames (GFs) are modeled. To further reduce the total number of degrees of freedom for each analysis model, the GFs are merged into a single "consolidated GF" by summing the stiffnesses and strengths of their individual members. The resulting consolidated GFs for LA3, LA9, and LA20[1] are shown in Figure B-5, Figure B-8, and Figure B-11 to Figure B-12. The model of each consolidated GF is slaved (in the horizontal direction) at every floor to the corresponding MRF model to form a complete (yet 2-D) model in the north-south direction.

The analysis models described above that take into account both the perimeter MRFs and the (consolidated) interior GFs are referred to in this dissertation as M1+ models; this is in contrast to M1 models, which only consider the lateral resistance of the perimeter MRFs. (typically used for analysis by SAC Steel Project Phase II participants). An M1+ model differs from an M1 model in two significant ways: (1) as already mentioned, interior GFs are included in the model, and (2) shear connections are modeled with some stiffness and strength (details given below) rather than modeling them as "pins". Figure B-1 compares static pushover curves for the M1 and M1+ models of LA9. Also shown in Figure B-1 is the corresponding curve for the "M1#" model of LA9, which is the same as the M1+ model except with the shear connections modeled as pins. Based on the figure it is evident that even with shear connections modeled as pins (i.e., model M1#), the (consolidated) interior GFs can contribute significantly to the lateral resistance (and potentially alter significantly the lateral response). This contribution is due in part to the lateral restraint at the ground level (i.e., 1st floor) of the LA9 that results in more base-fixity for the interior gravity columns even thought they are in fact pinned at their bases. This is also the case for LA20, whereas for LA3 the columns from the interior GFs that are also part of the east-west perimeter MRFs are actually fixed at their bases.

[1] For LA20, (half of) the columns from the east-west perimeter MRFs that are not part of the two north-south GFs are consolidated and included in the analysis model; of course one of the two (identical) north-south GFs is also modeled.

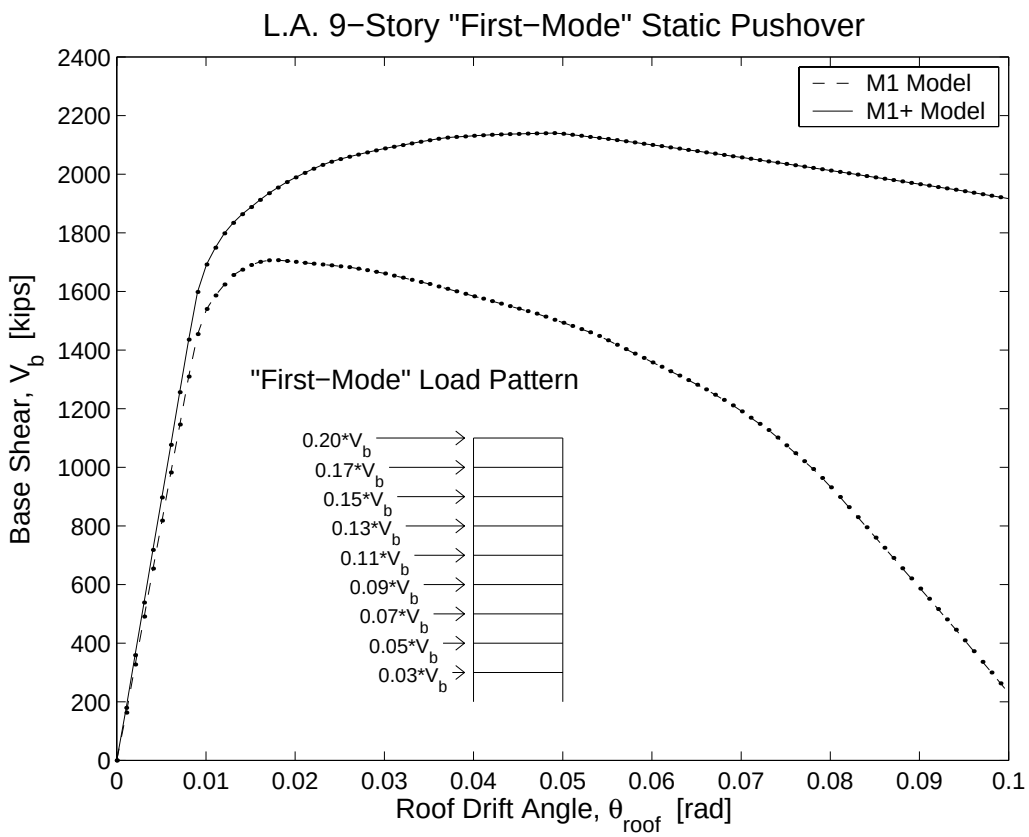

Figure B-1. Comparing SPO's for M1, M1#, & M1+ models of LA9.

For the M1+ model, each shear connection is modeled with a rotational spring (at an end of an elastic beam) with moment-rotation characteristics as displayed in Figure B-2. The strength in positive bending is larger to account for the contribution of a slab (in compression). The assumed properties are reasonably close to those observed in laboratory tests performed by (Liu & Astaneh-Asl 2000). In any case, the static pushover curves in Figure B-1 suggest that the influence of the stiffness and strength of the shear connections is perhaps less than the influence of the GF columns.[2]

As for the shear connections, each moment-resisting connection is modeled with a rotational spring (at an end of an elastic beam) that emulates beam-connection hinging (point plasticity). These rotational springs are rigid-plastic, yielding at $M_{\mathrm{p,beam}}$ with a post-yield stiffness (i.e., strain hardening) equal to 3% of $6EI/L$ of the beam. Note that this is a model of a ductile beam-column connection.

[2] Due to an input error, the shear connection at the right end of each beam was modeled with larger strength in *negative* bending. The effect on the first and second mode periods and the nonlinear static pushover curve is found to be minimal.

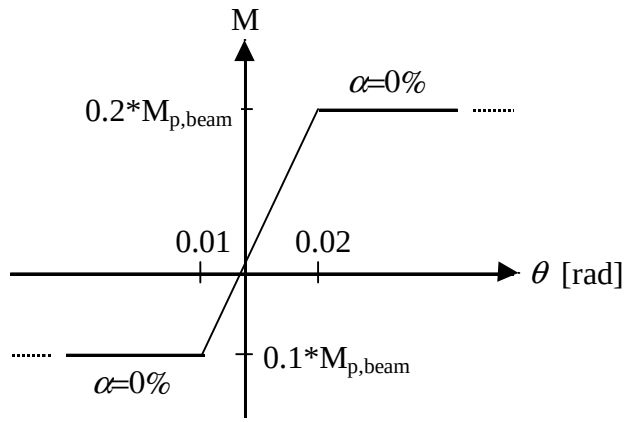

Figure B-2. Moment-rotation model for shear connections.

Plastic hinging at the ends of each column (and at column splices) is modeled intrinsically with the DRAIN-2DX beam-column element, which also accounts for *P-M* interaction and *P-Δ* effects. For the columns, a strain-hardening ratio of 3% is specified.

B.3 Loads

The assumed dead and live gravity loads are listed below in Table B-1. Only the dead loads are considered in calculating the mass.

Table B-1. Assumed dead and live loads.

Location (1)	Dead Load (psf) (2)	Live Load (psf) (3)
typical floor	96 [a]	20
roof [b]	83	20
penthouse	116	--
exterior wall	25	--

[a] 86psf for mass calculations (excludes partitions)
[b] excludes penthouse

Although the penthouse atop each of the buildings is not modeled (nor shown in Figure B-3 through Figure B-12), its weight (and mass) is considered. The penthouse

covers the area delineated by grid lines 3→5 and B→C in Figure B-3 for LA3, 3→4 and B→D in Figure B-6 for LA9, and 3→5 and C→D in Figure B-9 for LA20.

For the dead loads (only), each floor envelope (including the penthouse envelope) extends 1ft. beyond the perimeter girder (or beam) centerlines. Additional weight (and mass) is attributed to a 42in.-high parapet on the roof of each of the buildings.

The resulting distributed (beam) and point (column) gravity loads applied to each of the three building models are detailed in Table B-4 through Table B-9. Note that only loads on or above the ground level (i.e., 1st floor) are considered.

B.4 Modal Vibration Properties

The modal periods (up to T_5) for each of the three building models are listed below in Table B-2. Note that the mass of each building is lumped at the floors of its analysis model and is assumed to act horizontally only; thus, the number of degrees of freedom for modal analysis is equal to the number of floors (above ground).

Table B-2. Modal periods.

Building Model	T_1	T_2	T_3	T_4	T_5
LA3 (M1+)	0.98	0.30	0.14	--	--
LA9 (M1+)	2.23	0.82	0.46	0.30	0.21
LA20 (M1+)	3.96	1.35	0.78	0.55	0.41

Mass and stiffness proportional (Rayleigh) damping are assumed, with a damping ratio of 2% specified at the fundamental period T_1 of each building model and at T=0.2sec for LA3 and LA9, and T_5 for the LA20.

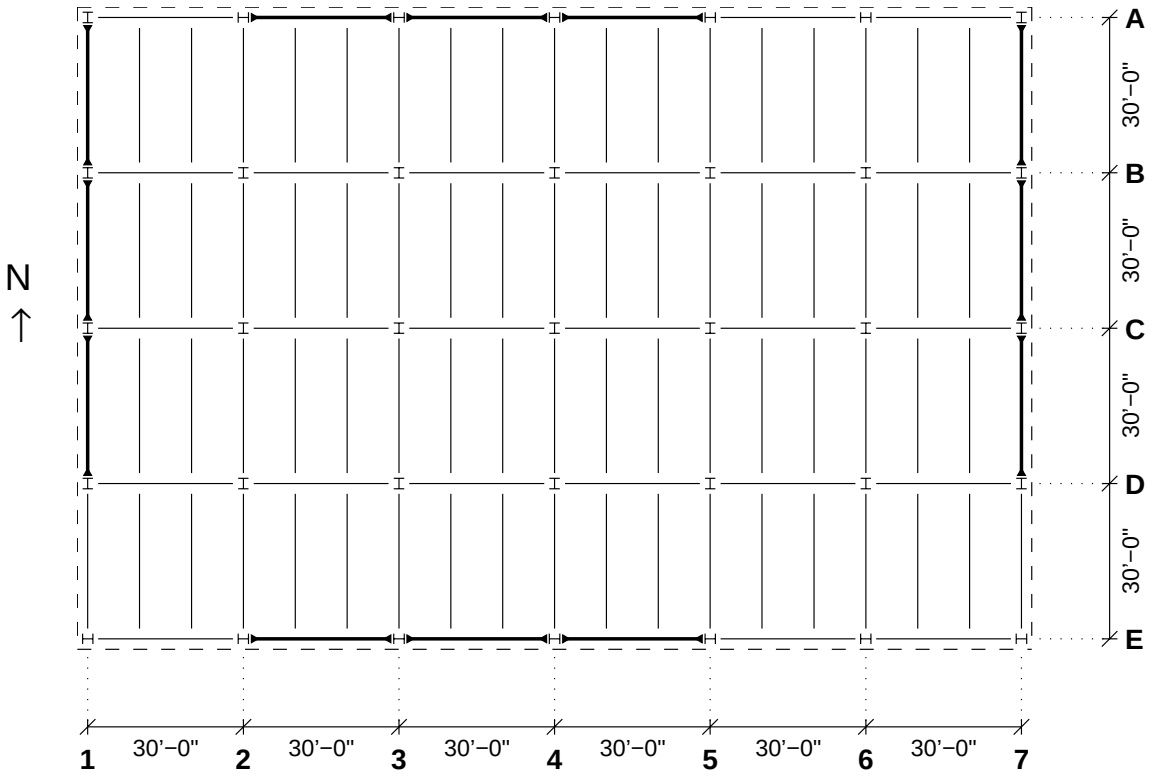

Figure B-3. L.A. 3-story typical floor plan.

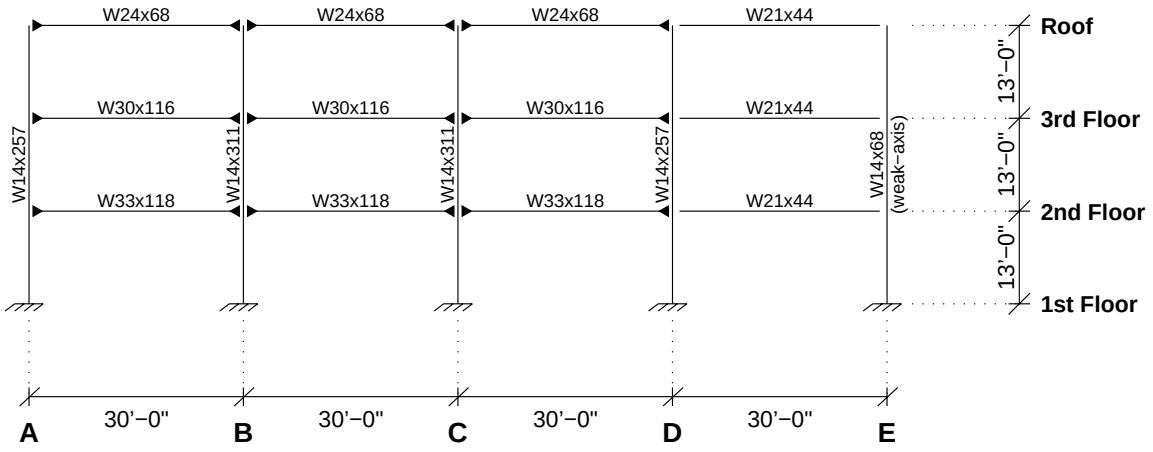

Figure B-4. L.A. 3-story perimeter MRF (N-S elevation).

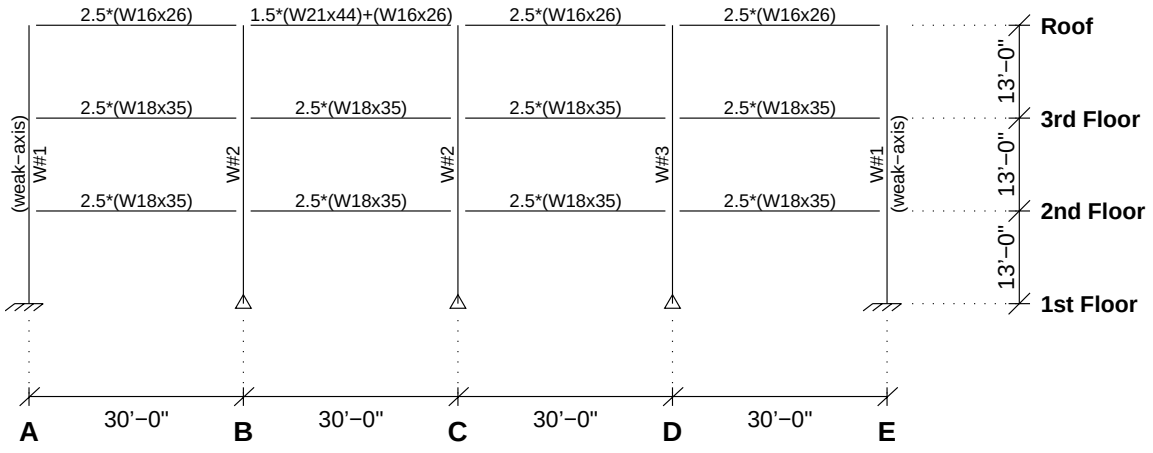

Figure B-5. L.A. 3-story (consolidated) interior gravity frame (N-S elevation).

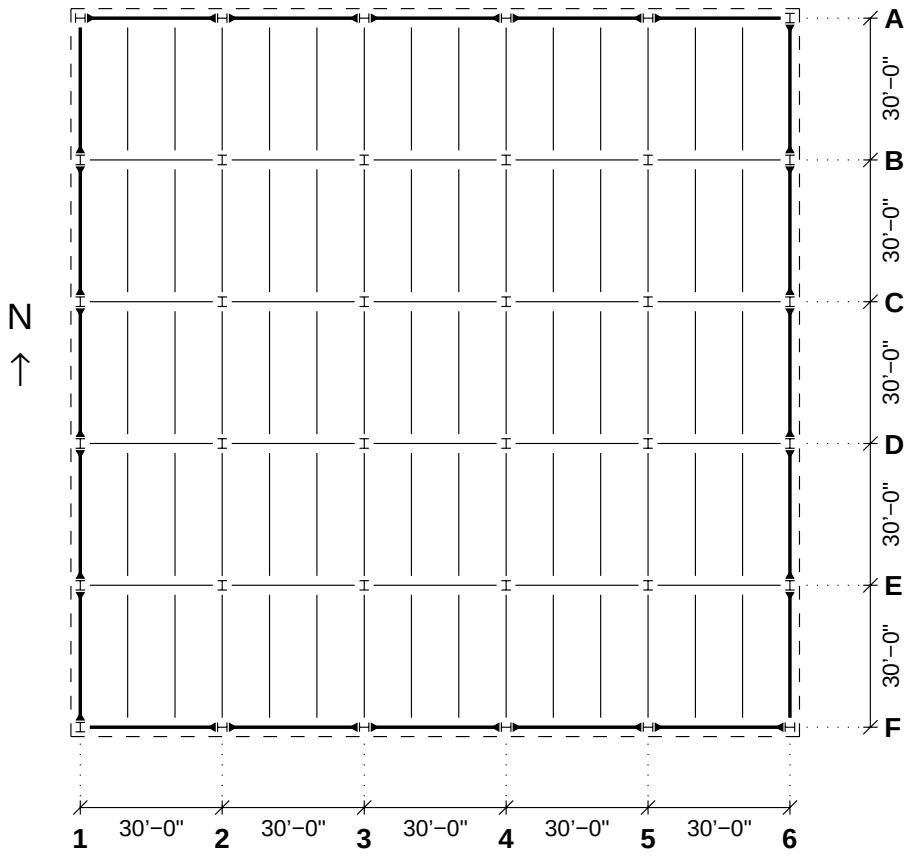

Figure B-6. L.A. 9-story typical floor plan.

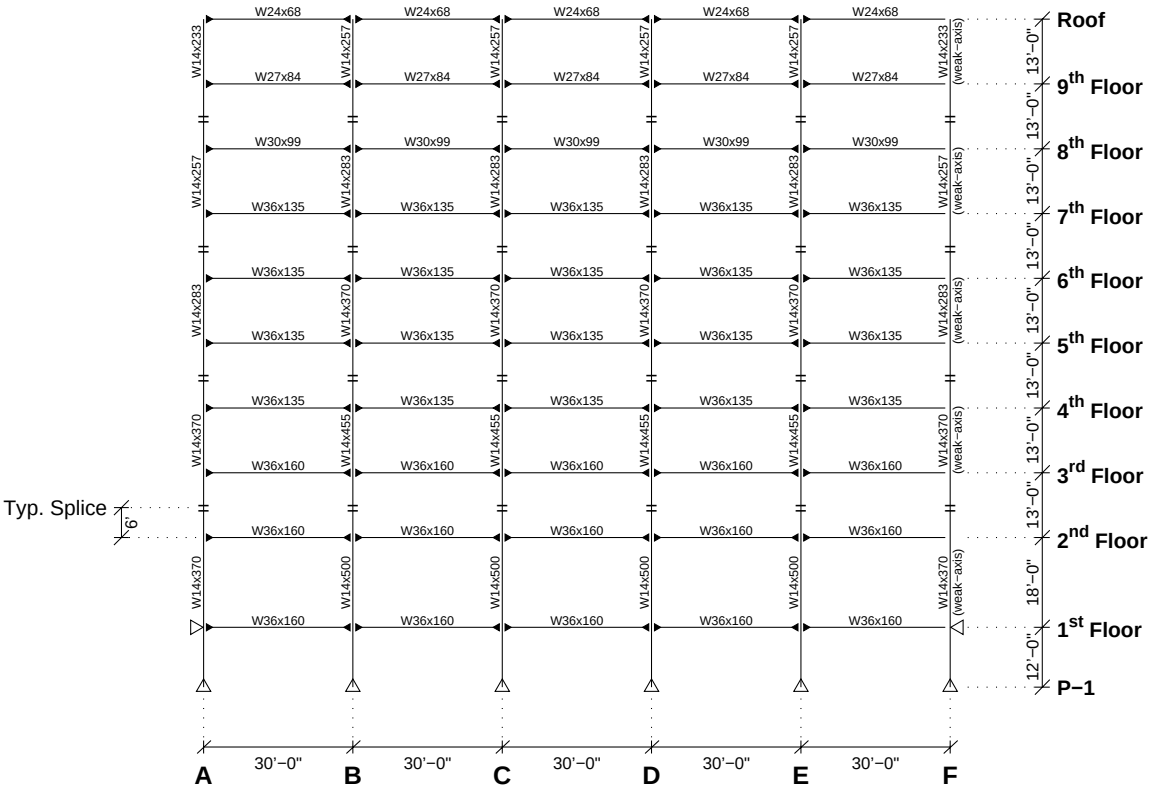

Figure B-7. L.A. 9-story perimeter MRF (N-S elevation).

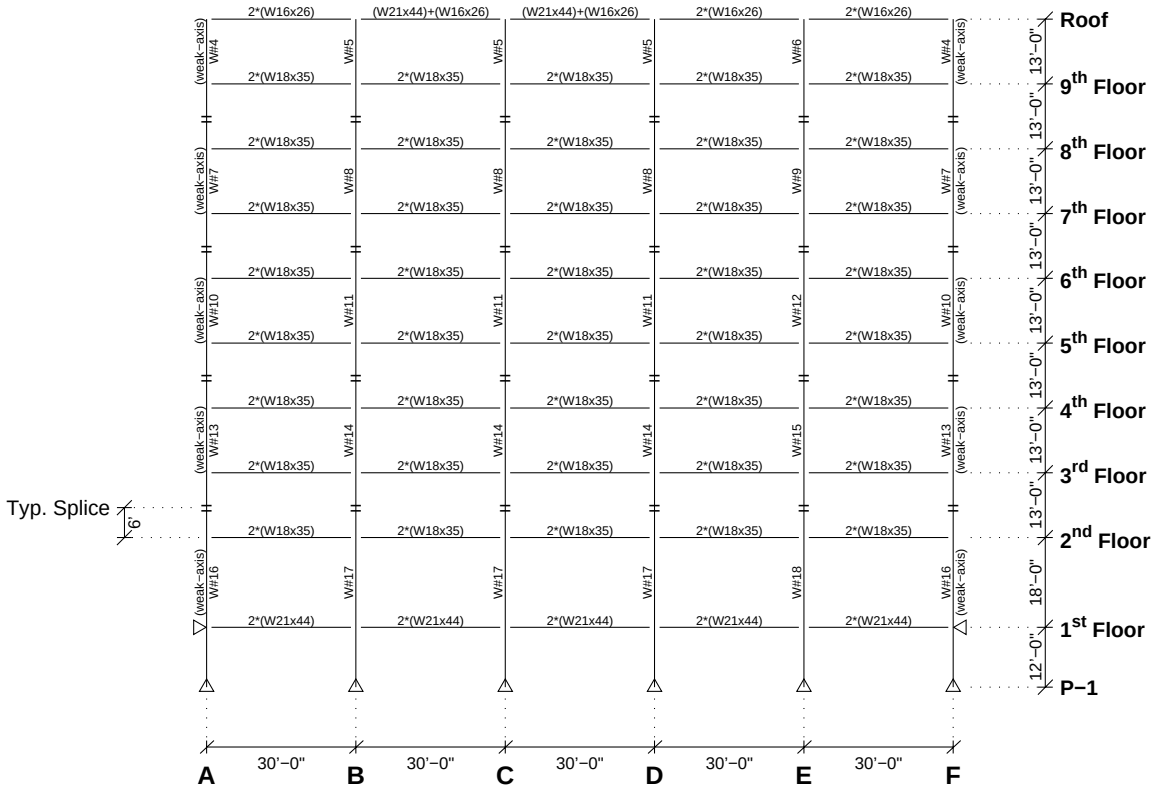

Figure B-8. L.A. 9-story (consolidated) interior gravity frame (N-S elevation).

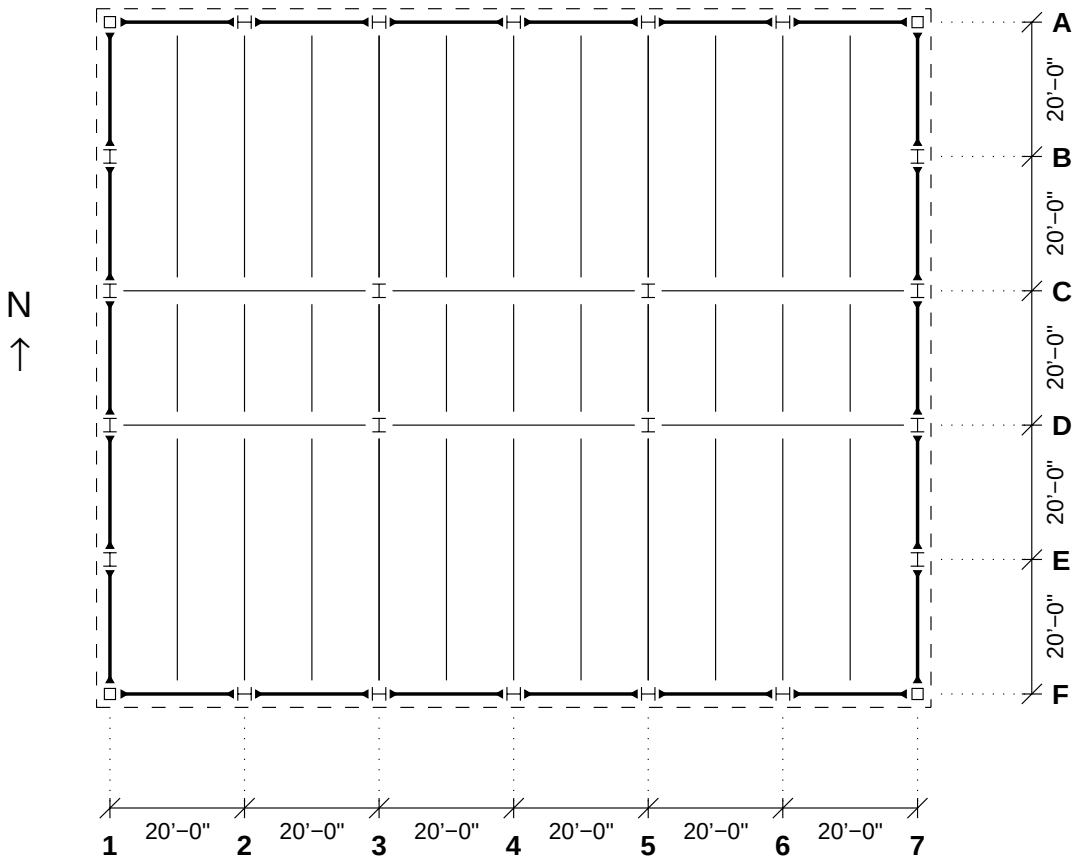

Figure B-9. L.A. 20-story typical floor plan.

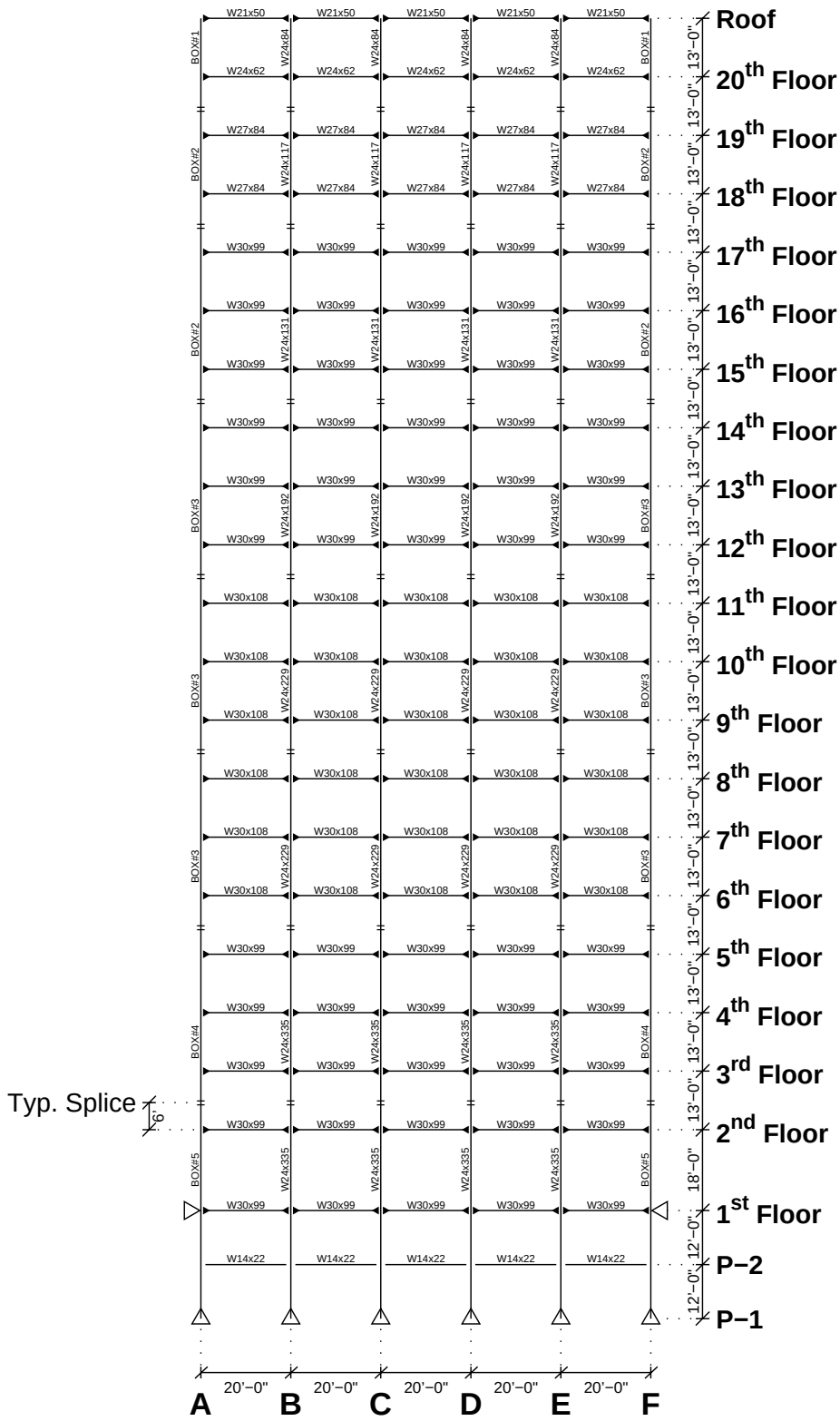

Figure B-10. L.A. 20-story perimeter MRF (N-S elevation).

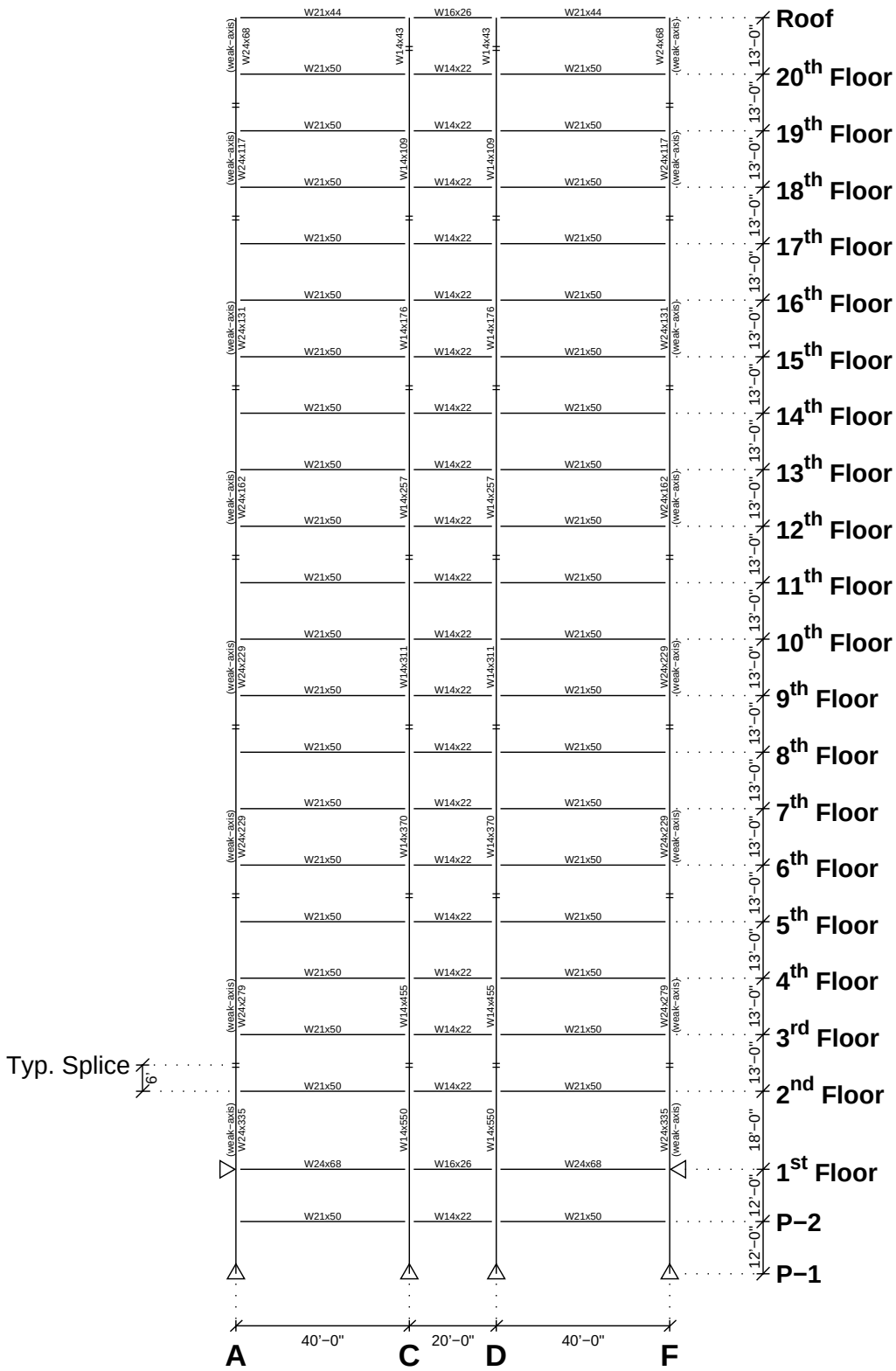

Figure B-11. L.A. 20-story interior gravity frame (N-S elevation).

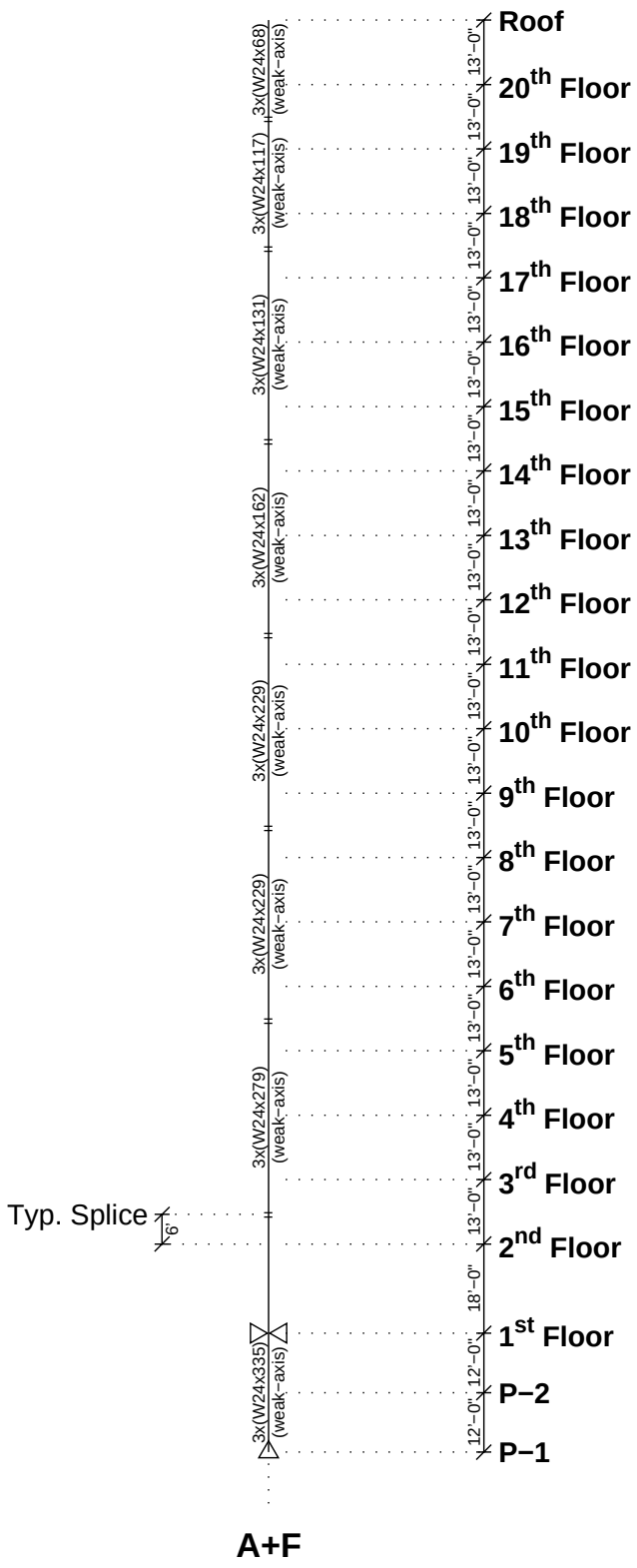

Figure B-12. L.A. 20-story (consolidated) exterior gravity column (N-S elevation).

Table B-3. Consolidated sections.

ID (1)	Section (2)
W#1	(W14x257)+0.5*(W14x311)+(W14x68)
W#2	(W14x68)+1.5*(W14x82)
W#3	2.5*(W14x68)
W#4	2*(W14x257)
W#5	(W14x61)+(W14x48)
W#6	2*(W14x48)
W#7	2*(W14x283)
W#8	(W14x90)+(W14x82)
W#9	2*(W14x82)
W#10	2*(W14x370)
W#11	(W14x120)+(W14x109)
W#12	2*(W14x109)
W#13	2*(W14x455)
W#14	(W14x159)+(W14x145)
W#15	2*(W14x145)
W#16	2*(W14x500)
W#17	(W14x211)+(W14x193)
W#18	2*(W14x193)
BOX#1	15x15x0.5 Box
BOX#2	15x15x0.75 Box
BOX#3	15x15x1 Box
BOX#4	15x15x1.25 Box
BOX#5	15x15x2 Box

Table B-4. Summary of beam (distributed) gravity loads for LA3.

Grid Line (1)	Distributed Load k/ft (2)	Length #[a] ft ft (3)	Total Load k (4)
(a) Floors 2,3			
7	1.00	4 * 30 = 120	120
(6+5+4)	1.16 + 1.16 + 0.58 = 2.90	4 * 30 = 120	348
(b) Roof			
7	0.85	4 * 30 = 120	102
(6+5+4) AB,CD,DE	1.03 + 1.03 + 0.52 = 2.58	3 * 30 = 90	232 + 125 = 356
(6+5+4) BC	1.03 + 2.03 + 1.10 = 4.15	1 * 30 = 30	

[a] # bays

Table B-5. Summary of column (point) gravity loads for LA3.

rid Point (1)	Point Load k (2)	# Locations (3)	Total Load k (4)
(a) Floors 2,3			
7 A,E	24.5	2	49 + 104 = 153
7 B,C,D	34.8	3	
(6+5+4) A,E	47.4 + 47.4 + 23.7 = 118.6	2	237 + 522 = 759
(6+5+4) B,C,D	69.6 + 69.6 + 34.8 = 174.0	3	
(b) Roof			
7 A,E	21.0	2	42 + 93 = 135
7 B,C,D	30.9	3	
(6+5+4) A,E	40.9 + 40.9 + 20.4 = 102.2	2	204 + 405 + 155 = 764
(6+5+4) B,C	61.8 + 86.2 + 54.5 = 202.5	2	
(6+5+4) D	61.8 + 61.8 + 30.9 = 154.5	1	

Table B-6. Summary of beam (distributed) gravity loads for LA9.

Grid Line (1)	Distributed Load k/ft (2)	Length #[a] ft ft (3)	Total Load k (4)
(a) Floor 1			
6	0.90	5 * 30 = 150	135
(5+4)	1.16 + 1.16 = 2.32	5 * 30 = 150	348
(b) Floor 2			
6	1.06	5 * 30 = 150	160
(5+4)	1.16 + 1.16 = 2.32	5 * 30 = 150	348
(c) Floors 3 to 9			
6	1.00	5 * 30 = 150	150
(5+4)	1.16 + 1.16 = 2.32	5 * 30 = 150	348
(d) Roof			
6	0.85	5 * 30 = 150	127
(5+4) AB,DE,EF	1.03 + 1.03 = 2.06	3 * 30 = 90	185 + 183 = 369
(5+4) BC,CD	1.03 + 2.03 = 3.06	2 * 30 = 60	

[a] # bays

Table B-7. Summary of column (point) gravity loads for LA9.

rid Point (1)	Point Load k (2)	# Locations (3)	Total Load k (4)
(a) Floor 1			
6 A,F	22.8	2	46 + 139 = 185
6 B,C,D,E	34.8	4	
(5+4) A,F	44.4 + 44.4 = 88.9	2	178 + 557 = 735
(5+4) B,C,D,E	69.6 + 69.6 = 139.2	4	
(b) Floor 2			
6 A,F	25.5	2	51 + 139 = 190
6 B,C,D,E	34.8	4	
(5+4) A,F	49.3 + 49.3 = 98.6	2	197 + 557 = 754
(5+4) B,C,D,E	69.6 + 69.6 = 139.2	4	
(c) Floors 3 to 9			
6 A,F	24.5	2	49 + 139 = 188
6 B,C,D,E	34.8	4	
(5+4) A,F	47.4 + 47.4 = 94.9	2	190 + 557 = 747
(5+4) B,C,D,E	69.6 + 69.6 = 139.2	4	
(b) Roof			
6 A,F	21.0	2	42 + 124 = 166
6 B,C,D,E	30.9	4	
(5+4) A,F	40.9 + 40.9 = 81.8	2	164 + 296 + 158 + 124 = 741
(5+4) B,D	61.8 + 86.2 = 148.0	2	
(5+4) C	61.8 + 96.6 = 158.4	1	
(5+4) E	61.8 + 61.8 = 123.6	1	

Table B-8. Summary of beam (distributed) gravity loads for LA20.

Grid Line (1)	Distributed Load k/ft (2)	Length #[a] ft ft (3)	Total Load k (4)
(a) Floor 1			
7	0.90	5 * 20 = 100	90
5	1.16	2 * 40 + 1 * 20 = 100	116
(b) Floor 2			
7	1.06	5 * 20 = 100	106
5	1.16	2 * 40 + 1 * 20 = 100	116
(c) Floors 3 to 20			
7	1.00	5 * 20 = 100	100
5	1.16	2 * 40 + 1 * 20 = 100	116
(d) Roof			
7	0.85	5 * 20 = 100	85
5 ABC, DEF	1.03	2 * 40 = 80	82 + 41 = 123
5 CD	2.03	1 * 20 = 20	

[a] # bays

Table B-9. Summary of column (point) gravity loads for LA20.

rid Point (1)	Point Load k (2)	# Locations (3)	Total Load k (4)
(a) Floor 1			
7 A,F	15.4	2	31 + 104 = 135
7 C,D	52.2	2	
5 A,F	29.6	2	59 + 209 = 268
5 C,D	104.4	2	
(6+4) A,F	52.8 + 26.4 = 79.2	2	158
(b) Floor 2			
7 A,F	17.3	2	35 + 104 = 139
7 C,D	52.2	2	
5 A,F	32.9	2	66 + 209 = 275
5 C,D	104.4	2	
(6+4) A,F	56.1 + 28.0 = 84.1	2	168
(c) Floors 3 to 20			
7 A,F	16.6	2	33 + 104 = 138
7 C,D	52.2	2	
5 A,F	31.6	2	63 + 209 = 272
5 C,D	104.4	2	
(6+4) A,F	54.8 + 27.4 = 82.2	2	164
(b) Roof			
7 A,F	14.2	2	28 + 93 = 121
7 C,D	46.4	2	
5 A,F	27.3	2	55 + 238 = 293
5 C,D	119.1	2	
(6+4) A,F	47.9 + 23.9 = 71.8	2	144

List of References

Aagaard, B.T., Hall, J.F., Heaton, T.H. (2001), "Characterization of near-source ground motions with earthquake simulations," *Earthquake Spectra*, 17(2): 177-207.

Abrahamson, N.A., Silva, W.J. (1997), "Empirical response spectral attenuation relations for shallow crustal earthquakes," *Seismological Research Letters*, 68(1): 94-127.

Alavi, B., Krawinkler, H. (2000), "Effects of near-fault ground motions on frame structures," *John A Blume Earthquake Engineering Center Report No. 138*, Department of Civil and Environmental Engineering, Stanford University, California.

Allen, D.W., Castillo, S., Cundy, A.L., Farrar, C.R., McMurry, R.E. (2001), "Damage detection in building joints by statistical analysis," *Proceedings of the 19th International Modal Analysis Conference*, Kissimmee, Florida.

Anderson, J.C., Bertero, V.V. (1987), "Uncertainties in establishing design earthquakes," *ASCE Journal of Structural Engineering*, 113(8): 1709-1724.

Anderson, J.C., Johnston, R.G., Partridge, J.E. (1996), "Testing of damaged steel moment resisting connections," *Proceedings of the 11th World Conference on Earthquake Engineering*, Acapulco, Mexico.

Anderson, J.C., Johnston, R.G., Partridge, J.E. (1998), "Post earthquake testing of damaged moment connections," *Proceedings of the NEHRP Conference and Workshop on Research on the Northridge, California Earthquake of January 17, 1994, Vol. III-B, pp. 478-486*, California Universities for Research in Earthquake Engineering (CUREe), Richmond, California.

Attalla, M.R., Paret, T.F., Freeman, S.A. (1998), "Near-source behavior of buildings under pulse-type earthquakes," *Proceedings of the 6th U.S. National Conference on Earthquake Engineering*, Earthquake Engineering Research Institute, Oakland, California.

Baez, J.I., Miranda, E. (2000), "Amplification factors to estimate inelastic displacement demands for the design of structures in the near field," *Proceedings of 12th World Conference on Earthquake Engineering, Paper No. 1561*, New Zealand Society for Earthquake Engineering, Upper Hutt, New Zealand.

Bazzurro, P. (1998), "Probabilistic seismic demand analysis," *Ph.D. Dissertation*, Department of Civil and Environmental Engineering, Stanford University, California.

Bazzuro P., Cornell, C.A. (1999), "Disaggregation of seismic hazard," *Bulletin of the Seismological Society of America*, 89(2): 501-520.

Bazzurro, P., Cornell, C.A. (2002), "Vector-valued probabilistic seismic hazard analysis (VPSHA)," *Proceedings of the 7th U.S. National Conference on Earthquake Engineering, Paper No. 61*, Boston, Massachusetts.

Benjamin J.R., Cornell C.A. (1970), Probability, Statistics, and Decision for Civil Engineers, *McGraw Hill, Inc.*, New York.

Bertero, V.V., Mahin, S.A., Herrera, R.A. (1978), "Aseismic design implications of near-fault San Fernando earthquake records," *Earthquake Engineering and Structural Dynamics*, 6(1): 31-42.

Carballo, J.E., Cornell, C.A. (2000), "Probabilistic seismic demand analysis," *Reliability of Marine Structures Program Report No. RMS-41*, Department of Civil and Environmental Engineering, Stanford University, California.

Chopra, A.K. (1995), Dynamics of Structures: Theory and Applications to Earthquake Engineering, 1st Edition, Prentice Hall, New Jersey.

Collins K.R., Wen Y.K., Foutch D.A. (1995), "Investigation of alternative seismic design procedures for standard buildings," *Civil Engineering Studies, Structural Research Series No. 600*, Department of Civil Engineering, University of Illinois at Urbana-Champaign.

Collins, K.R., Wen, Y.K., Foutch, D.A. (1996), "Dual-level seismic design: a reliability-based methodology," *Earthquake Engineering & Structural Dynamics*, 25(12): 1433-1467.

Cordova, P.P., Mehanny, S.S.F., Deierlein, G.G., Cornell, C.A. (2000), " Development of a two-parameter seismic intensity measure and probabilistic assessment procedure," *Proceedings of the 2nd U.S.-Japan Workshop on Performance-Based Seismic Earthquake Engineering Methodology for Reinforced Concrete Building Structures*, Sapporo, Japan: 195-214.

Cornell, C.A. (1968), "Engineering seismic risk analysis," *Bulletin of the Seismological Society of America*, 58(5): 1583-1606.

Cornell, C.A. (1996), "Calculating building seismic performance reliability: a basis for multi-level design norms," *Proceedings of the 11th World Conference on Earthquake Engineering, Paper No. 2122*, Acapulco, Mexico.

Cornell, C. A., Luco, N. (1999), "The effects of connection fractures on steel moment resisting frame seismic demands and safety: a report on SAC Phase II Task 5.4.6," *SAC Background Report No. SAC-BD/99-03*, SAC Joint Venture, Sacramento, California.

Cornell, C.A., Krawinkler, H. (2000), "Progress and challenges in seismic performance assessment," *PEER Center News*, Vol. 3, No. 2.

Cornell, C.A., Jalayer, F., Hamburger, R.O., Foutch, D.A. (2002), "The probabilistic basis for the 2000 SAC/FEMA steel moment frame guidelines," *ASCE Journal of Structural Engineering*, 128(4): 526-533.

FEMA 273 (1997), "NEHRP guidelines for the seismic rehabilitation of buildings," Federal Emergency Management Agency, Washington, D.C.

FEMA 274 (1997), "NEHRP commentary on the guidelines for the seismic rehabilitation of buildings," Federal Emergency Management Agency, Washington, D.C.

FEMA 289 (1997), "SAC Buildings Project Test Summaries (SAC Tech. Report No. 96-02)," Federal Emergency Management Agency, Washington, D.C.

FEMA 350 (2000), "Recommended seismic design criteria for new steel moment-frame buildings," *SAC Joint Venture*, Sacramento, California.

FEMA 351 (2000), "Recommended seismic evaluation and upgrade criteria for existing welded steel moment-frame buildings," *SAC Joint Venture*, Sacramento, California:.

FEMA 352 (2000), "Recommended post-earthquake evaluation and repair criteria for welded steel moment-frame buildings," *SAC Joint Venture*, Sacramento, California.

FEMA 353 (2000), "Recommended specifications and quality assurance guidelines for steel moment-frame construction for seismic applications," *SAC Joint Venture*, Sacramento, California.

FEMA 355C (2000), "State of the art report on systems performance of steel moment frames subject to earthquake ground shaking," *SAC Joint Venture*, Sacramento, California.

Foutch, D.A., Shi, S. (1996), "Connection element (type 10) for DRAIN-2DX," Department of Civil Engineering, University of Illinois at Urbana-Champaign.

Freeman, S.A., Nicoletti J.P., Tyrell J.V. (1975), "Evaluations of existing buildings for seismic risk – A case study of Puget Sound Naval Shipyard, Bremerton, Washington," *Proceedings of the 1st U.S. National Conference on Earthquake Engineering*, Berkeley, California: 113-122.

Gupta, A., Krawinkler, H. (1999), "Seismic demands for performance evaluation of steel moment resisting frame structures," *John A. Blume Earthquake Engineering Center Report No. 132*, Department of Civil and Environmental Engineering, Stanford University, California.

Gupta, A., Krawinkler, H. (2000), "Behavior of ductile SMRFs at various seismic hazard levels," *ASCE Journal of Structural Engineering*, 126(1): 98-107.

Hall, J.F., Heaton, T.H., Malling, M.W., Wald, D.J. (1995), "Near-source ground motion and its effects on flexible buildings," *Earthquake Spectra*, 11(4): 569-605.

Hall, J.F. (1998), "Seismic response of steel frame buildings to near-source ground motions," *Earthquake Engineering & Structural Dynamics*, 27(12): 1445-1464.

Heaton, T. H., Hall, J.F., Wald, D.J., Halling, M.W. (1995),"Response of high-rise and base-isolated buildings to a hypothetical M_w 7.0 blind thrust earthquake," *Science*, 267(5195): 206-211.

Inoue, T., Cornell, C.A. (1990), "Seismic hazard analysis of multi-degree-of-freedom structures," *Reliability of Marine Structures Program Report No. RMS-8*, Department of Civil and Environmental Engineering, Stanford University, California.

Iwan, W.D. (1980), "Estimating inelastic response spectra from elastic spectra," *Earthquake Engineering and Structural Dynamics*, 8(4): 375-388.

Iwan, W.D. (1996), "The drift demand spectrum and its application to structural design and analysis," *Proceedings of the 11th World Conference on Earthquake Engineering, Paper No. 1116*, Acapulco, Mexico.

Lee, K.H., Stojadinovic, B., Goel, S.C., Margarian, A.G., Choi, J., Wongkaew, A., Reyher, B.P., Lee, D.Y. (2000), "Parametric tests on unreinforced connections," *SAC Background Report No. SAC/BD-00/01*, SAC Joint Venture, Sacramento, Californias.

Lee, K., Foutch, D.A. (2002), "Seismic performance evaluation of pre-Northridge steel frame buildings with brittle connections," *ASCE Journal of Structural Engineering*, 128(4): 546-555.

Liu, J., Astaneh-Asl, A. (2000), "Cyclic testing of simple connections including effects of slab," *ASCE Journal of Structural Engineering*, 126(1): 32-39.

Luco, N., Cornell, C.A. (1998), "Effects of random connection fractures on the demand and reliability for a 3-story pre-Northridge SMRF structure," *Proceedings of the 6th U.S. National Conference on Earthquake Engineering*, Seattle, Washington.

Luco, N., Cornell, C.A. (2000), "Effects of connection fractures on SMRF seismic drift demands," *ASCE Journal of Structural Engineering*, 126(1): 127-136.

Luco, N., Cornell, C.A. (2002), "Structure-specific scalar intensity measures for near-source and ordinary earthquake ground motions," *Under revision for publication in Earthquake Spectra*.

Luco, N., Mori, Y., Funahashi, Y., Cornell, C.A., Nakashima, M. (2002a), "Evaluation of predictors of nonlinear seismic demands using "fishbone" models of SMRF buildings," *In preparation, to be submitted to Earthquake Engineering and Structural Dynamics*.

Luco, N., Cornell, C.A., Yeo, G.L. (2002b), "Annual limit-state frequencies for partially-inspected earthquake-damaged buildings," *Structural Safety*, 24: 281-296.

Mai, P.M., Beroza, G.C. (2000), "Source scaling properties from finite-fault-rupture models," *Bulletin of the Seismological Society of America*, 90(3): 604-615.

Mai, P.M. (2002), "Characterizing earthquake source complexity for improved strong motion prediction," *Ph.D. Dissertation*, Department of Geophysics, Stanford University, California.

Mai, P.M., Guatteri, M., Beroza, G.C. (2002), "A stochastic-dynamic earthquake source model for strong motion prediction," *Proceedings of the 7th U.S. National Conference on Earthquake Engineering*, Boston, Massachusetts.

Maison, B.F., Bonowitz, D. (1999), "How safe are pre-Northridge WSMFs? A case study of the SAC Los Angeles nine-story building," *Earthquake Spectra*, 15(4): 765-789.

Mehanny, S.S.F. (1999), "Modeling and assessment of seismic performance of composite frames with reinforced concrete columns and steel beams," *Ph.D. Dissertation*, Department of Civil and Environmental Engineering, Stanford University, California.

Nakashima, M., Ogawa, K., Inoue, K. (2002), "Generic frame model for simulation of earthquake responses of steel moment frames," *Earthquake Engineering & Structural Dynamics*, 31(3): 671-692.

Niazi, M. (1986), "Accelerograms of the 1978 Tabas, Iran, earthquake," *Earthquake Spectra*, 2(3): 635-651.

Porter, K.A., Kiremidjian, A.S. (2001), "Assembly-based vulnerability of buildings and its uses in seismic performance evaluation and risk management decision-making," *John A. Blume Earthquake Engineering Center Report No. 139*, Department of Civil and Environmental Engineering, Stanford University, California.

Porter, K.A., Kiremidjian, A.S., LeGrue, J.S. (2001), "Assembly-based vulnerability of buildings and its use in performance evaluation," *Earthquake Spectra*, 17(2): 291-312.

Prakash, V., Powell, G.H., Campbell, S. (1993), "DRAIN-2DX base program description and user guide, version 1.10," *Report No. UCB/SEMM-93/17*, Department of Civil Engineering, University of California at Berkeley.

SAC 95-04 (1995), "Analytical and field investigations of buildings affected by the Northridge earthquake of January 17, 1994," SAC Joint Venture, Sacramento, California.

SEAOC Blue Book (1999), "Recommended lateral force requirements and commentary," Structural Engineers Association of California, Sacramento, California.

Shi, S. (1997), "Evaluation of connection fracture and hysteresis type on the seismic response of steel buildings," *Ph.D. Thesis*, Department of Civil Engineering, University of Illinois at Urbana-Champaign.

Shome, N., Cornell, C.A., Bazzurro, P., Carballo, J.E. (1998), "Earthquakes, records, and nonlinear responses," *Earthquake Spectra*, 14(3): 469-500.

Shome N., Cornell C.A. (1999), "Probabilistic seismic demand analysis of nonlinear structures," *Reliability of Marine Structures Program Report No. RMS-35*, Department of Civil and Environmental Engineering, Stanford University, California.

Shome, N., Cornell, C.A. (2000), "Structural seismic demand analysis: consideration of collapse," *ASCE Specialty Conference on Probabilistic Mechanics and Structural Reliability*, Notre Dame, Indiana.

Silva, W. (1999), "Strong Motion Database CD-ROM," Pacific Engineering and Analysis, El Cerrito, California (also available at http://peer.berkeley.edu/smcat).

Somerville, P.G., Smith, N., Punyamurthula, S., Sun, J. (1997a), "Development of ground motion time histories for phase II of the FEMA/SAC steel project," *SAC Background Report No. SAC/BD-97/04*, SAC Joint Venture, Sacramento, California.

Somerville, P.G., Smith, N.F., Graves, R.W., Abrahamson, N.A. (1997b), "Modification of empirical strong ground motion attenuation relations to include the amplitude and duration effect of rupture directivity," *Seismological Research Letters*, 68(1): 199-222.

Somerville, P.G. (1998), "Development of an improved ground motion representation for near-fault ground motions," *SMIP98 Seminar on Utilization of Strong Motion Data*, Oakland, California.

Somerville, P.G., Irikura, K., Graves, R., Sawada, S., Wald, D., Abrahamson, N., Iwasaki, Y., Kagawa, T., Smith, N., Kowada, A. (1999), "Characterizing crustal earthquake slip models for the prediction of strong ground motion," *Seismological Research Letters*, 70(1): 59-80.

Somerville, P.G. (2001), "Issue A – Should near fault directivity be modeled in national ground motion mapping?" *Proceedings of the 2nd ATC-35 Workshop on National Earthquake Ground-Motion Mapping*, San Francisco, California.

Song, J., Ellingwood, B.R. (1998), "Seismic reliability evaluation of steel frames with damaged welded connections," *Ph.D. Dissertation*, Department of Civil Engineering, Johns Hopkins University, Baltimore, Maryland.

Song J., Ellingwood, B.R. (1999), "Seismic reliability of special moment steel frames with welded connections, II," *ASCE Journal of Structural Engineering*, 125(4): 372-384.

UBC (1994), "Uniform Building Code," International Conference of Building Officials, Whittier, California.

Vamvatsikos, D., Cornell, C.A. (2002), "Incremental dynamic analysis," *Earthquake Engineering & Structural Dynamics*, 31(3): 491-514.

Veletsos, A.S., Newmark, N.M. (1960), "Effect of inelastic behavior on the response of simple systems to earthquake motions," *Proceedings of the 2nd World Conference on Earthquake Engineering, pp. 895-912*, Tokyo, Japan.

Veletsos, A.S., Newmark, N.M., Chelapati, C.V. (1965), "Deformation spectra for elastic and elastoplastic systems subjected to ground shock and earthquake motions," *Proceedings of the 3rd World Conference on Earthquake Engineering, Vol. II, pp. 663-682*, New Zealand National Committee on Earthquake Engineering, Wellington, New Zealand.

Younan A., Banon H., Marshall P., Crouse C.B., Cornell C.A. (2001), "An overview of the ISO Seismic Guidelines," *Proceedings of the Offshore Technology Conference 2001*, Houston, Texas.

Yun, S.Y., Foutch, D.A. (2000), "Performance prediction and evaluation of low ductility steel moment frame for seismic loads," *SAC Background Report No. SAC/BD-00/26*, SAC Joint Venture, Sacramento, California.

Wen, Y.K. (1997), "Proposed statistical and reliability framework for comparing and evaluating predictive models for evaluation and design, *SAC Background Report No. SAC/BD-97/03*, SAC Joint Venture, Sacramento, California.

Woodward-Clyde Consultants (1991), "Evaluation of site response and design earthquake motions: Stanford University, Palo Alto, California," *Draft Report prepared for Stanford University Facilities Project Management*, Stanford, California.

Working Group on California Earthquake Probabilities (1999), "Earthquake probabilities in the San Francisco bay region: 2000 to 2030," *U.S. Geological Survey Open-File Report 99-517*, Menlo Park, California.